UNIVERSIDADE ESTADUAL DE CAMPINAS
FACULDADE DE ENGENHARIA MECÂNICA
E INSTITUTO DE GEOCIÊNCIAS

HENRIQUE BUENO DOS SANTOS

# INITIAL DEPTH MODEL BUILDING USING ROBUST TIME-MIGRATION VELOCITY ANALYSIS METHODS

# CONSTRUÇÃO DE UM MODELO INICIAL EM PROFUNDIDADE USANDO MÉTODOS ROBUSTOS DE ANÁLISE DE VELOCIDADE POR MIGRAÇÃO EM TEMPO

CAMPINAS
2015

HENRIQUE BUENO DOS SANTOS

# INITIAL DEPTH MODEL BUILDING USING ROBUST TIME-MIGRATION VELOCITY ANALYSIS METHODS

# CONSTRUÇÃO DE UM MODELO INICIAL EM PROFUNDIDADE USANDO MÉTODOS ROBUSTOS DE ANÁLISE DE VELOCIDADE POR MIGRAÇÃO EM TEMPO

Thesis presented to the Mechanical Engineering Faculty and Geosciences Institute of the University of Campinas in partial fulfillment of the requirements for the degree of Doctor in Petroleum Sciences and Engineering in the area of Reservoirs and Management.

Tese apresentada à Faculdade de Engenharia Mecânica e Instituto de Geociências da Universidade Estadual de Campinas como parte dos requisitos exigidos para a obtenção do título de Doutor em Ciências e Engenharia de Petróleo na área de Reservatórios e Gestão.

Orientador: Prof. Dr. Joerg Dietrich Wilhelm Schleicher
Coorientadora: Profa. Dra. Maria Amélia Novais Schleicher

Este exemplar corresponde à versão final da Tese defendida pelo aluno Henrique Bueno dos Santos, e orientada pelo Prof. Dr. Joerg Dietrich Wilhelm Schleicher.

Assinatura do Orientador

CAMPINAS
2015

**Agência(s) de fomento e nº(s) de processo(s):** Não se aplica.
**ORCID:** https://orcid.org/0000-0001-9055-6990

Ficha catalográfica
Universidade Estadual de Campinas
Biblioteca da Área de Engenharia e Arquitetura
Luciana Pietrosanto Milla - CRB 8/8129

Santos, Henrique Bueno dos, 1986-
Sa59i Initial depth model building using robust time-migration velocity analysis methods / Henrique Bueno dos Santos. – Campinas, SP : [s.n.], 2015.

Orientador: Joerg Dietrich Wilhelm Schleicher.
Coorientador: Maria Amélia Novais Schleicher.
Tese (doutorado) – Universidade Estadual de Campinas, Faculdade de Engenharia Mecânica.
Em regime multiunidades com: Instituto de Geociências.

1. Geofísica. 2. Método sísmico de reflexão. 3. Propagação de ondas. I. Schleicher, Joerg Dietrich Wilhelm, 1964-. II. Schleicher, Maria Amélia Novais, 1967-. III. Universidade Estadual de Campinas. Faculdade de Engenharia Mecânica. IV. Título.

Informações para Biblioteca Digital

**Título em outro idioma:** Construção de um model inicial em profundidade usando métodos robustos de análise de velocidade por migração em tempo
**Palavras-chave em inglês:**
Geophysics
Seismic reflection method
Wave propagation
**Área de concentração:** Reservatórios e Gestão
**Titulação:** Doutor em Ciências e Engenharia de Petróleo
**Banca examinadora:**
Joerg Dietrich Wilhelm Schleicher [Orientador]
Ricardo Caetano Azevedo Biloti
Lúcio Tunes dos Santos
Reynam da Cruz Pestana
Claudio Guerra Cardoso
**Data de defesa:** 25-11-2015
**Programa de Pós-Graduação:** Ciências e Engenharia de Petróleo

UNIVERSIDADE ESTADUAL DE CAMPINAS
FACULDADE DE ENGENHARIA MECÂNICA
E INSTITUTO DE GEOCIÊNCIAS

TESE DE DOUTORADO

# INITIAL DEPTH MODEL BUILDING USING ROBUST TIME-MIGRATION VELOCITY ANALYSIS METHODS

# CONSTRUÇÃO DE UM MODELO INICIAL EM PROFUNDIDADE USANDO MÉTODOS ROBUSTOS DE ANÁLISE DE VELOCIDADE POR MIGRAÇÃO EM TEMPO

Autor: Henrique Bueno dos Santos
Orientador: Prof. Dr. Joerg Dietrich Wilhelm Schleicher
Coorientadora: Prof. Dr. Maria Amélia Novais Schleicher

A Banca Examinadora composta pelos membros abaixo aprovou esta Tese:

Prof. Dr. Joerg Dietrich Wilhelm Schleicher, Presidente
DMA/IMECC/UNICAMP

Prof. Dr. Ricardo Caetano Azevedo Biloti
DMA/IMECC/UNICAMP

Prof. Dr. Lúcio Tunes dos Santos
DMA/IMECC/UNICAMP

Prof. Dr. Reynam da Cruz Pestana
DGN/IGEO/UFBA

Dr. Claudio Guerra Cardoso
PETROBRAS/RJ

A Ata da defesa com as respectivas assinaturas dos membros encontra-se no processo de vida acadêmica do aluno.

Campinas, 25 de novembro de 2015.

*To my beloved parents*

*"Till now, madness has been thought a small island in an ocean of sanity. I am beginning to suspect that it is not an island at all but a continent."*

— Machado de Assis, *The Psychiatrist*

# Acknowledgments

*Nanos gigantum humeris insidentes.*
— Bernard of Chartres, a twelfth-century
French Neo-Platonist philosopher

*If I have seen further it is by standing on the shoulders of Giants.*
— Sir Isaac Newton (1976)

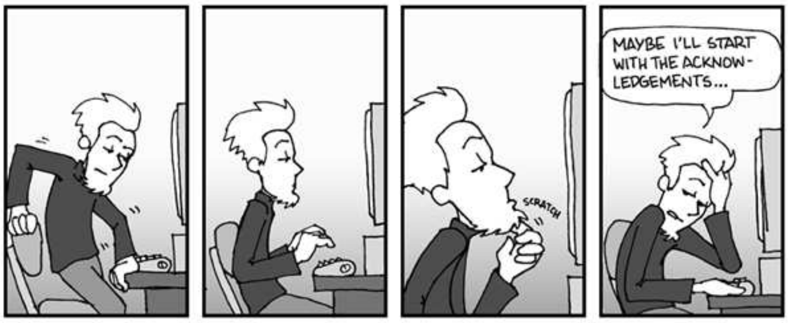

JORGE CHAM ©THE STANFORD DAILY phd.stanford.edu/comics

Even Sir Isaac Newton, one of the most brilliant and influential scientists in history, dedicated a time to express his gratitude. I am far from his brilliance and influence, but I have so many people and institutions to thank, without whom/which this thesis would not have been possible.

First of all, I would like to thank my advisor Professor Dr. Jörg Schleicher (Institute for Mathematics, Statistics, and Scientific Computing of University of Campinas, IMECC/UNICAMP) and my co-advisor Professor Dr. Amélia Novais (IMECC/UNICAMP), for the unlimited disposition to help me and to discuss academic and also personal issues. During all my Ph.D. you gave me the freedom to learn in my time, trying to find and fix my mistakes. Today, I recognize that I had a rare opportunity, possible only due to your respect, patience, and comprehension.

I use to tell my friends that I do not have advisors, but “professional godparents”. Moreover, I thank both of you for opening many doors in my professional life.

Also from IMECC/UNICAMP, I would like to thank Professors Dr. Lúcio T. Santos, Dr. Ricardo Biloti, and Dr. Martin Tygel for the great classes that were my basis at the very beginning of my doctoral studies.

Special thanks to Professor Dr. Jessé C. Costa (Federal University of Pará, UFPA) and his former student M.Sc. Leandro da Silva Sadala Valente (Petrobras) for their support concerning the use and development of computational codes employed in this work.

I thank the Center for Petroleum Studies (CEPETRO) and the Geophysical Computational Laboratory (LGC) for the infrastructure and support made available for the development of this work. Moreover, I would like to thank all my labmates for (not always scientific, but always pleasant) discussions, helpful technical support, and friendship, in special, Bruno Monserrat Perillo, José Jadsom Sampaio de Figueiredo, and Momoe Sakamori Pisnitchenko.

I would like to thank the Petroleum Science and Engineering (CEP) Program staff, in special, Michelle Cristina Fulaneto for being always helpful, competent and provident.

I would also like to thank some guys I had the opportunity to work with: Daniel L. Macedo, Edgar B. Santos, and Tiago A. Coimbra. Their valuable geophysical discussions and suggestions were critical to the development of this work.

I am very thankful to all the Karlsruhe Institute of Technology (KIT) team: mainly to Professor Dr. Thomas Bohlen for accepting me as an intern; to André Kurzmann, Niklas Thiel and Laura Gassner for many scientific discussions and their support concerning the seismic forward modeling and inversion codes. Many thanks also go to Claudia Payne for the constant help with all administrative and personal issues. Also to my Russian friend Renat Shigapov for sharing the office and for funny conversations. I would like to thank all the staff at KIT International Affairs (INTL), International Scholars and Welcome Office (IScO), Petra Roth, Anika Menchen and Oliver Kaas.

During my stay at Karlsruhe, I had the big pleasure to know the advisor of my advisor, Professor Dr. Peter Hubral, who I wish to thank for sharing his extensive knowledge and enthusiasm.

I thank Professor Dr. Alison Malcolm for inviting me for a short research visit at the Department of Earth, Atmospheric and Planetary Sciences (EAPS), at the Massachusetts Institute of Technology (MIT). During this visit, we discussed projects of mutual interest.

I thank Dr. Tadeu Vidal and Dr. Thomas Hertweck for discussions and insightful comments.

Big thanks to Professor Dr. Valéria C. F. Barbosa (Brazilian National Observatory, ON). I could not have met a more friendly professor.

I would like to thank the Compagnie Générale de Géophysique (CGG), Petrobras, and the Brazilian National Petroleum Agency (ANP) for my fellowships, as well as the Brazilian research agencies National Council for Scientific and Technological Development (CNPq), National Institute of Petroleum Geophysics (INCT-GP), São Paulo Research Foundation (FAPESP), Coordination for the Improvement of Higher Education Personnel (CAPES) and the Brazilian Innovation Agency (FINEP). Moreover, I thank INCT-GP for providing me the Technology and Industrial Development Grant (DTI-2-2, grant no. 382209/2015-0). Additional support for was provided by the sponsors of the Wave Inversion Technology (WIT) Consortium.

During these five years, I had the privilege of participating in relevant scientific events, presenting a significant part of the research contained in this thesis. I would like to acknowledge the European Association of Geoscientists & Engineers (EAGE) for providing me the travel grant through the Programme for Association and Cooperation in Earth Sciences (PACE) Delegate Support, which enabled me to attend at the 75th EAGE Conference & Exhibition incorporating SPE EUROPEC 2013 in London, United Kingdom.

My sincere gratitude to KIT, Alexander von Humboldt Foundation, and the German Ministry of Education and Research (BMBF) for choosing and supporting me to attend the 2nd Research Alumni Conference Germany 2014, in Berlin.

I would like to thank the Society of Exploration Geophysicists (SEG), SEG Foundation, SEG Travel Grant Committee, and Chevron, for providing me the SEG/Chevron Student Leadership Symposium (SLS) travel grant to participate in the SLS program representing the SEG Chapter Campinas, and to attend the 2015 SEG International Exposition and 85th Annual Meeting in New Orleans, USA. Moreover, I want to acknowledge the Student and Early Career Team, especially, the Student and Early Career Advisor, Johnna Yoder, for assisting me several times.

I appreciate the opportunity to work with different seismic data sets, velocity models and processing codes that were made available to me. In particular, I thank Gilles Lambaré and Pascal Podvin for making the Marmousoft data set available. I would like to thank Institut Français du Pétrole (IFP) and the University of Houston (UH) for generating and distributing the Marmousi models. I would like to thank the Subsalt Multiples Attenuation and Reduction Team Joint Venture (SMAART JV) for providing the Sigsbee2B NFS data set. I thank the Center for

Wave Phenomena (CWP) of Colorado School of Mines for providing the open-source software project Seismic Un*x (SU). I would like to thank the open-source software project Madagascar for providing the codes, scripts and North Sea data used in this work.

Furthermore, I am grateful for using the supercomputers Jülich Research on Petaflop Architectures (JUROPA) at Jülich Supercomputing Centre (JSC), bwUniCluster, and InstitutsCluster II (IC2) at Steinbuch Centre for Computing (SCC) at KIT, and on the computational resource ForHLR, funded by Ministry of Science, Research and the Arts Baden-Württemberg and the German Research Foundation (DFG, "Deutsche Forschungsgemeinschaft").

Although I wish to thank all my friends and relatives, it is impossible to mention everyone's name. However, I would never forgive me if I failed to mention some friends who have been helping me to face life's challenges. They are Cleiton Keforf Pavan, Danilo Milaré, Franklin Bispo-Santos, Garrafa Borges Boldo, Marco Poli, Renan Antonialli, Rúbia Zanutto Bianchini Milaré, and Soraia Carlos Mendes. Among my relatives, I would like to extend my sincere gratitude to my grandparents Lúzia Gomes dos Reis and Pedro Ferreira dos Reis, my in-laws Vera Lúcia Pereira Ramos and Antonio (Kiko) Carlos Ramos (*in memoriam*). Also, special thanks go to my cousin Douglas Silvestre who is always willing to help me and to review my most simplistic texts. Doga, you rock!

My beloved wife Carolina Ramos Bueno, I thank you with all my heart and soul. First to be my best friend since we met in 2001, for all your attention, companionship, complicity, patience and respect. I cannot imagine how hard it is for you abdicate your professional dreams in favor of mine. Thank you for your unwavering belief in my potential. Furthermore, I thank you for giving me the most valuable gifts of my life, our daughter Olívia Ramos Bueno and our son Antônio Ramos Bueno. Carol, I have no words to express my feelings. Please, I ask you to consider each character of this thesis as proof of my love and gratitude.

And what to say to Olívia and Antônio? My little princess, I thank you for giving me "superpowers". Since you were born, I have learned a lot from you and with you. Moreover, I have figured out that I can do much more, and this it is only possible due to the restorative energy that I get every time I see the brightness of your eyes and your wonderful smile. My little prince, you had not even been born and had already changed the whole dynamic of my life. I was extremely anxious awaiting your birth, and I want you to know that much of this work was done thinking about you. Paradoxically, at the same time that you two are my Sun, you are also my Kryptonite. I love you.

The last, but not the least, of my most heartfelt thanks, are reserved for my brother Edgar Bueno dos Santos and my parents, Valter Bueno dos Santos and Nelci Aparecida dos Reis dos Santos, for your unconditional love, union, education, for long conversations, laughter, and tireless dedication. Thank you, Dad, for always encouraging me to ask questions and to be curious about the functioning of all. Join you in building our house and learn how to use your tools, provided me with the knowledge that no school is capable of. Thank you, Mom, for teaching me to be disciplined and above all dedicated. Your passion for reading is a contagious virtue. By the way, the epigraph of this thesis refers to one of the first books you ~~forced~~ encouraged me to read when I was a kid. Mom and Dad, both of you are examples not only for me but for everyone who has the pleasure of knowing you. Without you I am nothing! I love you so much, and it is with great pride that I dedicate this thesis to you, because in the "Land of Giants" you are the bigger ones.

# Resumo

A necessidade de investigar regiões formadas por estruturas geológicas complexas tem motivado o desenvolvimento de métodos de imageamento que atuem no domínio da profundidade. Exemplos notáveis são as técnicas de migração pré-empilhamento em profundidade (PSDM, do inglês "*prestack depth migration*") e a tomografia de onda completa (FWT, do inglês "*full-waveform tomography*"). No entanto, a aplicação desses métodos enfrenta ao menos dois desafios: eles requerem (1) um modelo de velocidade (inicial) preciso, e (2) elevado poder computacional. Por outro lado, a migração em tempo provou ser um processo robusto e muito rápido, tornando-se rotineiramente empregado para o imageamento sísmico. Além disso, a construção de modelos de velocidade em tempo é um processo bem compreendido. Portanto, é altamente desejável usar as técnicas de conversão tempo-profundidade para construir, a partir desses modelos de velocidade no domínio do tempo, modelos de velocidade iniciais para técnicas que operam em profundidade. Neste trabalho, investigamos a aplicabilidade de um fluxo de trabalho formado por alguns recém-desenvolvidos métodos (semi-) automáticos de análise de velocidade de migração em tempo (MVA, do inglês "*migration velocity analysis*"), capazes de gerar modelos de velocidade e imagens migradas no tempo sem precisar de informações a priori, seguido por uma técnica robusta de conversão tempo-profundidade. Discutimos as vantagens e limitações desse fluxo de trabalho e suas perspectivas para se tornar uma ferramenta plenamente automática, capaz de gerar modelos de velocidade sísmica para o uso subsequente em métodos de FWT. Nos nossos testes em diferentes versões dos dados Marmousi, o procedimento proposto produziu modelos de velocidade iniciais suficientemente precisos para uma FWT sob condições quase ideais. Começando no modelo de velocidade do domínio do tempo convertido para profundidade, a FWT convergiu para um modelo final com qualidade comparável a quando feito a partir de uma versão suavizada do modelo de velocidade verdadeiro. Isso indica que a correta informação sobre a velocidade de fundo pode ser extraída com sucesso pela MVA automática no domínio do tempo mesmo em meios onde a migração em tempo não pode fornecer imagens sísmicas satisfatórias. Como resultado, esta tese não só contribui para o desenvolvimento de um fluxo de trabalho para a construção de modelos de velocidade iniciais para a FWT, mas também apresenta várias aplicações inovadoras.

**Palavras-chave:** Geofísica; Método sísmico de reflexão; Propagação de ondas.

# Abstract

The need to investigate regions with complex geology has encouraged the development of imaging methods that act in the depth domain. Notable examples are prestack depth migration (PSDM) and full-waveform tomography (FWT). However, the application of these techniques faces at least two challenges: they require (1) an accurate (initial) velocity model and (2) massive computation power. In contrast, time migration has proven to be a fast and robust process, making it routinely used for seismic imaging. Moreover, time-domain velocity-model building is a well-understood process. Therefore, it is highly desirable to use time-to-depth conversion to construct starting models for depth-imaging techniques from these time-domain velocity models. In this work, we investigate the applicability of a workflow consisting of some recent (semi-) automatic time migration-velocity-analysis (MVA) methods, which can generate a velocity model and a time-migrated image without a priori information, followed by a robust time-to-depth conversion technique. We discuss advantages and limitations of this workflow and its perspectives to become a fully automatic tool, capable of generating initial seismic depth velocity models for subsequent FWT methods. In our tests on different versions of the Marmousi data, the proposed procedure produced sufficiently accurate initial models for an FWT under nearly ideal conditions. Starting at the depth-converted time-domain model, FWT converged to a final model of comparable quality as when starting at a smoothed version of the true velocity model. This indicates that correct background velocity information can be successfully extracted from automatic time-domain MVA even in media where time-migration cannot provide satisfactory seismic images. In effect, this thesis not only contributes to the development of a workflow for the construction of initial velocity-models for FWT but also presents several innovative applications thereof.

**Keywords:** Geophysics; Seismic reflection method; Wave propagation;

# List of figures

# List of tables

# List of algorithms

# List of acronyms and abbreviations

This list provides short definitions for most of the acronyms and abbreviations that are used in this thesis. All acronyms and abbreviations are defined at least briefly where they first appear in the text. Here, they are sorted alphabetically. Wherever possible, we used conventional acronyms and abbreviations.

| | |
|---|---|
| 1D | One-dimensional. |
| 2D | Two-dimensional. |
| 3D | Three-dimensional. |
| ANP | Brazilian National Petroleum Agency. |
| API | Application Programming Interface. |
| BCE | Before Common Era. |
| BMBF | German Ministry of Education and Research. |
| BSD | Berkeley Software Distribution (license). |
| bwUniCluster | Universal HPC cluster of Baden-Württemberg's universities. |
| CAPES | Coordination for the Improvement of Higher Education Personnel. |
| CE | Common Era. |
| CEP | Petroleum Science and Engineering. |
| CEPETRO | Center for Petroleum Studies. |
| CGG | Compagnie Générale de Géophysique. |
| CIG | Common-Image Gather. |
| CMP | Common-MidPoint. |
| CNPq | National Council for Scientific and Technological Development. |
| CRS | Common Reflection Surface. |
| CSEM | Controlled-Source Electromagnetic. |
| CSM | Colorado School of Mines. |
| CWP | Center for Wave Phenomena. |
| DEP | Department of Petroleum Engineering. |
| DFG | German Research Foundation. |

| | |
|---|---|
| DMA | Department of Applied Mathematics. |
| DSR | Double-Square-Root. |
| EAGE | European Association of Geoscientists & Engineers. |
| EAPS | Department of Earth, Atmospheric and Planetary Sciences. |
| EM | Electromagnetic. |
| FAPESP | São Paulo Research Foundation. |
| FD | Finite-Difference. |
| FEM | Faculty of Mechanical Engeneering. |
| FFD | Fourier Finite-Difference. |
| FINEP | Brazilian Innovation Agency. |
| FORTRAN | IBM Mathematical FORmula TRANslation System. |
| FSF | Free Software Foundation. |
| FWI | Full-Waveform Inversion. |
| FWT | Full-Waveform Tomography. |
| GCC | GNU Compiler Collection. |
| GG | Gravity Gradiometry. |
| GGT | Gravimetry Gradient Tensor. |
| GPL | General Public License. |
| HPC | High Performance Computing. |
| IC2 | InstitutsCluster II. |
| IFP | Institut Français du Pétrole. |
| IG | Geosciences Institute. |
| IGEO | Institute of Geosciences. |
| IMECC | Institute for Mathematics, Statistics, and Scientific Computing. |
| INCT-GP | National Institute of Petroleum Geophysics. |
| INTL | International Affairs. |
| IScO | International Scholars and Welcome Office. |
| JMI | Joint Migration Inversion. |
| JSC | Jülich Supercomputing Centre. |
| JUROPA | Jülich Research on Petaflop Architectures. |
| JV | Joint Venture. |
| KIT | Karlsruhe Institute of Technology. |
| LaTeX | Lamport TeX. |
| LGC | Geophysical Computational Laboratory. |
| LPPL | LaTeX Project Public License. |
| MATLAB | MATrix LABoratory. |
| MIT | Massachusetts Institute of Technology. |

| | |
|---|---|
| MPI | Message Passing Interface. |
| MT | Magnetotelluric. |
| MVA | Migration Velocity Analysis. |
| NFS | No Free Surface. |
| NMO | Normal-Moveout. |
| OBS | Ocean-Bottom Seismometer. |
| OMPI | Open MPI. |
| ON | Brazilian National Observatory. |
| OpenMP | Open Multi-Processing. |
| PACE | Programme for Association and Co-operation in Earth sciences. |
| Petrobras | Brazilian Petroleum Corporation. |
| PML | Perfectly Matched Layer. |
| PSDM | Prestack Depth Migration. |
| PSF | Python Software Foundation. |
| PSFL | Python Software Foundation License. |
| RMO | Residual-Moveout. |
| RMS | Root-Mean-Square. |
| SBGf | Brazilian Geophysical Society. |
| SCC | Steinbuch Centre for Computing. |
| SEC | Student Leadership Symposium. |
| SEG | Society of Exploration Geophysicists. |
| SLS | Student Leadership Symposium. |
| SLURM | Simple Linux Utility for Resource Management. |
| SMAART | Subsalt Multiples Attenuation and Reduction Technology. |
| SOFI2D | 2D viscoelastic time domain Seismic mOdeling with FInite differences. |
| SU | Seismic Un*x. |
| UFBA | Federal University of Bahia. |
| UFPA | Federal University of Pará. |
| UH | University of Houston. |
| UNICAMP | University of Campinas. |
| WIT | Wave Inversion Technology Consortium. |

# List of symbols

The main symbols and indices used in this thesis are listed below. They are sorted alphabetically, uppercase letters precede lowercase letters, and bold fonts precede regular fonts. The Greek letters succeed the Latin letters. Some symbols are composed and may have subscripts, superscripts, exponents, and indexes. More extensive explanations of all indices and symbols can be found in the text at those places where they appear for the first time. Other temporary symbols used in specific parts of the thesis are not presented in this list.

## Variables and symbols

### Latin letters

| | |
|---|---|
| $a$ | Constant; unknow in system equation. |
| $b$ | Constant; unknow in system equation. |
| $\mathbf{c}_n$ | Conjugate gradient. |
| $c$ | Constant; unknow in system equation; background velocity. |
| $c_0$ | Velocity in the background medium. |
| $D$ | Indicate the data space. |
| $D_h$ | Local slopes (event dips) in the migrated volume in the midpoint direction at all offsets $h$. |
| $D_{h_0}$ | Local slope (event dip) in the migrated common-offset section. |
| $\mathbf{d}_{mod}$ | Seismic data recorded at receivers on a medium represented by a set of model parameters $\mathbf{m}$. |
| $\mathbf{d}_{obs}$ | Seismic data recorded at receivers on a medium represented by a set of model parameters $\mathbf{m}$. |
| $E\left(\mathbf{m}\right)$ | Object function. |
| $\exp$ | Exponential function. |
| $f$ | Frequency; nonlinear forward operator. |
| $f_{max}$ | Maximum frequency of the wavefield. |

| | |
|---|---|
| $f_{min}$ | minimum frequency of the wavefield. |
| $f_{peak}$ | Peak frequency. |
| $\mathbf{H}$ | Hessian matrix of dimensions $M \times M$. |
| $\mathbf{H}_a$ | Approximate Hessian matrix. |
| $h$ | Half-offset. |
| $h_0$ | Zero-offset. |
| $i$ | Numbering. |
| $\mathbf{J}$ | Jacobian matrix also called the Fréchet derivate matrix. |
| $\mathbf{J}^T$ | Transpose of the Jacobian matrix. |
| $j$ | Numbering. |
| $K$ | Bulk modulus. |
| $k$ | Numbering. |
| $k_0$ | Single wavenumber component of a single source-receiver pair. |
| $k_x$ | Horizontal wavenumber. |
| $k_y$ | Horizontal component. |
| $k_z$ | Vertical wavenumber. |
| $L$ | Propagation distance. |
| $M$ | Indicate the model space. |
| $\mathbf{m}$ | Model vector of dimension $M$. |
| $\mathbf{m}_0$ | Starting model. |
| max | Maximum. |
| min | Minimum/optimization. |
| $N_\lambda$ | Propagation distance in wavelengths. |
| $N_t$ | Total number of times steps. |
| $N_x$ | Number of the grid points in $x$. |
| $N_z$ | Number of the grid points in $z$. |
| $\mathbf{n}$ | Direction of the gradient at each point $(x_j, z_j)$. |
| $n$ | Number of grid points per minimum wavelength $\lambda_{min}$. |
| $P$ | A quantity describing the dynamic property along the ray; preconditioning operator. |
| $P_j^n$ | Denotes the value of $P$ at the $j$th image-ray at $\gamma_j$ and at the $n$th time sample $\tau_n$. |
| $\mathbf{p}$ | Slowness vector. |
| $\mathbf{p_n}$ | Gradient. |
| $p$ | Pressure data. |
| $p^{'}$ | Backpropagated residual wavefield. |

| | |
|---|---|
| $p(\mathbf{x})$ | Two-dimensional function incorporated along the image-wavefront. See also $P$ and $\mathbf{x}$. |
| $p(x, z, t)$ | Pressure field. |
| $Q$ | A quantity describing the dynamic property along the ray. |
| $q(\mathbf{x})$ | Two-dimensional function incorporated along the image-wavefront. See also $Q$ and $\mathbf{x}$. |
| $R$ | Half offset-to-depth ratio. |
| $\hat{\mathbf{r}}$ | Unit tangent vector for the propagation direction of the receiver. |
| $S(t)$ | Source time function. |
| $\hat{\mathbf{s}}$ | Unit tangent vector for the propagation direction of the source. |
| $s$ | Scaling factor. |
| $T$ | Time coordinate; total arrival time of a event. |
| $T(h, x)$ | Time coordinate. |
| $\hat{\mathbf{t}}$ | Unit tangent vector to the wavefront. |
| $t$ | Time coordinate. |
| $t_0$ | Vertical time at zero-offset ($h_0$). |
| $t_h$ | Source-receiver traveltime. |
| $t_{h_0}$ | Source-receiver traveltime. |
| $t_r$ | Residual time displacement. |
| $V_P$ | P-wave velocity. |
| $V_{P_{max}}$ | Maximum P-wave velocity. |
| $V_{P_{min}}$ | Minimum P-wave velocity. |
| $V_S$ | S-wave velocity. |
| $v$ | True average medium velocity, i.e., the “ideal” time-migration velocity that would correctly position the image. |
| $v_0$ | Constant initial velocity. |
| $v^{\mathrm{Dix}}$ | Dix velocity at $(\gamma, \tau)$. |
| $v_{int}$ | Pseudo-time interval velocity in pseudo-time from the stratigraphic velocity. |
| $v_m$ | (incorrect) time migration velocity. |
| $v_n$ | NMO velocity. |
| $v_p$ | P-wave velocity. |
| $v_{rms}$ | Root-mean-square velocity model in pseudo-time from the stratigraphic velocity using vertical conversion only. |
| $v_s$ | S-wave velocity. |
| $v_u$ | Updated (time) migration velocity for $(x_m, \tau_{h_0})$ that minimizes the variation of $\tau_r$ in the offset direction. |

| | |
|---|---|
| $v(\mathbf{x})$ | Depth velocity field at $\mathbf{x}$. |
| $v(\mathbf{x}(\gamma, \tau))$ | Velocity field in depth along the image rays trajectories. |
| $v(x, z)$ | Depth velocity model. |
| $\mathbf{w}$ | Particle velocity. |
| $w_x(x, z, t)$ | Particle velocity in $x$ direction. |
| $w_z(x, z, t)$ | Particle velocity in $z$ direction. |
| $\mathbf{x}$ | Spatial position vector. |
| $\mathbf{x}_r$ | Receiver locations. |
| $\mathbf{x}_s$ | Source locations. |
| $x$ | Horizontal spatial coordinate; Spatial (image) position. |
| $x_m$ | Spatial coordinate of the image point in the time-migrated CIG. |
| $x_r$ | Residual lateral displacement. |
| $x_u$ | Updated (corrected) spatial position of the selected image point. |
| $\hat{\mathbf{z}}$ | Unit vector in the vertical direction. |
| $z$ | Vertical (depth) coordinate; depth of the scattering layers. |

## Greek letters

| | |
|---|---|
| $\alpha$ | Branch-cut rotation angle. |
| $\beta$ | Scalar (factor) computed through Polak-Ribiere method. |
| $\Delta$ | Specifies a difference quantity; difference operator; difference in the quantity that follows this symbol. |
| $\Delta h$ | Grid spacing. |
| $\Delta t$ | Time step. |
| $\Delta \tau$ | Time interval. |
| $\delta \mathbf{d}$ | Data misfit vector of dimension $N$. |
| $\delta \mathbf{m}$ | Perturbed model. |
| $\delta \mathbf{m}_n$ | Steepest descent gradient. |
| $\delta t$ | Travel time error. |
| $\delta \mathbf{x}$ | Dirac delta function. |
| $\eta$ | Coordinate direction perpendicular to the ray. |
| $\gamma$ | Spacial coordinate for a image point in a time migrated section. |
| $\gamma(\mathbf{x})$ | Spatial coordinate of a image-ray at $\mathbf{x}$. |
| $\lambda$ | Dominant wavelength. |
| $\lambda_{min}$ | Minimum wavelength. |
| $\mu$ | Step length. |
| $\nu$ | Dix interval velocity. |
| $\nu_j^n$ | Dix interval velocity $\nu(\gamma_j, \tau_n)$. |

| | |
|---|---|
| $\phi(\mathbf{x})$ | Image-wavefront represented as a zero-level set of a two-dimensional function. |
| $\rho$ | Density. |
| $\sigma$ | Standard deviation. |
| $\tau$ | Time coordinate. |
| $\tau_0$ | Time coordinate. |
| $\tau_h$ | Time coordinate at half-offset $h$ of the image point within the CIG at image position $x_m$. |
| $\tau_{h_0}$ | Time coordinate. |
| $\tau_n$ | $n$th time sample coordinate of a image-ray. |
| $\tau_r$ | 3D residual moveout. |
| $\tau_u$ | Updated (corrected) temporal position of the selected image point. |
| $\tau(\mathbf{x})$ | Time field at $\mathbf{x}$. |
| $\xi$ | Midpoint between source and receiver. |

## Math symbols

| | |
|---|---|
| $\approx$ | Approximately equal. |
| $*$ | Denotes the time convolution. |
| $\cdot$ | Symbolizes the scalar (or inner) product of two vectors. |
| $\equiv$ | Symbolizes the relation of equivalence. |
| $\in$ | Indicates that a variable is an element of a set. |
| $\Vert\ldots\Vert$ | Euclidian distance; norm. |
| $\Vert\ldots\Vert^2$ | Quadratic norm. |
| $\vert\ldots\vert$ | Absolute value; modulus. |
| $\cdots$ | Indicates omitted values from a pattern. |
| $\rightarrow$ | From . . . to. |
| $\infty$ | Infinity; an element of the extended number line that is greater than all real numbers; it often occurs in limits. |
| $\nabla$ | Gradient; differential operator given in a Cartesian coordinates $\{x, y, z\}$. |
| $\nabla_{\mathbf{x}}$ | Gradient; differential operator at $\mathbf{x}$. |
| $\partial$ | Partial derivative. |
| $\sum_i$ | Summation (operator). |
| $\sum\limits_i$ | Summation (operator). |
| $\times$ | Symbolizes the vector product of two vectors. |

# Indices

## Subscripts

| | |
|---|---|
| $a$ | Approximate. |
| $i$ | Numbering indices; $i$th. |
| $init$ | Initial. |
| $j$ | Numbering indices; specify quantity of $P$ belonging to the $j$th image-ray at $\gamma_j$. |
| $m$ | Numbering indices; $m$th. |
| $max$ | Maximum. |
| $min$ | Minimum. |
| $n$ | Numbering indices; $n$th. |
| $r$ | Residual. |
| $rms$ | Root-mean-square. |
| $st$ | Steps (sampling theorem). |
| $u$ | Updated. |
| $v$ | Velocity. |

## Superscripts

| | |
|---|---|
| © | Copyright. |
| ® | Registered. |
| ™ | Trademark. |
| $*$ | Denotes the adjoint of the operator $\frac{\partial \mathbf{d}(D)}{\partial \mathbf{m}}$. |
| $\mathrm{Dix}$ | Dix (velocity). |
| $n$ | Numbering indices; indicates a time step of $\tau_n$. |
| $PR$ | Polak-Ribiere (method). |
| $T$ | Denotes the matrix transpose. |

# Contents

*Is it a wave that looks like a mountain or a mountain that looks like a wave?*

The Great Wave off Kanagawa (Hokusai, 1830).

Being the best-known print in the series *Thirty-six Views of Mount Fuji*, Katsushika Hokusai's *The Great Wave off Kanagawa* has become one of the most famous work of art in the world and has inspired from music to poetry.

Some of the main elements which compose this two-dimensional image are: the sea and waves, which dominates the composition; three fishermen's boats, that may be used as reference to estimate the magnitude of the wave; a mountain, at the right of the image's center with a snow-capped peak, which represents the Mount Fuji, the highest mountain in Japan; the author's signature in the upper left-hand corner (it has two inscriptions); the sky in the background; the mesmerizing set of colors; and such more elements that should themselves deserve a whole book.

That said, let's disregard the many interpretations that the image may have and focus on the following: once we already know where we are and once we already know the elements mentioned above, the process for identifying them within the image can be done more easily. So, in few words, we need *a priori* information to be able to interpret the image. A quite simple representation of the reality. Just a two-dimensional image, but there is so much we can extract from a 2D image.

# Chapter 1

# Introduction

> *"Begin at the beginning," the King said gravely, "and go on till you come to the end: then stop."*
>
> — Carroll (1865), *Alice in Wonderland*

## 1.1 What is Geophysics?

Geophysics is a field of science focused on the investigation of the Earth with a multidisciplinary nature, e.g., knowledge of Physics, Mathematics, Chemistry, and Geology. Usually, it is subdivided into three major groups: Spatial Geophysics, which develops studies of terrestrial atmosphere and its interaction with environment; Solid Earth Geophysics, which investigates the structure and composition of Earth's interior; and Applied Geophysics, associated with the study of the structure and composition of the subsurface at lower depths (Telford et al., 1990).

Inside the field of Applied Geophysics, magnetic, electrical, electromagnetic, gravimetric and seismic methods are used mainly in studies for minerals and hydrocarbons exploration. They can be applied individually or together depending on the objective and necessity of the study, like regions of complex geology as the sedimentary basins.

Understanding sedimentary basins is critical to assessing oil potential. The knowledge of the distribution and evolution of the depositional sequences and its facies allow rational and realistic diagnostics about the localization of the oil-producing, oil-reservoir, and oil-bearing rocks, establishing, in this way, the fundamental elements of an oil system (Milani et al., 2000; Ribeiro, 2001; Pedreira et al., 2008; Allen and Allen, 2013).

Among all the geophysical tools applied to the hydrocarbons exploration, it is essential to highlight the importance of so-called seismic methods. Seismic investigations have a long history of use in the exploration, monitoring and management of the oil reservoirs, being the primary tool to delineate the subsoil structures and to detect the presence of hydrocarbons before drilling, which contributes to the economic evaluation and the exploratory risks (Telford et al., 1990; Sheriff and Geldart, 1995; Ribeiro, 2001).

We can say that the development of scientific and technological research related to seismic methods contributed significantly to Brazil's success in deepwater exploration and production, leading to the exploratory framework called Brazilian Pre-Salt (Mohriak et al., 2008).

Therefore, for the development of this study, two lines of research are vital:

- **Reservoir geophysics:** It is based on the study of the reservoir characterization and behavior through geophysical methods, especially those that refer to the modeling (simulation) of the propagation of acoustic and elastic waves, and the imaging of synthetic and real seismic data. The approach seeks to integrate the quantitative (analytical or numerical) study with geological and geophysical observations.

- **Seismic imaging:** Consists of the development and application of new seismic imaging methods. Being an inherent part of the seismic data processing sequence, seismic imaging aims to produce sharp and accurate images of the subsurface of the Earth, with direct application in reservoir studies. Following this line of research, we highlight some relevant topics for assessment of reservoirs:
    - Seismic data processing;
    - Seismic migration methods;
    - Migration velocity analysis;
    - Inversion and estimation of petroleum parameters;
    - Wave propagation;
    - Reservoir management through exploration/exploitation simulations.

In the next section, we present a brief overview of the early history of the geophysical development, focusing on the principles of seismic imaging, the subject of this thesis.

## 1.2 Early geophysics and the seismic underpinnings

### 1.2.1 In the beginning, everything was dark

Although geophysics is currently a sophisticated, multidisciplinary, and constantly evolving science, it was born in ancient times to meet humankind's needs in comprehending Earth's physical structures and processes. Throughout history, Earth's investigations were commonly made without physically consistent methods, in a form that was almost purely observational and based on natural philosophy, a mixture of divine speculations and explanations.

Magnetism can be considered one of the oldest observations, and it dates to the prehistoric development of iron smelting, although the knowledge of the Earth's magnetic field (the geomagnetic field) has developed slowly. The magnetite attraction properties were known in China and Europe, from about 500 BCE. On the other hand, the orientation properties of magnetite appear subtly in Europe at the end of the 12th century (Mitchell, 1946; Needham, 1962; Kono, 2015)[1].

In the Western world, the properties of attraction were observed by Thales in the sixth century BCE, according to a quote from Aristotle from the fourth century BCE (Chapman and Bartels, 1940). Orientation and polarity properties were discovered in China but were not widely used in navigations, in part because the country's civilization throughout the Middle Ages was agrarian and terrestrial with navigation only in rivers and canals. The first clear and complete description of the magnetic compass was made by Shen Kua in 1088, before any European reference (Harradon, 1943). In Europe, the first reference is due to the English monk Alexander Neckham, around 1190, when he describes that the sailors touched the magnet with a needle, which was later used for orientation[2].

The extensive overseas exploration, between the centuries 15th-18th, defined the period in European history named Age of Exploration (or Age of Discovery). During this period, a cultural, technical and scientific movement promoted, among other things, the improvement of nautical and the development of physical geography, and cartography, revealing with more precision the size of the Earth. The Italian Christopher Columbus (1451-1506), with the support of the Spanish crown, was the pioneer of transatlantic travel. He bet on the theory that the Earth was round and intended to find a way for the Indies always sailing west. He reached America in 1492.

---

[1] Needham (1962) is the most comprehensive work about Chinese contributions in the early history.

[2] A detailed description of the seamen's procedure is given by Guyot de Provins of France (1184-1210) in his satirical poem "La Bible" in 1205 (Kono, 2015).

It is interesting to see how knowledge was acquired and fragmented over the centuries. The spherical Earth paradigm appeared in Greek philosophy in the around 500 BCE with Pythagoras, though most pre-Socratic philosophers defended the flat Earth model. Aristotle accepted the sphericity of the Earth by empirical bases in 330 BCE. Years later, in 240 BCE, the Greek mathematician Eratosthenes of Cyrene was the first to estimates the size of the Earth using a simple scheme that combined geometric calculations with physical observations.

### 1.2.2 The beginning of the modern geophysics exploration

Historically, gravity method was the first geophysical technique to be used in geophysical exploration. More precisely, gravity gradiometry was the first potential field to be widely measured in oil and mining applications (Blakely, 1995; Bell et al., 1997; While et al., 2006). This, thanks to the Hungarian scientist Baron Roland von Eötvös (Loránd Eötvös) who created the torsion balance, which is mostly a gravity gradiometer, at the end of the 19th century with the initial aim of determining some physical constants (Shaw and Lancaster-Jones, 1922; Barton, 1932; Gillies and Ritter, 1993; Szabó, 2015). However, it did not take long to arouse the interest of exploration geophysicists, who made this instrument an essential ally in the search for oil fields. Unfortunately, the robustness of the torsion balance, coupled with the difficulty in obtaining and interpreting the data made this method excessively expensive, and with the emergence of gravimeters in the 1930s, gravity gradiometers fell into disuse (Telford et al., 1990; Bell et al., 1997; de Oliveira Lyrio et al., 2004; Mikhailov et al., 2007; Pajot et al., 2008).

Moreover, by measuring only the vertical gravity component, interpretation of data occurred much more simply and directly (Mikhailov et al., 2007). This impacted on gradiometers being left aside until the 1970s, when the U.S. Navy, interested in developing an instrument capable of assisting with navigation and detection of missiles, invested in the development of mobile platforms of high performance, which gave rise to the first gradiometers capable of measuring all components of the gravity gradient tensor (GGT). Only after the end of the Cold War in the 1980s, the technology developed by the military was applied to geophysical exploration and other fields (Bell et al., 1997). Since then, ways of improving these instruments, with respect primarily to mobility and precision, have begun to be studied. Eventually, it pushed researchers to look for forms of numerical processing and simulations (Parker, 1973; Oldenburg, 1974; Bell et al., 1997; Mickus and Hinojosa, 2001; de Oliveira Lyrio et al., 2004; Nabighian et al., 2005; While et al., 2006; Mikhailov et al., 2007; Pajot et al., 2008, among others). A detailed account of the early history of the gravity method can be found in Nabighian et al. (2005). Even today, the gravity method continues to be an essential and sometimes crucial constraint in many exploration areas. Nevertheless, it was undoubtedly eclipsed by seismology.

The foundation of seismology dates from the 17th century. In 1678, the English physicist Robert Hooke (1635–1703) enunciated his law, known as Hooke's law, which expresses the linear relationships existing between strains and stresses, when strains are small. However, only in 1822, the modern theory of elasticity started to be developed, when Augustin Louis Cauchy (1789–1857), a French mathematician and military engineer, generalized Hooke's law to three-dimensional forces and elastic bodies. In the following years, numerous discoveries were made. Siméon Poisson (1828) showed the separated existence of P- and S-waves, Cargill Gilston Knott (1899) demonstrated the reflection and refraction concepts in the seismic wave propagation. Lord Rayleigh (1885) and Augustus Edward Hough Love (1911) developed the theories of their eponymous surface waves.

We have now essentially sketched the development of the mother lodes of seismic wave propagation. At the same time that the theoretical development occurred, numerous advances happened in instrumental development and different empirical works emerged. The first "seismograph", an instrument used to detect and record earthquakes, was developed by L. Palmiere in 1855. A few years early, Robert Mallet (1848, 1851) began experimental seismology by measuring the velocity of seismic waves in sand and granite using gunpowder. Similarly, Henry Larcom Abbot (1878) used massive explosions to measured P-wave velocities. Years later, John Milne (1885) introduced the drop-weight as an energy source (as well as explosives).

According to DeGolyer (1935)[3], L. P. Garret was the first to suggest the use of seismic refraction to find salt domes, but suitable instruments had not yet been developed. The first discovery by the seismic method was the Orange salt dome in Gulf Coast Texas. It happened thanks to Ludger Mintrop's pioneer work, which developed the first mechanical seismograph (Domenico, 1996). As mentioned by Keppner (1991), Mintrop laid the foundations of applied seismic, making it not only technically but also economically attractive. A revolution started in the exploration of oil and gas, significantly increasing the number of geophysical companies in the U.S. This drove the continuous search for better and more accurate equipment. The

---

[3] Everette DeGolyer (1886-1956) was a renowned geophysicist, petroleum geologist, and successful petroleum industry leader. DeGolyer is often called "the father of (American) Geophysical Exploration" (or "the father of Applied Geophysics") (Robertson, 1986). DeGolyer accompanied by Donald C. Barton (1889-1939), another famous petroleum geoscientists, introduced the torsion balance into the U.S. (Robertson, 2000).

mechanical seismographs were then replaced by electronic seismometers (electronic recorders and electromagnetic transducers) in the 1930's. As the seismometers are several times more sensitive, they boosted the initiation of seismic exploration worldwide after having proven the seismic reflection are much more useful than the refraction method in the search for petroliferous subsurface structures.

The reader interested in learning more about the historical development of seismic wave propagation, the seismic reflection method, and the history of the first geophysical companies should consult the excellent book “Exploration Seismology” by Sheriff and Geldart (1995).

### 1.2.3 Early seismic imaging

This thesis contributes to the literature of seismic imaging, and we review much of the concepts regarding this subject in the following chapters. It is not within the scope of this section to go into too much detail, but there are many works on this topic, so we reserve the chance to mention those most relevant researchers and their ideas which have been contributed with geophysical history.

The term *imaging* can be found in different disciplines such as medical imaging, oil exploration, non-destructive evaluation, and remote sensing. In what concerns the geophysical exploration, *seismic imaging* can be read as the whole set of imaging methods (Schleicher et al., 2007).

Among the imaging methods, *migration*, in particular, are used to reconstructing of the best possible undistorted depth image of the subsurface structures. In parallel to the geophysical exploration and instrumental development reviewed in Section 1.2.2, migration had already been recognized as an important imaging method by 1920's.

It is not clear when the term “migrating” was first used neither where it came from, but it is often thought that it came from the geologic conception of how oil migrates updip. Also, both theoretical and practical aspects of migration can be seen easily as a map-migration (Bednar, 2005; Schleicher et al., 2007).

In the mid-1930s, the new reflection-seismic method started to be primarily applied by the leading oil companies. The routinely use of seismic reflection raised challenging questions. It was not yet known why it produced sufficient seismic records in some regions and not in others.

The earliest advance of seismic imaging appears to be that of Frank Rieber in 1936. He was a man of vision. In two articles, “A new reflection system with controlled directional sensitivity” (Rieber, 1936a) and “Visual presentation of elastic wave patterns under various structural conditions” (Rieber, 1936b), he explained why the seismic reflection method produced inferior seismic records in many places and he designed and constructed an analog device (named Geosonograph) for modeling waves from realistic but straightforward geologically styled models.

> *The idealized reflection system would be one in which a simple impulse could be generated at the earth's surface, and thereafter would travel downwards in the earth until it encountered a succession of simple strata from each of which a reflection would be returned to the surface. In this ideal system, the direct wave from the explosion would pass the receiving system before any reflected waves had arrived – and hence no disturbance or interference with the reflections would be occasioned by the direct wave. (Rieber, 1936a)*

It is therefore natural to think that the concepts described by Rieber were employed in geophysics since then. However, they were not pursued until technological developments made it more practical. It remains true, however, that the description by Rieber greatly influenced the works which came in the following decades.

When we talk about the earliest methods of the seismic imaging, we should be careful and remember that many strategies came before the digital computers era. The first seismic migration method was done manually. Known as the Hagedoorn's "ruler and compass" method, it was proposed in 1954 and emerged inspired by the Huygens' principle. In the Hagedoorn's method, the reflections are found as an envelope of equal traveltime curves (Hagedoorn, 1954).

Another big leap in seismic imaging happened in the early-1960s when Mayne (1962) showed what came to be the first stacking technique, the common-midpoint (CMP) method.

About a decade later, it was Claerbout (1970, 1971) who contributed innovative work. Noting how a wavefield propagates through the subsurface, the interaction of downgoing and upgoing wavefields inside the earth, he developed the first "wave-equation migration" method. For purposes of convenience, however, the "one-way" wave equation migration dominated migration practices until approximately 2000. In addition, the pioneering work of Claerbout introduced the basis of so-called migration "imaging condition".

Another valuable contribution was the "migration by Fourier transform" developed by Stolt (1978), which expressed a seismic wavefield in the frequency-wavenumber domain. Indeed, comparing with Claerbout's work, we could see the "Stolt's migration" like an alternative approach to the same problem (Bednar, 2005). However, since it was developed to operate in the frequency domain, for a constant-velocity assumption, the Stolt's method is the fastest one.

Shortly after, Gazdag (1978) adapted the Stolt's original algorithm. Sometimes called "phase shift" or "Gazdag migration", it is a frequency-domain phase-shifting step-by-step downward continuation algorithm. In addition, it was initially designed to handle only a vertically varying velocity. Gazdag and Sguazzero (1984) improved the method to handle mildly lateral velocity variations by creating the "phase-shift-plus interpolation" or "PSPI migration".

In addition to these major implementations, Kelly et al. (1976) showed full acoustic and elastic wavefield simulations by a suitable finite-difference representation. Also, Schneider (1978) provided the wave-equation basis for Kirchhoff migration through the application of the Green's third identity to the recorded data to produce a seismic wavefield at depth. Bleistein (1987) showed how to solve for reflectivity.

The late 1970s continued to bear fruit. Hemon (1978) presented the reverse-time migration (RTM). It showed promise in imaging steeply dipping structures, using the full acoustic wave equation, i.e., two-way, thus eliminating the dip limitations of one-way equations. Besides its precision, the RTM is, unfortunately, computationally expensive even for the computers of today.

Yilmaz and Claerbout (1980) presented the dip-moveout (DMO) correction. This method mitigates the problem with attenuation of steeply dipping events present in the CMP stack because of the flat-earth assumption. On the other hand, such strategy addressed a new issue. To apply the DMO correction, one needs either to perform first the normal-moveout (NMO) correction and its corresponding velocity analysis. For a comprehensive discussion of the DMO and NMO application in imaging, see Hale (1984) and Forel and Gardner (1988).

The migration velocity is of key importance for almost all the methods briefly reviewed above. To provide appropriate information for the investigated geologic area, the reference velocity model needs to be vertically or laterally inhomogeneous, elastic isotropic, or anisotropic.

Those readers wishing to understand from the basic principles of seismic imaging to imaging algorithms, we recommend the books of Schleicher et al. (2007), Jones (2010), and Stolt and Weglein (2011), as well as the papers by Gray et al. (2001), Bednar (2005), Etgen et al. (2009), and references therein.

## 1.3 Modern seismic imaging and the present state of the art

Some of the greatest scientific and technological inventions in human history occurred in the 1990s and 2000s. The computational advances enabled most of the scientific breakthroughs of that time and allowed the application of methods that until then were computationally impossible.

With larger and larger computations becoming possible, advances in seismic have been occurring from the planning of the acquisition survey, through the search for more accurate data, software development, and the most frontend steps of seismic processing. In what follows, we point some of the most relevant advances concerning the seismic imaging, which can be placed in two categories, namely, standard and nonstandard seismic imaging. By standard seismic imaging, we refer to those contextualized on the Huygens' principle, the Born approximation, and the like, whereas, nonstandard imaging rely on interferometric imaging, Marchenko imaging, and representation theorems applied to vector acoustic or elastic data (Gray et al., 2001).

### 1.3.1 Standard seismic imaging

As seen previously, most efforts of seismic imaging relying on image regions with complex geology and in the presence of a significant amount of noise, where the use of the classical flow (NMO, stacking, and migration) may be insufficient. Among others, this has boosted the development of:

- methods of seismic-velocity assessments. Two of the most important are the seismic reflection tomography, and the full-waveform inversion (FWI) (Lailly, 1983; Tarantola, 1984; Bishop et al., 1985; Stork, 1992; Virieux and Operto, 2009; Biondi and Almomin, 2014);

- three-dimensional seismic acquisition and migration (Cordsen et al., 2000; Biondi, 2006);

- wide-azimuth procedures for acquisition and migration, and the choice between a narrow-azimuth and a wide-azimuth acquisition design. It is a strategic decision depending on the survey's purpose. For example, wide-azimuth procedures have proved themselves successful in imaging deepwater structures, but, on the other hand, they are costlier than narrow-azimuth surveys. For economy, it is a common practice to have larger source and receiver spacings which unfortunately implies in a spatial-sampling issue which, in addition, shows behaving differently with land and marine data (Pratt et al., 1996; Sirgue, 2003; Sirgue and Pratt, 2004; Malinowski and Operto, 2008; Bleibinhaus et al., 2009; Etgen et al., 2009; Prieux et al., 2012);

- enhanced bandwidth mainly those at low frequencies. The benefits with a broadband acquisition are many but briefly, we could mention the better conditioning for an inverse problem. Even today, and even for a robust procedure like an FWI application, the frequency content is crucial to ensure an accurate velocity estimation. Moreover, the search for enhanced bandwidth has shown useful to improve the seismic response at high frequencies (Alkhalifah, 2014; Biondi and Almomin, 2014);

- rock-property analysis through seismic amplitude analysis, which can be performed using the amplitude variation with offset (AVO), or using the amplitude variation with angle (AVA). Both of them have been employed to reduce the exploratory risk, primarily in less-complex areas (Berkhout, 1997);

- rock-property analysis for the estimation of azimuthal properties, which can be estimated from amplitude-variation-with-azimuth (AVAZ) or velocity-variation-with-azimuth (VVAZ) investigations (Castagna and Backus, 1993);

- methods which emphasize coherency and continuity of reflectors. Two distinguish techniques are common-reflection-surface (CRS) stacking and multifocusing stacking (Jäger et al., 2001; Hertweck et al., 2007).

### 1.3.2 Nonstandard seismic imaging

By nonstandard seismic imaging, we refer to any alternative that, one way or another, seems to break the paradigm presented in the majority of the technologies of imaging the earth's interior developed since the early days of mechanical migration. Examples of particular importance are:

- the use of multiple reflections which can increase the accuracy in the velocity models and seismic images (Verschuur, 2006; Vasconcelos et al., 2008; Malcolm et al., 2009);

- the multiple-migration method, or "mirror-migration method", which provides a much broader illumination of the subsurface than is possible for conventional imaging using the primaries, especially for the very shallow reflections and sparse ocean-bottom seismometer (OBS) spacing (Dash et al., 2009);

- the concepts and applications based on the inverse scattering theory, like the inverse-scattering series proposed by Weglein et al. (1997) that allows removing internal multiples without knowledge of subsurface reflectors (Ramírez and Weglein, 2009; Behura et al., 2014);

- full-wavefield migration (Berkhout, 2012) to migrate internal multiples;
- interferometric imaging (Schuster et al., 2004; Schuster, 2009), that inverts correlated seismic data for the reflectivity or source distributions, and can be used to migrate first-order free-surface multiples or peg-leg multiples in CDP data (see, also, Vasconcelos et al., 2008; Ramírez and Weglein, 2009; Vasconcelos et al., 2010);
- Marchenko imaging. A new inverse-scattering theory based on the Marchenko equation (Marchenko, 1955; Agranovich and Marchenko, 1963), presented by Rose (1989, 2001, 2002) under the name of "autofocusing", and then adapted to the seismic concepts for acoustic (Broggini and Snieder, 2012; Wapenaar et al., 2013) and also elastodynamic (da Costa Filho et al., 2014; Wapenaar et al., 2014) wavefields;
- least-squares migration (Nemeth et al., 1999);
- joint migration inversion (JMI) (Verschuur and Berkhout, 2011; Berkhout, 2012; Staal and Verschuur, 2012b,a);
- the development of theorems and methodologies applied to vector acoustic (Vasconcelos and Snieder, 2008a; Vasconcelos et al., 2009; Fleury and Vasconcelos, 2013; Vasconcelos, 2013) or elastic data (Shapiro and Hubral, 1999; Vasconcelos and Snieder, 2008b);
- incorporating non-seismic data like marine electromagnetic (EM), controlled-source EM (CSEM), magnetotelluric (MT), and gravity gradiometry (GG). The use of multi-physics datasets may reduce the ambiguity of the seismic data, which is, for example, particularly important for velocity model building in a complex area dominated by salt tectonics. The topic is also subject of active ongoing research. For example, recent papers on the subject of joint inversion of seismic and EM, CSEM, MT, and GG include those of Hoversten et al. (2006); Commer and Newman (2008); Chen and Hoversten (2012); Colombo et al. (2014).

## 1.4 Problem statement

In the previous section, we have revisited essential concepts and approaches of seismic imaging. Generally, a common feature of these methods is that their success depends on the accuracy of a priori reference velocity model, typically a smooth model — also called *macrovelocity model* — which plays the role of an initial guess of the actual velocity model to be constructed in time or depth domain depending on the need. However, how to establish the macrovelocity model is a complicated problem on its own. In the last decades, many authors have played a central role in the development of methods for the construction of macrovelocity models, and the improvements concerning their resolution to the image purpose under consideration (see, e.g., Jannane et al., 1989; Versteeg, 1993; Liu, 1997; Billette and Lambaré, 1998; Sacchi, 1998; Zhu et al., 1998; Chauris and Noble, 2001; Billette et al., 2003; Sirgue, 2003; Schleicher et al., 2007; Jones, 2010).

As critical as the velocity model accuracy is knowing how to retrieve information from the data set and understand its limitations. In this subject, important assertions were made by Jannane et al. (1989). Motivated initially to clear up the convergence problem occurred when starting earth model is far from the true earth (Kolb et al., 1986; Mora, 1987b; Pica et al., 1990), Jannane et al. (1989) determined which wavelengths of earth structures that can be resolved from seismic reflection data. The investigation showed there exists a gap in resolution between short and long wavelength. That is, the intermediate wavenumbers are invisible to the data (Sirgue, 2003; Biondi and Almomin, 2014). Another important work was that provided by Mora (1989). He proposed that a nonlinear iterative inversion that updates a varying background velocity obtains all wavenumbers that are resolvable separately by migration and tomography. In other words, Mora (1989) recognized that FWI has a migration component and a tomographic component.

The decomposition by spatial scale is, therefore, a topic of fundamental interest. Though a variety of methods for velocity model construction methods exist, for acoustic data (the assumption of this thesis), they can be classified in two categories: those devoted to inverting the long-wavelength (smooth) components of the velocity model and those dedicated to resolving the short-wavelength components (Claerbout, 1985).

They accomplish this because of two independent attributes of seismic wavefields used in the inversion. One of these attributes, the geometrical behavior of the wavefield, it is described mainly by its kinematics and is particularly successful at stores/provides mostly smooth (long-wavelength) elements of the velocity field. Various methods are suitable for this, providing background velocity information of the subsurface structures unless sharp discontinuities are imposed on the model. Possible seismic approaches for initial-models building rely on traveltime tomography, wave equation tomography, and migration-based velocity analysis (Prieux et al., 2012; Biondi and Almomin, 2014). The second attribute, amplitude or phase behavior of the wavefield, however, can contain sharp (short-wavelength) components of the model represented as scattering. Moreover, depending on the frequency, it may be reasonably insensitive to an equivalent cycle-induced change in the long-wavelength component of the velocity model (Alkhalifah, 2014).

Geophysical exploration seeks to characterize the subsurface as much as possible. Thus, low frequencies are required to understand the geological properties of rocks, while high frequencies are required to address structural challenges. Therefore, imaging methods that exploit the full information contained in seismograms are desired. These needs also together with the increase of the computational power occurred in the last decades have contributed to FWI became a favorite imaging technique able to reveal arbitrary complex subsurface models despite its ill-posedness (e.g., Tarantola, 1987; Pratt, 1999; Virieux and Operto, 2009). However, regardless of any technological advances, FWI is a strong nonlinear inverse problem and requires an accurate initial guess and sufficient data to succeed (a consequence of the strong nonlinear relationship between the seismic data and the model parameters).

Therefore, the frequency content in seismic data plays a key role in the converging of the inversion processing. FWI is most successful when applied to the low frequencies in the data. Unfortunately, however, low-frequency data are rarely available due to acquisition limitations faced even by the industry of today. Such limitation (the lack of information of the long wavelengths) can be attenuated by the wide-aperture arrivals recorded by long-offset acquisition geometries (Pratt and Worthington, 1990; Sirgue and Pratt, 2004). If in one hand diving waves and super-critical reflections contribute for improvement of the wave illumination in challenge environments (e.g., sub-salt and sub-basalt targets; Planke et al., 1999), on the other there are more wavelengths propagating in the subsurface. In this fashion, long-offset data increase the ill-posedness of FWI. This fact has motivated further development of multiscale strategies in the time domain (Bunks et al., 1995), and in the frequency domain (Pratt and Worthington, 1990; Pratt, 1999).

All the comments presented in this section are just a few examples to stress the importance of the velocity model to guarantee both quality and performance in the most diverse seismic imaging techniques and inversion approaches. More examples can be seen in reviews that show the state-of-the-art of full waveform inversion, e.g., Virieux and Operto (2009), and Fichtner (2011) for those interested in a seismological point of view. Furthermore, the reader is referred to the works of Sirgue (2003); Sirgue and Pratt (2004) for details concerning to produce a velocity model which contains the lowest wavenumbers of the velocity field. This is an important subject also discussed in the present work. This thesis first seeks to develop a workflow for the construction of initial velocity-models for FWI methods. Therefore, we investigate new methods for seismic imaging and velocity model building. The purpose of this thesis and the parts that compose it are detailed in the following sections.

## 1.5 The purpose of this work

In spite of the great number of geophysical imaging methods created in the last decades to study the coupling between the physical and geometric properties of the Earth's subsurface, there is a lack of methods that are able to process a significant amount of information, with high computation efficiency. Furthermore, it is usual that a geophysical method and/or processing strategy focus in a few, even only one, specific characteristic/property of the investigated geology. Basically because adding information usually means to make the problem more complex.

Aiming to further contribute on the study of seismic imaging, this work presents some methods that try to construct the best possible undistorted image in time- and in depth-domain from the acquired seismic data. Another aim of this work is to confront the newly proposed techniques with classical and frontend other ones, providing a more in-depth look at the motivation and inner workings of these methods.

However, the aim of this thesis is not only to develop new methods to estimate the velocity of the subsurface. More than this, the primary purpose of this work is to study how the combination of these methods allow a complete processing workflow, incorporating different pieces of information, always taking into account the computational efficiency and prioritizing fully automatic alternatives. Thus, we present a workflow for the construction of starting velocity-models for FWI methods consisting of automated time-migration velocity analysis, followed by time-to-depth conversion. Figure 1.1 shows a sketch representing this workflow. The dark gray rectangles represent the three main blocks of the processing workflow, which, in turn, compose the three fronts researched in this thesis.

In general, the methods proposed here are means to build improved velocity models for simple and complex geology structures, being their final images a by-product obtained, in most cases, by time- or depth-migration of the dataset with this extracted velocity model.

Since it is known that methods which act in the time-domain are usually faster than those in the depth-domain, most of the project time was devoted to the study and development of algorithms to construct starting velocity models for time-domain migration-velocity-analysis. Thus the first chapters of this thesis are dedicated to describe, evaluate and propose time-domain approaches (Chapters 2 and 3). Their results can be better assessed in the second part of this work when they are converted from time to depth domain (Chapter 4). The third part of this thesis is devoted to discuss and study methods that work in the depth-domain (Chapter 5).

The chapters in this thesis also contribute to the body of literature and can be read independently depending on the reader's interest. The following section presents a detailed summary of the thesis structure.

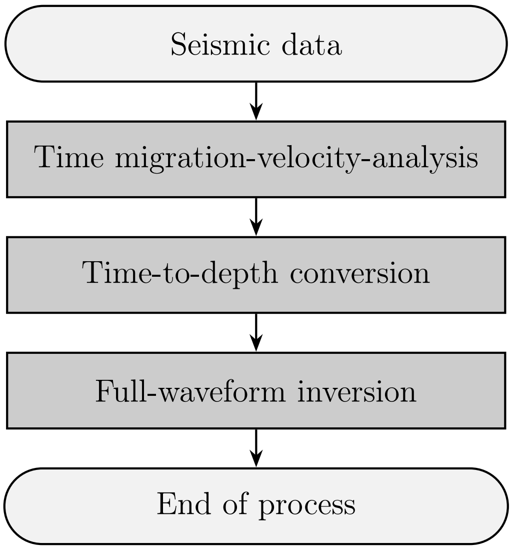

Figure 1.1: Velocity model building flowchart.

## 1.6 Outline of this thesis

This thesis is divided in two parts, thesis body and appendices. The former is composed by six chapters, of which this Introduction is the first. The others are described as follows.

**Chapter 2** discusses two recent time MVA methods, being common-image-gather image-wave propagation (Schleicher et al., 2008) and double multi-stack migration (Schleicher and Costa, 2009), and compare their potential for the construction of initial models for more sophisticated MVA techniques. In the example of the Marmousoft dataset, we show that both methods can be used in a fully automated procedure to produce a velocity model and a time-migrated image without a-priori information at comparable cost.

**Chapter 3** presents a prestack time-migration tool for local improvement of the seismic migration-velocity model, based on time-remigration trajectories. Kinematic parameters from local-slope information of seismic reflection events are used to locally correct the velocity model. The main advantage of this technique is that it allows to carry out a residual-moveout correction for all offsets of a common-image gather (CIG), taking into account the reflection-point displacement in the midpoint direction. Tests on synthetic data from four simple models, the Marmousoft data (Billette et al., 2003) and SMAART-Sigsbee2B data demonstrated the feasibility of the method in more realistic situations with strong velocity variations in different directions.

**Chapter 4** presents an improved derivation of a new strategy for time-to-depth conversion and velocity estimation based only on image-wavefront propagation. This method was initially proposed by Valente (2013). In particular, it makes use of a geometric manipulation to directly compute both the velocity field and the traveltime, avoiding a previous ray-tracing step. Moreover, it requires only the knowledge of the image-wavefront of the previous time step. Its robustness is proved with its application on a simple synthetic example and on the Marmousi model. The quality of the results are evaluated by depth migrated images from the Marmousi data set with the extracted velocity models. We use a two-dimensional Fourier finite-difference (FFD) migration with the complex Padé approximation as discussed in Amazonas et al. (2007). One of the reasons that led us to choose this method is that it was proven to be fast and robust. Another important point is that Amazonas et al. (2007) performed several depth migrations with different migration methods for the Marmousi data set using the true velocity mode. The use of their migration method allows us to compare our results to their migrated images, in this way increasing our information database.

**Chapter 5** presents a workflow for the construction of initial velocity-models for full-waveform tomography (FWT) methods consisting of automatic time-migration velocity analysis by means of double multi-stack migration (Chapter 2), followed by time-to-depth conversion by image-ray wavefront propagation (Chapter 4). Evaluation of the converted velocity model as an initial velocity model in an acoustic FWT process indicates the potential to achieve a fully automatic tool for initial-model building in a FWT workflow.

**Chapter 6** reviews the work accomplished in this thesis, the advantages and limitations of the methods as well as perspectives for a fully automatic tool, capable of generating seismic velocity models and images in time and/or in depth domain.

# Chapter 2

# Initial-model construction for MVA techniques

> *The beauty of the multipath summation method is that it eliminates the need to construct a migration velocity model before imaging.*
>
> — Schleicher and Costa (2009)

## 2.1 Summary

For iterative migration-velocity-analysis (MVA) methods, accurate starting models are required. We discuss the parameterization of two recent time MVA methods, namely common-image-gather image-wave propagation and double multi-stack migration, and compare their potential for the construction of initial models for more sophisticated MVA techniques. Both approaches generate a velocity model and a time-migrated image without a priori information. While multi-stack MVA is already fully automatic by design, we eliminate human intervention from image-wave MVA by introducing automated picking of the involved flattening velocities. In the example of the Marmousoft data set, we show that both methods can produce equivalent results at comparable cost.

## 2.2 Introduction

A major challenge both in seismic exploration and in seismological investigations is the construction of the best possible undistorted image in depth from the acquired data. For this purpose, imaging methods that rely on the knowledge of a subsurface velocity model are employed. Most present-day model-building techniques are iterative procedures that improve a starting model based on intermediate results. Among these, the most important are model-building methods based directly on migration itself, so-called migration velocity analysis (MVA). All of these techniques strongly depend on the accuracy of the starting model.

Conventionally, techniques for constructing a starting model are based on an analysis of the traveltime of seismic waves. Among the most commonly used methods are the common-midpoint (CMP) and common reflection surface (CRS) stacks (see, e.g., Hertweck et al., 2007).

Both these methods operate in the data-acquisition time domain. Thus, there is a need for transforming such a velocity model to the migration domain, be it in time or depth. This conversion is problematic in that it depends on the actual values of the velocity model to be converted (Hubral, 1977). Therefore, alternative velocity-analysis methods are desirable that work directly in the desired migration domain, so that there is no need for a conversion of the model domain.

Motivated by the importance of the subject, MVA methods have been proposed by many authors. Because of its conceptual clarity and simplicity, residual moveout (RMO) analysis has become the favorite tool for MVA. In recent years, many improvements have been proposed. However, few authors have studied the problem of how to construct the best possible starting model. Schleicher et al. (2008) and Schleicher and Costa (2009) proposed two MVA methods for time migration that can fill this gap. The first one treats the events in common-image gathers (CIGs) similar to wavefronts and lets them propagate until they are flat, updating the migration velocity model from the flattening velocities (Schleicher et al., 2008). The second method stacks twice over migrated images for many models with different weights in order to extract stationary migration velocities from the ratio of the images (Schleicher and Costa, 2009). Both MVA methods' purpose is to begin the analysis from scratch, without the need to specify an initial velocity model that has already certain features of the searched model. Thus, they differ fundamentally from tomographic methods (Billette et al., 2003; Clapp et al., 2004) or full waveform inversion (FWI, see, e.g., Virieux and Operto, 2009), which require a good initial model to ensure convergence.

After the application of an adequate time-to-depth conversion algorithm (Cameron et al., 2007, 2008; Iversen and Tygel, 2008), a high-quality time-migration initial model may even provide sufficient quality to serve for subsequent depth MVA or FWI methods.

Schleicher et al. (2008) and Schleicher and Costa (2009) tested their time-migration MVA methods on the synthetic Marmousoft data set (Billette et al., 2003). These synthetic data were obtained by Born modeling in a smoothed version of the original Marmousi model, using the original reflectivity. However, although these authors applied both methods to the same data set, they did not compare their performance or try to combine them.

In this work, we deliver this comparison using the Marmousoft model, not only concerning the quality of the resulting velocity models and migrated images, but also regarding the human and computational effort required to achieve a certain quality. Another goal of our research is to study the setting of the parameters involved in the methods, in order to optimize their performance. Parameter to be cited in this respect are the measure of nonflatness of the events in the common image gather (CIG) or the number of CIGs necessary for a successful analysis.

## 2.3 MVA techniques

We start with a brief review of the MVA techniques under consideration.

### 2.3.1 MVA by image-wave propagation of CIGs

#### Theoretical description

Schleicher et al. (2008) started from the position of a horizontal reflector below a homogeneous medium with constant-velocity $v$ as a function of vertical time $\tau$, half-offset $h$, and migration velocity $v_m$, as derived by Al-Yahya (1989). It reads

$$\tau = \sqrt{\tau_0^2 + h^2\left(\frac{1}{v^2} - \frac{1}{{v_m}^2}\right)}\ , \tag{2.1}$$

where $\tau_0$ is vertical time at zero offset, i.e., the true migrated position of the reflector's image. They arrived at the image-wave equation for the continuation of a CIG,

$$\frac{\partial \tilde{p}}{\partial \tau} + \frac{v^3 \tau}{h^2}\frac{\partial \tilde{p}}{\partial v} = 0\ . \tag{2.2}$$

Note that equation (2.2) does not depend on the medium velocity $v$ nor the correct zero-offset vertical time $\tau_0$ of the reflector. This equation was independently derived by Fomel (2003a), who called it the kinematic RMO equation.

Schleicher and Biloti (2007) presented the equivalent of equation (2.1) for depth migration

$$z = \sqrt{\frac{v_m^2}{v^2} z_0^2 + \left( \frac{v_m^2}{v^2} - 1 \right) h^2} \ , \tag{2.3}$$

where $z_0$ is the true depth of the supposedly horizontal reflector and $z$ is the migrated pseudodepth.

Based on equation (2.3) and in analogy to the procedure in time, Schleicher et al. (2008) showed that the equation for continuation of the CIGs in depth can be written as

$$\frac{\partial p}{\partial z} + \frac{v_m z}{h^2 + z^2} \frac{\partial p}{\partial v_m} = 0 \ . \tag{2.4}$$

Because of the initial hypothesis of a horizontal reflector, equations (2.2) and (2.4) do not describe a dislocation of the image along the half-offset axis. The complete equation for dipping reflectors, which includes a derivative with respect to $h$, can be found in Fomel (2003a). However, since the dislocation in the $h$ direction is the smaller, the closer the model is to the true one, equations (2.2) and (2.4) are sufficient for an iterative procedure (see also Al-Yahya, 1989).

### Iterative model building

For a velocity model construction using the continuation of a single CIG, Schleicher et al. (2008) proposed the following iterative procedure (Figure 2.1):

1. Migrate data with inhomogeneous velocity model $v_j$.
2. Organize data into CIGs.

If CIGs are not flat:

3. Let CIGs propagate as if obtained with constant velocity $v_c$.
4. For each event, determine the flattening velocity $v_f$.
5. Use $v_f$ to update the velocity model $v_j$ to $v_{j+1}$.
6. Go to 1.

A flowchart of this algorithm is depicted in Figure 2.2.

In this way, we can update the velocity model using the concepts of residual migration (Rocca and Salvador, 1982; Rothman et al., 1985; Larner and Beasley, 1987). Residual migration is based on the fact that migrating a time-migrated image a second time yields a time-migrated image as if it was directly obtained with an

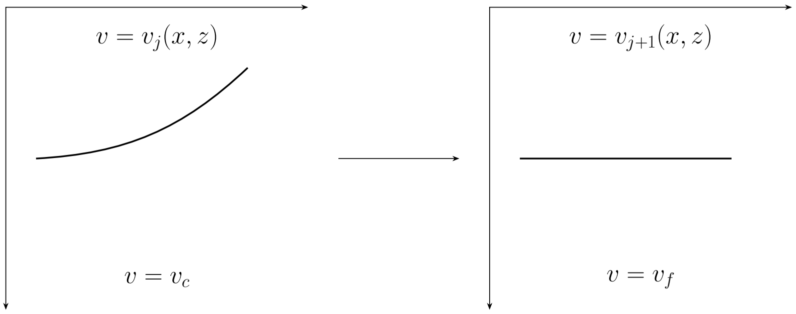

Figure 2.1: Iterative velocity model construction by image-wave propagation of CIGs. Here $v_j$ represents the present velocity model at the $j$th iteration; $v_{j+1}$ is the updated velocity model; $v_c$ is the constant velocity to begin the image continuation (e.g., water velocity $v_0 = 1500$ m/s for marine data or near-surface velocity for land data); and $v_f$ is the constant velocity that flattens an event.

effective migration velocity (please, see the supplementary text in Appendix D). If the first migration uses velocity $v_1$ and the second migration velocity $v_2$, then the effective migration velocity $v_{ef}$ can be expressed as

$$v_{ef} = \sqrt{v_1^2 + v_2^2}\ . \tag{2.5}$$

Equation (2.5) can be called the Pythagoras theorem of time migration as illustrated in Figure 2.3. Rewriting it as

$$v_2 = \sqrt{v_{ef}^2 - v_1^2}\ , \tag{2.6}$$

it allows determining the necessary residual migration velocity $v_2$ that will transform an image after migration with velocity $v_1$ into an image for the desired effective migration velocity $v_{ef}$.

In our image continuation procedure, the initial image was obtained by migration with model $v_j$, which thus is our $v_1$. The desired velocity model flattens events, hopefully, achieved at the next iteration, i.e.,

$$v_{j+1} = v_{ef}\ . \tag{2.7}$$

Thus, we need a residual velocity

$$v_2 = \sqrt{v_{j+1}^2 - v_j^2}\ . \tag{2.8}$$

On the other hand, we have treated the image as it was migrated with $v_c$, which thus may also assume the role of $v_1$ in equation (2.6). The event is approximately

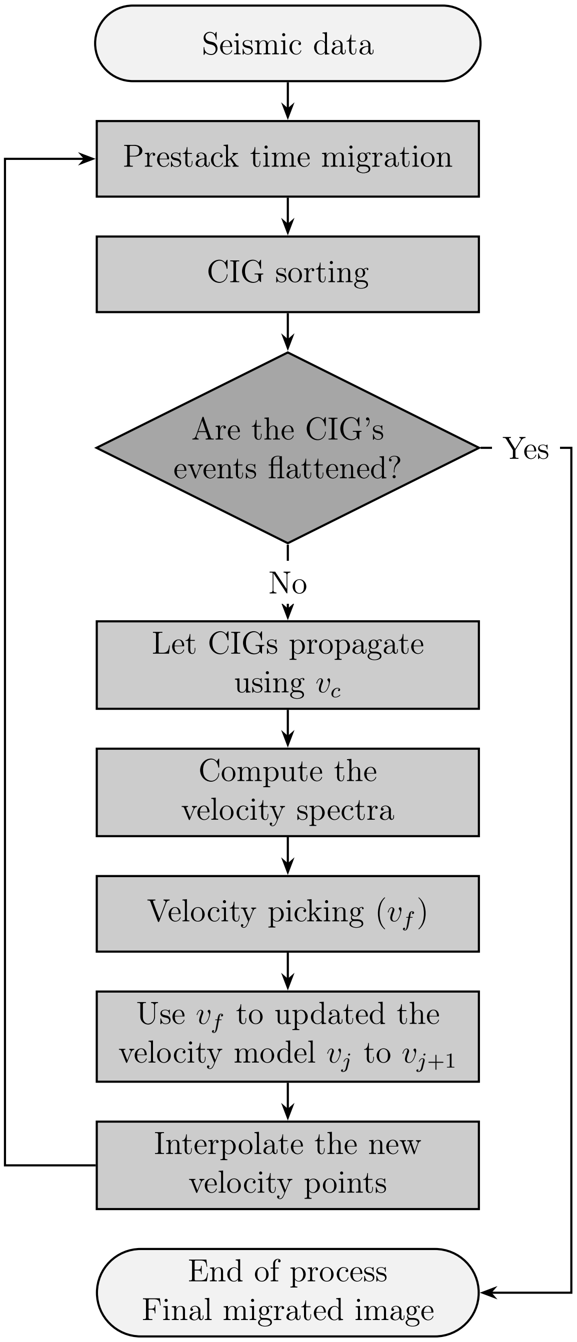

Figure 2.2: Image-wave propagation process flowchart.

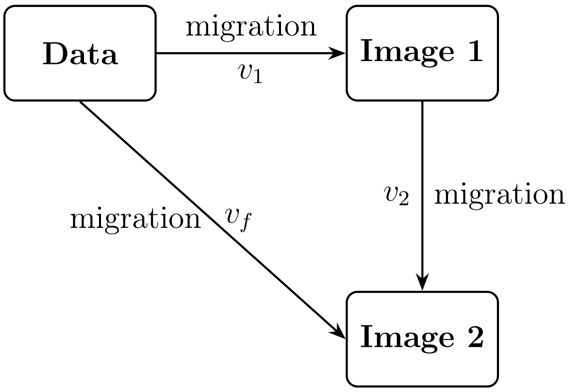

Figure 2.3: Pythagoras theorem of time migration.

flattened at $v_f$, which thus also represents $v_{ef}$, implying that the residual velocity should be approximated by

$$v_2 \approx \sqrt{v_f^2 - v_c^2}\ . \tag{2.9}$$

Equating these two expressions for the residual-migration velocity $v_2$, the velocity updating formula reads (Schleicher et al., 2008)

$$v_{j+1} \approx \sqrt{v_j^2 + v_f^2 - v_c^2}\ . \tag{2.10}$$

This formula allows obtaining an updated velocity model ($v_{j+1}$) as a function of the present velocity model ($v_j$), the constant velocity that flattens an event ($v_f$) and the constant velocity used to start the image continuation ($v_c$). The model should be smoothed between iterations (see again Figure 2.2) to avoid a so-called Deregowski loop (Deregowski, 1990), with velocity improvements only at the CIG positions without achieving overall improvement between the CIGs. Further details on the design of velocity models are discussed in Section 2.5.

### 2.3.2 MVA by double multi-stack migration

#### Theoretical description

Based on the principles of the Feynman path integral (Feynman and Hibbs, 1965). The path-summation method renewed attention in seismics in the last two decades after its application in seismic wave modeling (Lomax, 1999; Schlottmann, 1999). Shortly afterward, Keydar (2004), Landa (2004), Keydar and Shtivelman (2005), Landa et al. (2005), Shtivelman and Keydar (2005), and Landa et al. (2006) shown that path integral can be used to obtain a subsurface image without any velocity information.

Here, we compare the procedure and result of the above technique (Section 2.3.1) to the one of Schleicher and Costa (2009), which is based on the multipath-summation imaging process of Landa et al. (2006). The fundamental idea is to stack the migration results for “all possible” velocities, or at least as much models as practically reasonable. Since only “good” models yield flat events in common-image gathers, these will prevail in the overall stacked image, which thus will show the geologic structure without the need for a migration-velocity model. Below, we will refer to this technique as multi-stack migration.

Using the notation of Landa et al. (2006), the multi-stack time-migration operator can be written as

$$V_W(\mathbf{x}) = \int d\alpha\, w(\mathbf{x},\alpha) \int d\xi \int dt\, U(t,\xi)\delta(t - t_d(\xi,\mathbf{x};\alpha)) \;, \tag{2.11}$$

where $V_W$ is the resulting time-migrated image at an image point with coordinates $\mathbf{x} = (x,\tau)$, $x$ being the lateral distance, $\tau$ vertical time, $U(t,\xi)$ a seismic trace at coordinate $\xi$ in the seismic data, $t_d(\xi,\mathbf{x};\alpha)$ is a stacking surface corresponding to a set of possible velocity models that are parameterized using variable $\alpha$, and $w(\mathbf{x},\alpha)$ is a weight function, which serves to attenuate contributions from unlikely trajectories and emphasize contributions from trajectories close to the optimal.

There are several possible choices for the weight function (see, e.g., Moser et al., 2008; Shtivelman and Keydar, 2008, which present a related idea). In the application of Schleicher and Costa (2009), $\alpha$ directly represented the time-migration velocity and the weight $w(\mathbf{x},\alpha)$ was given by a bell-shaped exponential formula with peak value at zero dip in the common-image gather at $\mathbf{x}$. That is,

$$w(\mathbf{x},\alpha) = \exp\left[\frac{-P(\mathbf{x};\alpha)}{\sigma^2}\right] \;, \tag{2.12}$$

where $P(\mathbf{x};\alpha)$ is the squared average of the absolute value of the local event slopes in the CIG at $\mathbf{x}$. The local event slopes are estimated using the corrected least-squares plane-wave filters (Schleicher et al., 2009). Parameter $\sigma$ adjusts the half-width of the Gaussian bell function away from the desired events with $P = 0$. Here, we follow Schleicher and Costa (2009), who chose $\sigma = 0.1\Delta\tau/\Delta x$, where $\Delta\tau$ and $\Delta x$ are the intervals of the migration grid.

Through Laplace’s method and an asymptotic evaluation of the integral (2.11),

$$V_W(\mathbf{x}) \approx \sqrt{\frac{2\pi\sigma^2}{P''(\alpha_0)}}Q_0(\mathbf{x};\alpha_0) \;, \tag{2.13}$$

Schleicher and Costa (2009) showed that the result of a multipath summation produces a migrated image that is, at each image point $\mathbf{x}$, proportional to the migration with stationary velocity value $\alpha_0$, i.e., the one for which the weight function in integral (2.11) takes its maximum value at $P = 0$, and to the weight factor calculated for this velocity. In equation (2.13), $P''(\alpha_0)$ denotes the second derivate of the squared local slope mean $P$ as a function of the varying migration velocity $\alpha$. Furthermore, $Q_0(\mathbf{x};\alpha_0)$ denotes the desired migration result with the stationary migration velocity $\alpha_0$,

$$Q_0(\mathbf{x};\alpha_0) = \int d\xi \int dt\, U(t,\xi)\delta(t - t_d(\xi,\mathbf{x};\alpha_0)) \; . \tag{2.14}$$

This analysis implies that the use of a slightly modified weight function,

$$\tilde{w}(\mathbf{x},\alpha) = \alpha w(\mathbf{x},\alpha) \; , \tag{2.15}$$

provides, at each point $\mathbf{x}$, a second migration result,

$$\tilde{V}_W(\mathbf{x}) \approx \alpha_0 \sqrt{\frac{2\pi\sigma^2}{P''(\alpha_0)}} Q_0(\mathbf{x},\alpha_0) \; , \tag{2.16}$$

that is proportional to the first one, the factor being the stationary value of the velocity at point $\mathbf{x}$. Thus, the ratio between the migration results provides this velocity value

$$\alpha_0(\mathbf{x}) \approx \frac{\tilde{V}_W(\mathbf{x})}{V_W(\mathbf{x})} \; . \tag{2.17}$$

This property allows for the determination of a velocity value for all points with a nonzero multi-stack image. This idea of extracting quantities from multiple stacks has already been previously discussed in the framework of Kirchhoff migration (Bleistein, 1987; Tygel et al., 1993).

Caution should be taken to avoid division by zero since the image in the denominator will disappear from the actual reflector images. We need to keep in mind that velocity values outside the range of velocities used in the path-integral summation should be discarded. According to Costa and Schleicher (2011), possible modifications of weight function 2.15 can be thought of,

$$\tilde{w}(\mathbf{x},\alpha) = \alpha^q \exp\left[\frac{-P(\mathbf{x};\alpha)}{\sigma^2}\right] \; , \tag{2.18}$$

with exponents $q$ of $\alpha$ other than $q = 1$. Moreover, for the sake of convenience, we cannot consider values $q > 1$, which will imply raising the amplitude variation of the integral 2.11, diminishing the applicability of Laplace's method. Future research, not addressed in this thesis, can verify if the values $0 < q < 1$ improve the resulting velocity model. A complete velocity model can then be constructed by intelligent regularization which is further discussed in Section 2.5 and Appendix C.

### Automatic model building

For the velocity model extraction using the multipath summation, Schleicher and Costa (2009) proposed the following automatic approach:

1. Organize data into CIGs, $U(t, \xi)$.
2. Define a set of velocity models $\alpha$.
3. Migrate data $U(t, \xi)$ with each (constant) velocity models withing $\alpha$.
4. Define a weight function $w(\mathbf{x}, \alpha)$.
5. Compute the resulting time-migrated image $V_W(\mathbf{x})$ using the stacking operator $w(\mathbf{x}, \alpha)$.
6. Define a slightly modified weight function $\tilde{w}(\mathbf{x}, \alpha)$.
7. Compute the resulting time-migrated image $\tilde{V}_W(\mathbf{x})$ using the stacking operator $\tilde{w}(\mathbf{x}, \alpha)$.
8. Extract the migration velocity $\alpha_0$ by simply dividing the two migration results $\tilde{V}_W(\mathbf{x})$ (item 7) and $V_W(\mathbf{x})$ (item 5).

A flowchart of this algorithm is depicted in Figure 2.4.

## 2.4 Numerical examples

We use the Marmousoft data (Billette et al., 2003) to evaluate the above techniques of velocity model building. These synthetic data were constructed by Born modeling in a smoothed version of the original Marmousi model (Versteeg, 1994) (Figure 2.5). The smoothing is done using a Gaussian filter with correlation length $\tau = 240$ m (Billette et al., 2003). The smoothed velocity model is depicted in Figure 2.6.

For comparison with results of the presented techniques, we computed the interval ($v_{int}$) and the root-mean-square ($v_{rms}$) velocity models in pseudotime from

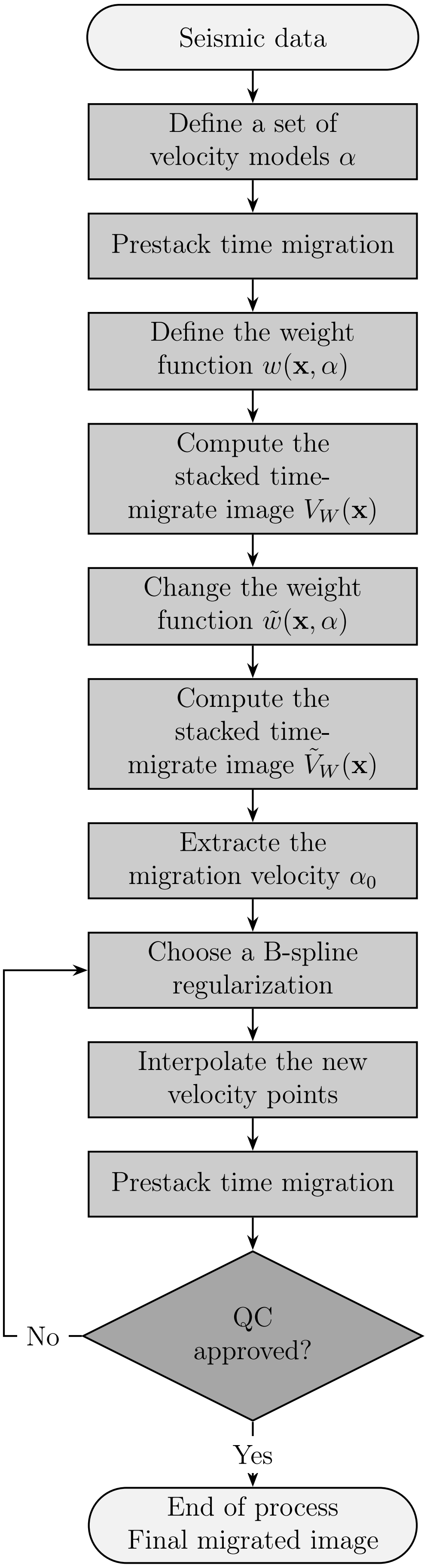

Figure 2.4: Double multi-stack migration process flowchart.

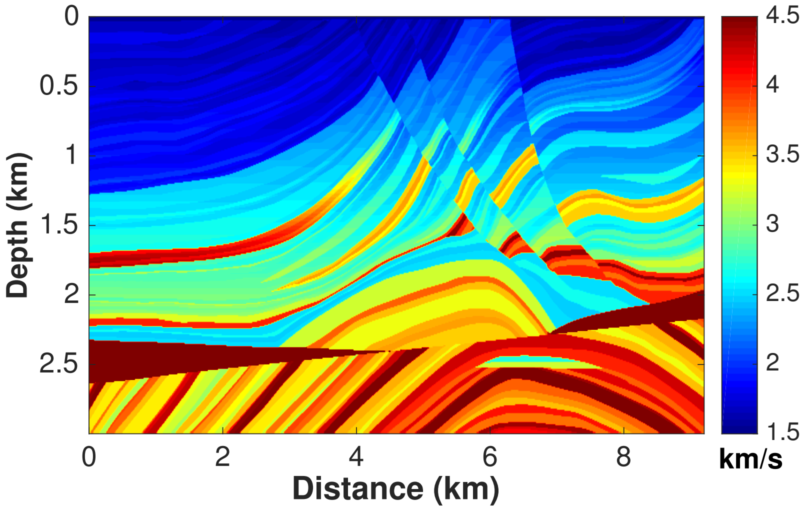

Figure 2.5: Stratigraphic Marmousi depth velocity model.

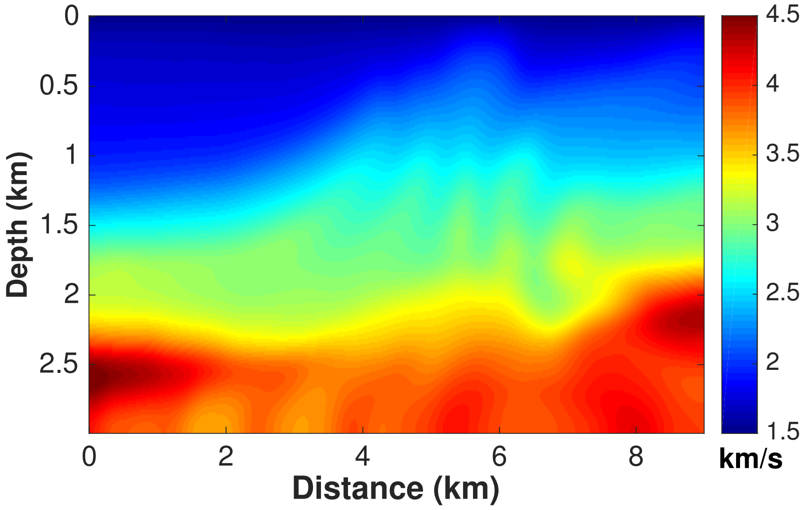

Figure 2.6: Marmousoft depth velocity model.

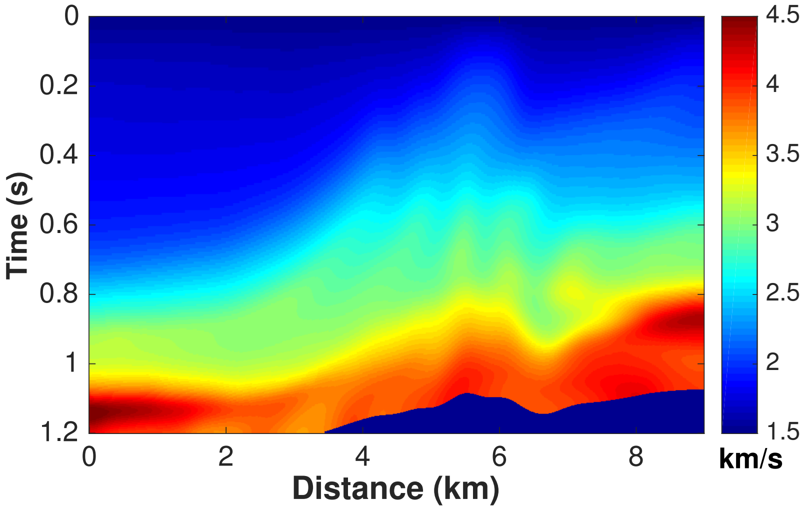

Figure 2.7: Marmousoft vertical pseudotime interval velocity model ($v_{int}$) computed from Figure 2.6 by vertical depth-to-time conversion.

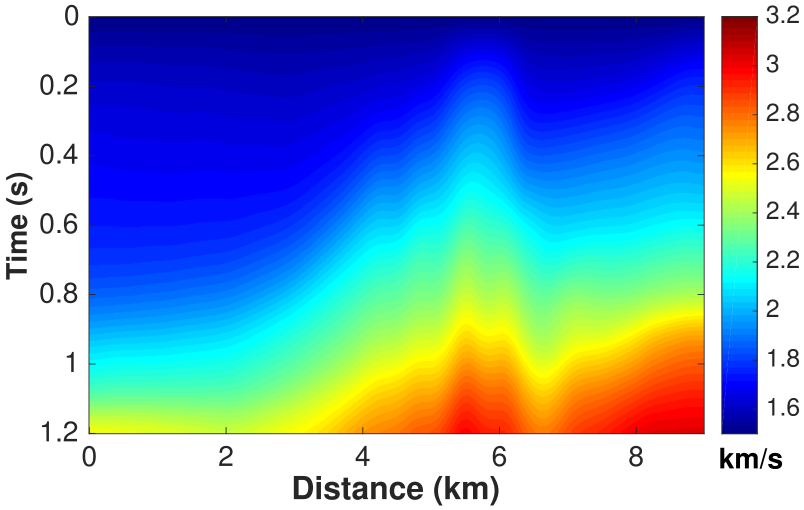

Figure 2.8: Marmousoft vertical pseudotime root-mean-square velocity model ($v_{rms}$) computed from Figure 2.6 by vertical depth-to-time conversion.

Figure 2.6, both using vertical conversion only. Figures 2.7 and 2.8 show the pseudotime interval velocity model and rms velocity respectively.

The Marmousoft data contain 261 shots with 96 receivers in each shot. Both shots and receivers at every 25 m with source-receiver offsets between 100 m and 2475 m. The first shot located at 2600 m and the last at 9100 m. The registration time of 3.6 s with a sampling rate of 4 ms (two-way traveltime). Figure 2.9 shows the near-offset section. Table 2.1 summarizes the acquisition parameters of Marmousi data set.

Table 2.1: Acquisition parameters of Marmousoft data set

| **Acquisition parameters of Marmousoft** | |
|---|---|
| Number of shots | 261 |
| Shot spacing | 25 m |
| Shot depth | 10 m |
| Hydrophone spacing | 25 m |
| Hydrophone depth | 10 m |
| Minimum offset | 100 m |
| Maximum offset | 2475 m |
| Offset interval | 12.5 m |
| Number of offsets | 96 |
| Minimum midpoint | 1387.5 m |
| Maximum midpoint | 9050 m |
| Midpoint interval | 25 m |
| Number of time samples | 900 |
| Time samples | 4 ms |

We then contaminated those data with random white noise at a level of 30 % of the maximum amplitude (see Figure 2.10 for a near-offset section).

For better comparison with our results, we thus time-migrated the zero-noise Marmousoft data using the rms velocity (Figure 2.8). Figure 2.11a depicts the migrated image, along with the coherence panel (Figure 2.11b) associated with the CIGs of the migrated image, which can be seen as an indicator of the reliability of different reflectors. Figures 2.11c to 2.11h show six selected CIGs at different locations, useful for assessing the quality of the velocity model and migration. Finally, Figure 2.12 brings the resulting time migration to the noise-contaminated Marmousoft data.

One natural constraint for ray-based methods is a smooth velocity model. Both MVA methods by image-wave propagation (Schleicher et al., 2008) and double multi-stack migration (Schleicher and Costa, 2009) provide such a smooth model. Since in the original works, both methods were tested for the Marmousoft model, we

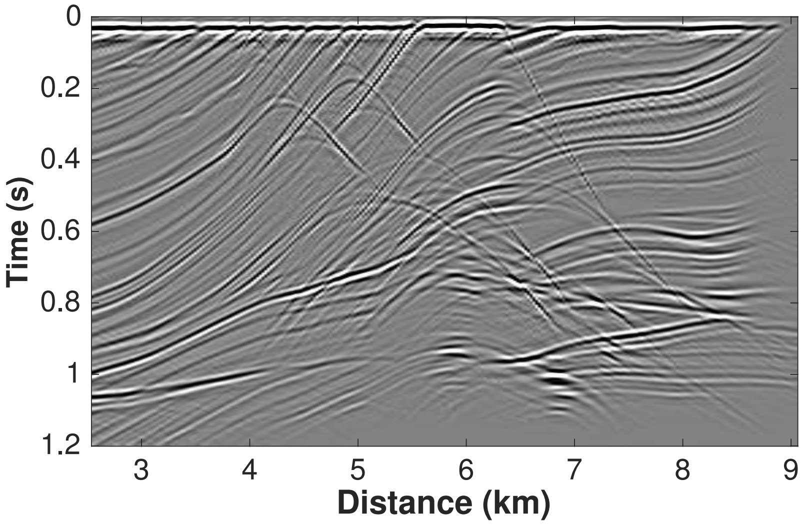

Figure 2.9: Near-offset section with source-receiver offset 100 m of the Marmousoft data.

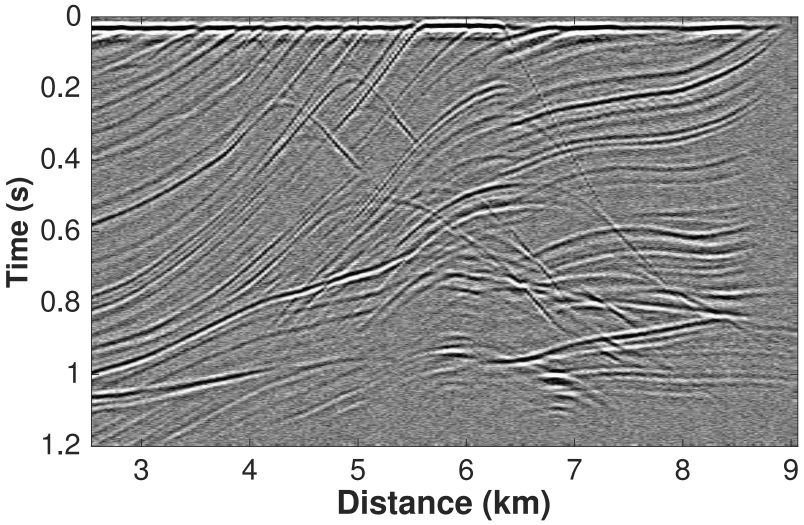

Figure 2.10: Noise-corrupted near-offset section with a signal-to-noise ratio equal 30 %.

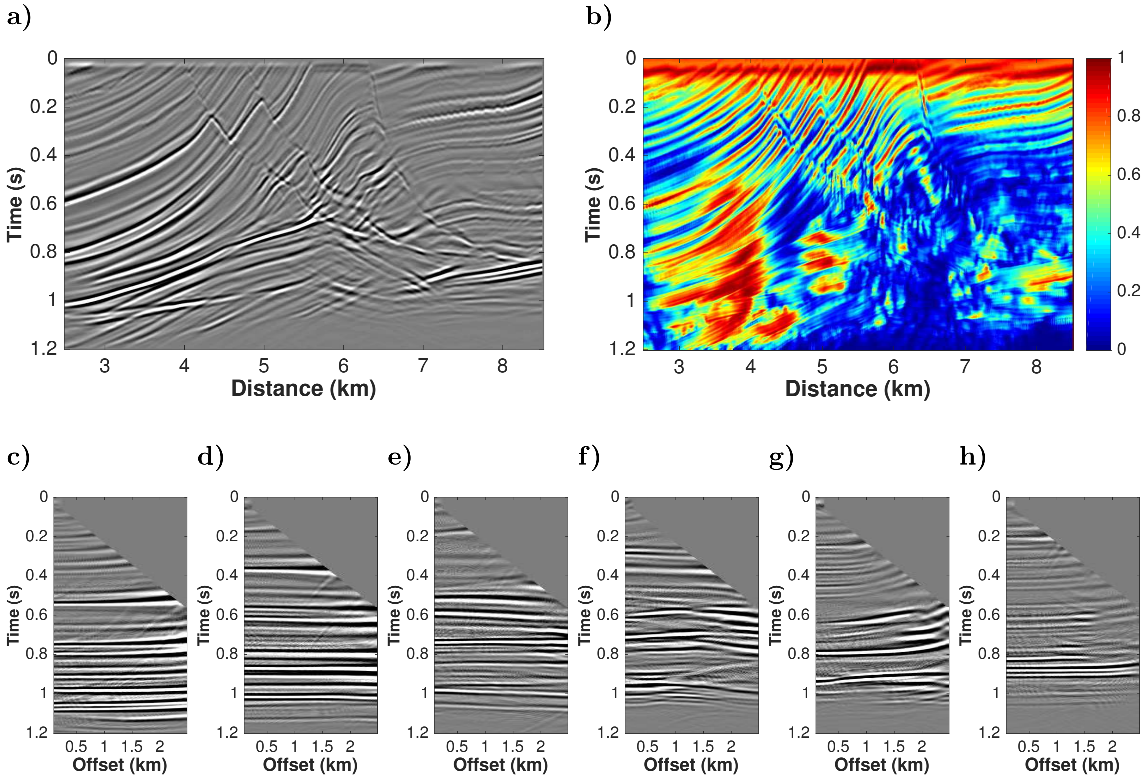

Figure 2.11: Time-migration (a) of Marmousoft data with the $v_{rms}$ velocity model (Figure 2.8), its corresponding coherence panel (b), and the common-image gathers from time migration at (c) 3000 m, (d) 4000 m, (e) 5000 m, (f) 6000 m, (g) 7000 m and (h) 8000 m.

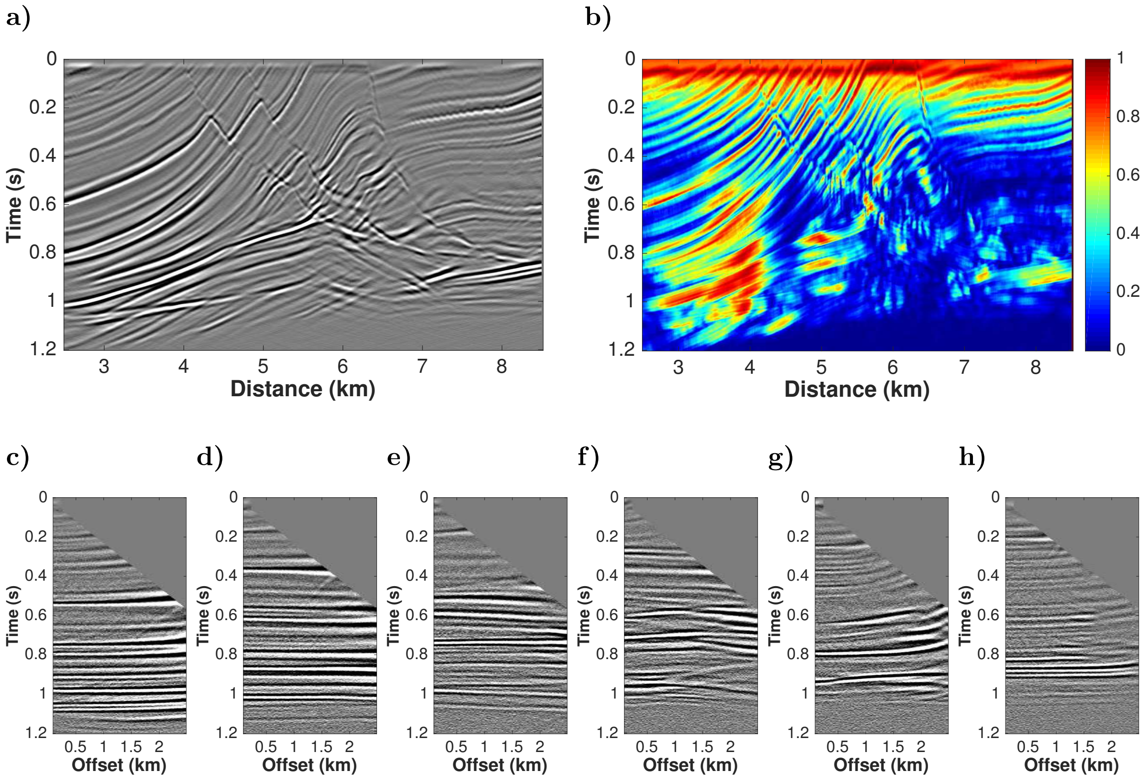

Figure 2.12: Time-migration (a) of noise-corrupted Marmousoft data with the $v_{rms}$ velocity model (Figure 2.8), its corresponding coherence panel (b), and the common-image gathers from time migration at (c) 3000 m, (d) 4000 m, (e) 5000 m, (f) 6000 m, (g) 7000 m and (h) 8000 m.

can directly compare the results. Comparing the best velocity models obtained by image-wave (Figure 2.13a) and double multi-stack (Figure 2.14a) MVA methods, we can see that both produce similar models in the geologically simple parts of the model. However, they yield some visible differences in the geologically complex central part, probably due to the limitations of time migration in such a situation.

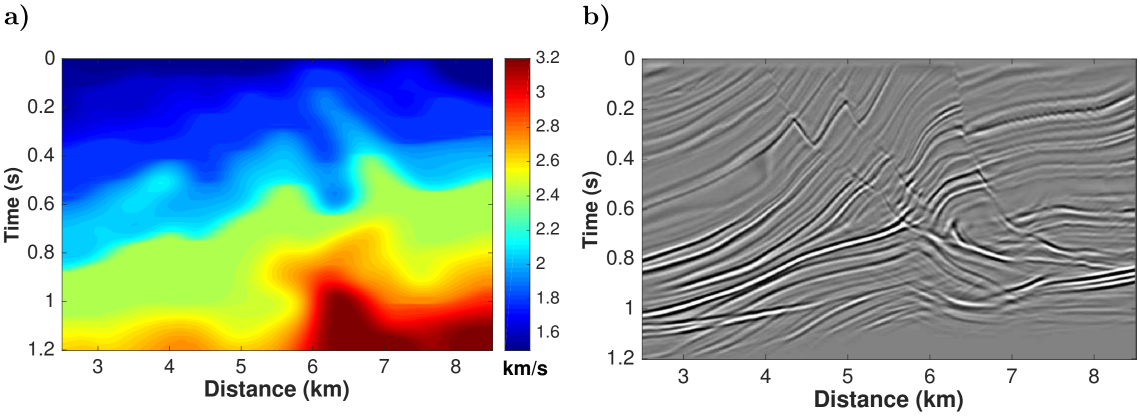

Figure 2.13: (a) Best time-migration velocity model obtained from MVA after five iterations of image-wave RMO correction and (b) corresponding final time-migrated image (from Schleicher et al., 2008).

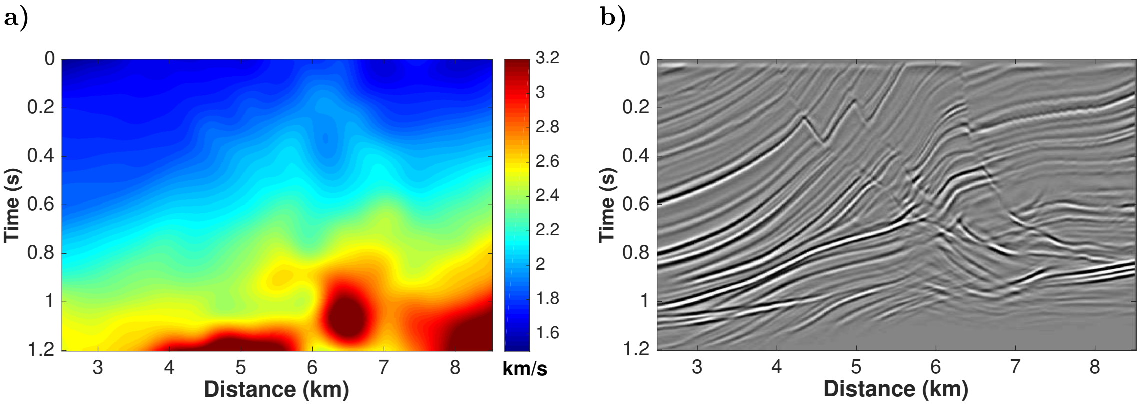

Figure 2.14: (a) Best time-migration velocity model obtained using the multi-stack migration process and (b) corresponding final time-migrated image (from Schleicher and Costa, 2009).

While there is a notable difference between the velocity models (Figures 2.13a and 2.14a), it is not easy to detect significant differences in the images resulting from time-migration with these models (Figures 2.13b and 2.14b). This illustrates the ambiguity in the determination of a starting model for more sophisticated iterative methods. Further investigations will need to decide which of the models is better suited for this purpose. This subject is discussed in Appendix E.

## 2.5 Results

To perform a qualitative and quantitative analysis comparing the results obtained by image-wave propagation of CIGs and double multi-stack migration, we have considered in our analysis:

- the interpolation method applied;
- the influence of noise in the data set;
- the number of iterations and computer time required to complete the process;
- the necessity and duration of human intervention;
- and the quality of the time-migrated image produced.

Table 2.2 summarizes the numerical experiments presented in this chapter which will be detailed in the next sections.

### 2.5.1 Velocity interpolation

One natural constraint for ray-based methods is a smooth velocity model. Consequently, a time-migration velocity model must not present abrupt variations. So, when an MVA method generates a grid with blank points, it is necessary to complete these gaps and smooth this velocity model before the migration process can be executed (Costa et al., 2008; Schleicher and Costa, 2009). In this regard, linear interpolation can be useful but requires input be filtered (e.g., by a moving average) to avoid discontinuities in the velocity derivatives. In our experiments, the B-splines smoothing was constrained by requiring the first and second Cartesian derivatives to be minimum. A Lagrangian multiplier defines the relative weight of each constraint in the cost function. In Appendix C, Table C.1 summarizes all the seven different sets of Lagrangian multipliers categorized from “very hard” to “very soft” regularization, utilized during the experiments.

In our tests, B-splines interpolation turned out to be the best way to interpolate the data, since it smoothed the velocity models even in edge regions. Therefore, all results presented in this chapter were obtained using B-splines interpolation.

An important parameter in this process is the number of B-splines nodes for the velocity interpolation. However, it is often not clear how to choose the number of nodes, and the bigger the number of nodes the costlier is the process. We can think that the more nodes are used, the more detail of the original function will be presented by the smoothed function. Schleicher and Biloti (2008) shown that more nodes mean a better approximation of Fourier coefficients for higher frequencies. That is, the number of nodes can be determined by specifying a frequency up to which all Fourier coefficients must be preserved and increased the number of nodes until this criterion is met.

We have tested different grid sizes (not present here). In most tests performed with Marmousoft, we did not find any significant influence on the quality of the results, due to the lack of high frequencies in the original data. Furthermore, our tests point to a similar discussion as Costa et al. (2008), which proposed a reflection-angle-based kind of smoothness constraint as regularization in slope tomography. They found an evident effect of the smoothness constrains on the estimated velocity model but a weaker effect on the seismic images. We note similar conclusion even with the data contaminated with noise. The influence of noise will be discussed in the upcoming sections 2.5.2 and 2.5.3. In the following examples, the number of B-splines nodes along the vertical axis (in vertical time) was 14 and along the horizontal axis (in horizontal distance) 52. The nodes are spaced at 0.1 s vertically and 200 m laterally.

Table 2.2: Experiments gallery.

| **Method** | **Experiment** | **Semblance (picking)** | **Noise (%)** | **Time (s)** |
|---|---|---|---|---|
| Image propagation | 1 | original | - | 5551 |
| | 2 | smoothed | - | 10523 |
| | 3 | original | 30 | 9612 |
| | 4 | smoothed | 30 | 9148 |
| Multi-stack migration | 5 | - | - | 4431 |
| | 6 | - | 30 | 4331 |

## 2.5.2 Image continuation

### Parameter setup

For the image-wave propagation of CIGs, we started in all the tests from a $v_0 = 1500\,\mathrm{m/s}$ (water velocity) constant velocity model. Velocities ranged from 1500 m/s to 4500 m/s. Moreover, to use the migration velocity as the propagation

Table 2.3: General setup of the MVA by image-wave propagation of CIGs.

| **Image continuation - Parameter setup** | |
|---|---|
| Initial constant migration velocity | 1500 m/s |
| Initial time for migration | 0 s |
| Final time for migration | 1.2 s |
| Initial $x$ for migration | 2500 m |
| Final $x$ for migration | 8500 m |
| Sampling rate in $t$ for migration | 0.002 s |
| Sampling rate in $x$ for migration | 12 m |
| Number of B-spline nodes in $t$ direction | 14 |
| Number of B-spline nodes in $x$ direction | 52 |
| Distance between nodes of B-splines in $t$ direction | 0.1 s |
| Distance between nodes of B-splines in $x$ direction | 200 m |
| Coordinate of first CIG for velocity analysis | 2500 m |
| Distance between CIGs for velocity analysis | 12 m |
| Number of CIGs for velocity analysis | 501 |
| Minimum velocity for 1st continuation | 1400 m/s |
| Maximum velocity for 1st continuation | 3500 m/s |
| Velocity interval for 1st continuation | 25 m/s |
| Reference velocity for subsequent iterations of continuation | 2000 m/s |
| Velocity variation for subsequent iterations of continuation | 1000 m/s |
| Velocity interval for subsequent iterations of continuation | 10 m/s |
| Regularization for first two iterations | very hard |
| Regularization for later iterations | intermediate |
| Minimum velocity allowed in the model | 1500 m/s |
| Maximum velocity allowed in the model | 4500 m/s |

variable in the image continuation, we have to treat the CIGs as if they were obtained with a constant velocity $v_c$ (see equation 2.10). The choice of $v_c$ is rather arbitrary because the principle does not depend on its actual value. In practice, it is helpful to avoid too large velocity differences to the background model. Given the range of true velocities in the Marmousoft model, we chose $v_c = 2000\,\mathrm{m/s}$. From this reference velocity, we continued CIGs to larger velocities up to 4500 m/s and to lower velocities down to 1500 m/s in steps of $\Delta v = 25\,\mathrm{m/s}$. In contrast with previous tests presented in Santos et al. (2013f,g), here we used a smaller range of velocity values with a bigger velocity step ($\Delta v$) in the CIG continuation. Such parametrization implies in a straight decrease in the computational cost without any loss of quality. Table 2.3 summarizes the parameter setup used in the image continuation tests.

The following tests were done twice, first considering the original Marmousoft data set and after for a noise-corrupted version with a signal-to-noise ratio equal 30 % (see Figures 2.9 and 2.10). For simplicity, we split the tests in four different experiments, where Experiments 1 and 2 treat the true Marmousoft data set and Experiments 3 and 4 the noise-corrupted one (see Table 2.2). Furthermore, we set different regularizations to the B-splines interpolation depending on the iteration number. We used a very hard regularization for the first two iterations and an intermediate regularization for the next three ones (see Tables 2.3 and C.1).

### Automated velocity picking from propagated CIGs

Schleicher et al. (2008) showed that MVA in time by image-wave propagation of CIGs allows determining a meaningful velocity model and a migrated image of acceptable quality (Figure 2.13). However, to do so, they had to manually pick the flattening velocities, which made the process rather cumbersome.

In this work, we perform the process without any human intervention using two automatic picking procedures. Both consider the semblance values along horizontal lines in the propagated CIGs. The first procedure picks the velocities for all maxima in the semblance panel while the second procedure picks the velocities for all maxima in the semblance panel after a least-square smoothing.

In Figure 2.15a, we show the semblance panel computed in the first iteration for the original Marmousoft data (Experiments 1 and 2), and in Figure 2.15b the noise-contaminated one (Experiments 3 and 4). The profiles in pink and white color represent the picks for all maxima in the semblance (first procedure) and the picks for the maxima after smoothing (second procedure) respectively. Here, we differentiate Experiment 1 from 2, and Experiment 3 from 4, depending on the procedure chosen from the first iteration (see Table 2.2). Figures 2.16a and 2.16b depict the semblance panel and the pink profile extracted in Experiments 1 and 3 for the third iteration, and Figures 2.17a and 2.17b depict the semblance panel and the white profile extracted (after smoothing) in Experiments 2 and 4 for the third iteration. Although we used the same automatic-picking procedure in each of the experiments, we emphasize that the choice between these procedures can be made at each iteration.

These velocity values are corrected with equation 2.10 to provide the new velocity-time function for the subsequent iteration. Both panels in Figure 2.15 show that with only one iteration, the highest velocity values are still close to the initial value $v_0 = 1500\,\mathrm{m/s}$, especially in the shallowest parts. Analyzing Figures 2.16 and 2.17, we observed an increase in velocity values in contrast with Figure 2.15, as well as an increase in the coherence. Further, the profiles depicted in Figures 2.16 and 2.17 suggest a good correlation between them in the shallower regions of Marmousoft. In other words, the models become more different as the depth increases. Compare the profiles to times after 0.8 s.

Figure 2.18 shows the extracted velocity points for Experiments 1 to 4 for the third and fifth iterations. Just for illustration, we use linear interpolation to make the grid regular. The extracted velocity points are interpolated with B-splines as mentioned in section 2.5.1. The velocity model and its respective migrated image for the third iteration are depicted in Figures 2.19, 2.23, 2.21 and 2.25, and for the fifth iteration in Figures 2.20, 2.24, 2.22 and 2.26. The accuracy of the results can be confirmed, for example, by comparing with the Marmousoft rms velocity model (Figure 2.8), as well as the time-migrated images and the CIGs located at different positions (Figures 2.11 and 2.12). Also, a significant correlation was observed between our results and those obtained by Schleicher et al. (2008) and Schleicher and Costa (2009) shown in Figures 2.13 and 2.14.

#### Reliability

Figure 2.27 shows the horizontal semblance in the corresponding CIG at each point of the migrated images mentioned above. In these panels, low coherence values indicate regions where further improvements are required, while high values indicate where the obtained velocity model can already be trusted.

Our results indicate that already after the third iteration we can produce an acceptable velocity model in the vicinity of the geologically complex regions. In the more complex central part of the model, additional improvement is achieved up to the fifth iteration (even in the presence of noise corrupted data set). Through the analysis of the migrated images, the CIGs, and the panels of coherence, we see that the MVA method employed produces similar results to those obtained using the rms velocity model (Figures 2.8, 2.11 and 2.12). A more detailed comparison of the coherence panels obtained after five iterations (Figures 2.27b, 2.27d, 2.27f and 2.27h), even suggests that the image-wave propagation of CIGs produced better results than those using the rms velocity model. More iterations of the process led to no significant improvement, indicating that time migration cannot resolve the remaining inaccuracies.

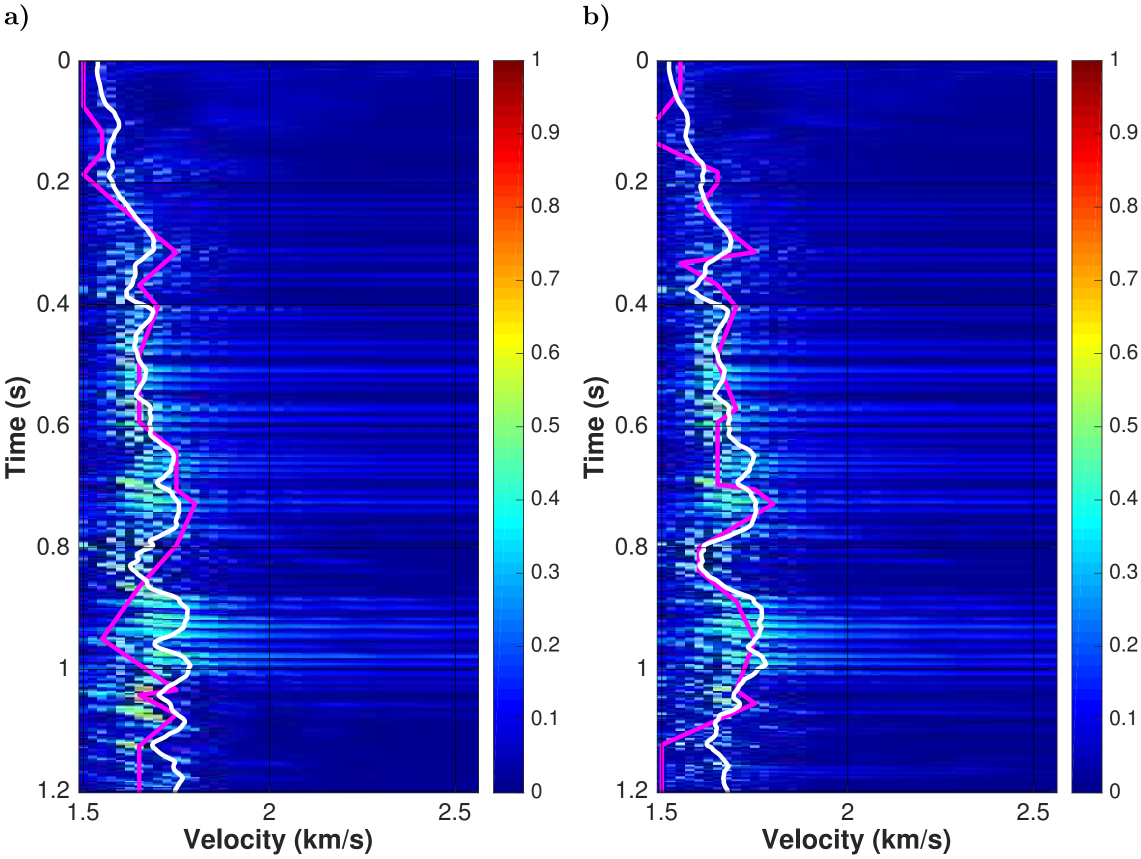

Figure 2.15: Velocity spectrum obtained from the set of continued CIGs. Semblance plot of CIG at 6000 m, iteration 1, for the (a) Experiments 1 and 2, and (b) Experiments 3 and 4. The velocity profiles interpreted at this location also is shown. The pink profile presents the picked velocities for all maxima in the semblance panel while the white profile shows the picked velocities for all maxima in the semblance after smoothing.

### Computational Cost

The largest part of the computation cost of image-wave remigration resides in the migrations necessary at each iteration. The image-wave propagation of the CIGs is about two orders of magnitude faster. In the original implementation of Schleicher et al. (2008), a severe human interaction was required. They picked

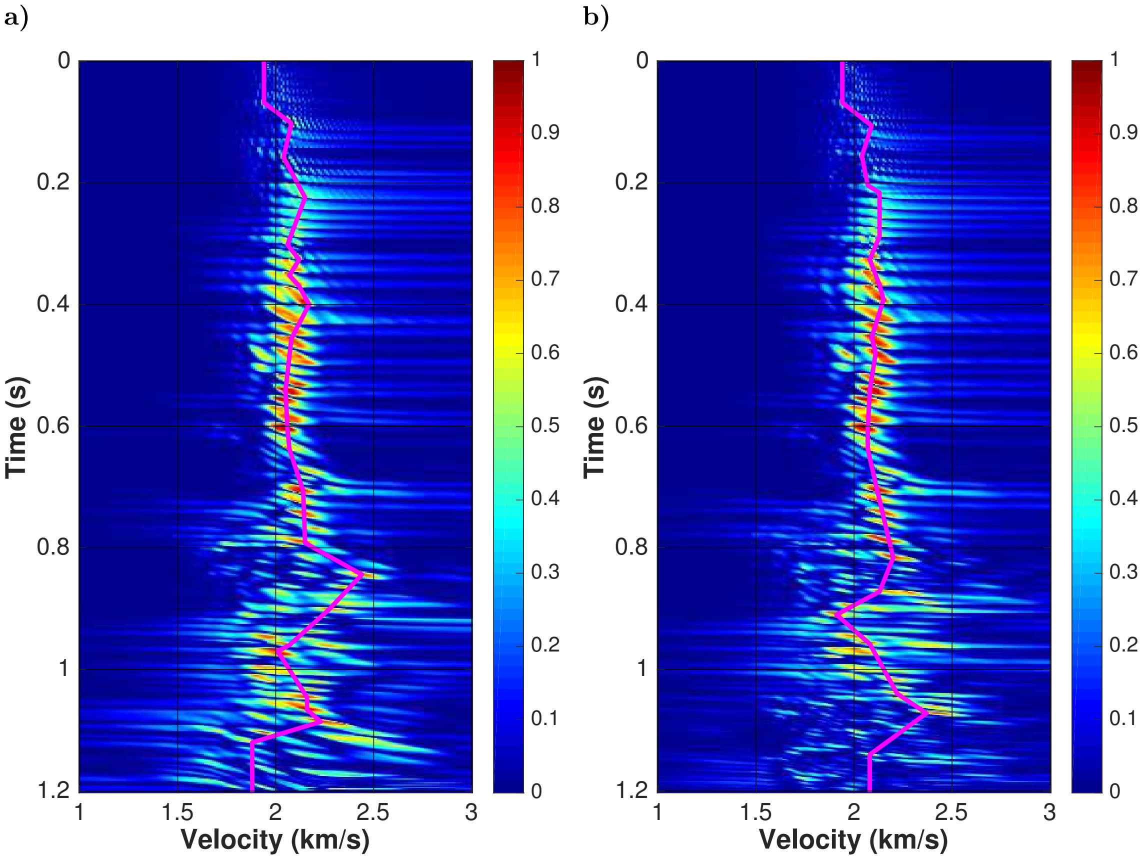

Figure 2.16: Velocity spectrum obtained from the set of continued CIGs. Semblance plot of CIG at 6000 m, iteration 3, for the (a) Experiment 1, and (b) Experiment 3. The velocity profile interpreted at this location also is shown (pink line). It presents the picked velocities for all maxima in the semblance panel.

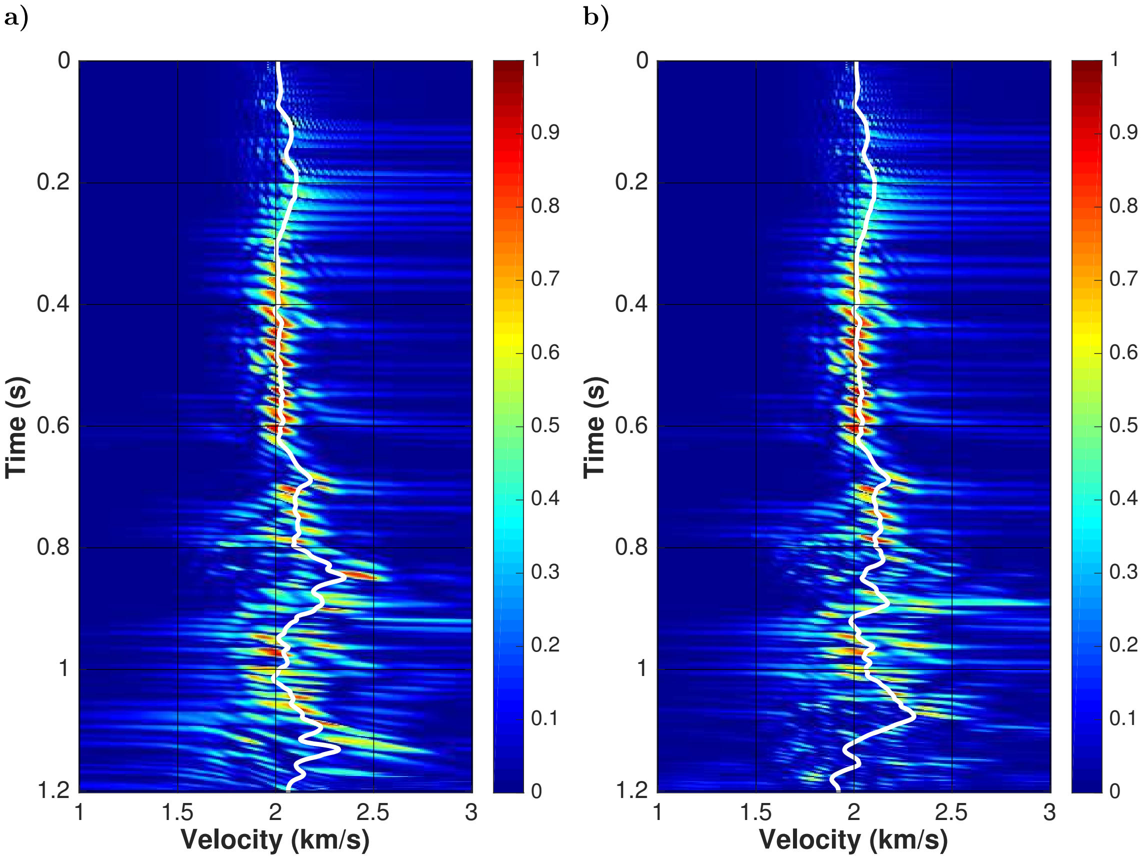

Figure 2.17: Velocity spectrum obtained from the set of continued CIGs. Semblance plot of CIG at 6000 m, iteration 3, for the (a) Experiment 2, and (b) Experiment 4, The velocity profile interpreted at this location also is shown (white line). It presents the picked velocities for all maxima in the semblance panel after smoothing.

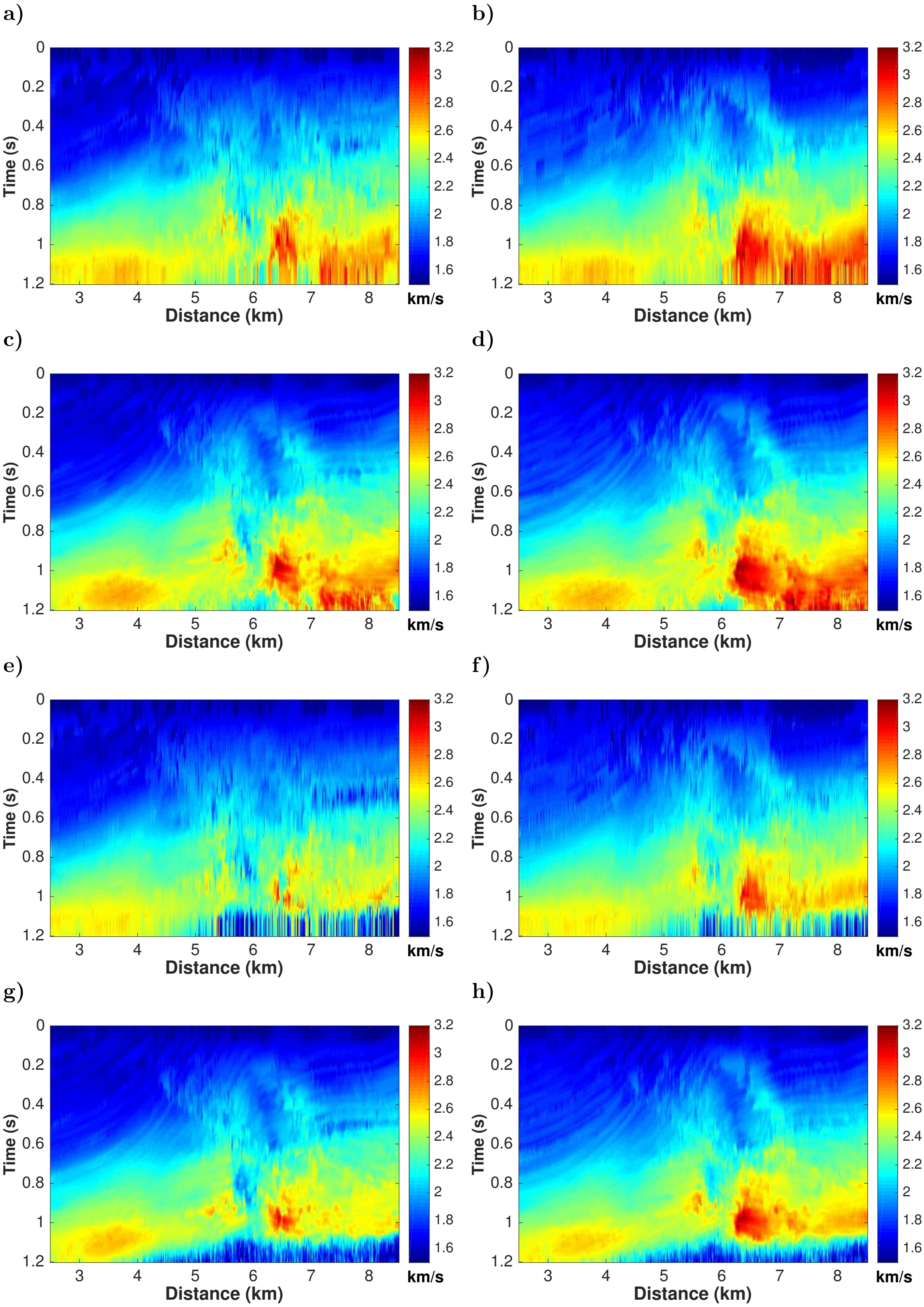

Figure 2.18: Velocity extracted by the image-wave propagation method after three (left) and five (right) iterations for the Experiments 1 (a)-(b), 2 (c)-(d), 3 (e)-(f), and 4 (g)-(h).

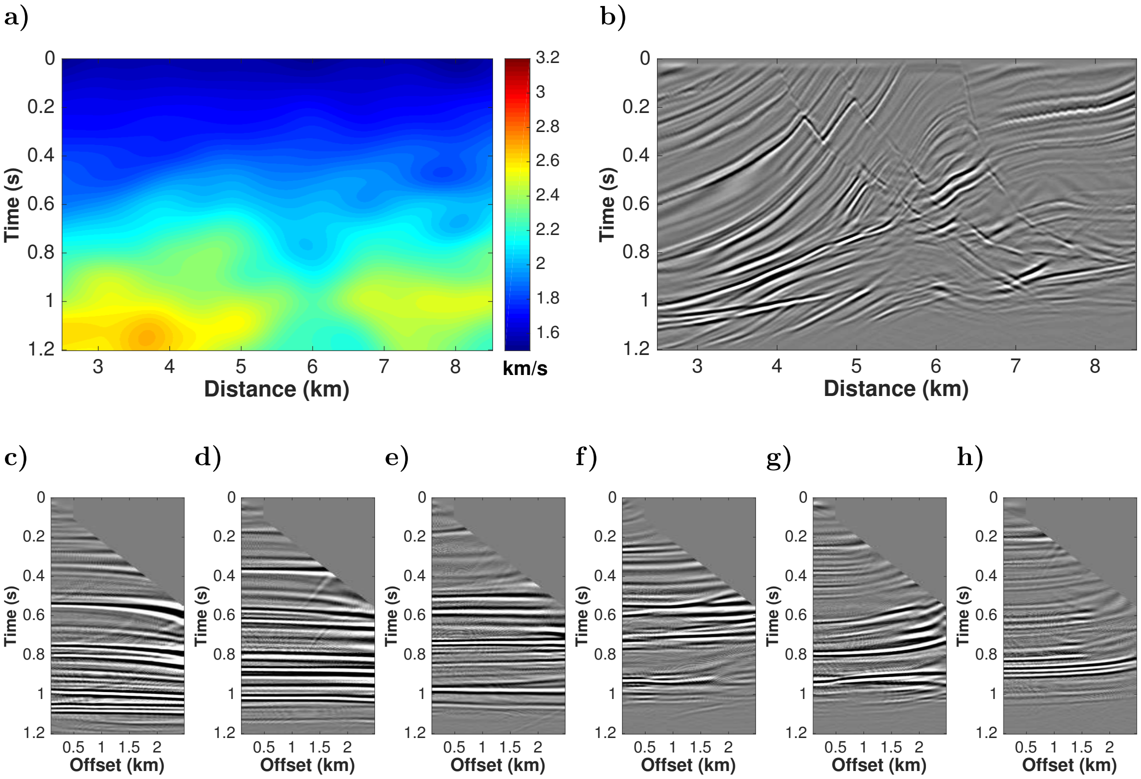

Figure 2.19: Experiment 1. Third iteration of the image-wave propagation method using auto-picks at the maxima of horizontal semblance. Shown are the velocity model (a), the final migrated image (b), and common-image gathers from time migration at (c) 3000 m, (d) 4000 m, (e) 5000 m, (f) 6000 m, (g) 7000 m and (h) 8000 m.

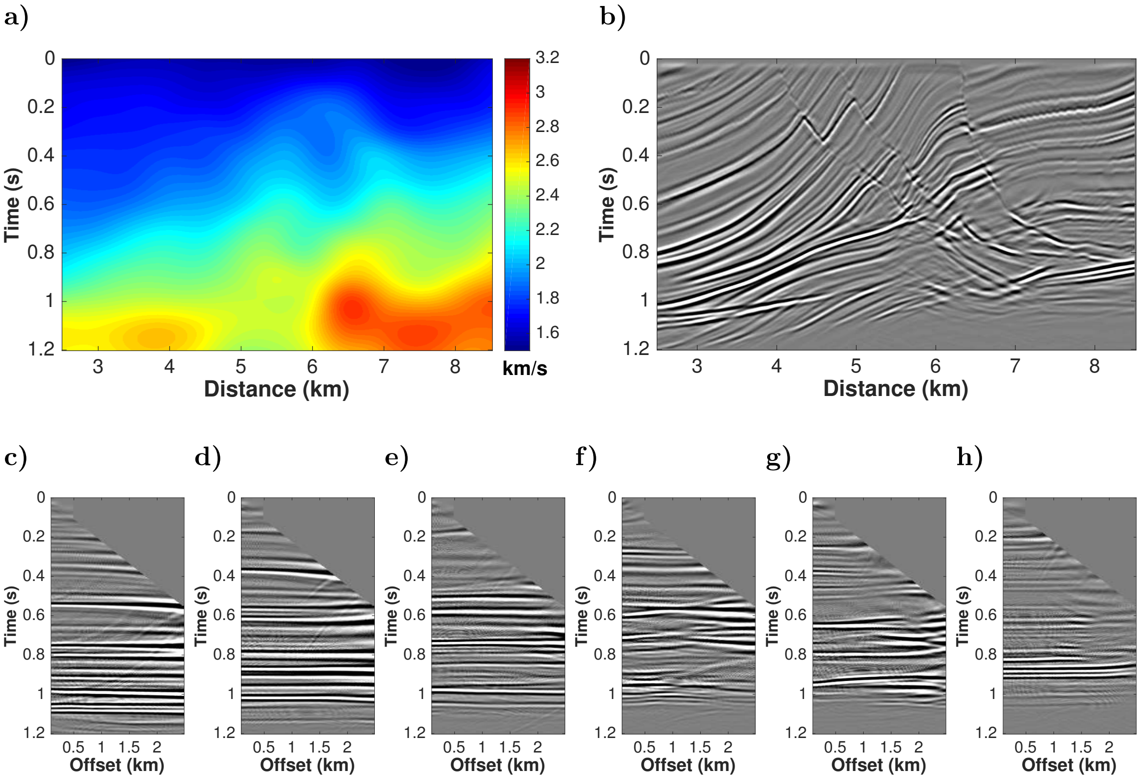

Figure 2.20: EXPERIMENT 1. Fifth iteration of the image-wave propagation method using auto-picks at the maxima of horizontal semblance. Shown are the velocity model (a), the final migrated image (b), and common-image gathers from time migration at (c) 3000 m, (d) 4000 m, (e) 5000 m, (f) 6000 m, (g) 7000 m and (h) 8000 m.

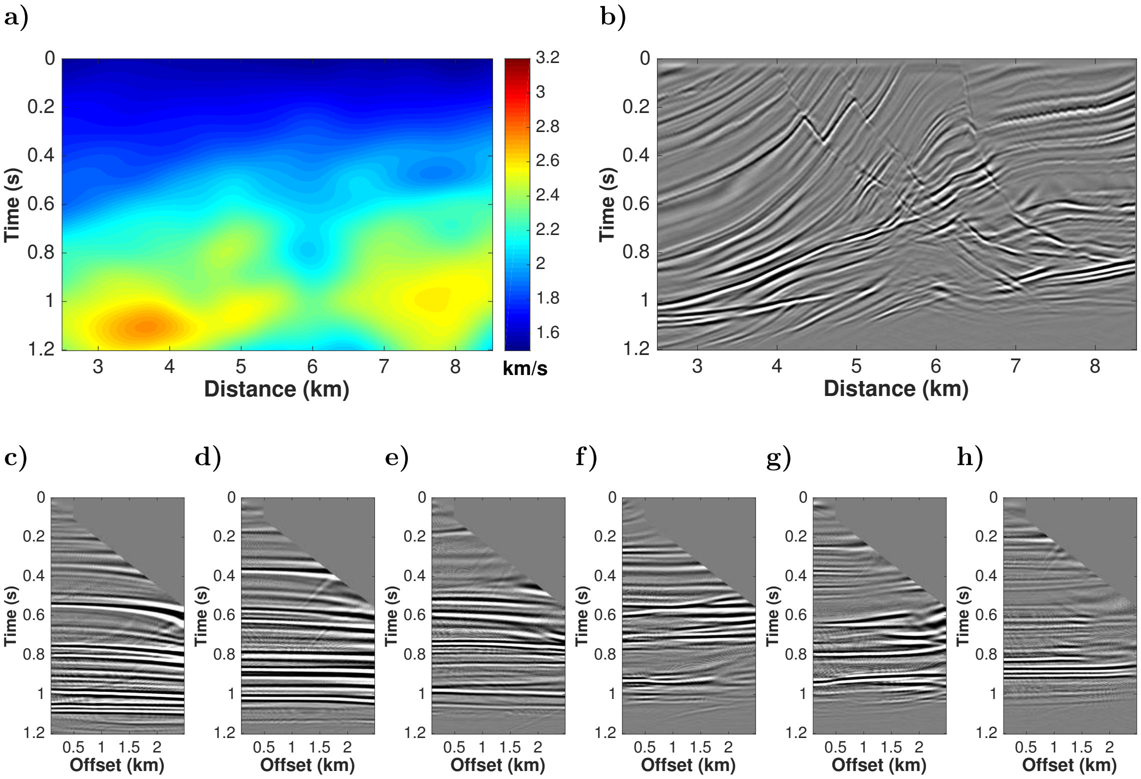

Figure 2.21: Experiment 2. Third iteration of the image-wave propagation method using auto-picks at the maxima of smoothed horizontal semblance. Shown are the velocity model (a), the final migrated image (b), and common-image gathers from time migration at (c) 3000 m, (d) 4000 m, (e) 5000 m, (f) 6000 m, (g) 7000 m and (h) 8000 m.

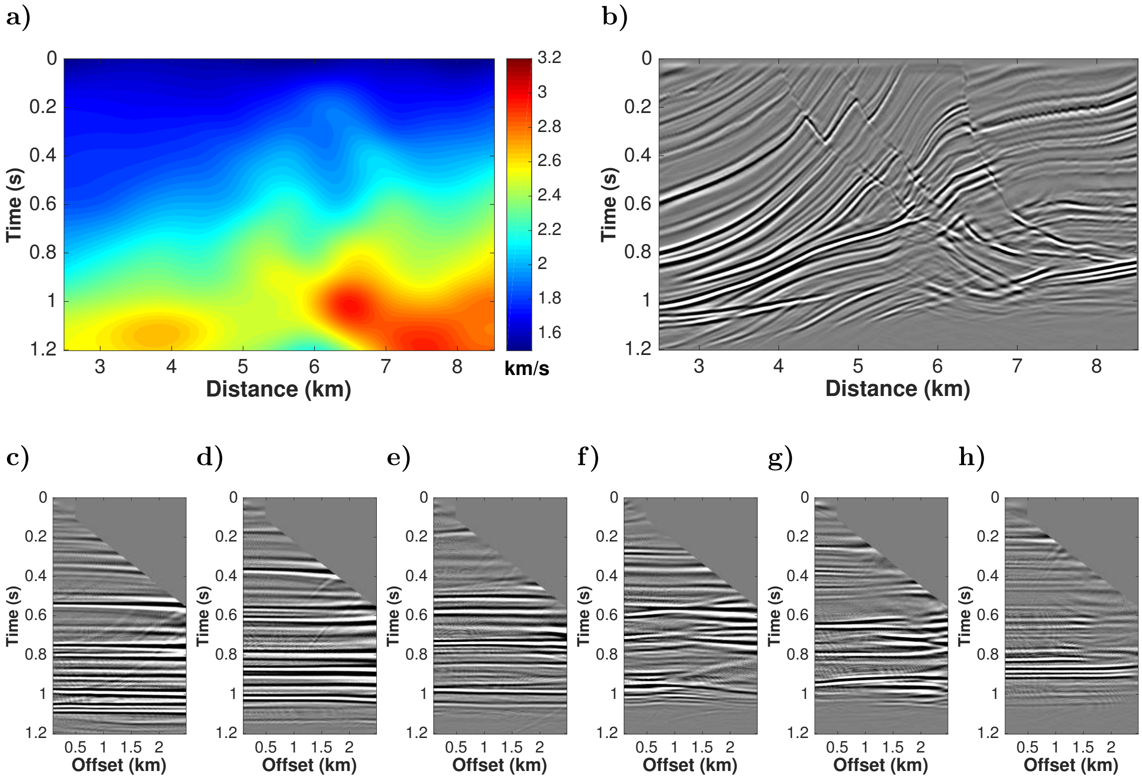

Figure 2.22: Experiment 2. Fifth iteration of the image-wave propagation method using auto-picks at the maxima of smoothed horizontal semblance. Shown are the velocity model (a), the final migrated image (b), and common-image gathers from time migration at (c) 3000 m, (d) 4000 m, (e) 5000 m, (f) 6000 m, (g) 7000 m and (h) 8000 m.

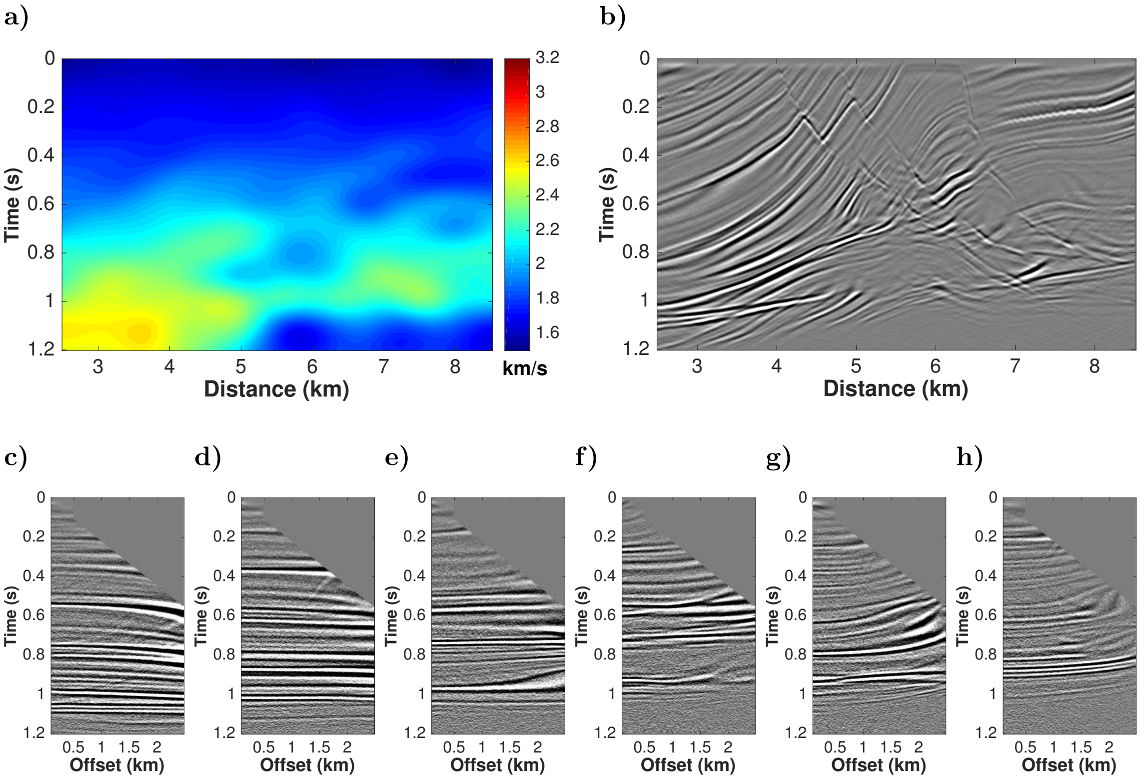

Figure 2.23: EXPERIMENT 3. Third iteration of the image-wave propagation method using auto-picks at the maxima of horizontal semblance. Shown are the velocity model (a), the final migrated image (b), and common-image gathers from time migration at (c) 3000 m, (d) 4000 m, (e) 5000 m, (f) 6000 m, (g) 7000 m and (h) 8000 m.

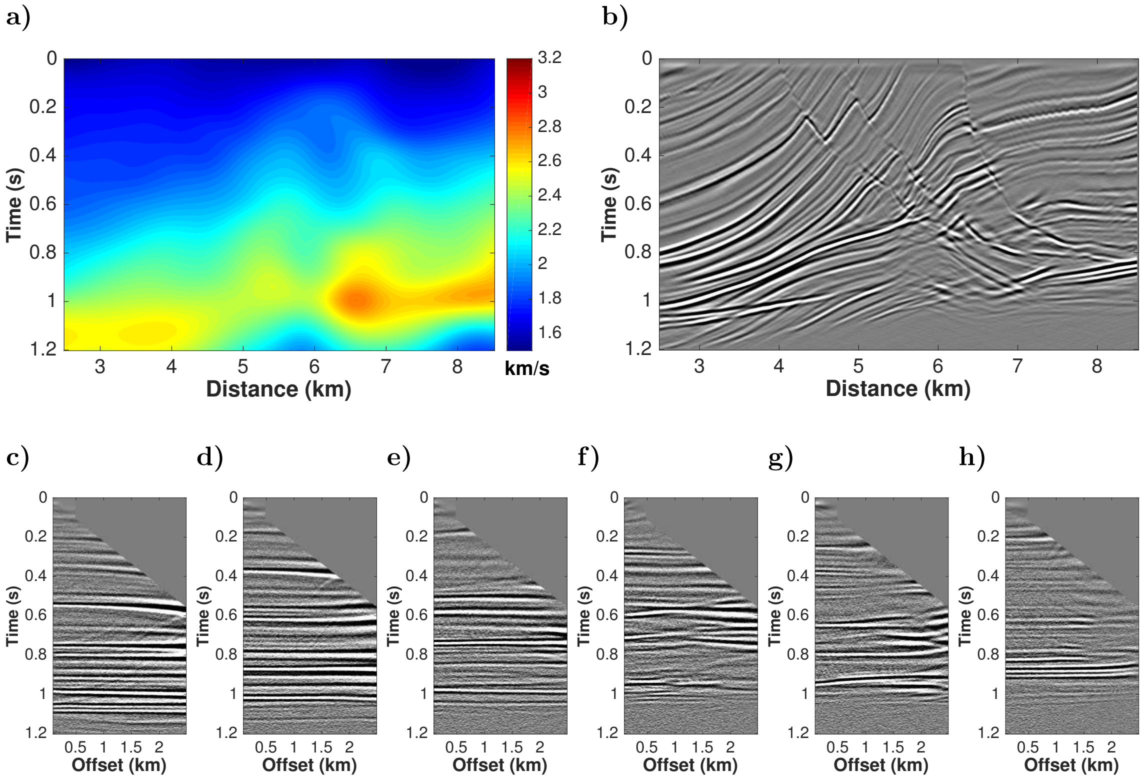

Figure 2.24: EXPERIMENT 3. Fifth iteration of the image-wave propagation method using auto-picks at the maxima of horizontal semblance. Shown are the velocity model (a), the final migrated image (b), and common-image gathers from time migration at (c) 3000 m, (d) 4000 m, (e) 5000 m, (f) 6000 m, (g) 7000 m and (h) 8000 m.

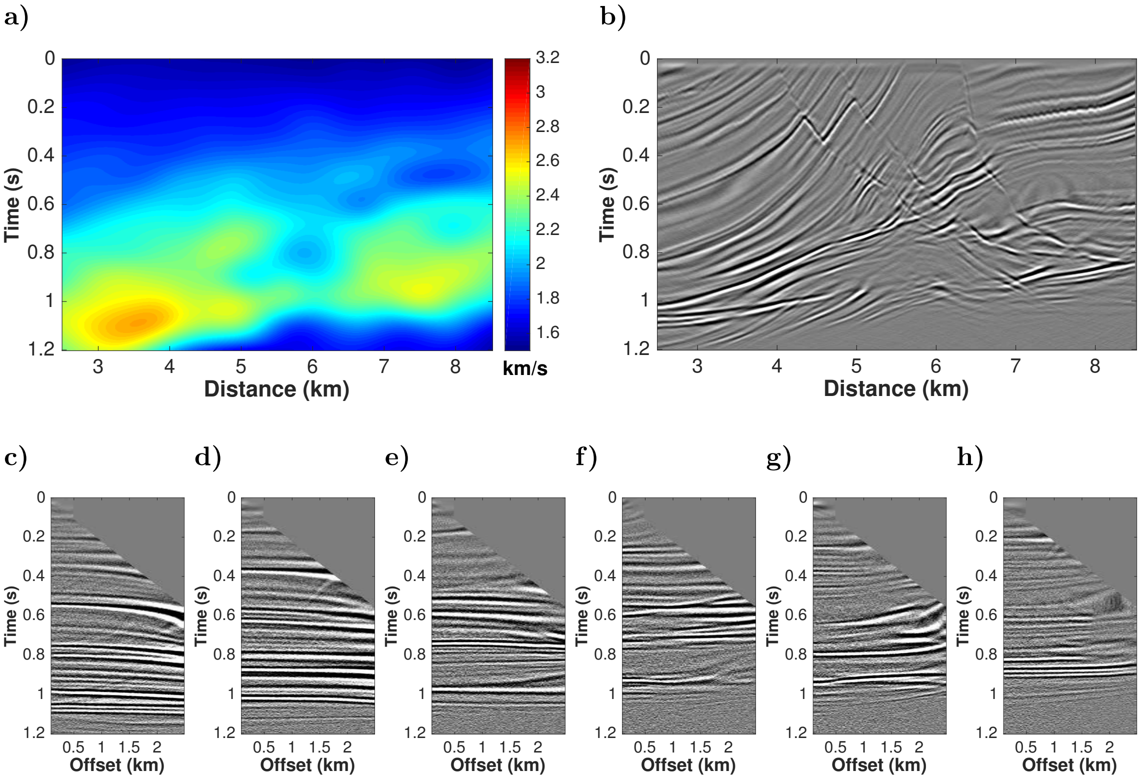

Figure 2.25: EXPERIMENT 4. Third iteration of the image-wave propagation method using auto-picks at the maxima of smoothed horizontal semblance. Shown are the velocity model (a), the final migrated image (b), and common-image gathers from time migration at (c) 3000 m, (d) 4000 m, (e) 5000 m, (f) 6000 m, (g) 7000 m and (h) 8000 m.

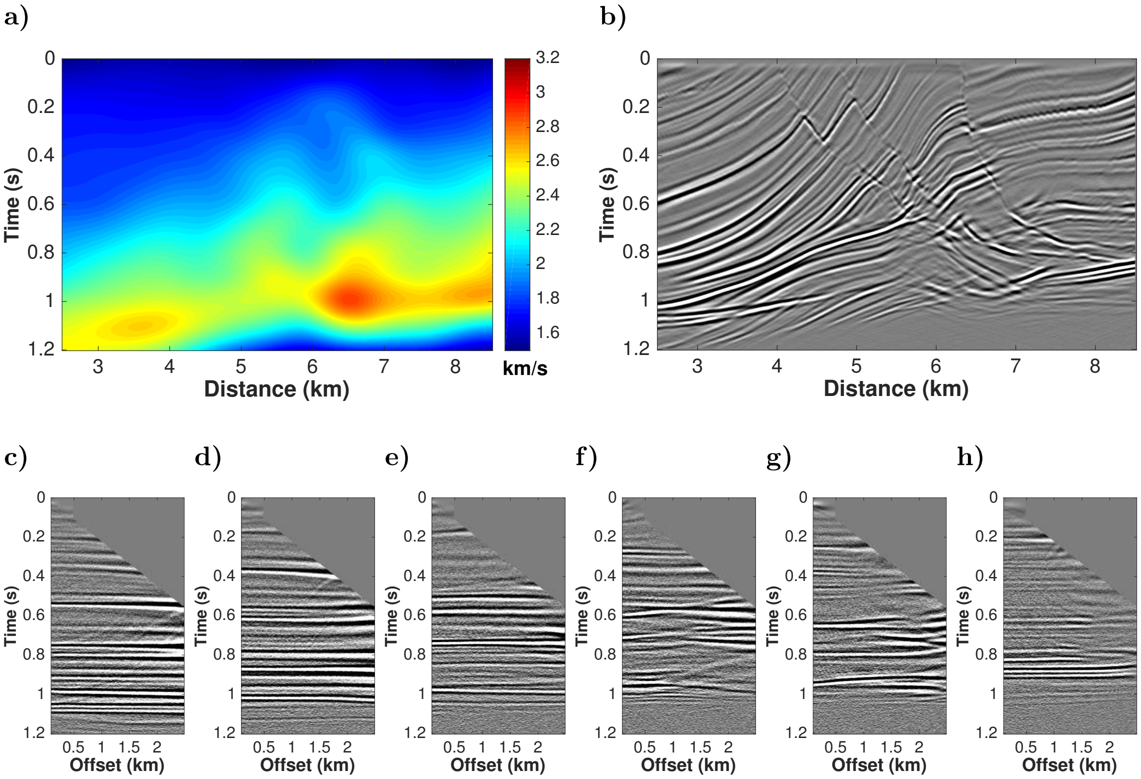

Figure 2.26: Experiment 4. Fifth iteration of the image-wave propagation method using auto-picks at the maxima of smoothed horizontal semblance. Shown are the velocity model (a), the final migrated image (b), and common-image gathers from time migration at (c) 3000 m, (d) 4000 m, (e) 5000 m, (f) 6000 m, (g) 7000 m and (h) 8000 m.

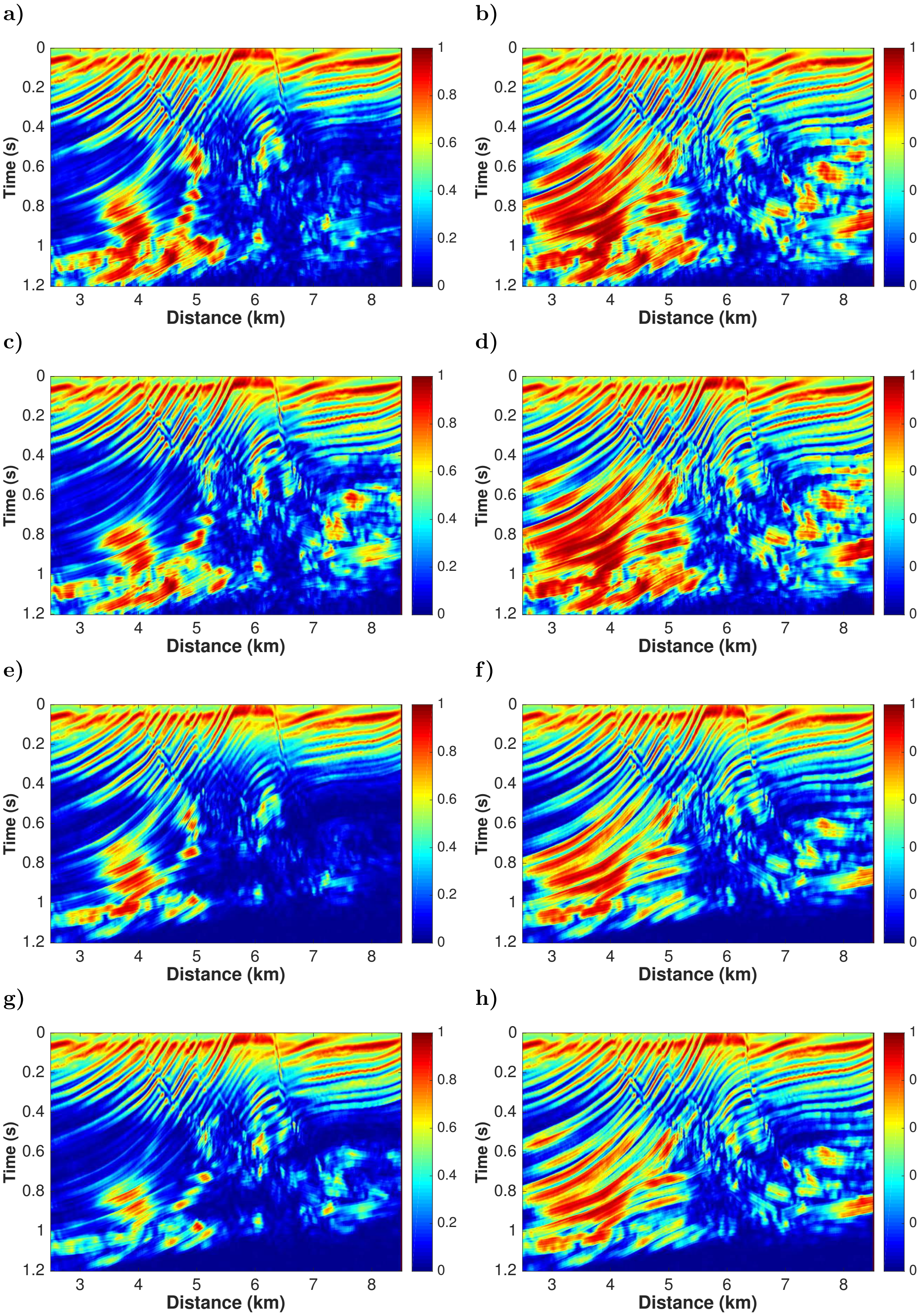

Figure 2.27: Coherence panels after the third (left) and fifth (right) iterations of the image-wave propagation method for the Experiments 1 (a)-(b), 2 (c)-(d), 3 (e)-(f), and 4 (g)-(h).

flattening velocities at 95 CIGs in 5 iterations (Figure 2.13). Here, we tested how automatic picking could be used to accelerate the procedure. The experience was quite positive. Although the automatic picking provides slightly less quality in the extracted velocities, there was no need for more iterations in the automatic process than in the interactive process to achieve a final model of about the same quality.

We also investigated the computational time spent in each experiment of this MVA processing. The results presented in Table 2.2 show that the time spent on the image-wavefront propagation accounts for approximately the same even for the noise-contaminated data. The processing was performed on a workstation with a Intel®, Xeon® E5-2450, 2.10 GHz processor, running a serial Fortran source code. Appendix B presents detailed information regarding the hardware and software used.

### 2.5.3 Multi-stack migration

#### Parameter setup

The most fundamental parameter in multi-stack migration velocity analysis is the quantity used to measure the flatness of an event in a CIG. We use the same parameter as in the original work of Schleicher and Costa (2009), namely the sum over the squares of the local slopes along a horizontal line in the CIG. Please, see the theoretical description in Section 2.3.2.

We separated the multi-stack migration into two experiments (Table 2.2). The Experiments 5 and 6 show the double multi-stack migration applied respectively to the true Marmousoft data set and the noise-corrupted one (Section 2.4). Table 2.4 summarizes the parameter setup considered in these experiments.

As in the image-wave propagation of CIGs, the double multi-stack migration needs to scan between a minimum ($v_{min}$) and maximum ($v_{max}$) velocity values. The results presented here were obtained setting up $v_{min} = 1400\,\mathrm{m/s}$ and $v_{max} = 4200\,\mathrm{m/s}$, with a velocity sampling interval $\Delta v = 25\,\mathrm{m/s}$. These values can be chosen almost arbitrarily as long as the velocity range is large enough to ensure the properties and limitations of the method. It is possible to use a priori information to reduce the number of migrations, for example, discarding unrealistic velocity values.

Figures 2.28 and 2.29 show the results of Experiments 5 and 6 respectively. Figures 2.28a and 2.29a show the resulting stacked migrated images ($V_W$, Equation 2.11). The results show that the method used produces accurate images. The primary structures of the Marmousi model (Figure 2.5) are noted, even with the presence of noise in the data. Figures 2.28b and 2.29b depict the second multipath-summation computed by the use of the migration velocity as an additional

Table 2.4: General setup of the MVA by doble multi-stack migration.

| **Multi-stack migration - Parameter setup** | |
|---|---|
| Initial time for migration | 0 s |
| Final time for migration | 1.2 s |
| Initial $x$ for migration | 2500 m |
| Final $x$ for migration | 8500 m |
| Sampling rate in $t$ for migration | 0.002 s |
| Sampling rate in $x$ for migration | 12 m |
| Number of B-spline nodes in $t$ direction | 14 |
| Number of B-spline nodes in $x$ direction | 52 |
| Distance between nodes of B-splines in $t$ direction | 0.1 s |
| Distance between nodes of B-splines in $x$ direction | 200 m |
| Coordinate of first CIG for velocity analysis | 2500 m |
| Distance between CIGs for velocity analysis | 12 m |
| Number of CIGs for velocity analysis | 501 |
| Minimum velocity to be scanned | 1400 m/s |
| Maximum velocity to be scanned | 4200 m/s |
| Velocity sampling interval | 25 m/s |
| Regularization for B-splines interpolation | See Table C.1 |

weight factor in the stack ($\tilde{V}_W$, Equation 2.16). They look quite similar to their corresponding unweighted stack results (Figures 2.28a and 2.29a), except for their amplitudes which increases with depth. The division (Equation 2.17) of the images of Figures 2.28a and 2.28b, and Figures 2.29a and 2.29b, result in the migration velocity models presented in Figures 2.28c and 2.29c respectively. A fraction of the maximum amplitude was added to the denominator to make the division more stable. However, there are many image points with unreliable (nongeological) values, indicating the needs to postprocess these velocity models.

A simple way to avoid the nonrealistic velocity values is to remove velocities from outside the range of the velocities that were used for the multi-path migration and to avoid division where the absolute value of the denominator is too small, setting all these velocities to zero. Figures 2.28d and 2.29d show the extracted velocity by masked division obtained in Experiments 5 and 6, where linear interpolation was applied to create each one of the illustrations. Therefore, we can use this masked division to eliminates the incorrect velocity values, but a smoothing and interpolation step becomes necessary.

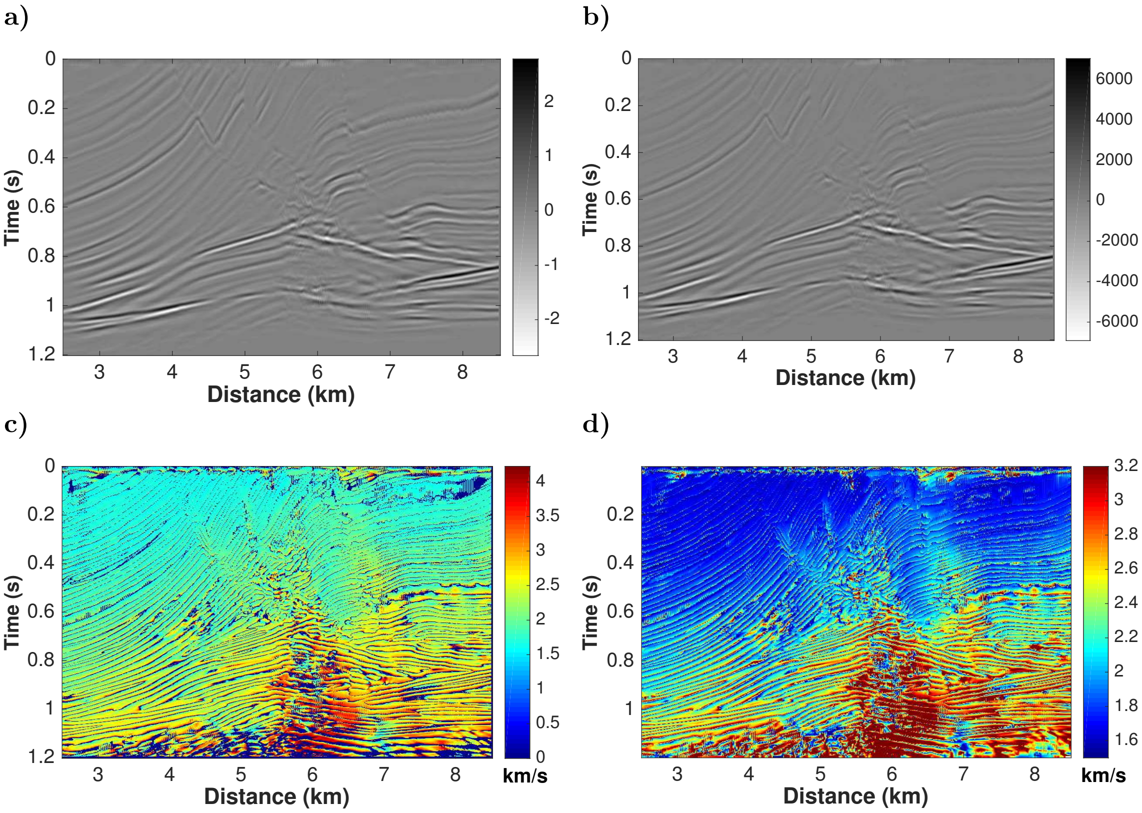

Figure 2.28: Experiment 5. Shown are the multipath-summation time imaging (a), and the one resulting with additional velocity weight (b), the velocity extracted by stabilized division (c), and the velocity extracted by masked division (d).

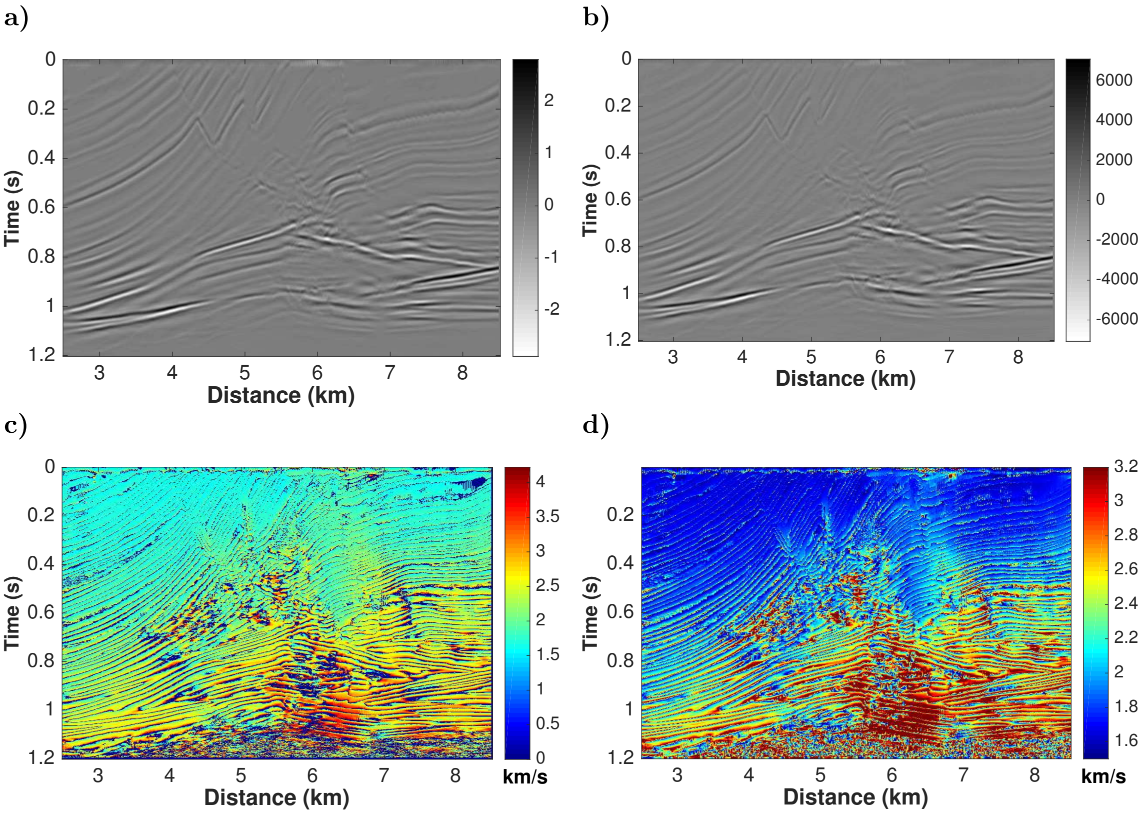

Figure 2.29: EXPERIMENT 6. Shown are the multipath-summation time imaging (a), and the one resulting with additional velocity weight (b), the velocity extracted by stabilized division (c), and the velocity extracted by masked division (d).

### Regularization

Since the method extracts velocity values only at points where the image is nonzero, the B-splines interpolation needs some regularization. Such regularization is achieved by a relative weight of each constraint in the cost function (Costa and Schleicher, 2011). The resulting model is rather sensitive to the choice of the regularization parameter (see, Appendix C). Here, we tested how to chose this parameter in order to arrive at a comparable model to the one from CIG continuation. Figures 2.30 to 2.32 and Figures 2.33 to 2.35 show the results of the velocity extraction using double multi-stack migration velocity analysis under three different forms of regularization. Note that the resulting velocity models are considerably different.

Parts (a) of Figures 2.30, 2.31 and 2.32 show the velocity model computed by a very hard, intermediate, and very soft regularization, respectively (the same for the Figures 2.33 to 2.35 for the Experiment 6). In comparison with the models of Figures 2.19 to 2.26, it is easy to see that the velocity model obtained with a very hard regularization (Figures 2.30 and 2.33) is much smoother but still maintains a long-wavelengths feature of true model (see the Marmousoft rms velocity model in Figure 2.8). In turn, after very soft regularization the model presents too much detail for a time-migration model. Also, boundary effects of the B-splines interpolation start affecting the resulting model. Note the high-velocity values in the upper part and low values in the bottom part of the velocity model (Figures 2.32 and 2.35). The velocity model obtained from an intermediate regularization (Figures 2.31 and 2.34) seems to be more compatible with the ones obtained by the image-wave propagation of CIGs (Figures 2.19 to 2.26), as well as those ones obtained by Schleicher et al. (2008) and Schleicher and Costa (2009) depicted in Figures 2.13 and 2.14.

On the other hand, when we compare the migrated images obtained with these models (parts (b) of Figures 2.30 to 2.35), we see that they are virtually identical (also, compare with the examples depicted in Figures 2.11 and 2.12). Even in the image gathers (parts (c) to (h)), it is hard to spot significant differences. Thus, from an imaging point of view, there is a broad range of regularization (Table C.1) that can provide suitable velocity models for an acceptable time-migrated image. Future investigations with subsequent depth conversion will be necessary to decide which level of regularization is most suited to find a suitable initial model for depth MVA. This topic will be covered in Chapters 4 and 5 and Appendix E.

### Reliability

Our results show that the multipath-summation approach improved the positioning of key reflectors in the time-migrated images. All the images obtained in the Experiments 5 and 6 exhibit the main structures of the Marmousi model (Figure 2.6).

Following the control tests presented in Figures 2.11 and 2.12 and the previous discussion made in section 2.5.2, we calculated the coherence panels for each one of the final migrated images obtained by the multi-stack migration (Figures 2.30b, 2.31b, 2.32b, 2.33b, 2.34b and 2.35b). All the coherence panels are plotted in Figure 2.36. Those panels spot where the obtained velocity models can or cannot be trusted.

Comparing the panels in Figure 2.36 with those shown in Figure 2.27, we see a positive correlation between the two MVA approaches evaluated in this chapter. Also, the high coherence values presented in Figure 2.36 match with those obtained when using the rms velocity model (Figures 2.11 and 2.12), mainly in the vicinity of less-complex geology, mostly located in the shallower regions and at the portion of the center-left side. On the other hand, the central part of the images is not perfectly recovered. We believe this is because the limitations of time migration rather than those of the method applied. Thus, we expect smaller values of coherence where time migration could not flatten the image gathers. Such assumption can be easily confirmed with the coherence panels shown in Figure 2.36.

From the analysis of the coherence panels of Experiment 5 (Figures 2.36a to 2.36c) and Experiment 6 (Figures 2.36d to 2.36f), we observe the influence in the results originated by the noise present in the data. The semblances of Experiment 6 have lower values of coherence. Furthermore, a visual inspection of Figures 2.36a to 2.36c (Experiment 5), suggests better results in the region located approximately at 4 and 5 km and below 0.6 s, when applied the intermediate and very soft regularization instead of the very hard regularization. However, the same observation cannot be made for the contaminated data (Experiment 6) shown in Figures 2.36d to 2.36f. Although perceptible with a very meticulous analysis, mainly in Figure 2.36f (very soft regularization).

### Computational Cost

The computational cost of double multi-stack migration is only slightly higher than for a single multi-stack migration. All that is needed is the multiplication of the migrated image by the present velocity, a summation into a second, velocity-weighted image, and a division of the final results at each point in the image. The computationally most expensive part, the time migration for each of the chosen velocities, is done only once. The computational cost of a single multi-stack migration is, of course, $N_v$ times the cost of a single time migration, where $N_v$ is the number of velocities used. However, constant-velocity time migrations are the cheapest possible migrations. Moreover, these time migrations are entirely independent, making the process fully parallelizable.

The total cost of the proposed velocity analysis is just the one of double multi-stack migration. The velocity extraction, interpolation, and smoothing can be done fully automatically, without the need for human interpretation or other intervention. Such automatization makes it highly advantageous over conventional velocity-analysis techniques which strongly rely on human interaction.

Table 2.2 shows the computational time spent on the Experiments 5 and 6. There is no significant variation concerning the presence of noise in the data. However, the computational cost of Experiments 5 and 6 are considerably lower than those measured in Experiments 1 and 4. Although part of this reduction is due to the parallelization of processing. Description of the computational codes and resources can be found in Appendix B.

## 2.6 Conclusions

We have studied two different time migration-velocity-analysis methods: image-wave common-image-gather continuation (Schleicher et al., 2008) and multi-stack migration (Schleicher and Costa, 2009). Our comparison of the velocity models obtained with both methods revealed that rather different models are obtained depending on the parameterization. However, the associated time-migrated images exhibit fairly much the same quality, indicating that for time-migration, all velocity models are equivalent.

In the original version of (Schleicher et al., 2008), the strongly interactive character of CIG-continuation MVA is a significant drawback. In this work, we have demonstrated that an automatic implementation of the picking of flattening velocities does not degrade the final image or lead to additional iterations. In this way, the technique becomes competitive regarding the computational cost to multi-stack migration MVA, which is entirely automatic and exclusively relies on constant-velocity migrations.

We have seen that multi-stack migration MVA can provide a broad range of differently smoothed velocity models. Since in our implementation of CIG-continuation MVA, the velocity model is represented in an identical way, the same should be possible for that method. How a smoother or more detailed model affects the result of the image-wave propagation is a topic of ongoing research.

One difference between the methods is that multi-stack migration allows extracting a velocity model without any a priori information whatsoever, while the velocity continuation method needs an (fairly arbitrary) initial model. In our applications, starting from a constant-velocity model (e.g., water velocity) was always sufficient to reach a reasonable time-migration velocity model. A fairly intuitive extension of the present research is to use the velocity model generated by multi-stack imaging as an initial model in velocity continuation.

Our evaluation demonstrates that both methods are equivalent regarding the final result, i.e., the time-migrated image. In summary, the methods were shown to be qualitatively and quantitatively consistent. Both of them proved to be capable of calculating a representative velocity model, with their results depending on the choice of some fundamental parameters.

The broad range of obtainable models that produce equivalent image quality in time migration is a reliable indicator that the investigated techniques can be employed to construct initial models for a subsequent more sophisticated depth migration-velocity analysis. In order to evaluate which parameterization will lead to the best-suited starting models, a time-to-depth conversion will be necessary to compare the attainable model quality. This subject is discussed further in Chapters 4 and 5 and Appendix E.

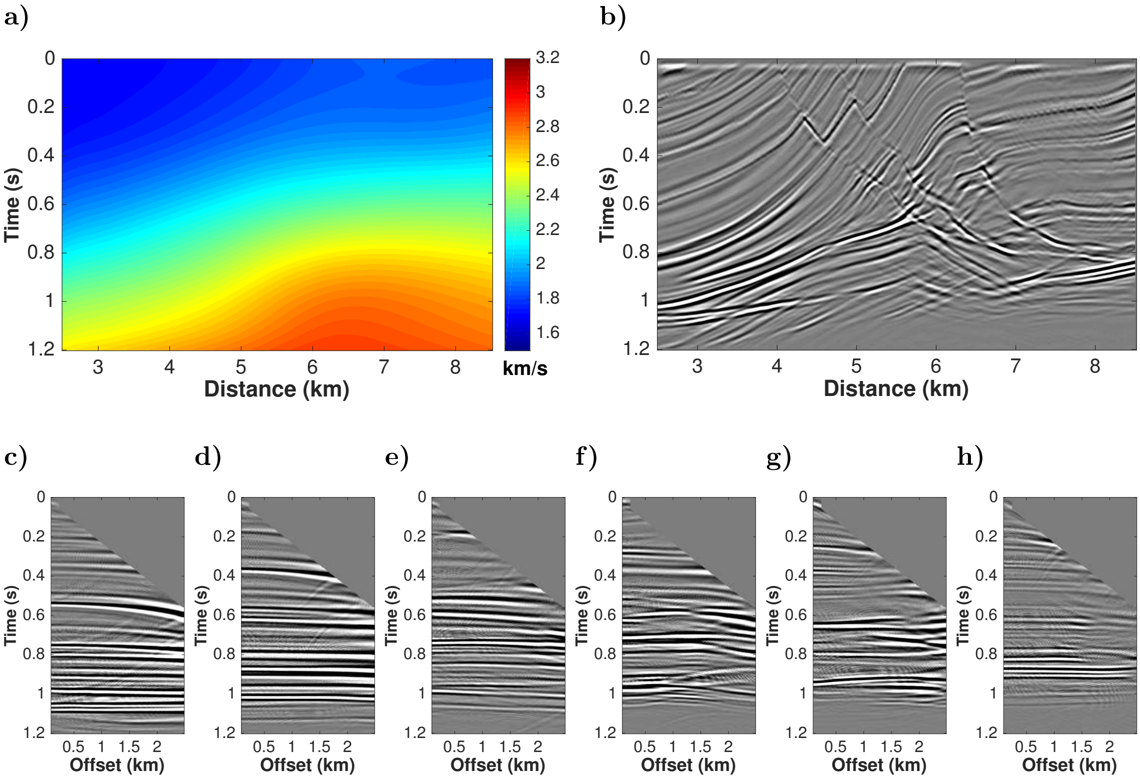

Figure 2.30: Experiment 5. Results of multi-stack MVA with very hard regularization. Shown are the velocity model (a), the final migrated image (b), and common-image gathers from time migration at (c) 3000 m, (d) 4000 m, (e) 5000 m, (f) 6000 m, (g) 7000 m and (h) 8000 m.

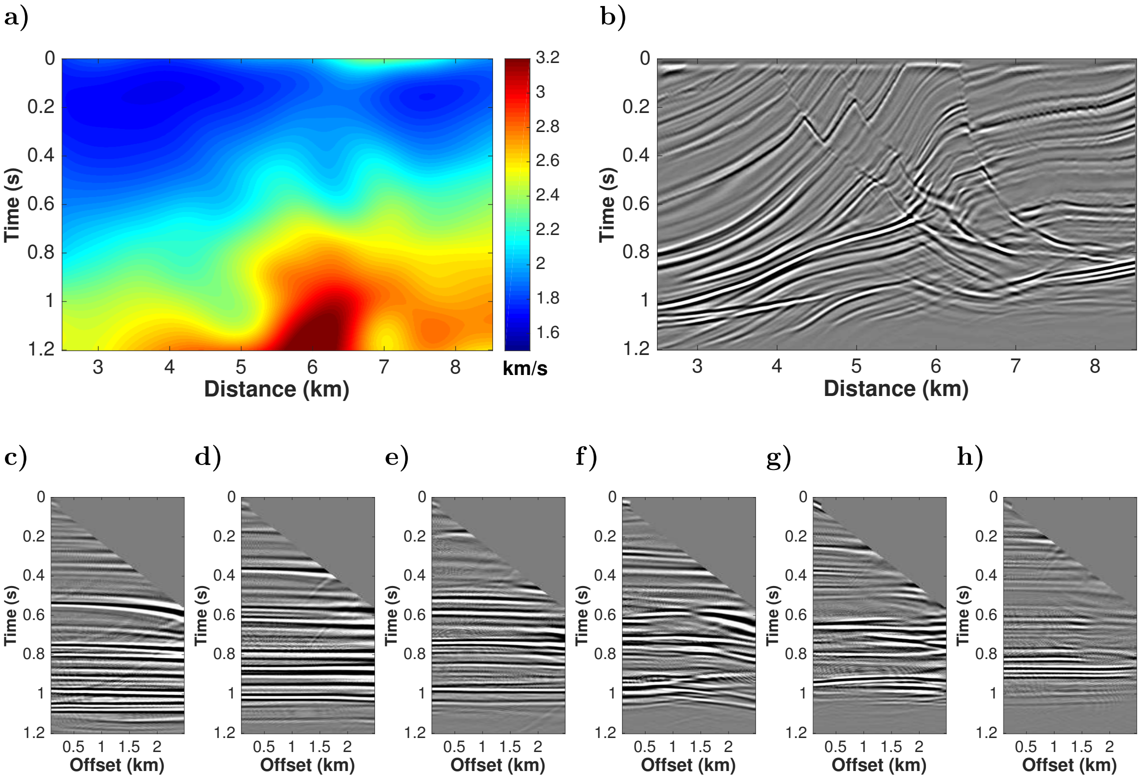

Figure 2.31: Experiment 5. Results of multi-stack MVA with intermediate regularization. Shown are the velocity model (a), the final migrated image (b), and common-image gathers from time migration at (c) 3000 m, (d) 4000 m, (e) 5000 m, (f) 6000 m, (g) 7000 m and (h) 8000 m.

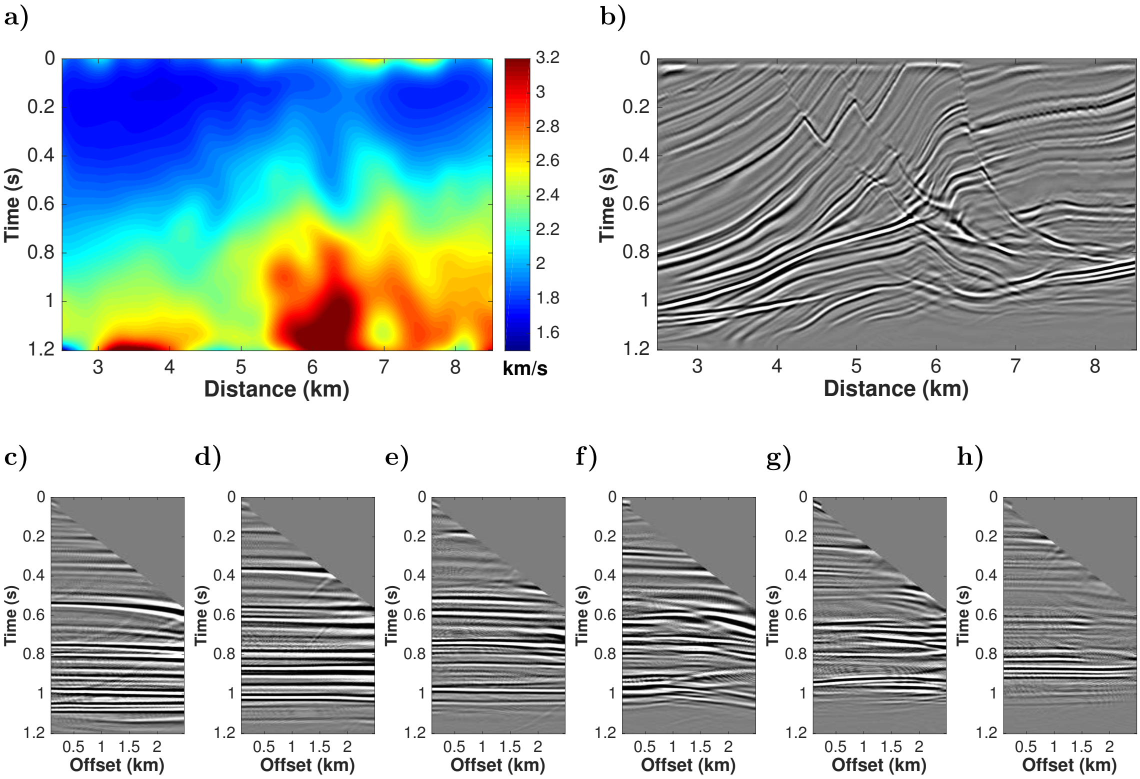

Figure 2.32: Experiment 5. Results of multi-stack MVA with very soft regularization. Shown are the velocity model (a), the final migrated image (b), and common-image gathers from time migration at (c) 3000 m, (d) 4000 m, (e) 5000 m, (f) 6000 m, (g) 7000 m and (h) 8000 m.

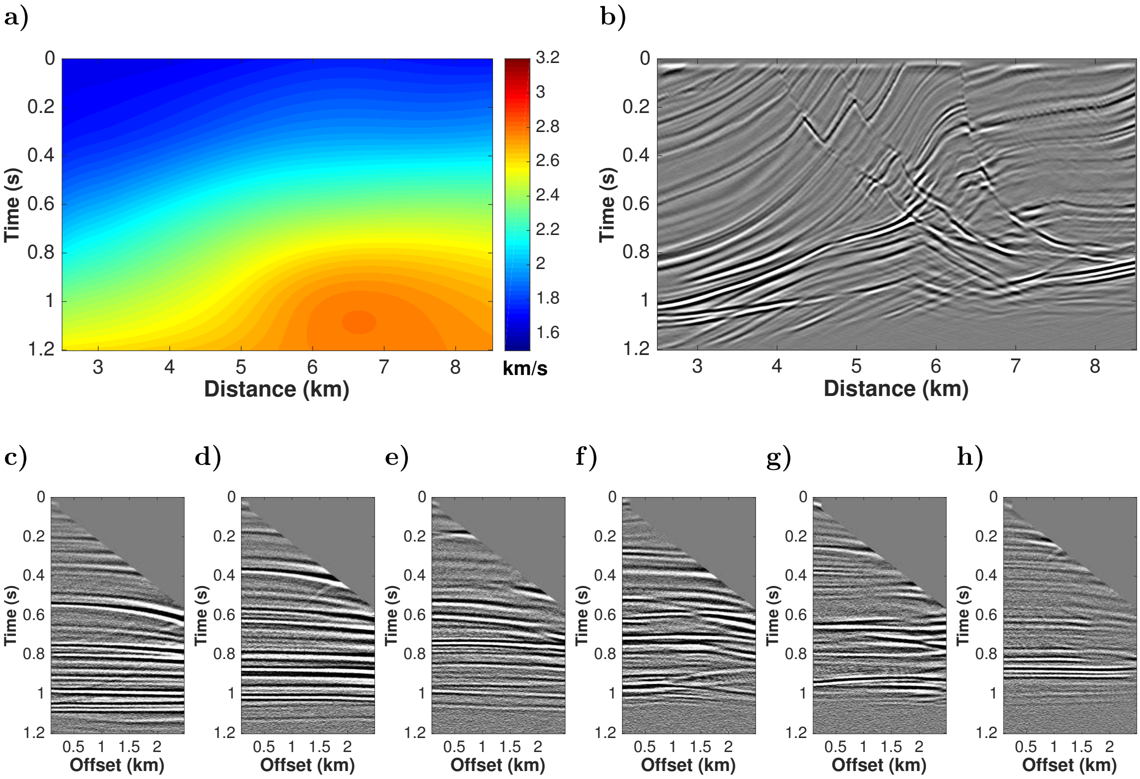

Figure 2.33: Experiment 6. Results of multi-stack MVA with very hard regularization. Shown are the velocity model (a), the final migrated image (b), and common-image gathers from time migration at (c) 3000 m, (d) 4000 m, (e) 5000 m, (f) 6000 m, (g) 7000 m and (h) 8000 m.

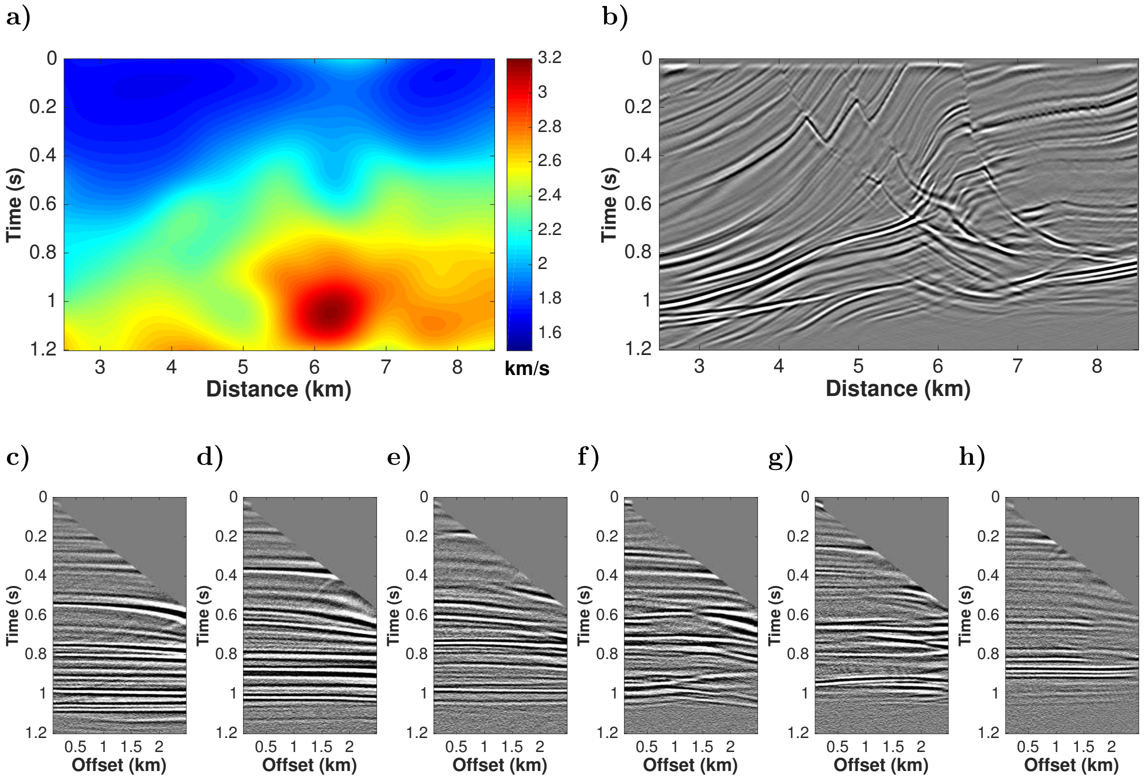

Figure 2.34: Experiment 6. Results of multi-stack MVA with intermediate regularization. Shown are the velocity model (a), the final migrated image (b), and common-image gathers from time migration at (c) 3000 m, (d) 4000 m, (e) 5000 m, (f) 6000 m, (g) 7000 m and (h) 8000 m.

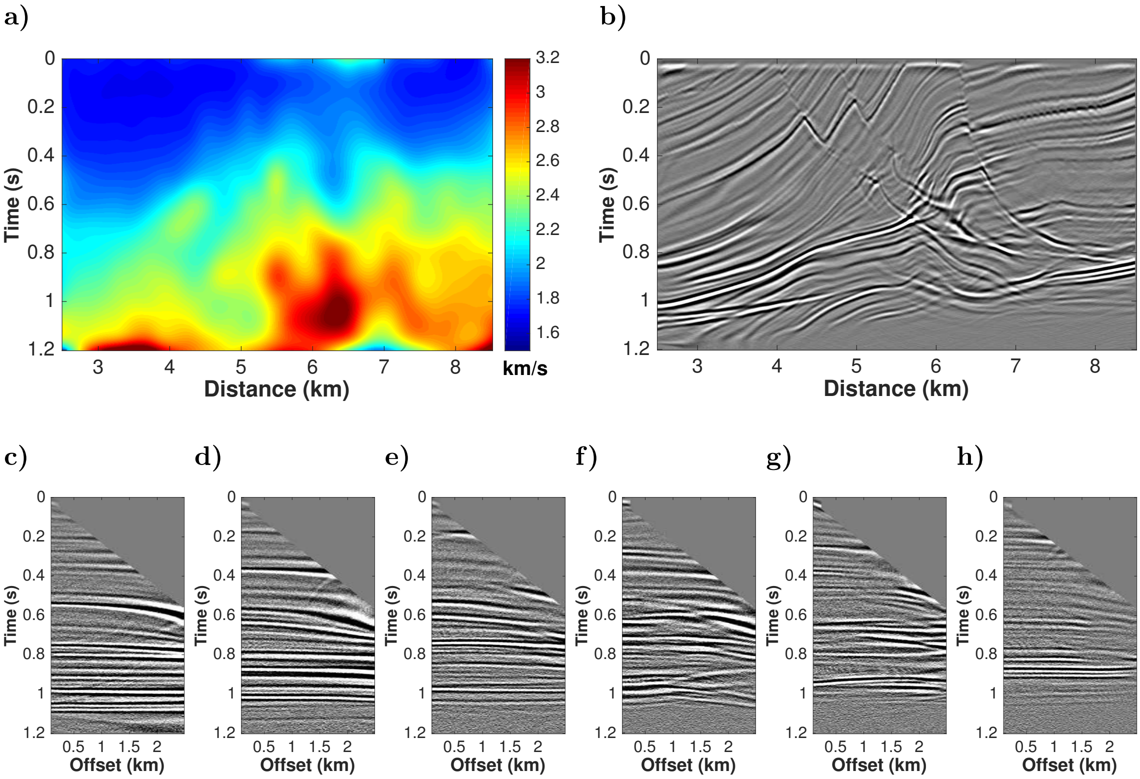

Figure 2.35: Experiment 6. Results of multi-stack MVA with very soft regularization. Shown are the velocity model (a), the final migrated image (b), and common-image gathers from time migration at (c) 3000 m, (d) 4000 m, (e) 5000 m, (f) 6000 m, (g) 7000 m and (h) 8000 m.

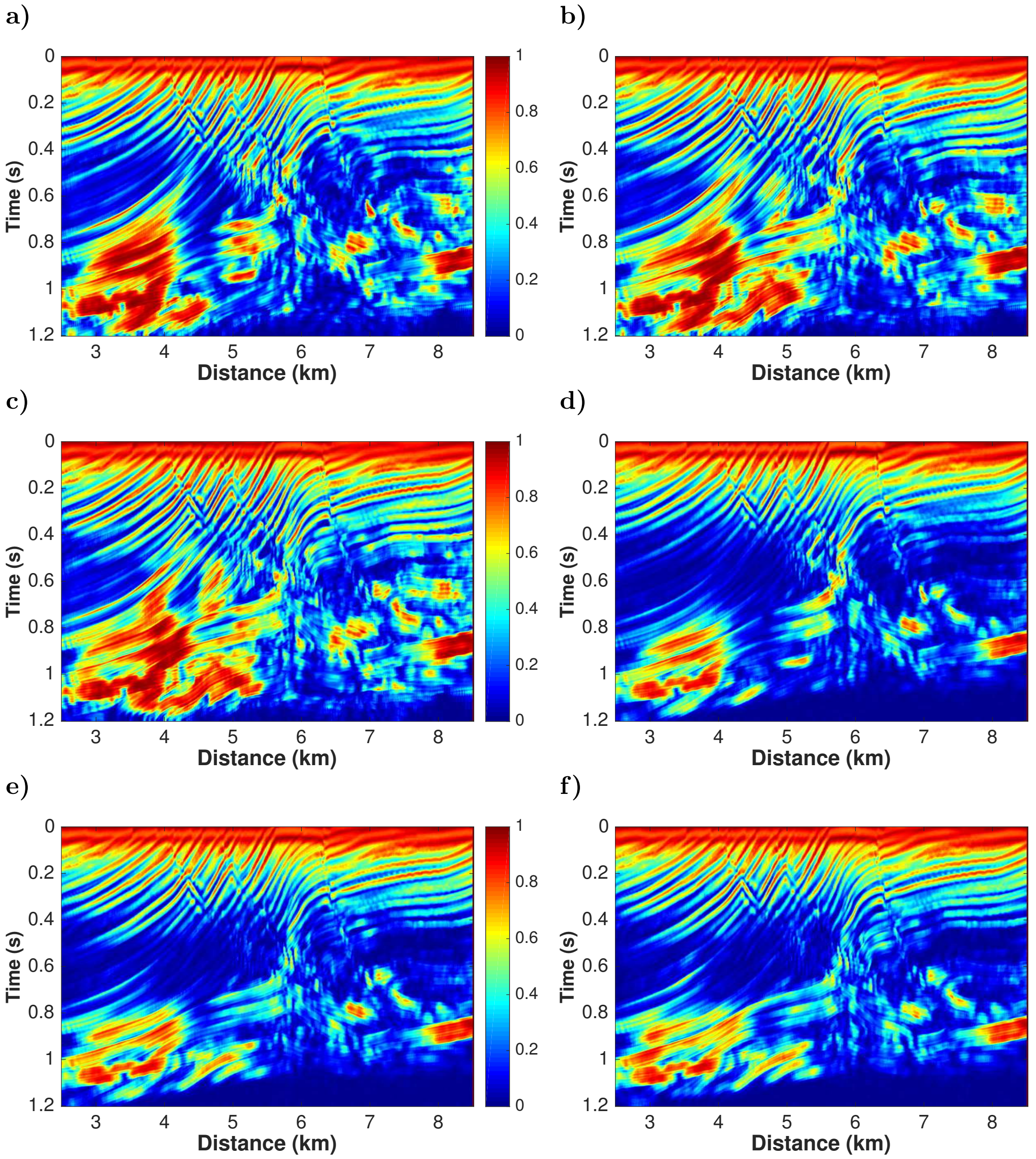

Figure 2.36: Coherence panels of the multi-stack MVA corresponding to the time migrations obtained in Experiments 5 and 6 respectively depicted in Figures 2.30 to 2.35.

# Chapter 3

# Prestack time-migration velocity analysis using remigration trajectories

## 3.1 Summary

We have developed a prestack time-migration tool for local improvement of the seismic migration-velocity model. The method is based on remigration trajectories that describe the position of an image point in the image domain for different source-receiver offsets as a function of the migration velocity. It determines kinematic migration parameters using local-slope information of migrated seismic reflection events. These parameters, in turn, are used to locally correct the velocity model. The main advantage of this technique is that it allows to carry out a moveout correction not just at a fixed point in a zero-offset (post-stack) time-migrated gather, but varying through all offsets of a common image gather (CIG), taking into account the reflection-point displacement in the midpoint direction. In other words, it provides for time-migration velocity analysis (MVA) from prestack data. We have tested the feasibility of the method on synthetic data from four simple models, and the Sigsbee2B data. Our tests determined that the proposed tool increases the velocity-model resolution and provides a plausible time-migrated image. The quality of the initial model is not critical. The procedure is quite efficient. Significant effort was spent on manual event picking.

## 3.2 Introduction

Migration velocity analysis (MVA) is an important seismic processing step in prestack time-imaging. Basically, MVA exploits the redundancy of seismic data to improve an a-priori velocity model. As first observed by Sattlegger (1975), seismic data from different offsets need to migrate to the same positions when using the correct velocity model. Hence, these images must be horizontally aligned, regardless of structure. However, the use of too-low or too-high migration velocities leads to offset-dependent mispositioning, known as *migration smiles* or *frowns* (Al-Yahya, 1989; Zhu et al., 1998).

Over the years, substantial effort has been directed towards the development of new MVA methods. Because of its conceptual clarity and simplicity, residual-moveout (RMO) analysis has become one of the favorite tools for MVA (Liu and Bleistein, 1995). Many algorithms are based on the moveout formula for a horizontal reflector (Al-Yahya, 1989). However, in the case of strongly dipping reflectors, this correction does not take into account the lateral displacement of the reflector image that is caused by a change in migration velocity, thus requiring iterative procedures. Schleicher and Biloti (2007) try to improved Al-Yahya's process and achieve higher accuracy in the updated velocity by inclusion of the reflector dip as an additional parameter.

Another MVA principle is to follow migrated reflection events through the image domain under variation of the migration velocity (Fomel, 1994; Liptow and Hubral, 1995). Hubral et al. (1996b) use the term *image waves* to describe such a process of transforming time-migrated images according to the changes in migration velocity. Schleicher et al. (1997) derive equations for remigration trajectories in the zero-offset case and connected the concept to of residual migration. In a related way, Adler (2002) describes the change in the superposition of seismic data along isochrons at a predicted image point as a function of the velocity perturbation, a process he calls *Kirchhoff image propagation.* Fomel (2003a,b) further develops and tests the velocity-continuation or image-wave concept for the prestack situation. Iversen (2006) describes the position of a migrated image point as a function of migration velocity by velocity rays.

Velocity continuation can also be used on migrated diffractions (Sava et al., 2005; Fomel et al., 2007; Novais et al., 2008) for MVA. Based on velocity continuation, Coimbra et al. (2011, 2012, 2013b) recently introduce a new process of extracting velocity updates for depth migration from the moveout of incorrectly migrated diffraction events by tracing so-called remigration trajectories to their focus point in post-stack migrated images, and Coimbra et al. (2013a) extend their work to the

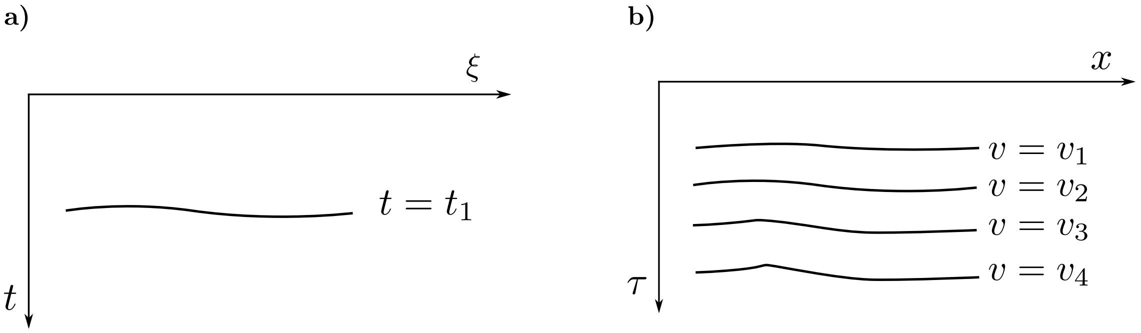

Figure 3.1: Sketch of: (a) A single reflection event in the time domain and (b) its time migrated images for four different migration velocities.

prestack case. This technique makes use of local-slope information extracted from the data with the help of stacks along local trial surfaces. In this work, we modify this remigration-trajectory MVA method to make it suitable for an application to time-migration of reflection events in prestack data. Tests on synthetic data from four simple models, on the Marmousoft data and on the Sigsbee2B data confirm the potential of our method to produce a plausible velocity model in a region with strong dip variations. At this point, the technique is a 2D procedure. An extension to 3D is conceptually straightforward.

## 3.3 Theoretical description

Prestack migration methods are useful to reconstruct an image of the subsurface from seismic reflection data. In general, prestack migration is considered a robust method due to the fact that it focuses energy that conventional data processing based on normal-moveout (NMO) correction and stacking of the common-midpoint (CMP) gathers cannot focus. In addition, the kinematics of prestack data considers the distance between the source and receiver, where the source-receiver offset defines a prestack volume (Bancroft et al., 1998).

It is well known that a single reflection event in a CMP stacked zero-offset section leads to different reflector images when migrated with different migration velocities (Figure 3.1). That is, the image can be thought of as "propagating" as a function of migration velocity (Fomel, 1994), forming a so-called "image wave" (Hubral et al., 1996b). In an attempt to achieve more realistic velocity models and migrated images, many methods have been proposed (Rothman et al., 1985; Liptow and Hubral, 1995; Hubral et al., 1996a; Schleicher et al., 1997; Adler, 2002; Fomel, 2003a,b; Schleicher et al., 2008). Such image-wave remigration procedures can even be extended to anisotropic media (Schleicher and Aleixo, 2007; Schleicher

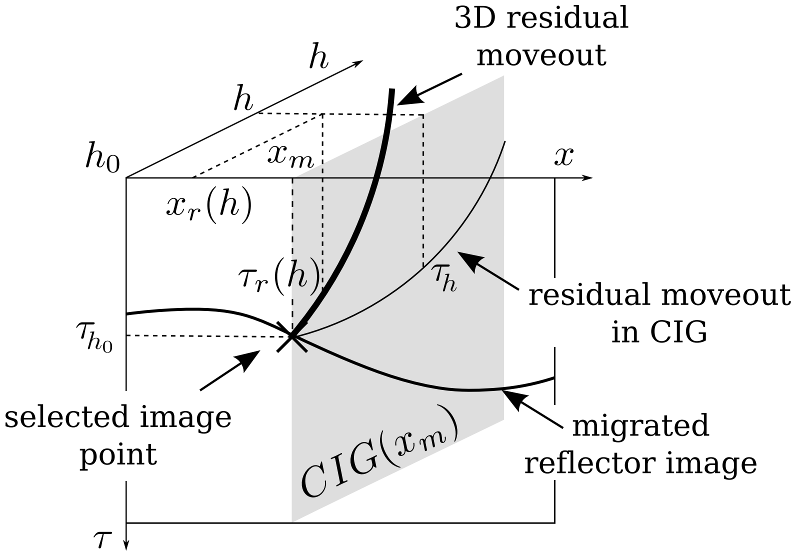

Figure 3.2: The residual moveout of a dipping reflector in a single CIG at $x_m$ after migration with a wrong velocity is described by curve $\tau_h$ (fine line). However, the image of a unique reflection point moves out of the CIG through the whole migrated data volume along a 3D moveout curve $\tau_r(h)$ (bold solid line). This curve can be approximated from information found at point $(h_0, x_m, \tau_{h_0})$. For details, see text.

et al., 2008). These methods have been named residual (or cascaded) migration, remigration, or velocity continuation. Their purpose is to construct a seismic image for a refined velocity model, starting at a previous image that was obtained by migration with a different velocity model (Hubral et al., 1996a; Tygel et al., 1996).

### 3.3.1 Remigration trajectory

Residual-moveout (RMO) analysis is generally carried out in a single common-image gather (CIG) (Liu and Bleistein, 1995). However, in the case of dipping reflectors, the image of a single reflection point is displaced laterally, i.e., out of the CIG (see Figure 3.2).

We are looking for an expression for the remigration trajectory, that is, a formula that describes the position of a reflection point in the prestack-migrated data volume as a function of migration velocity, keeping the half-offset fixed, but considering the reflection-point displacement in the midpoint direction. Repositioning the event along remigration trajectories brings it back into the CIG under consideration in order to flatten it (see Figure 3.3).

As mentioned above, if the migration velocity is incorrect, the images for different offsets of a single point on a dipping reflector will be positioned in different CIGs (Figure 3.2). For the mathematical derivation of the remigration trajectory, we need a quantification of this observation. Based on the kinematic analysis of velocity

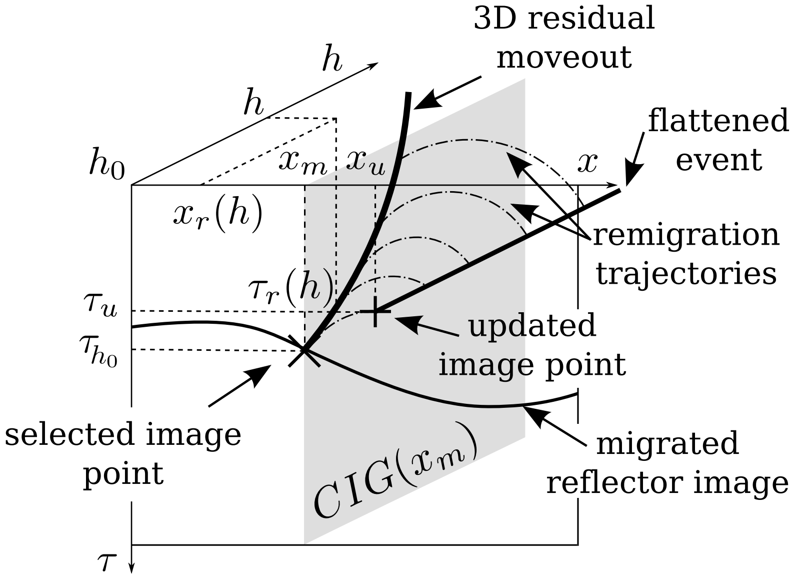

Figure 3.3: Remigration trajectories (dash-dotted lines) for selected points on the 3D moveout curve (bold solid line) of an incorrectly migrated reflector point $(x_m, \tau_{h_0})$. Also shown is the flattened position of the event at $(x_u, \tau_u)$.

continuation, Fomel (2003b) approximated the positioning of the displaced image point up to second order in half-offset $h$ as

$$\tau_r(h,x) = \sqrt{\tau_h^2 - \frac{4(x-x_m)^2}{v_m^2 - v^2} + 4h^2\left(\frac{1}{v_m^2} - \frac{1}{v^2}\right)}\,, \tag{3.1}$$

where $v$ is the true average medium velocity (i.e., the "ideal" time-migration velocity that would correctly position the image) and $v_m$ is the (incorrect) migration velocity. Moreover, $\tau_h$ is the time coordinate at half-offset $h$ of the image point within the CIG at image position $x_m$, and $x - x_m$ denotes the relative lateral coordinate, i.e., the distance to the original CIG at $x_m$ (see again Figure 3.2).

The envelope of these curves at all $x$ determines the lateral displacement $x_r$ as a function of $h$. This envelope can be determined by setting the derivative with respect to $x$ equal to zero, i.e.,

$$\left.\frac{\partial \tau_r(h,x)}{\partial x}\right|_{x_r} = 0\ . \tag{3.2}$$

We find

$$x_r(h) = x_m + \frac{1}{4}\left(v_m^2 - v^2\right)\tau_h D_h\,, \tag{3.3}$$

where $D_h$ denotes the event dip in the off-CIG or common-offset direction at lateral coordinate $x_m$ and half-offset $h$. In other words, $D_h$ is given at any $h$ by

$$D_h = \left.\frac{\partial \tau_h}{\partial x}\right|_{x_m} . \tag{3.4}$$

For $h = 0$, equations (3.1) and (3.3) reduce to the zero-offset equations derived by Schleicher et al. (1997).

Combining equations (3.1) and (3.3), we arrive at the residual-moveout expression as a function of the event dip,

$$\tau_r(h) = \sqrt{\tau_h^2 \left(1 + \frac{v_m^2 - v^2}{4} D_h^2\right) + 4h^2 \left(\frac{1}{v_m^2} - \frac{1}{v^2}\right)} . \tag{3.5}$$

Expressions (3.3) and (3.5) together approximately describe the residual moveout of the image of a reflection point in the migrated data volume for a given migration velocity $v_m$ at a given half-offset $h$ (see again Figure 3.3), if the position $\tau_h$ at that offset is known. For not too large offsets, the approximation is valid to the same extend as time migration, i.e., as long as the medium is acceptably described by a locally constant average velocity (which may vary from CIG to CIG). The derivation of more general expressions can be conceived of by using improved approximations for the out-of-CIG displacement (equation 3.1).

However, for the use in velocity analysis, equations (3.3) and (3.5) together are still insufficient, since they do not allow to predict the continuation from an image point at some half-offset $h_0$ to the corresponding point at another half-offset $h$ without additional information. For this purpose, we need a relationship between the image-time coordinates $\tau_{h_0}$ and $\tau_h$.

To find such a relationship, we start at considering a CMP section for a single reflector below an isotropic constant-velocity overburden with (true) average medium velocity $v$. At a given reflection point, the conventional NMO traveltimes for two different half-offsets $h_0$ and $h$ read

$$t_{h_0}^2 = t_0^2 + \frac{4h_0^2}{v_n^2} , \tag{3.6}$$

$$t_h^2 = t_0^2 + \frac{4h^2}{v_n^2} , \tag{3.7}$$

where $t_{h_0}$ and $t_h$ are the source-receiver traveltimes, $t_0$ is the vertical time at zero offset, which is independent of the half-offset $h$, and $v_n$ is the NMO velocity, found by means of a coherence analysis during the processing in a tentative to flatten the events present in the CMP section.

Taking the difference between equations (3.6) and (3.7), we find a direct relation between $t_{h_0}$ and $t_h$ that is independent of $t_0$,

$$t_h^2 = t_{h_0}^2 + \frac{4}{v_n^2}(h^2 - h_0^2)\,. \tag{3.8}$$

Now, consider time migration using an (incorrect) migration velocity $v_m$. The traveltime for a source-receiver pair with a half-offset $h$ is defined by the usual double-square-root (DSR) equation,

$$t_h = \sqrt{\frac{\tau_h^2}{4} + \frac{(x_m - \xi + h)^2}{v_m^2}} + \sqrt{\frac{\tau_h^2}{4} + \frac{(x_m - \xi - h)^2}{v_m^2}}\,, \tag{3.9}$$

where $\xi$ is the midpoint between source and receiver and, as before, $x_m$ and $\tau_h$ are the coordinates of the image point in the time-migrated CIG (Figure 3.2).

To simplify this expression, we use the fact that for small $h$, the square roots in equation (3.9) can be approximated as

$$\sqrt{\frac{\tau_h^2}{4} + \frac{(x_m - \xi \pm h)^2}{v_m^2}} \approx \sqrt{\frac{\tau_h^2}{4} + \frac{(x_m - \xi)^2 + h^2}{v_m^2}} \pm \frac{h(x_m - \xi)}{v_m^2\sqrt{\frac{\tau_h^2}{4} + \frac{(x_m-\xi)^2+h^2}{v_m^2}}}\,. \tag{3.10}$$

With this approximation, equation (3.9) can be written for two different half-offsets $h$ and $h_0$ as

$$t_{h_0} = \sqrt{\tau_{h_0}^2 + 4\frac{(x_m - \xi)^2 + h_0^2}{v_m^2}}\,, \tag{3.11}$$

$$t_h = \sqrt{\tau_h^2 + 4\frac{(x_m - \xi)^2 + h^2}{v_m^2}}\,. \tag{3.12}$$

Substituting equations (3.11) and (3.12) in equation (3.8) yields the relationship between migrated times $\tau_{h_0}$ at $h_0$ and $\tau_h$ at $h$ as

$$\tau_h = \sqrt{\tau_{h_0}^2 + 4\,(h^2 - h_0^2)\left(\frac{1}{v_n^2} - \frac{1}{v_m^2}\right)}\,. \tag{3.13}$$

Another way to reach this relation is to solve the classical expression of Al-Yahya (1989) describing the position of the image of a horizontal reflector in a time-migrated image, viz.,

$$\tau_h = \sqrt{\tau_0^2 + 4h^2\left(\frac{1}{v^2} - \frac{1}{v_m^2}\right)}\,, \tag{3.14}$$

for $\tau_0$ at two half-offsets $h$ and $h_0$ and equal the results. The advantage of our derivation is that it demonstrates that equation (3.13) remains valid for a dipping reflector up to first order in $h$.

It is important to notice that equation (3.13) is used exclusively to estimate the event position $\tau_h$ within the CIG at $x_m$. The provisional NMO velocity $v_n$ is not needed for any other purpose than fitting the event. Therefore, any expression that reasonably approximates the event can be used instead of equation (3.13), even without any physical justification.

Equation (3.13) allows us to estimate the vertical time $\tau_h$ at $h$ as a function of $\tau_{h_0}$ at $h_0$ without the need for any information of the zero-offset section. However, we still need the values of the event dip $D_h$ in the migrated volume in the midpoint direction (see equation 3.4) at all offsets $h$. To avoid the necessary dip estimations in all involved common-offset migrated sections, we use that the event dip $D_h$ at $h$ is approximately related to the one at $h_0$ as

$$D_h = D_{h_0}\frac{\tau_{h_0}}{\tau_h}\,. \tag{3.15}$$

This relationship is obtained from the derivative of equation (3.13) with respect to $x$ under the assumption that the variation of $v_n$ can be neglected. It can also be inferred from equation (3.3) upon noticing that at a fixed $h$ the dislocation $x_r(h) - x_m$ out of the CIG must be the same independently of the initial point of the moveout curve. Note that in agreement with the physics involved, $D_h \to 0$ when $\tau_h \to \infty$.

The set of expressions (3.3), (3.5), (3.13), and (3.15) describes the so-called remigration trajectory, i.e., the variation of the position of each point on the 3D residual moveout in the 3D migrated data volume as a function of the migration velocity $v_m$ (see Figure 3.3). With this trajectory, we can estimate whereto in the data volume a point $(h_0, \tau_{h_0})$ in a CIG will move when the migration velocity is changed. When applying this equation to all points in a CIG at a chosen image point, we can estimate the velocity value for which the resulting set of moved points becomes closest to a horizontal line.

To calculate the image-point positions with this set of equations, we need an estimate of all image times $\tau_h$ in the initial CIG and all event dips $D_h$ in the direction perpendicular to the CIG. For the estimation of $\tau_h$, we fit a curve of the form of equation (3.13) to the migrated event within the CIG at $x_m$. The local slopes

$D_h$ in all migrated common-offset sections are calculated from the dip $D_{h_0}$ in the initial migrated common-offset section according to equation (3.15). To estimate this local slope $D_{h_0}$, we use a generalization of local slant stacks. Upon the use of equation (3.15), we define a surface $T = T(h,x)$ as

$$T(h,x) = \tau_h + (x - x_m)D_h = \tau_h + (x - x_m)\frac{\tau_{h_0}}{\tau_h}D_{h_0}\,. \tag{3.16}$$

This surface is composed of all tangent lines to the event surface in the migrated data volume, if the correct value of $D_{h_0}$ is used. This fact can be used to estimate this parameter from the data by semblance maximization using trial surfaces of the form of equation (3.16). Since the estimate employs a surface rather than a line stack, it provides more reliable results.

### 3.3.2 Velocity analysis

With the remigration trajectory established, we can now devise a migration-velocity-analysis algorithm based on the local-slope estimation and approximate image-wave propagation of the CIG. For the purpose of velocity analysis, the residual moveout of the remigration trajectory must be minimized, since at the correct velocity, the event in the CIG must be horizontal. Therefore, we can choose the derivative of $\tau_r(h)$ as the objective function. Thus, the optimization condition is

$$\min_v \left\| \frac{\partial \tau_r}{\partial h} \right\| \approx \min_v \sum_i \left| \tau_r(h_i) - \tau_r(h_{i-1}) \right| \,. \tag{3.17}$$

In this paper, we minimize this derivative analytically using an exhaustive search. For this purpose, we use the time position $\tau_{h_0}$, slope parameter $D_{h_0}$, and NMO velocity $v_n$ extracted from the data to calculate the remigration trajectory according to equation (3.5) with the help of equation (3.13). Doing so for a reasonable set of migration velocities allows us to look for the velocity value that produces the lowest variation of $\tau_r$ as a function of $h$. This procedure turned out to be equally successful but much faster than trying to flatten event in the data by means of an optimization process using Newton's method.

The minimum value of the variation of $\tau_r$ as a function of $h$ defines the desired updated time-migration velocity $v_u$ associated with the image point at $(x_m, \tau_{h_0})$. For velocity building, $v_u$ is attributed to its updated position $(x_u, \tau_u)$, determined equations (3.3) and (3.5) upon the use of $v_u$ instead of $v$ (see again Figure 3.3).

### 3.3.3 Model building algorithm

To construct the final velocity model, we propose to use the above corrections in an iterative process. The information contained in a CIG at a selected migrated reflection point allows to construct the approximate time-remigration trajectory, which then provides an update for the velocity value and the spacial and time coordinates of that point. The algorithm for this procedure consists of the following steps:

1. Time migrate the data with a given initial velocity model $v_m = v_m(x, \tau)$. In our numerical tests, a constant-velocity migration was sufficient to start the process.

2. Select an image point $(x_m, \tau_{h_0})$ in the shortest-offset migrated section or stacked migrated image. Normally, it is useful to choose points on already visible reflector images. In our numerical examples, we chose the points by visual inspection. Automatic picking might be an option, but weak reflector amplitudes, usually discarded by automatic picking procedures, often indicate the need for velocity improvements.

3. Perform a coherence analysis in the CIG at $(x_m, \tau_{h_0})$ using equation (3.13) for a consistent range of NMO velocities $v_n$. The maximum coherence value defines a (temporary) NMO velocity $v_n$ that best describes the event at all half-offsets $h$.

4. Compute $\tau_h$ for all $h$ using equation (3.13) with the so-determined $v_n$ and the current migration velocity $v_m$.

5. Estimate the off-CIG dip $D_{h_0}$ by means of a coherence analysis along the surface defined by equation (3.16).

6. Compute $D_h$ for all $h$ using equation (3.15).

7. Calculate a set of remigration trajectories using equations (3.3) and (3.5) for a range of velocities $v$. In our numerical tests, this range had to be finer sampled than the above one for $v_n$.

8. Determine the updated migration velocity $v_u$ for $(x_m, \tau_{h_0})$ that minimizes the variation of $\tau_r$ in the offset direction, according to equation (3.17).

9. Calculate the corrected position $(x_u, \tau_u)$ of the selected image point.

10. Loop over steps (2) to (8) until a sufficient number of image points are processed.
11. Interpolate the set of new velocity values.
12. Smooth the resulting model, if necessary. In some of our numerical tests, a moving average filter turned out to be useful to improve the correlation between adjacent image points.
13. Time migrate the original data with the new velocity model.
14. Loop over steps (2) to (13) until the events in all CIGs are satisfactorily flattened.

A flowchart of this algorithm is depicted in Figure 3.4.

Let us emphasize again that velocity $v_n$ (equation (3.13); step (3)) is a provisional velocity estimate that is used only to determine the values of $\tau_h$ in the current CIG at point $(x_m, \tau_{h_0})$. In turn, these values of $\tau_h$ are used to flatten the event along the remigration trajectory (equation (3.3) and (3.5); step (7)) by minimization of the residual moveout (equation (3.17); step (8)), which then determines the updated migration velocity $v$.

By its principle, the proposed MVA algorithm is a *local* procedure, updating the velocity at a single image point at a time. If sufficient image points are available in a certain region, a smooth model can be interpolated for that region. In the interpolation stage, a-priori information or constraints can be taken into account. In our numerical tests on synthetic data, reported below, the method was able to build time-migration velocity models without an initial model, starting with a constant-velocity migration, as long as the model complexity lies within the validity range of time migration.

## 3.4 Numerical examples

We have applied our time remigration technique to one constant-velocity model with a curved reflector, three constant-gradient velocity models with sets of dipping reflectors, and the more complex Sigsbee2B data set.

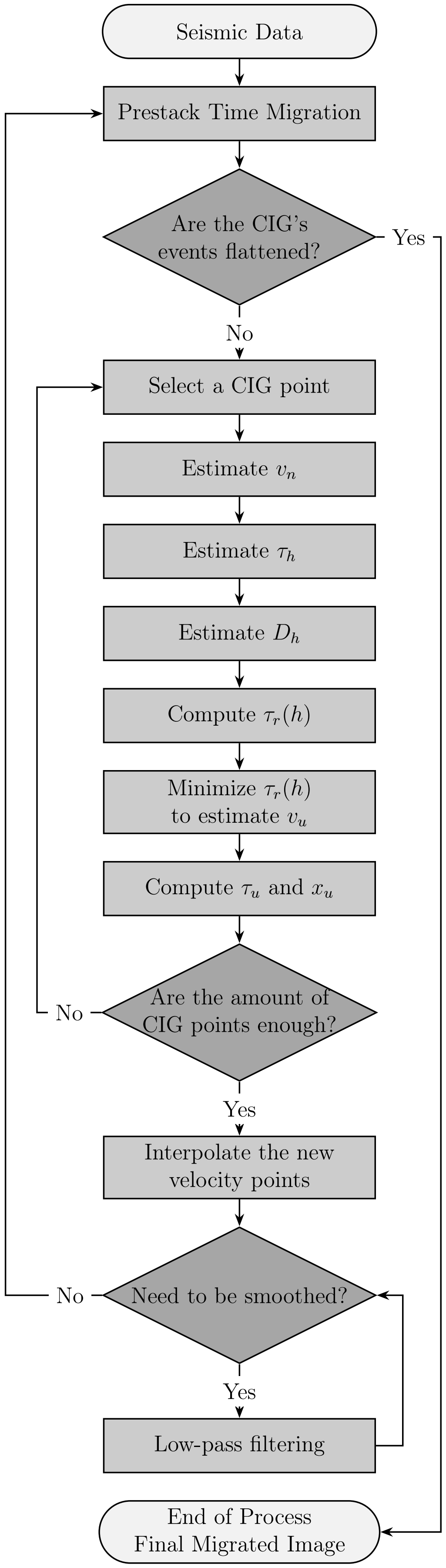

Figure 3.4: Remigration trajectory process flowchart.

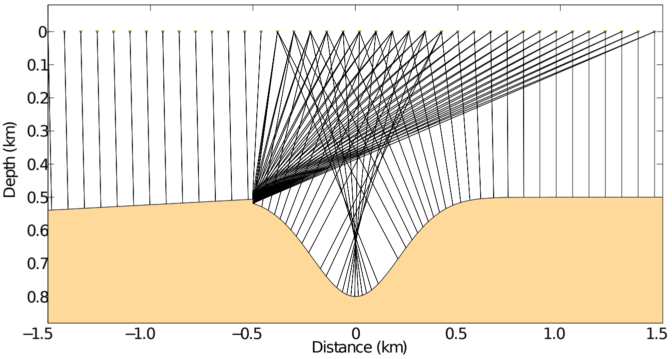

Figure 3.5: 2D sketch of a simple synthetic model and ray family. The model consist of two homogeneous halfspaces, separated by a reflector consisting of a straight segment with small dip in the left portion, an edge diffractor caused by an abrupt change of dip, followed by a syncline and a horizontal reflector segment on the right-hand side.

### 3.4.1 Application to a synthetic data set from a simple constant-velocity model

As a first test, we applied the MVA technique using time-remigration trajectories as outlined above on a synthetic data set from a simple constant-velocity model (Figure 3.5). It consists of a single trough-shaped reflector separating two homogeneous half-spaces with velocities 1.7 km/s and 1.9 km/s. Note that the reflector has a slight dip on the left side of the trough and is horizontal on the right side. Moreover, there is an edge diffractor caused by an abrupt change of direction on the left shoulder of the syncline, indicated by the set of diffraction rays plotted in Figure 3.5.

We used Kirchhoff modeling to generate synthetic seismic data for 25 half-offsets between $h = 100$ m and $h = 580$ m. Each common-offset section consists of 151 data traces (see Figure 3.6 for a near-offset section) at every 20 m with a sampling rate of 4 ms. We then contaminated those data with white random noise at a level of 10% of the maximum amplitude. The trough-shaped reflector causes a caustic, evidenced by the distorted bow-tie structure in the data (Figure 3.6). The diffraction event has much smaller amplitude than the reflection event.

Supposing the true velocity of the upper layer to be unknown, we time-migrated these data with a constant initial velocity $v_0 = 1.5$ km/s (water velocity). In our tests, the range of possible values of the initial velocity was fairly large and not vital to the method. Figure 3.7 shows the time-migrated version of the near-offset section of Figure 3.6. It is easy to recognize in this migrated image that the employed migration velocity is not correct, because the bow-tie structure from the synclinal

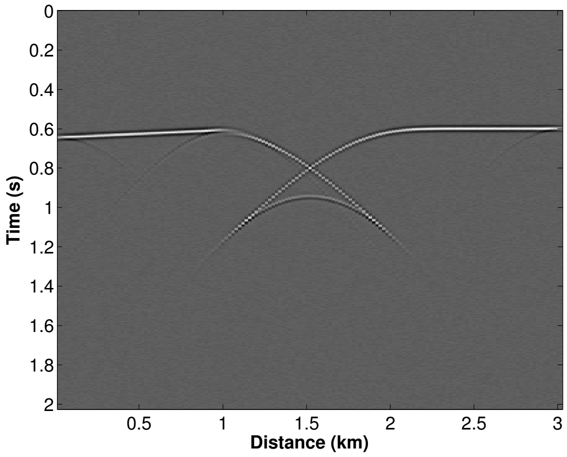

Figure 3.6: Noisy seismic near-offset section of the synthetic model presented in Figure 3.5. It was generated by Kirchhoff modeling with 151 traces at every 20 meters and a sampling rate of 4 ms and contaminated with white random noise at a level of 10% of the maximum amplitude.

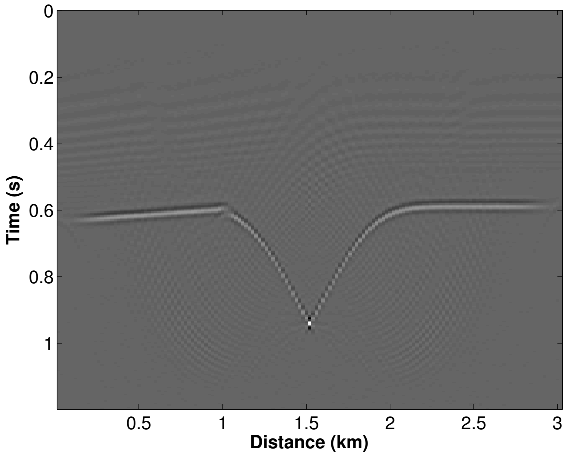

Figure 3.7: Time-migrated image of the seismic near-offset section of Figure 3.6 using a constant velocity $v_0 = 1.5$ km/s (water velocity) and a migration aperture of 101 traces.

reflector is not completely resolved. Also note that the edge diffractor is incorrectly imaged, with a spatial separation between the two reflector segments.

In this migrated section, we select specific points on the images of reflection events. As mentioned earlier, automatic picking might be an option, but weak reflector amplitudes, usually discarded by automatic picking procedures, may indicate the need for velocity improvements. Such points are more easily selected by an interpreter. Fortunately, the method is not very sensitive to the picks' location and density (Santos et al., 2014b). Because time migration requires a smooth velocity model, usually the number of required picks to define the velocity in a certain region of the model is not too large. For example, a region reasonably well described by a

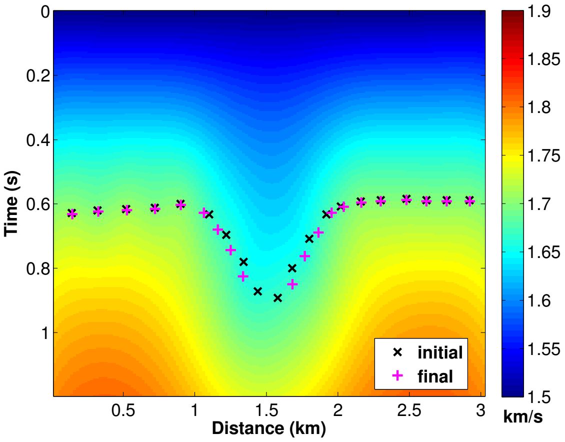

Figure 3.8: Updated velocity model using image point correction from constant velocity migration (one iteration). The 20 black crosses represent the initial picked points in the migrated image (Figure 3.7), and the pink plusses indicate the corrected coordinates for the new velocity. The overall model was obtained by B-spline interpolation, fixing the velocity at the top of the model at a constant 1.5 km/s.

constant velocity gradient can be represented by three picks. For these reasons, we restricted ourselves to manual event picking.

The coordinates of each of these selected points define the present values of $\tau_{h_0}$ and $x_m$. At $x_m$, we automatically determine the off-CIG event slope $D_{h_0}$ at $h_0$ as indicated in the context of equation (3.16). This slope value allows to apply an improved moveout correction to the migrated data at $x_m$ according to equation (3.5). Moveout minimization according to equation (3.17) yields an improved velocity value $v_u$ and a corrected position $(x_u, \tau_u)$ for the chosen point in the image.

From this information, we construct an updated velocity model by attributing the so-obtained improved velocity values to these corrected positions, and then applying a B-splines interpolation to determine the velocity values at a regular grid. Figure 3.8 shows the so-obtained velocity model after a single iteration of the described MVA procedure. The black crosses represent the 20 points initially picked in the migrated image of Figure 3.7, and the pink plusses indicate their corrected coordinates in the improved velocity model. Note that the determined velocity in the region of the picks closely approximates the true velocity of 1.7 km/s, with a maximum error of about 2%. Values outside the region of the picks are artifacts of the interpolation and carry no meaning.

Figure 3.9 compares the stack of all common-offset migrated images using the model of Figure 3.8 to the corresponding stack using the true velocity model. We see that MVA by time-remigration trajectories nicely positioned all parts of the

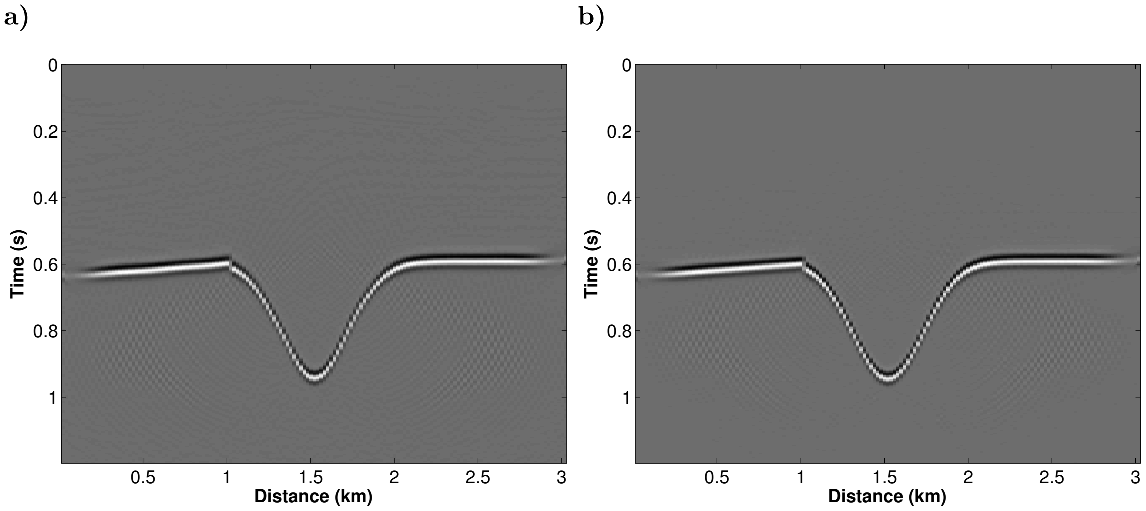

Figure 3.9: Final migrated image stack after time migration with a migration aperture of 101 traces using (a) the extracted velocity model using one iteration of image point correction; (b) the true velocity model.

reflector very closely to their true positions, confirming the good estimates for the time-migration velocities in the reflector region.

### 3.4.2 Application to constant-gradient models

For a more meaningful test, we applied the method to three constant-gradient models that can be thought of as representing subregions of a larger model. To verify the feasibility of our method, which was derived under the assumption of constant average velocities, in more realistic situations, we chose rather strong velocity gradients in the vertical, horizontal, and diagonal directions. The true interval velocity models are given by

$$v(z) = 2000 + 0.5z \text{ m/s} , \tag{3.18}$$

$$v(x) = 2000 + 0.5x \text{ m/s} , \tag{3.19}$$

$$v(x,z) = 2000 + 0.5x + 0.5z \text{ m/s} , \tag{3.20}$$

respectively.

All three models contain six interfaces with, from top to bottom, initial depths at the origin of 400 m, 500 m, 600 m, 700 m, 800 m, and 900 m, and dips of 0°, 4.8°, 10°, 15°, 23.6°, 39.5°, respectively. Moreover, they contain seven diffraction points in different parts of the models. The diffraction events were not used for velocity analysis. Their only purpose is the quality control of the extracted velocity models.

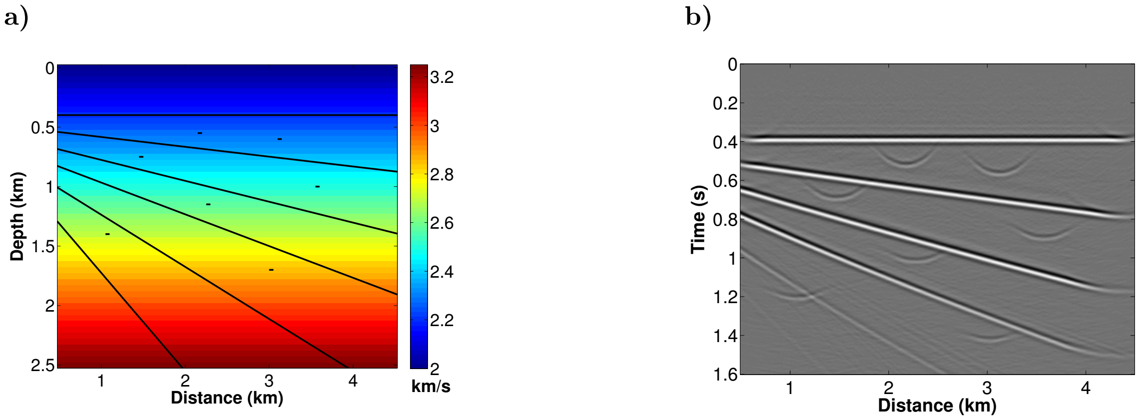

Figure 3.10: Vertical-gradient model: (a) Velocity model with reflectors and control diffractors. (b) Time-migrated image using $v_0 = 3.0$ km/s.

We generated the corresponding synthetic data sets using a Kirchhoff-modeling algorithm of Seismic Unix (Cohen and Stockwell, 2014). We simulated 25 common-offset sections for offsets between 200 m and 680 m spaced at 20 m, with a sampling rate of 2 ms up to a maximum time of 2.5 s, each with 400 source-receivers pairs spaced at 10 m between CMP coordinates 500 m and 4500 m, thus covering an extension of 4000 m. We used a symmetric Ricker wavelet with 20 Hz peak frequency, and contaminated the data with pseudorandom Gaussian noise with zero mean and at level of 5% of the maximum amplitude.

We then applied the present remigration-trajectory MVA method to these data. The first step was a constant-velocity time migration. For these examples, we used an intermediate velocity of $v_0 = 3.0$ km/s.

Figure 3.10 to Figure 3.12 summarize the results for the vertical-gradient model. Figure 3.10a depicts the true velocity model with reflectors and control diffractors, and Figure 3.10b shows the time-migrated zero-offset section using a constant migration velocity of 3000 m/s.

From this initial migration, we started the remigration-trajectory velocity analysis. To investigate the quality of the result as a function of the number of points picked, we performed the analysis twice, once with 21 image points and once with 100 image points. Figure 3.11a shows the 21 image points picked in the first run (black crosses) together with their updated positions (pink plusses) superimposed over the obtained updated velocity model after one iteration. This model results from a B-splines interpolation (Matlab implementation, see Sandwell, 1987) of the updated velocities at the 21 updated image-point locations. Figure 3.11b shows the corresponding time-migrated stacked section. In the velocity model, we recognize some undulations, indicating that the velocity estimate is better at the chosen image

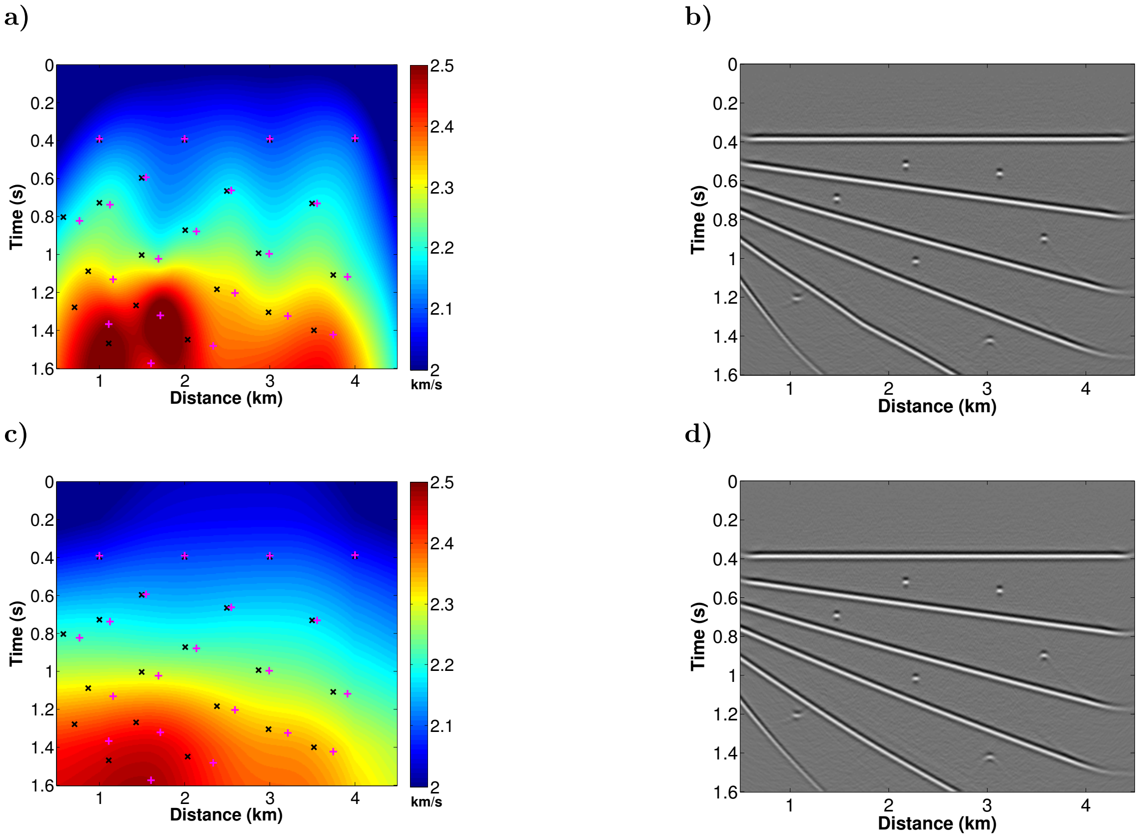

Figure 3.11: Vertical-gradient model: (a) Extracted velocity model after one iteration with 21 image points and (b) corresponding final time-migrated image. (c) Extracted velocity model after moving-average smoothing and (d) corresponding final time-migrated image. Also shown in parts (a) and (c) are the picked image points (black crosses) and their updated positions (pink plusses).

points than in their vicinity. Nonetheless, the control diffractors in the image are reasonably focused and the reflectors only slightly curved. This indicates that the model in Figure 3.11a already is an acceptable time-migration velocity model. For further improvement, we applied two passes of moving-average smoothing with a 1 km × 0.4 s (100 by 100 points) window. The idea is to carry the velocity information at the chosen image points over to their vicinities where no updated velocity values are available. Figure 3.11c and d show the so-obtained model and the corresponding image. While the model has improved and resembles the true model of Figure 3.10a more closely, the time-migrated image of Figure 3.11d is almost identical to that of Figure 3.11b.

Figure 3.12a shows the 100 image points picked in the second test (black crosses), also together with their updated positions (pink plusses) and superimposed over the obtained updated velocity model after one iteration. Again, Figure 3.12b shows the corresponding time-migrated stacked section. In comparison to Figure 3.11a,

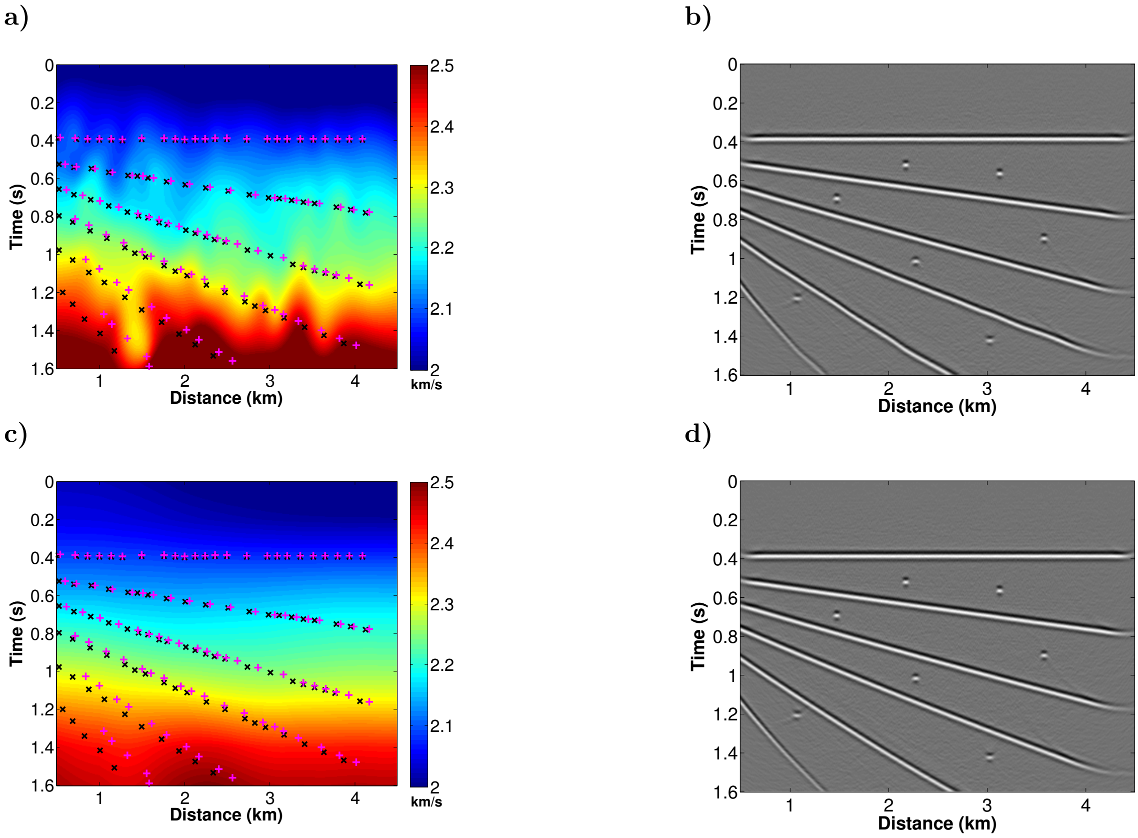

Figure 3.12: Vertical-gradient model: (a) Extracted velocity model after one iteration with 100 image points and (b) corresponding final time-migrated image. (c) Extracted velocity model after moving-average smoothing and (d) corresponding final time-migrated image. Also shown in parts (a) and (c) are the picked image points (black crosses) and their updated positions (pink plusses).

we observe that the velocity undulations in Figure 3.12a are reduced in amplitude and wavelength. The migrated image in Figure 3.12b has slightly improved as compared to Figure 3.11b, particularly regarding the positioning of the deepest reflector and the focusing of the deepest diffractor. Moving-average smoothing further improves the model (Figure 3.12c), but again has little effect on the resulting image (Figure 3.12d).

Similar conclusions can be drawn from the corresponding experiments with the horizontal (Figures 3.13, 3.14, and 3.15) and diagonal (Figures 3.16, 3.17, and 3.18) gradients. While the models extracted with 100 image points (Figures 3.15a and 3.18a) are slightly better than the ones extracted with 21 image points (Figures 3.14a and 3.17a), it is doubtful that the improvements warrant fivefold picking expense. The smoothed models using 21 points (Figures 3.14c and 3.17c) almost reach the same quality as the ones obtained with 100 points (Figures 3.15c and 3.18c).

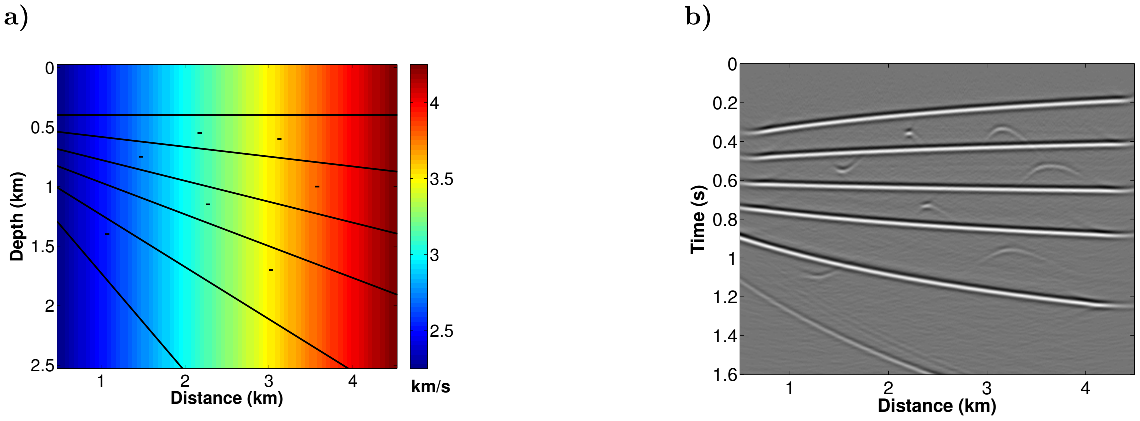

Figure 3.13: Vertical-gradient model: (a) Velocity model with reflectors and control diffractors. (b) Time-migrated image using $v_0 = 3.0$ km/s.

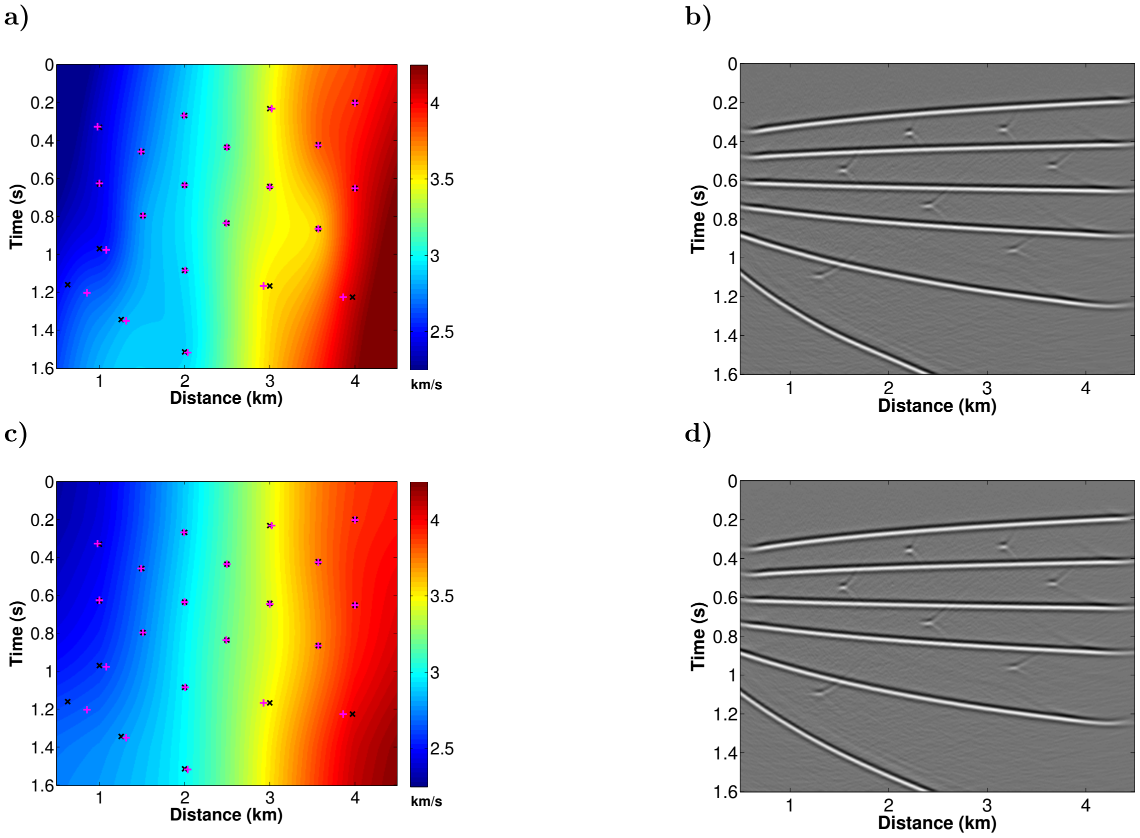

Figure 3.14: Horizontal-gradient model: (a) Extracted velocity model after one iteration with 21 image points and (b) corresponding final time-migrated image. (c) Extracted velocity model after moving-average smoothing and (d) corresponding final time-migrated image. Also shown in parts (a) and (c) are the picked image points (black crosses) and their updated positions (pink plusses).

These tests demonstrate that even in the presence of a strong velocity gradient, the method is capable of extracting meaningful time-migration velocity models using

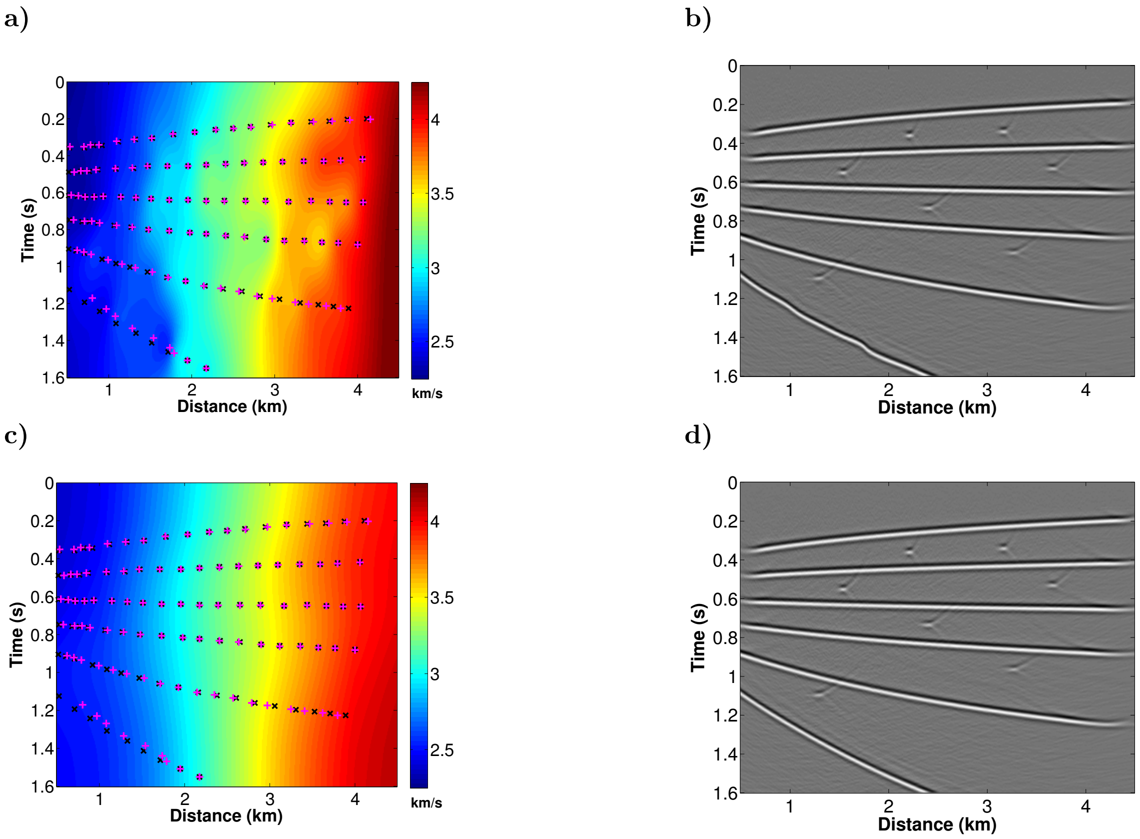

Figure 3.15: Horizontal-gradient model: (a) Extracted velocity model after one iteration with 100 image points and (b) corresponding final time-migrated image. (c) Extracted velocity model after moving-average smoothing and (d) corresponding final time-migrated image. Also shown in parts (a) and (c) are the picked image points (black crosses) and their updated positions (pink plusses).

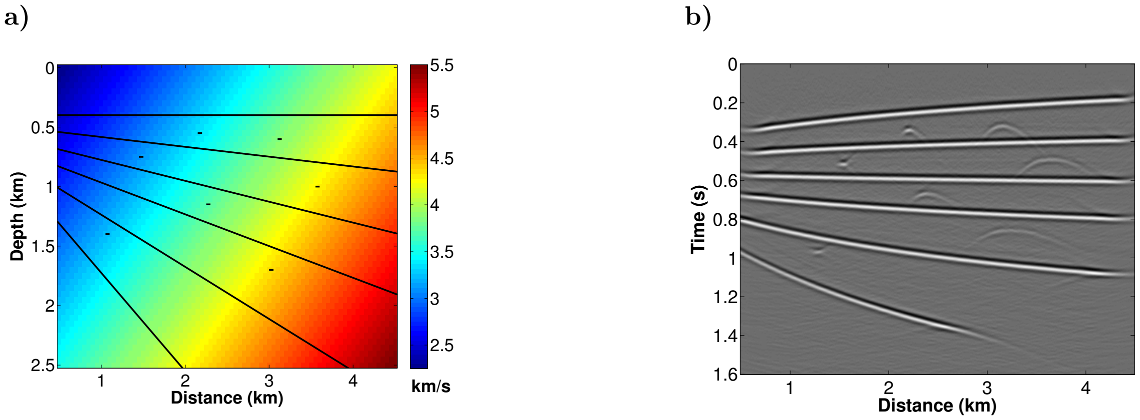

Figure 3.16: Diagonal-gradient model: (a) Velocity model with reflectors and control diffractors. (b) Time-migrated image using $v_0 = 3.0$ km/s.

a not too large number of image points where reflector images can be picked in the incorrectly migrated image.

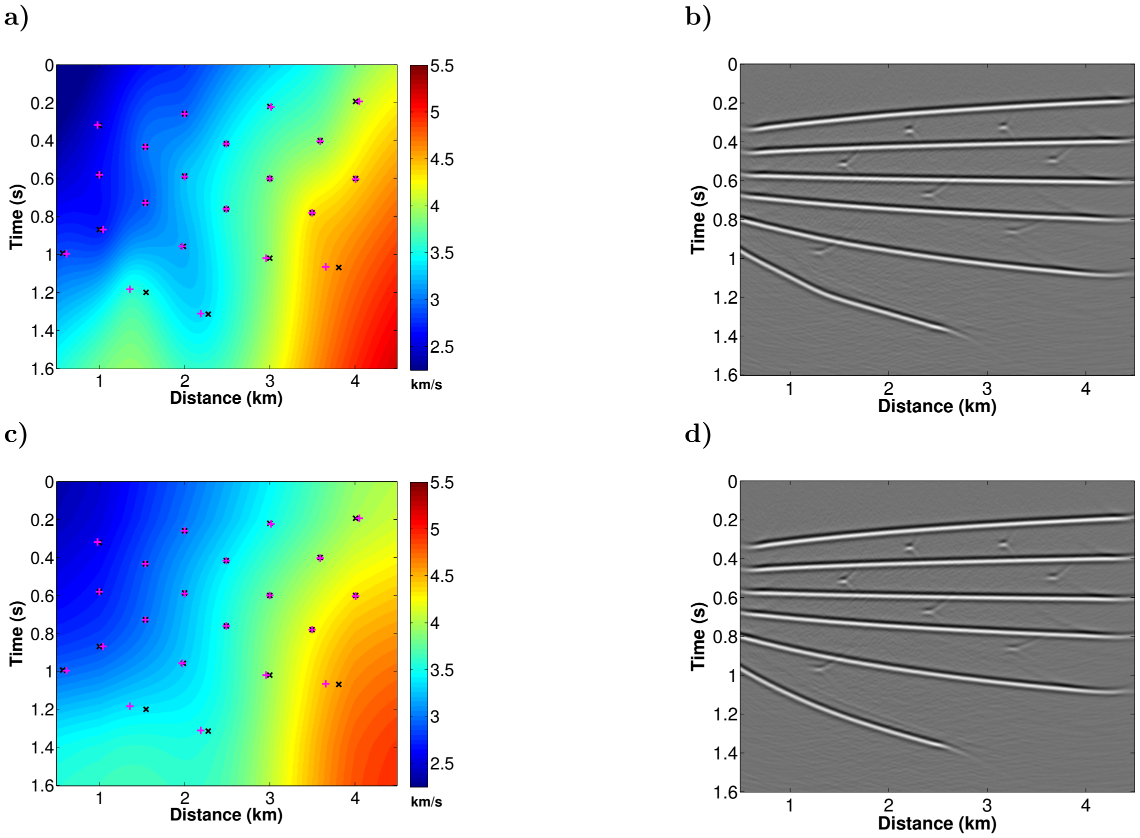

Figure 3.17: Diagonal-gradient model: (a) Extracted velocity model after one iteration with 21 image points and (b) corresponding final time-migrated image. (c) Extracted velocity model after moving-average smoothing and (d) corresponding final time-migrated image. Also shown in parts (a) and (c) are the picked image points (black crosses) and their updated positions (pink plusses).

### 3.4.3 Application to the Marmousoft data

Encouraged by these results, we set out for a more realistic test. We applied the described MVA technique to the Marmousoft data (Billette et al., 2003). These data were constructed by Born modeling in a smoothed version of the Marmousi model. The true (depth) Marmousoft velocity model is depicted in Figure 3.19a. We chose this model so as to analyze the behaviour of our MVA method in a complex sedimentary geology. We did not expect the method to work in the central part of the model because of the limits of time migration.

In order to simulate a time-migration velocity model we computed the root-mean-square ($v_{rms}$) velocity model in pseudo-time from the stratigraphic velocity using vertical conversion only. The resulting time-velocity model is depicted in Figure 3.19b. It indicates acceptable migration velocity values, though probably laterally mispositioned.

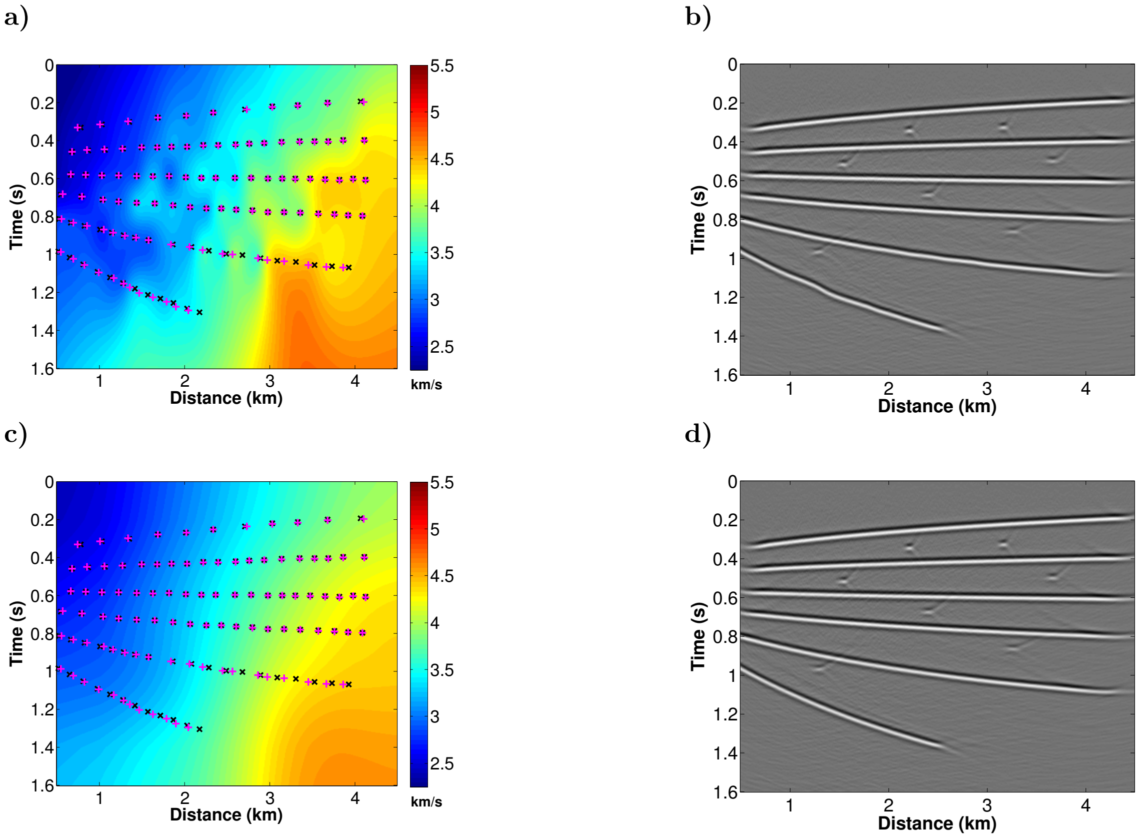

Figure 3.18: Diagonal-gradient model: (a) Extracted velocity model after one iteration with 100 image points and (b) corresponding final time-migrated image. (c) Extracted velocity model after moving-average smoothing and (d) corresponding final time-migrated image. Also shown in parts (a) and (c) are the picked image points (black crosses) and their updated positions (pink plusses).

The Marmousoft data contain traces at every 25 meters with a sampling rate of 4 ms. We used 96 common-offset sections with source-receiver offsets between 100 m and 2475 m. Figure 3.20a shows a short-offset section with a total source-receiver offset of 100 m.

To these data, we applied the remigration-trajectory MVA method. For the first migration, we chose $v_0 = 2.0$ km/s. Figure 3.20b depicts the migrated image obtained from the short-offset data of Figure 3.20a. The migration aperture used was 241 traces.

Next, we picked 70 points on some of the most prominent migrated events in the image of Figure 3.20b. At the positions of these picks, we extracted local slopes in the migrated common-offset section and then minimized the residual moveouts along the remigration trajectories as described above. Figure 3.20c shows the locations of our picks (black crosses) and their corrected positions after velocity updating

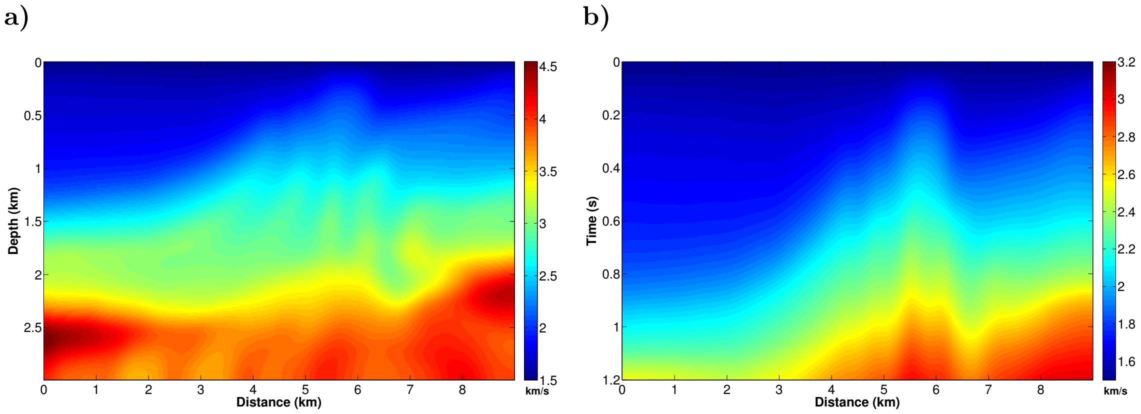

Figure 3.19: Marmousoft velocity models. (a) Depth velocity model (Billette et al., 2003). (b) Time-velocity model computed from (a) by vertical depth-to-time conversion.

(pink plusses) overlain on the resulting updated velocity model. As before, we used B-splines to interpolate the velocity model in the complete region.

We then used the velocity model of Figure 3.20c for a second migration. The result is depicted in Figure 3.20d. We recognize that the updated velocity model leads to an improved migrated image, particularly regarding the upper parts of the fault lines and the reflectors in the sedimentary regions on both sides of the model.

To eliminate the unrealistic oscillations in the velocity model, we smoothed it (Figure 3.20c) by two passes of a moving average with a 2.5 km×0.4 s (100 by 100 points) window (see Figure 3.20e). The Kirchhoff-migrated image corresponding to this velocity model is depicted in Figure 3.20f.

Although the velocity models of Figures 3.20c and 3.20e are rather different, the corresponding migrated images (Figures 3.20d and 3.20f) are quite similar, indicating that both velocity models are equivalent regarding the final time-migration result. These results are in agreement with those produced by common-image gather image-wave propagation and double multi-stack migration (see Santos et al., 2013f and Santos et al., 2013g for a parameterization discussion). For further evaluation of the model quality, a time-to-depth conversion will be necessary to compare the attainable model quality as well as to check its application as an initial model for tomographic or depth MVA methods.

### 3.4.4 Application to the Sigsbee2B data

Encouraged by these results, we set out for a more realistic test. We applied the described MVA technique to a subset of the Sigsbee2B NFS (no free surface) data set. We chose this model so as to analyze the behavior of our MVA method in the

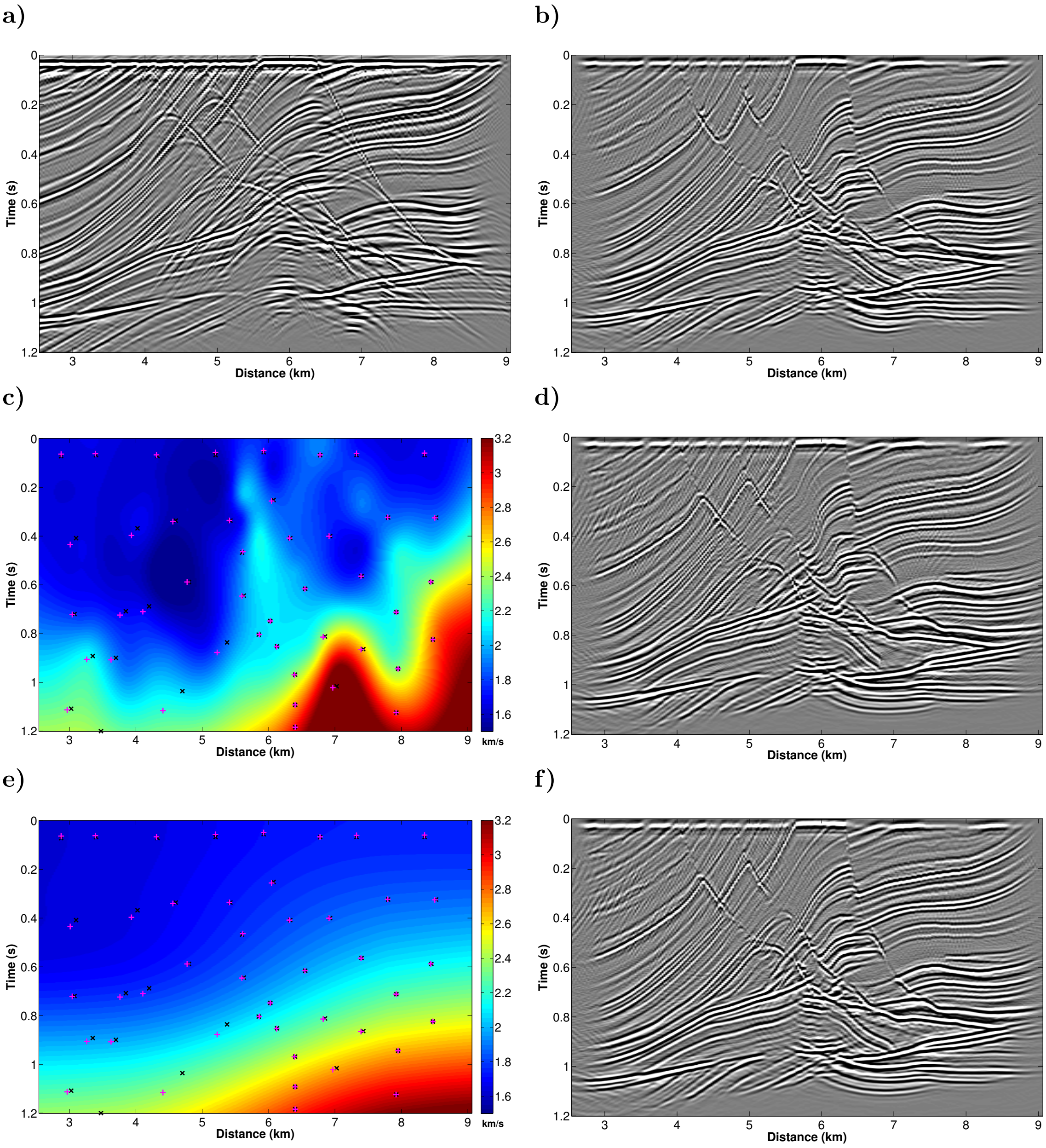

Figure 3.20: Single iteration of remigration-trajectory MVA on the Marmousoft data. (a) Seismic near-offset section. (b) Time-migrated image of the seismic near-offset section using a constant velocity $v_0 = 2$ km/s and migration aperture equal to 141 traces. (c) Extracted velocity model after one iteration. Also shown are the 70 picked image points (black crosses) and their updated positions (pink plusses). (d) Final time-migrated image by a migration aperture equal to 241 traces. (e) and (f) show the results after moving-average smoothing by two passes with a 2.5 km×0.4 s (100 by 100 points) window.

sedimentary region to the right of the salt body, in the more complex structures like the syncline segments above the salt body, and in the salt body itself. We did

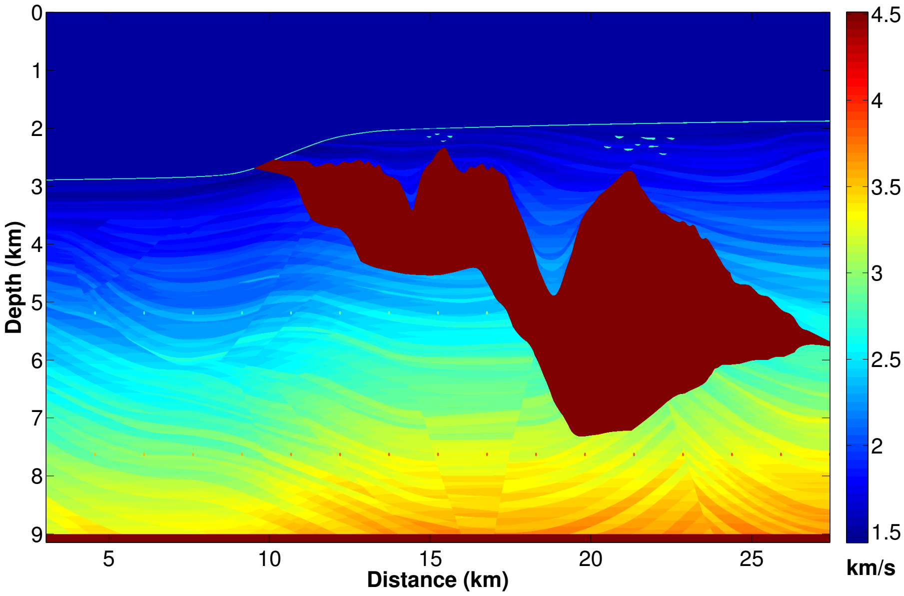

Figure 3.21: Complete Sigsbee2B stratigraphic velocity model.

not expect the method to work below the salt body because of the limits of time migration.

The Sigsbee2B data contains traces at every 45.7 meters with a sampling rate of 8 ms. We used 100 common-offset sections with source-receiver offsets between 183 m and 4709 m. Figures 3.21 and 3.22 show the Sigsbee2B stratigraphic velocity model and a short-offset section with a source-receiver offset of 183 m, respectively. This was the nearest offset used in our numerical test. Shorter offsets are present in the distribution of the Sigsbee2B data, but were discarded.

### Reference images

In order to simulate a time-migration velocity model and its respective migrated image, we computed the interval ($v_{int}$) and the root-mean-square ($v_{rms}$) velocity models in pseudo-time from the stratigraphic velocity, both using vertical conversion only. The pseudo-time interval velocity model (Figure 3.23) gives us an approximate idea of where to look for reflector images in the migrated image.

The RMS velocity $v_{rms}$ (Figure 3.24) is an average velocity that indicates acceptable migration velocity values, though probably laterally mispositioned. Therefore, rather than using the RMS velocity model of Figure 3.24 for comparisons to the models to be obtained with our method, we use $v_{rms}$ to migrate the Sigsbee2B data set. Figure 3.25 shows the time-migrated image of the seismic near-offset section using the average velocity $v_{rms}$ and migration aperture equal to 241 traces. This

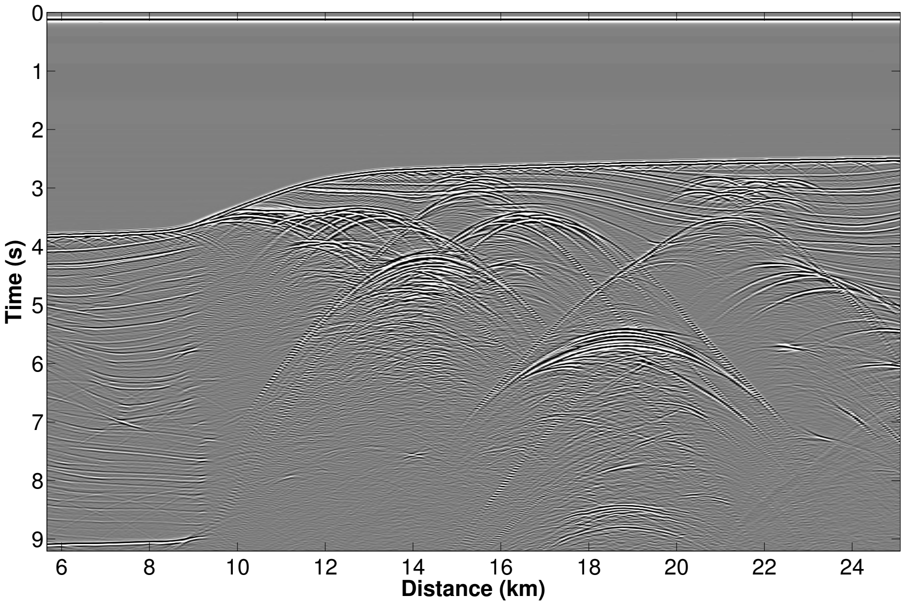

Figure 3.22: Seismic near-offset section ($2h = 183$ m) of the complete Sigsbee2B data.

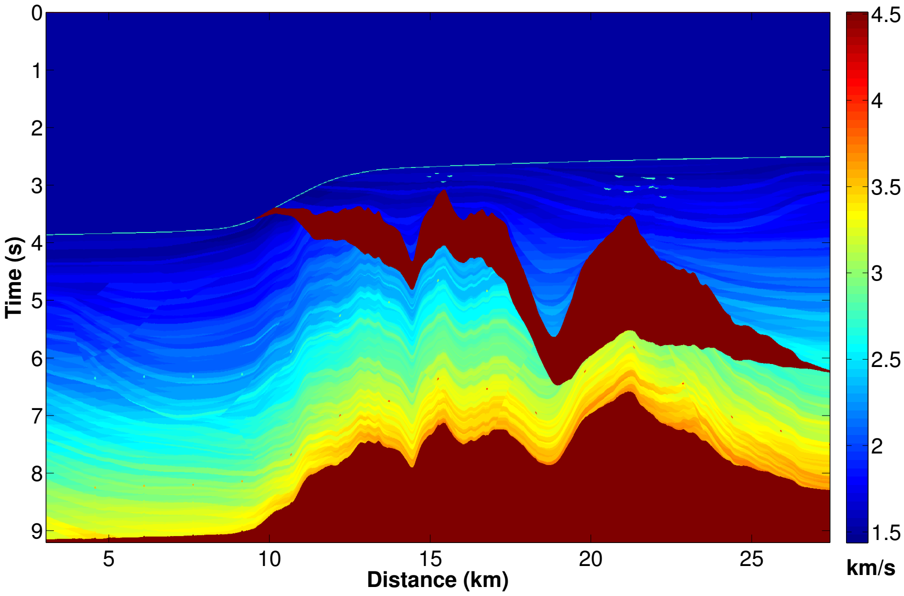

Figure 3.23: Sigsbee2B vertical pseudo-time interval velocity model ($v_{int}$).

figure will play the role of a benchmark for the migrated images using the velocity models obtained from our method.

By correlating the time-migrated image of Figure 3.25 with the pseudo-time interval velocity model of Figure 3.23, we can easily identify the positions of most reflectors. We note that the shallow events and most sedimentary parts are well focused, including the shallow diffraction events. However, the salt bottom and deepest parts are out of focus, indicating that the model of Figure 3.24 is only

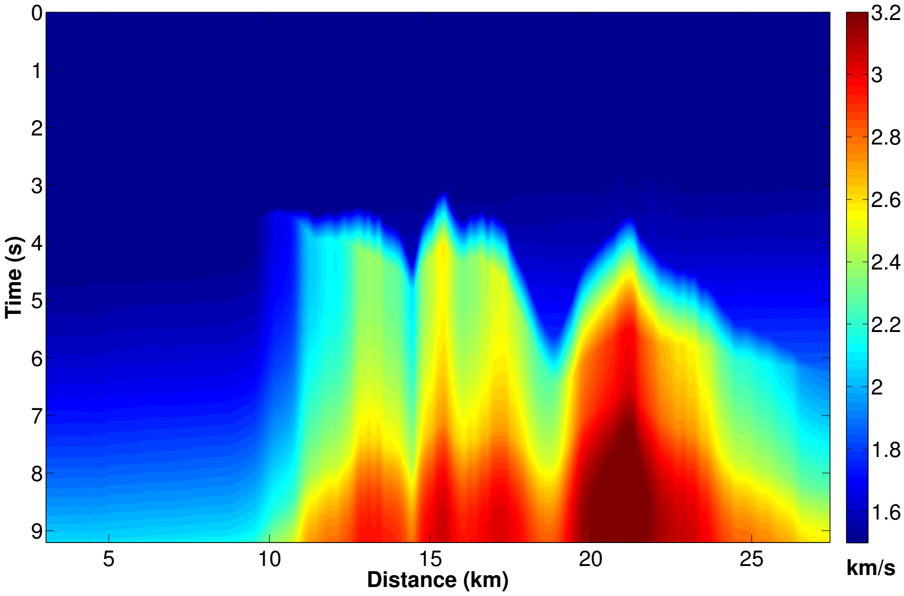

Figure 3.24: Sigsbee2B vertical pseudo-time root-mean-square velocity model ($v_{rms}$).

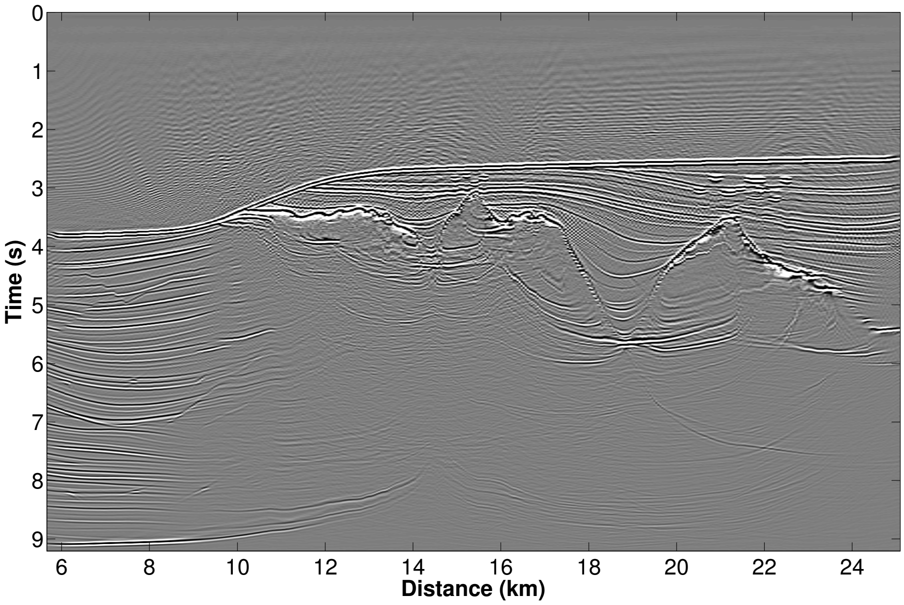

Figure 3.25: Time-migrated image of the seismic near-offset section using the average velocity $v_{rms}$ (Figure 3.24) and migration aperture equal to 241 traces.

acceptable down to a certain depth. This can be understood as an indication for the validity limit of time migration in this model.

### Velocity analysis

Since the Sigsbee2B data simulate a marine data set, we know the velocity of the first layer to be constant water velocity $v_0 = 1.5$ km/s. Thus, we choose this velocity

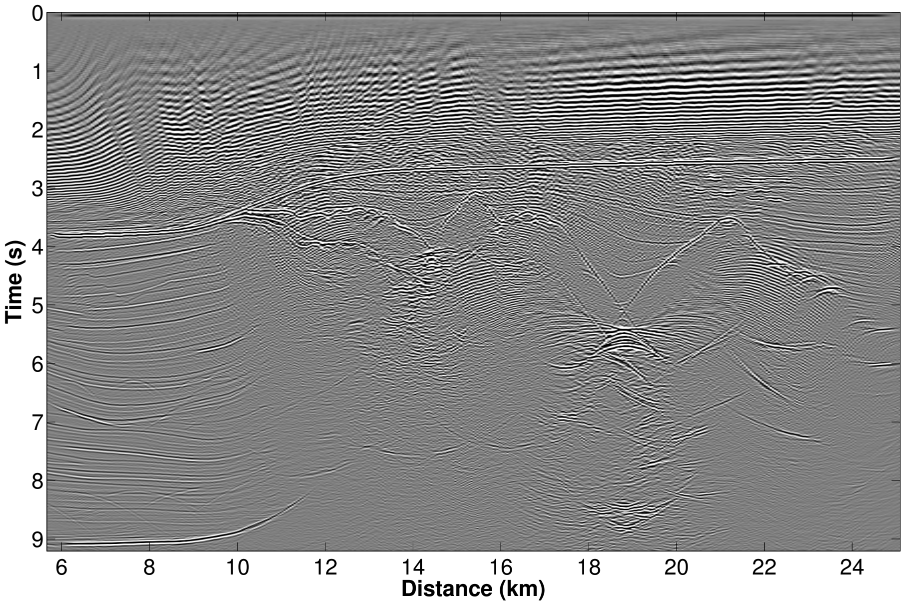

Figure 3.26: Time-migrated image of the seismic near-offset section using a constant velocity $v_0 = 1.5$ km/s (water velocity) and migration aperture equal to 141 traces.

for the first migration. Figure 3.26 depicts the migrated image obtained from the short-offset data of Figure 3.22. The migration aperture used was 141 traces. As expected, this first migration is not able to resolve the structures below the water bottom or focus the reflection energy.

Next, in order to apply our remigration-trajectory MVA as discussed above, we picked 254 points on some of the most prominent migrated events in the image of Figure 3.26. At the positions of these picks, we extract local slopes in the migrated common-offset section and then minimize the residual moveouts along the remigration trajectories. Figure 3.27 shows the locations of our picks (black crosses) and their corrected positions after velocity updating (pink plusses) overlain on the resulting updated velocity model. As before, we used B-splines to interpolate the velocity model in the complete region. It is easy to see that the picked image points are moved the furthest away from their original positions in the (large) syncline region between 16 and 22 km. In this part of the model, the difference between the initial and true migration velocities is larger than in the upper part of the model.

We then used the velocity model of Figure 3.27 for a second migration. The result is depicted in Figure 3.28. We immediately recognize that the shallower parts of the salt top have been nicely improved in this image, indicating that the velocity model in this region has reached already acceptable quality. Certainly, the same cannot be said of the salt flanks. Therefore, we repeated the procedure of reflector

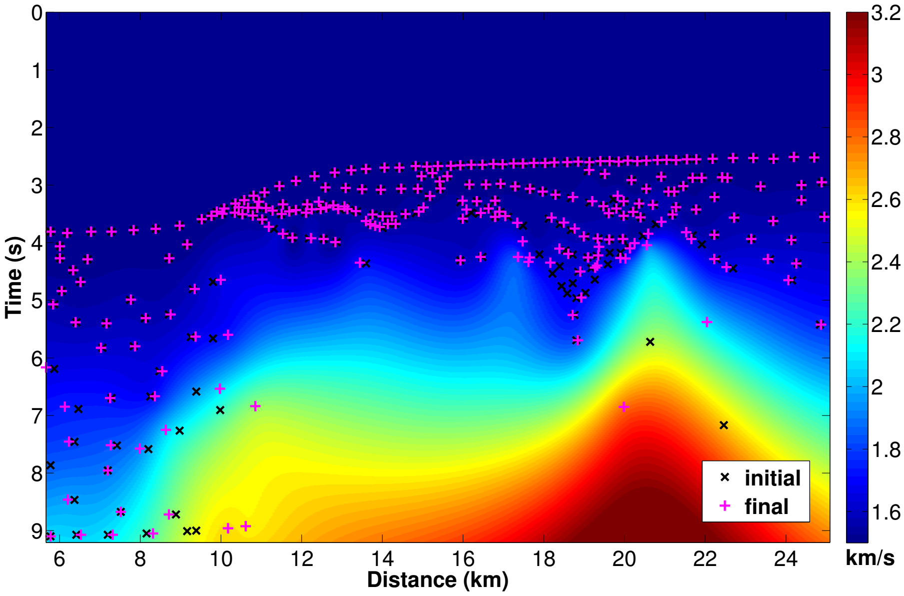

Figure 3.27: Velocity model extracted using image-point correction with remigration trajectories after constant-velocity migration (first iteration). The 254 black crosses represent the initial picked points in the migrated image of Figure 3.26, and the pink plusses indicate their corrected coordinates for the updated velocity. The overall model was obtained by B-spline interpolation.

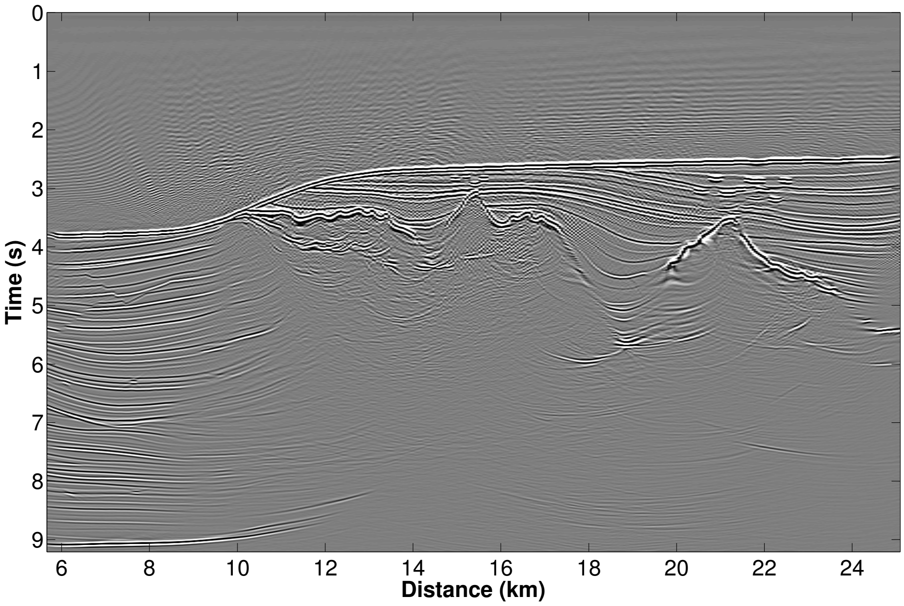

Figure 3.28: Migrated image after velocity extraction using one iteration of image point correction. The migration aperture used was 141 traces.

picking and velocity updating for a second set of points picked in this new migrated image.

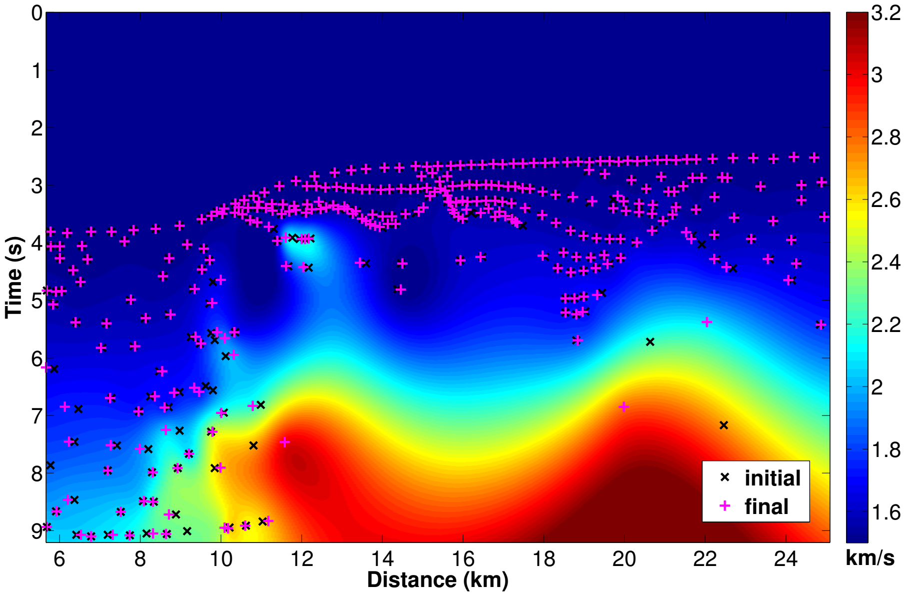

Figure 3.29: Velocity model after second iteration. The 322 black crosses represent the picked points in the migrated image of Figure 3.28, and the pink plusses indicate their corrected coordinates.

Figure 3.29 shows the velocity model after this second iteration together with the 322 picked points (black crosses) used in this iteration and their updated positions (pink plusses). We note that the displacements are smaller than in Figure 3.27, indicating convergence of the method. Note that the deeper events in the central part of the model are still not focused in the image and could therefore not be picked. The velocity model in this region is thus just obtained from B-splines extrapolation and must not be trusted.

The migrated image corresponding to this velocity model is depicted in Figure 3.30. For this migration, we used a migration aperture of 241 traces. In comparison to Figure 3.28, the flanks of the (large) synclinal structure are much better focused and the bottom of the trough is correctly positioned. Furthermore, we have also achieved an improvement in the left portion of the salt base. Actually, the image of Figure 3.30 is already visibly better than the one of Figure 3.25, obtained with the vertically converted RMS velocities. Not only is the top-salt reflector better focused, but also some of the events in the sedimentary parts show better continuity. This indicates that the velocities in the model of Figure 3.29 are already better time-migration velocities than those of Figure 3.24. In the central region of the model, the quality remains poor. No reflectors come into focus that could be picked to allow for another iteration. This is a strong indication that the strong velocity contrast at the salt border delimits the validity region of the method.

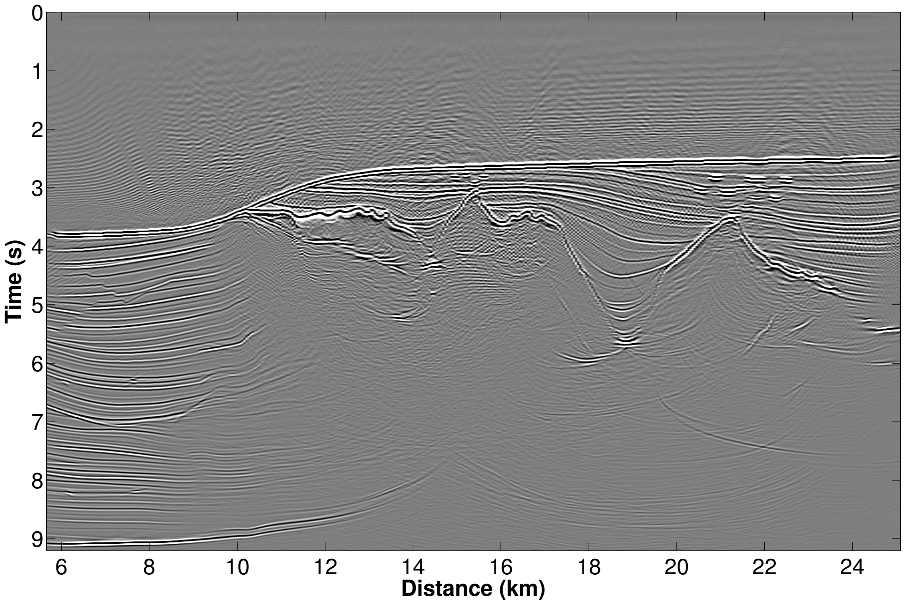

Figure 3.30: Final migrated image stack after two iterations of velocity extraction using remigration trajectories. The migration aperture was 241 traces.

To evaluate the quality of the final velocity model in more detail, let us look at six selected CIGs (Figure 3.31). On the whole, it is easy to observe that the strongest events, mainly the shallow ones, were completely flattened. The first CIG at 7.65 km (Figure 3.31a) lies in the most simple region where there are no abrupt velocity variation. In this CIG, all major events were flattened, including the diffraction event below 6 seconds, and the deepest flat salt layer at about 9 seconds (see also Figure 3.30). In the CIG at 13.68 km (Figure 3.31b), we can observe that the salt top ($\sim$3.6 s) and the diffraction event ($\sim$5.2 s) were well flattened, but the salt bottom ($\sim$4.2 seconds) still needs improvement at larger offsets. The third CIG at 16.56 km (Figure 3.31c) allow to analyze the edge diffraction at the salt bottom at about 4.2 seconds (see also the model in Figure 3.21). It shows that our method flattened this diffraction event, too. The fourth CIG at 18.85 km (Figure 3.31d) represents the central part of the Sigsbee2B syncline. Here, we call attention to the high amplitudes below 5 seconds due to multiple reflections in this syncline. Nevertheless, it is possible to observe the nearly flattened event of the bottom of the trough at about 5.6 seconds. The fifth CIG at 20.54 km (Figure 3.31e) shows the right portion of the syncline, where the salt structure is thicker and where shallow diffractors are present. We note that down to the salt top, all events are nicely flattened. The last CIG at 22.32 km (Figure 3.31f) enables us to evaluate the right portion of the salt structure, with a thinning of the salt body and a greater dip

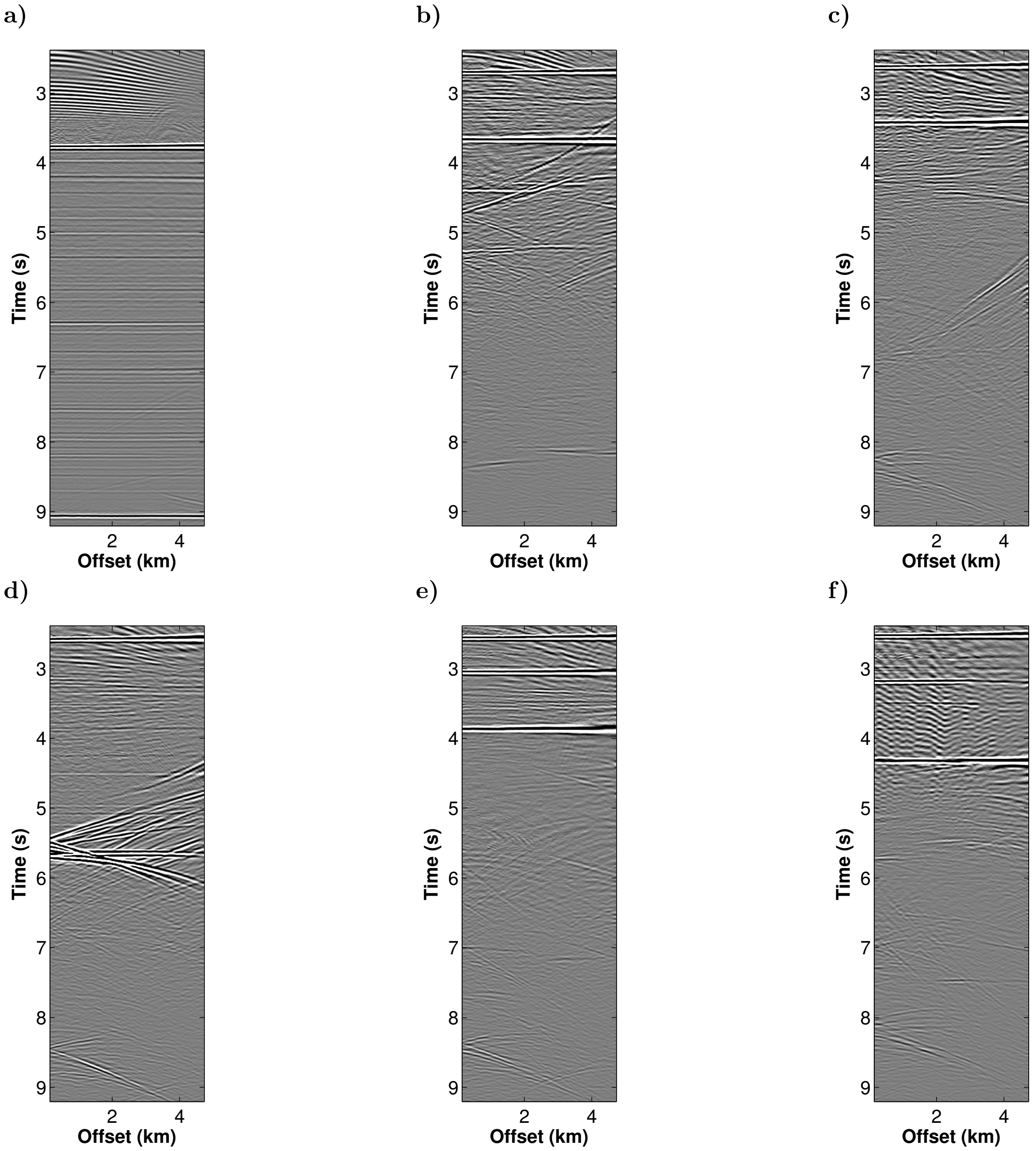

Figure 3.31: Common-image gathers at (a) 7.65 km, (b) 13.68 km, (c) 16.56 km, (d) 18.84 km, (e) 20.54 km, and (f) 22.32 km.

variation of its top. As expected, the deeper events below the salt are not well imaged with the present velocity model.

### Reliability

As a direct indicator of the reliability at different reflectors of the updated velocity model, we can study the coherence panel associated with the CIGs of the migrated image. Figure 3.32 shows the horizontal semblance in the corresponding

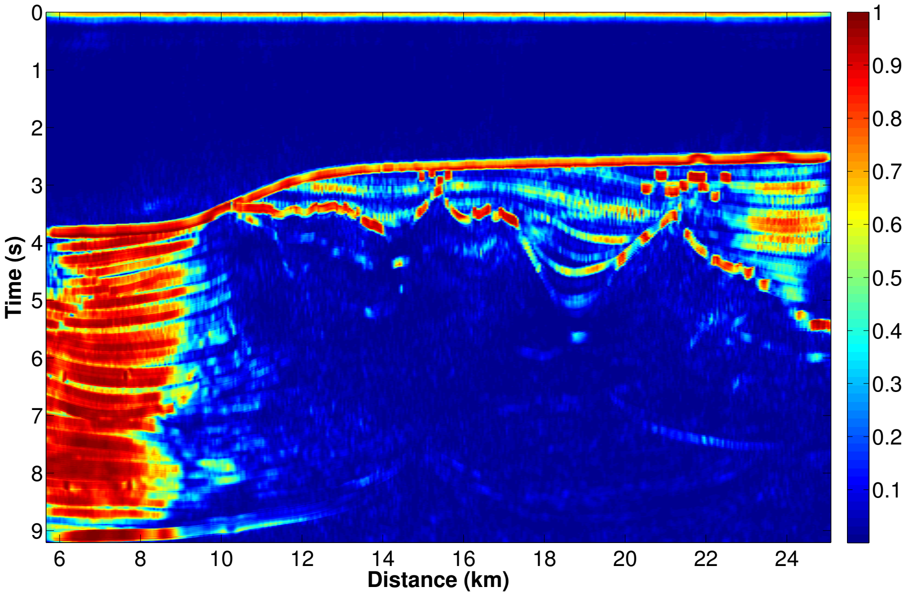

Figure 3.32: Coherence panel after the second iteration.

CIG at each point of the migrated image of Figure 3.30. High coherence values in this panel provide an indication of where the obtained velocity model can already be trusted, while low values indicate regions where further improvement is required. We see in Figure 3.32 that all main events down to the salt top are reliably imaged, and even the edge diffractor at the salt bottom is clearly visible. The residual moveout of the bottom-of-the-trough reflection in the CIG of Figure 3.31d results in its poor visibility in the coherence panel.

From the analysis of the final migrated image (Figure 3.30), the CIGs (Figure 3.31), and the coherence panel (Figure 3.32), we conclude that MVA using time-remigration trajectories constitutes a powerful tool to improve the positioning of key reflectors in a time-migrated image and update the velocity model correspondingly, at least in sedimentary regions. The focused edge diffraction event at the salt bottom gives rise to hopes that the method may even work in more complex areas. The computational cost of the technique is determined by the cost of prestack time migration in each iteration. Intermediate computations are negligible. Further investigations will have to show whether the picking of selected reflection event points can be carried out in an automated way.

When testing our method, we noted that the resulting velocity models were strongly dependent on the method chosen to interpolate the velocity between the positions of the picks. However, the resulting images were rather similar to each other, providing yet another confirmation for the robustness of time migration with respect to velocity errors. For the presentation in this work, we chose the models obtained by B-splines interpolation of Matlab (Sandwell, 1987).

## 3.5 Conclusions

We have developed a tool that uses the estimation of local kinematic attributes of selected events in seismic data to locally update a previous velocity model and improve the positioning of key reflectors. The method is based on image-wave propagation in the CIG domain described by the means of time-remigration trajectories in the prestack time-migrated domain. Such a trajectory is defined as the set of points at which a certain point on a reflection event is migrated to as a function of migration velocity.

The methods consist of analyzing the local slope of selected key reflections and determining the velocity value for which an approximate RMO expression is minimized. The advantage of this procedure over conventional MVA methods is that the RMO expression follows the events outside a fixed CIG. In this way, more accurate velocity information can be extracted from the data.

We have demonstrated by means of our numerical examples that the method is capable of extracting local time-migration velocity information from the data to improve a given velocity model. By relying on constant-velocity initial models, we have demonstrated that the quality of the initial model is not critical to our technique. In our numerical tests, the procedure led to acceptable velocity models in very few iterations, even if the starting model was constant water velocity. The sedimentary shallow part of the Marmousoft model was satisfactorily resolved in one iteration. The computational cost of the technique is determined by the cost of prestack time migration in each iteration. Intermediate computations are negligible. The most processing time was spent on the event picking. However, tests with different numbers of picked event points demonstrated that the number of points does not need to be very large. Future research will have to show if this picking process can be automatized. Our results indicated that a step of smoothing the data can be helpful, especially for deeper and/or steeper events.

By its principle, the proposed MVA algorithm is a *local* procedure, updating the velocity at a single image point at a time. If sufficient image points are available in a certain model region, a smooth velocity distribution can be interpolated for that region. In the interpolation stage, a priori information or constraints can be taken into account. In our numerical tests on synthetic data, we applied the method to simple models consisting of a single region and to multiple regions of the Sigsbee model to study its behavior under different conditions. The simple models could be inverted in a single iteration. In the sedimentary regions of the Sigsbee model, two iterations where sufficient to build an acceptable model. The salt body in this model marked the method's validity limit. We believe that its main application will be in the local improvement of previously existing velocity models to enhance the focusing of selected key horizons. Further research will be necessary to extend the method to depth MVA.

# Chapter 4

# Time-to-depth conversion and velocity estimation by image-wavefront propagation

## 4.1 Summary

A new strategy for time-to-depth conversion and interval-velocity estimation is based entirely on image-wavefront propagation without the need to follow individual image rays. The procedure has three main features: (1) it computes the velocity field and the traveltime directly, allowing to dispense with dynamic ray tracing; (2) it requires only the knowledge of the image-wavefront at the previous time step; and (3) it inherently smoothes the image-wavefront, inhibiting the formation of caustics. As a consequence, the method tends to be faster than usual techniques and does not carry the constraints and limitations inherent to common ray-tracing strategies. Synthetic tests using a Gaussian velocity anomaly as well as the Marmousi velocity model and two smoothed versions of it show the feasibility of the method. A field data example demonstrates the use of different numerical procedures. Our results indicate that the present strategy can be used to construct reasonable depth velocity models that can be used as reliable starting models for velocity-model building in depth migration or for tomographic methods.

## 4.2 Introduction

The need to investigate regions with complex geology has encouraged the development of imaging methods that act in the depth domain. Notable examples are prestack depth migration (PSDM) and full-waveform tomography (FWT) techniques. However, the application of these methods faces at least two problems: they require (1) an accurate (initial) velocity model and (2) massive computation power.

In contrast, time migration has proved to be a fast and robust process, making it routinely employed for seismic imaging. Moreover, time-domain velocity-model building is a well-understood process. Therefore, it is highly desirable to employ time-to-depth conversion in order to construct starting models for depth imaging techniques from these time-domain velocity models.

Therefore, vertical conversion from time to depth has been routinely employed for a long time, Hubral (1977) was the first to recognize the need for taking lateral displacements into account. He demonstrated that time and depth-domain coordinates are interconnected by the so-called image ray.

More recently, Cameron et al. (2007, 2008) derived the theoretical relation between the time-migration velocity and seismic velocity using image-ray theory and paraxial ray-tracing theory (Popov et al., 1978; Červeny, 2001; Popov, 2002). Their algorithm consists of image-ray tracing to convert time Dix velocities into ray coordinates velocities and then time-to-depth convert them based on Dijkstra-like fast marching methods (Sethian, 1999a,b). Iversen and Tygel (2008) proposed a similar but more efficient technique that even in 3D requires only a single-azimuth time-migration velocity field as an input to construct the depth velocity field.

Despite being an attractive method, time-to-depth conversion is an ill-posed problem (Cameron et al., 2007). It aggregates the limitations of all involved steps, that is, the constraints involved in time migration, ray-tracing, and Dix-based velocity conversion (Iversen and Tygel, 2008). Thus, regularization is essential for an adequate time-to-depth conversion. Such a regularization can be added in two phases of the process: (1) during the estimation of the Dix velocity field from an estimated time-migration velocity field, and (2) during the image-ray tracing. Valente et al. (2009) compared the three conversion techniques of Cameron et al. (2007), Cameron et al. (2008), and Iversen and Tygel (2008). They demonstrated that the different procedures react differently to different kinds of regularization. However, although the image-ray trajectories and the resulting depth velocity models depended on the regularization employed, the corresponding final depth images were very similar.

The objective of the present work is to present an alternative algorithm for the time-to-depth conversion, which does not require the tracing of individual image rays. Instead, it simulates the propagation of an image wavefront in the subsurface. In isotropic media, this image wavefront is perpendicular to a set of image rays. This approach has the advantage of directly computing the velocity field and the traveltime. We test the approach on a synthetic Gaussian example and on the

Marmousi data set. For the latter, we use Fourier Finite-difference (FFD) migration based on complex Padé approximations (Amazonas et al., 2007) to evaluate the quality of the depth-migrated images. Finally, we apply our method to the same field data example of the North Sea used by Cameron et al. (2008).

## 4.3 Time-to-depth conversion algorithms

We start with the formulation of the time-to-depth-conversion inverse problem based on image-ray theory and a brief description of some of the proposed newer algorithms.

### 4.3.1 Two-dimensional inverse problem

Consider an image point at coordinates $(\gamma, \tau)$ in a time-migrated section, with $\gamma_{\min} \leq \gamma \leq \gamma_{\max}$ and $0 \leq \tau \leq \tau_{\max}$. This image point can be associated with an image-ray that has reached the acquisition surface at the position $\gamma$ in time $\tau$. The problem of time-to-depth conversion consists of tracing this image-ray back into the medium, associated with a plane wave tangent to the acquisition surface at $\gamma$, until the time $\tau$ is consumed and the ray has reached its position $\mathbf{x} = (x, z)$ in the subsurface.

In other words, we want to simultaneously solve the set of equations for kinematic and dynamic ray tracing with plane-wave initial conditions. This set can be represented in two dimensions as

$$\begin{aligned} \frac{d\mathbf{x}}{d\tau} &= v^2(\mathbf{x})\mathbf{p} \ , \\ \frac{d\mathbf{p}}{d\tau} &= -\frac{1}{v(\mathbf{x})}\nabla_{\mathbf{x}} v(\mathbf{x}) \ , \\ \frac{dQ}{d\tau} &= v^2(\mathbf{x})P \ , \\ \frac{dP}{d\tau} &= -\frac{1}{v(\mathbf{x})}\frac{\partial^2 v}{\partial \eta^2}\,Q \ , \end{aligned} \tag{4.1}$$

where $\eta$ denotes the coordinate direction perpendicular to the ray. Moreover, $\mathbf{p}$ and $v(\mathbf{x})$ are the slowness vector and the wave speed at $\mathbf{x}$, and $P$ and $Q$ are quantities describing the dynamic properties along the ray. The initial conditions for image-ray tracing read

$$\begin{aligned} \mathbf{x}(\tau=0) &= (\gamma,0)\ , \\ \mathbf{p}(\tau=0) &= \frac{\hat{\mathbf{z}}}{v^{\mathrm{Dix}}}\ , \\ Q(\tau=0) &= 1\ , \\ P(\tau=0) &= 0\ , \end{aligned} \tag{4.2}$$

where $\hat{\mathbf{z}}$ is the unit vector in the vertical direction and $v^{\mathrm{Dix}}$ denotes the Dix velocity at $(\gamma,\tau)$.

### 4.3.2 Inversion algorithms

As an alternative, particularly to simplify the computation of the derivatives along the image-rays, Cameron et al. (2007) proposed an image-ray tracing algorithm which fits the image-wavefront by polynomial curves. Based on this algorithm, Valente (2013) proposed an additional regularization to the fitting, which increases the choice of the degree of the polynomial.

Based on their previous work, Cameron et al. (2008) presented a new ray tracing algorithm, in which the last two equations of system (4.1) are integrated based on the Lax-Friedrichs method (Lax, 1954). This results in the finite-difference (FD) scheme

$$\begin{aligned} P_j^{n+1} &= \frac{P_{j+1}^n + P_{j-1}^n}{2} - \frac{\Delta\tau}{4\Delta\gamma^2 \nu_j^n Q_j^n}\left(\frac{\nu_{j+2}^n Q_{j+2}^n - \nu_j^n Q_j^n}{Q_{j+1}^n} - \frac{\nu_j^n Q_j^n - \nu_{j-2}^n Q_{j-2}^n}{Q_{j-1}^n}\right)\ , \\ \frac{1}{Q_j^{n+1}} &= \frac{1}{Q_j^n} - \frac{\Delta\tau}{2}\left[(\nu_j^n)^2 P_j^n + (\nu_j^{n+1})^2 P_j^{n+1}\right]\ , \end{aligned} \tag{4.3}$$

where $P_j^n$ denotes the value of $P$ at the $j$th image-ray at $\gamma_j$ and at the $n$th time sample $\tau_n$. Moreover, $\nu_j^n$ denotes the Dix interval velocity $\nu(\gamma_j,\tau_n)$ (Dix, 1955). In this method, there is no need for additional regularization. The regularization is intrinsically performed by the $P$-averages that are computed along the wavefront of the image-wave, in this way avoiding instabilities in the FD scheme by damping high frequencies.

After the application of any of the cited inversion algorithms, the results are the image-rays and/or image-wavefronts and, above all, the velocity field $v(\mathbf{x}(\gamma,\tau))$ in depth along the image rays trajectories. Therefore, this velocity field is given on a non-regular grid. One way to transfer this field onto a regular grid is a direct fit at the regular grid points and an extrapolation in the border regions. Cameron et al. (2007) describe an efficient algorithm to solve this problem, using the eikonal equation based on the *fast-marching* method (Sethian, 1999a,b). This provides not only the depth velocity field $v(\mathbf{x})$, but also $\tau(\mathbf{x})$ and $\gamma(\mathbf{x})$ on a regular grid. The latter two fields can be used in the conversion of time-migrated images to depth-migrated images.

Cameron et al. (2007) also describe another way to approach the problem using the level-set method (Sethian, 1999b). This approach boils down to propagating the image-wavefront tangent to the acquisition surface in time $\tau = 0$ back into the subsurface. To do so, the image-wavefront is represented as a zero-level set of a two-dimensional function $\phi(\mathbf{x})$. Two two-dimensional functions $p(\mathbf{x})$ and $q(\mathbf{x})$ are also incorporated along the image-wavefront, defined in such a way that, for each time interval $\Delta\tau$, they are equivalent to the values of $P$ and $Q$, respectively. These functions satisfy the equation system

$$\begin{aligned} \frac{d\phi}{d\tau} &= v(\mathbf{x})\,\|\nabla\phi\|\ , \\ \frac{dq(\mathbf{x})}{d\tau} &= v^2(\mathbf{x})p(\mathbf{x})\,, \\ \frac{dp(\mathbf{x})}{d\tau} &= -\frac{1}{v(\mathbf{x})}\frac{\partial^2 v}{\partial\eta^2}q(\mathbf{x})\,, \end{aligned} \tag{4.4}$$

where the second derivative of $v$ in the direction perpendicular to the ray can be represented as

$$\frac{\partial^2 v}{\partial\eta^2} = \left(\frac{1}{\|\nabla\phi\|}\frac{\partial\phi}{\partial z}\right)^2\frac{\partial^2 v}{\partial x^2} - 2\left(\frac{1}{\|\nabla\phi\|}\frac{\partial\phi}{\partial x}\cdot\frac{1}{\|\nabla\phi\|}\frac{\partial\phi}{\partial z}\right)\frac{\partial^2 v}{\partial x\partial z} + \left(\frac{1}{\|\nabla\phi\|}\frac{\partial\phi}{\partial x}\right)^2\frac{\partial^2 v}{\partial z^2}\,. \tag{4.5}$$

The first equation implies that $\phi$ is monotonically increasing with $\tau$. If, as chosen here, $\phi$ is traveltime, the first subequation reduces to $d\phi/d\tau = 1$.

From equation system (4.2), we find the initial conditions for the auxiliary functions $p$ and $q$ as

$$q(\mathbf{x}(\tau = 0)) = 1\ , \qquad p(\mathbf{x}(\tau = 0)) = 0\ . \tag{4.6}$$

This scheme inherently uses the fast-marching conversion algorithm to calculate the velocity field $v(\mathbf{x})$.

### 4.3.3 Image-wavefront propagation

Based on the algorithm of the level-set method, we propose an alternative strategy to perform the time-to-depth conversion. In this new image-wavefront propagation strategy, instead of tracing individual rays for all positions $\gamma$ of interest, we start with a family of rays, associated with a plane wave at the acquisition surface at $\gamma$. This procedure has the advantage of directly obtaining the velocity field $v(\mathbf{x})$ and the traveltime $\tau(\mathbf{x})$, avoiding to calculate the auxiliary functions $p(\mathbf{x})$ and $q(\mathbf{x})$. By means of a modified fast-marching conversion algorithm, we can directly determine the set $\gamma(\mathbf{x})$ of image-ray emergence points from the already known values of $v(\mathbf{x})$ and $\tau(\mathbf{x})$. For details, see Valente (2013).

The wavefront-construction algorithm proposed in this work is slightly different from other algorithms discussed in previous works. For example, Vinje et al. (1993) construct the wavefront checking neighboring rays for significant deviation or crossing, adding new rays in the first case and removing one of the crossing rays in the second one. The new rays start at the midpoint between two known rays with ray quantities obtained by linear interpolation. Furthermore, the authors also use linear interpolation to output the involved ray quantities on a regular grid. In a different strategy, Silva et al. (2009) use a finite-difference scheme to evolve the wavefront along the image ray. This scheme makes use of the information at two points on the previous wavefront to determine the ray quantities at the new wavefront.

In this work, we proceed in yet another way. The principal advantage of our algorithm is that it immediately interpolates the ray quantities at the horizontal coordinates of the given grid, determining the vertical coordinate of the wavefront accordingly. In this way, it avoids the need to add or remove points on the wavefront. Moreover, this procedure requires the final interpolation of the output quantities in the vertical direction only. For the propagation, it needs only the knowledge of the image-wavefront at the previous time step.

At each time step, the first part of our algorithm is to determine the direction $\mathbf{n} = \nabla\phi / \left\|\nabla\phi\right\|$ of the gradient at each point $(x_j, z_j)$ along the wavefront. At the first time step, it is given by the vertical direction. At all later time steps, we first estimate an approximation to the the unit tangent vector $\hat{\mathbf{t}}$ to the wavefront,

$$\hat{\mathbf{t}} = \frac{(x_{j+1} - x_j, z_{j+1} - z_j)}{\sqrt{(x_{j+1} - x_j)^2 + (z_{j+1} - z_j)^2}} \ , \tag{4.7}$$

which is then rotated by $-90°$.

We then propagate the image-wavefront $\phi(\mathbf{x})$ along this normal direction $\mathbf{n}$, integrating the system

$$\begin{aligned} x_j^{n+1/2} &= x_j^n + v_j^n \, (\mathbf{n} \cdot \hat{\mathbf{x}})_j^n \, \Delta\tau \ , \\ z_j^{n+1/2} &= z_j^n + v_j^n \, (\mathbf{n} \cdot \hat{\mathbf{z}})_j^n \, \Delta\tau \ . \end{aligned} \tag{4.8}$$

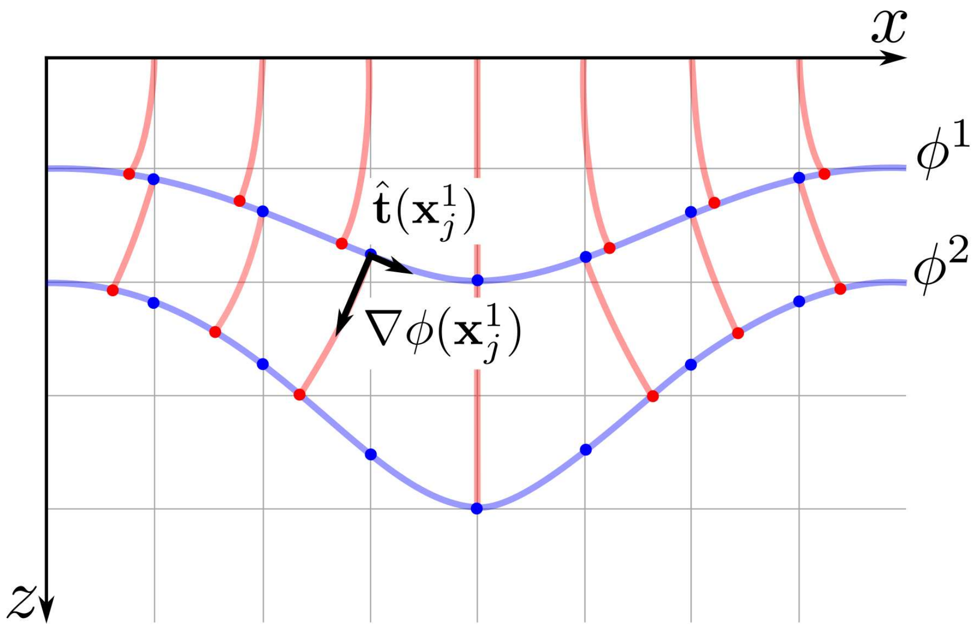

Figure 4.1: Sketch of the image-wavefront propagation algorithm. The ray quantities are not computed where the image-ray paths intersect the desired wavefront (red dots), but rather along vertical lines coincident with the lateral positions of the grid (blue dots). The next step starts from these new base points using tangent vector $\hat{\mathbf{t}}$ and the traveltime gradient $\nabla\phi$.

In this way, we obtain the coordinates (red points in Figure 4.1) of the image rays on new wavefront $\phi^{n+1}(\mathbf{x}(\gamma))$ from those of the previous one, $\phi^n(\mathbf{x}(\gamma))$, where $j$ indicates the number of the image ray and $n$ indicates the time step, as before.

From the set of points $\mathbf{x}^{n+1/2}$, we can find the points on the wavefront $\mathbf{x}^{n+1}$ that intersect the vertical grid lines (blue points in Figure 4.1). They are given by $x^{n+1} = \gamma$ and $z^{n+1} = z(x^{n+1}, \tau^{n+1})$, where the vertical coordinate is determined by means of linear interpolation. In other words, we redefine the calculation points so that they fall exactly on the lateral positions where the wavefront intersects the grid (see Figure 4.1). At the next time step, the algorithm starts over at the image-wavefront at these new coordinates. In this way, the sampling along the wavefront always remains regular, avoiding the need to add or remove rays.

We refer to this wavefront-construction strategy as image-wavefront propagation, because it does not follow any single image-rays through the model, but resamples the wavefront at each step. In this way, the sampling remains regular at all times. It is important to observe that, by construction, this procedure automatically inhibits the formation of caustics because the resampling inherently carries out a smoothing of the wavefront. This behavior is desired, because image rays must not have caustics.

In our implementation, we assume that the depth velocity $v(\mathbf{x})$ in system 4.7 is sufficiently well approximated by the Dix interval velocity $\nu(\gamma = x, \tau(\mathbf{x}))$, i.e.,

$$v(\mathbf{x}) \equiv \nu(\gamma = x, \tau(\mathbf{x}))\,. \tag{4.9}$$

This is equivalent to setting $Q = 1$ in the scheme of Cameron et al. (2008). Note that this is not a necessary assumption for the procedure. If desired, system 4.3 can be integrated together with system 4.7 to improve the estimation of the depth velocity.

## 4.4 Numerical examples

We tested our new wavefront-propagation strategy by applying it to different synthetic data sets. We start with presenting the results for a simple smooth Gaussian model. Next, we show its application to data from various versions of the Marmousi model. In all cases, we compare the determined depth velocity model to those estimated by image-ray tracing according to Cameron et al. (2008). Finally, we complement our numerical evaluation with a comparison of the depth-migrated sections obtained using the complex Padé Fourier finite-difference technique of Amazonas et al. (2007).

### 4.4.1 Gaussian model

As a first test, we applied time-to-depth conversion using our new wavefront-construction strategy to the same smooth Gaussian velocity model used in Cameron et al. (2007). The velocity distribution in this model (see Figure 4.2a) is given by

$$v(x, z) = 2 + 2\exp\{-(x^2 + (z-2)^2)\}\,, \tag{4.10}$$

where $x \in$ [-3, 3] and $z \in$ [0, 2].

As the input to the conversion, we computed the Dix velocity depicted in Figure 4.2b with a time sampling of 4 ms (two-way travel time). We start by mapping it from time to depth using image-ray tracing and *fast marching* conversion as proposed by Cameron et al. (2008). The result is presented in Figure 4.2c. We then converted the same time velocity model using the image-wavefront propagation strategy proposed here. The result can be seen in Figure 4.2d. There are notable differences between the converted depth models in Figures 4.2c and 4.2d. These differences are highlighted in Figures 4.2e and 4.2f, which show the relative error

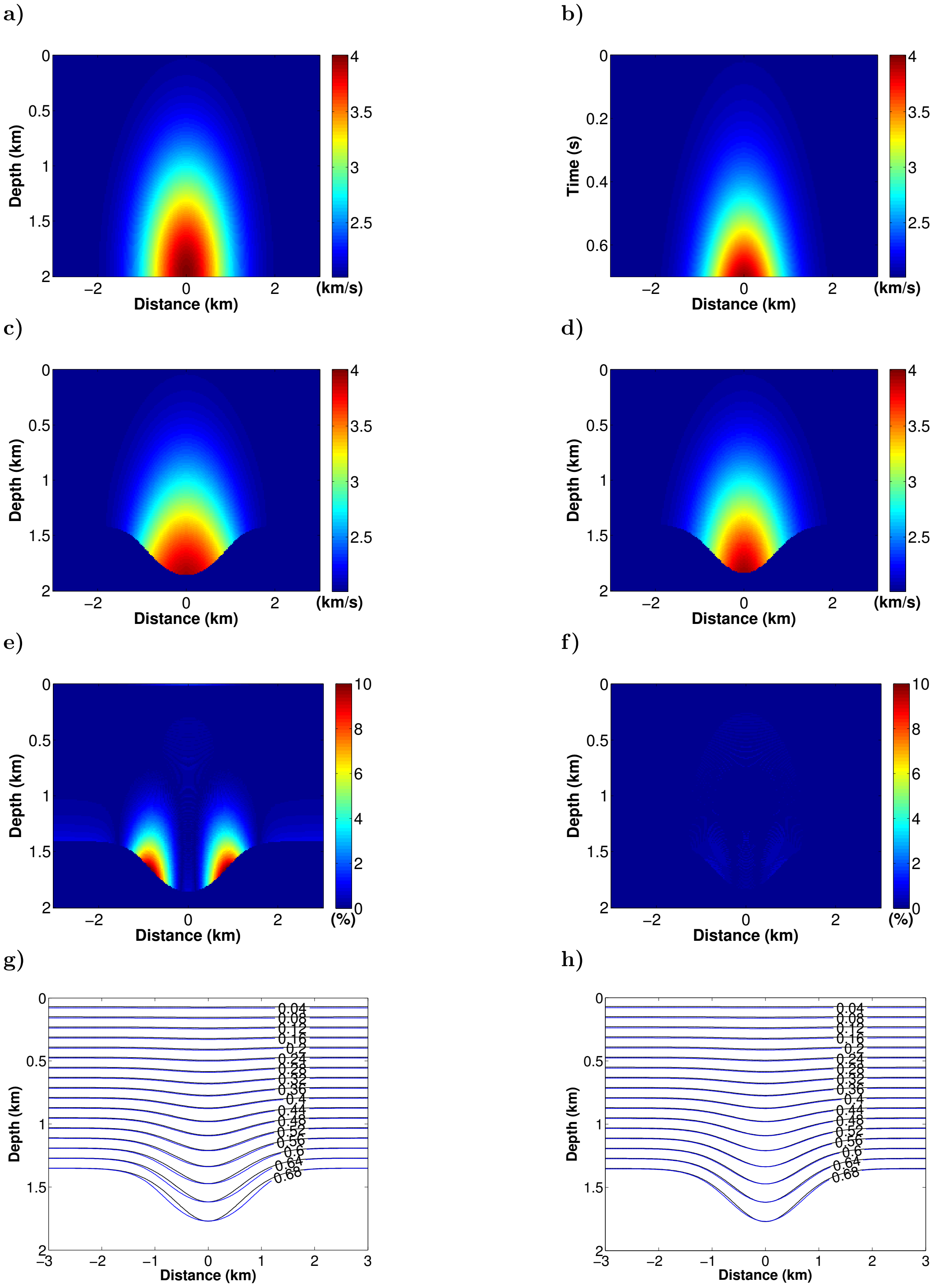

Figure 4.2: Synthetic test of time-to-depth conversion for a Gaussian-anomaly velocity model. True interval velocity model in (a) depth and (b) time. Time-to-depth conversion by (c) image-ray tracing and (d) image-wavefront propagation. Relative error of (f) image-ray tracing and (e) image-wavefront propagation. Wavefronts from (g) image-ray tracing (blue lines) and (h) image-wavefront propagation (blue lines), compared to wavefronts in the true model (black lines). Numbers indicate traveltimes in seconds.

of the converted models as compared to the true one (Figure 4.2a). We observe that the errors of both methods are relatively small in the shallow part, above 1 km depth. However, while the image-ray procedure then accumulates larger errors the wavefront-propagation technique remains fairly accurate. Figure 4.2e shows that the extracted velocity using image-ray tracing gets worse as the depth increases, reaching error values around 12%. This happens because the curvature of the rays increases with depth. In contrast, the maximum relative error of the image-wavefront propagation (Figure 4.2f) is about 0.6%, indicating that our method is quite accurate even being a first-order approximation.

Figures 4.2g and 4.2h represent an alternative way to evaluate the quality of the two procedures. They show the wavefronts as constructed by the two techniques for the models of Figures 4.2c and 4.2d in blue, over the corresponding wavefronts for the true model (Figure 4.2a) in black. The number at each line corresponds to the traveltime of the current wavefront. Again, we can see that both methods are quite similar in the shallow part, but the image-wavefront propagation provides better results at larger depths.

### 4.4.2 Marmousi model

Since our wavefront-propagation strategy does not require smooth input velocities, we could test it directly on the Marmousi velocity model (Versteeg, 1994), representing a more realistic geological setting. For a comparison to the conventional conversion procedures, we applied them to two differently smoothed versions.

**Original Marmousi model without smoothing**

Paraxial ray theory needs a smooth velocity field without strong velocity variations. Otherwise, the ray field becomes irregular and cannot be trusted. As a consequence, the time-to-depth conversion methods based on paraxial ray tracing can be applied only if the input model is smooth. In contrast, our new wavefront-propagation strategy can be applied to velocity models with hard interfaces. The reason is it is an adaptation of the level-set method (Cameron et al., 2007, 2008) that does not rely on the ray-tracing step. Therefore, we can evaluate its behavior in the original Marmousi model without smoothing. This example highlights an important feature of our method: It *does not require* any previous regularization. Thus, it can be applied directly in high-frequency or noise-corrupted models, i.e., the kind of models frequently obtained by automatic velocity-model-building methods.

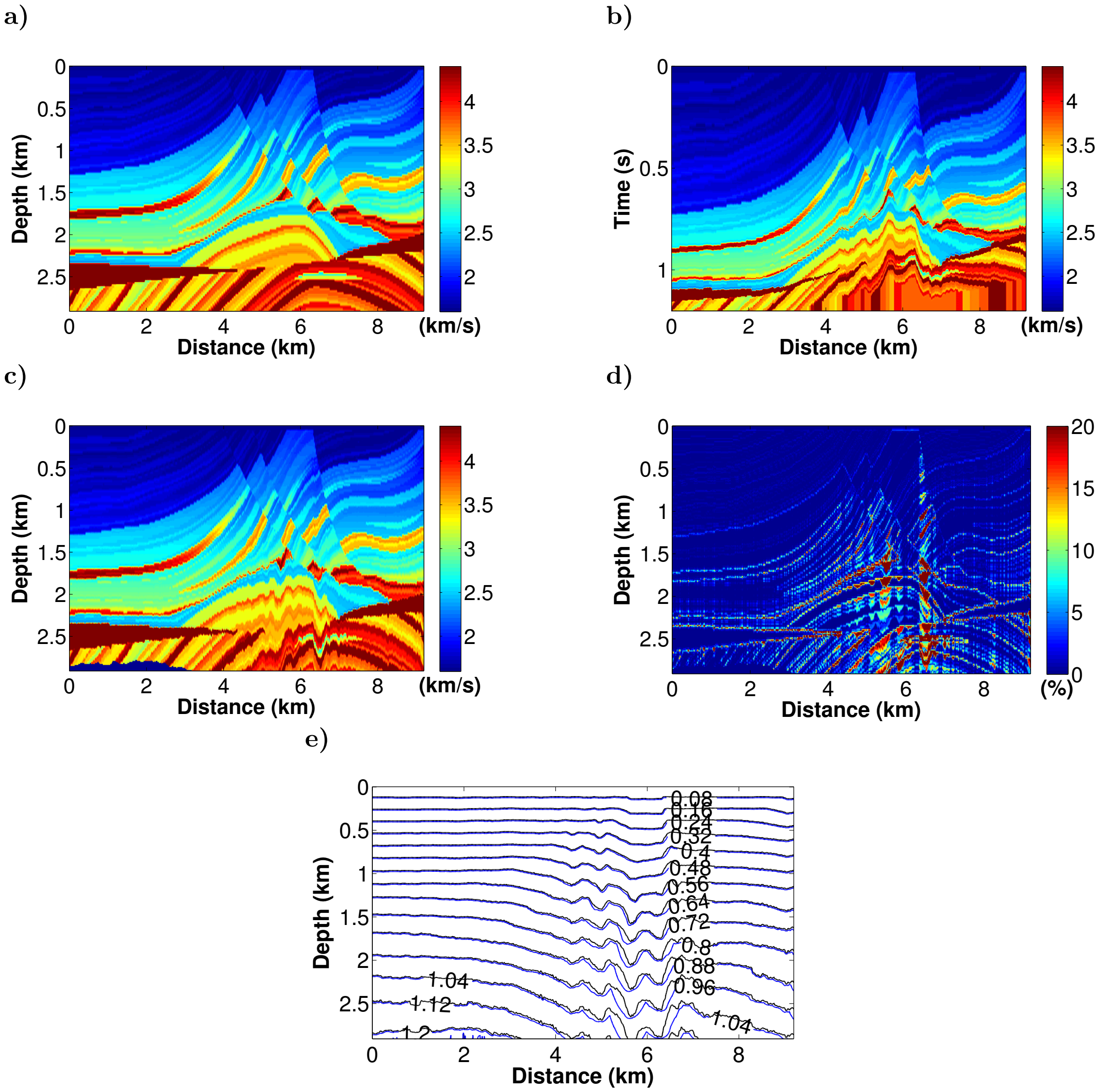

Figure 4.3: Test on the stratigraphic Marmousi velocity model without smoothing. (a) True Marmousi depth model. (b) Time interval velocity. (c) Time-to-depth conversion by image-wavefront propagation. (d) Relative model error. (e) Wavefronts in converted (blue lines) and true (black lines) models. Numbers indicate traveltimes in seconds.

Figure 4.3a shows the original Marmousi velocity model in depth without smoothing. As before, we compute the Dix velocity (Figure 4.3b) and use it as the input for the time-to-depth conversion by image-wavefront propagation. The resulting converted depth model is depicted in Figure 4.3c.

We observe that time-to-depth conversion by image-wavefront propagation recovers a high-quality version of the original model in the central part down to a depth of about 1.5 km and in the sedimentary parts on the sides of the model down to the salt intrusions. Even the intrusions themselves and sediments below them are quite reasonably recovered. The high velocity of these salts does not seem to have a strong influence on the sediments below them.

The faults present in the central part of the Marmousi model bring out another interesting feature. Apparently, our technique does not suffer from the strong dip variation present in that area. However, below the strong lateral velocity variations in the central part of the model, where the time velocity model shows some high-frequency irregularities, these are amplified in the converted depth model.

The quality of the converted model is confirmed in Figure 4.3d, which shows the relative error between the extracted (Figure 4.3c) and original (Figure 4.3a) velocity models. The error accumulates in the regions of strong lateral velocity variations, where the image-ray principle is known to become problematic. Particularly at misplaced velocity contrasts, the error can locally reach almost 100%.

Finally, Figure 4.3e presents the superposition of the wavefronts. This figure confirms the previous observations, showing a better fit of the wavefronts in the upper and lateral parts of the model. Moreover, we see in Figure 4.3e that even in the central areas of the model, the long wavelengths of the wavefronts in the extracted model adjust to those of the wavefronts in the true model.

### Smoothed versions of the Marmousi model

To allow for a comparison between the ray-tracing-based time-to-depth conversion techniques of Cameron et al. (2007, 2008) with our image-wavefront propagation, we need a smooth input velocity model. For this reason, we smoothed the original Marmousi velocity model (Figure 4.3a) by a single pass of a moving-average filter. In the first test, we used a 600 m×600 m (50 by 50 points) window. The resulting reference model is depicted in Figure 4.4a.

Figures 4.4c and 4.4d show the depth velocity models obtained, respectively, by image-ray and wavefront-propagation conversion of the Dix velocities in Figure 4.4b, and Figures 4.4e and 4.4f show the corresponding errors. As a first observation, we notice that both models resemble the original model quite closely. The errors of the conversion of the smooth model are much smaller than the ones from the conversion of the hard model (compare Figure 4.4f to Figure 4.3d). We conclude that, though not a requirement, conversion of a smooth model is advantageous for the wavefront-propagation method. As in the case of the Gaussian velocity anomaly, image-ray conversion produces, below a certain depth, significantly larger errors (up to 20%) than wavefront-propagation conversion (up to 7%), even in the sedimentary part of the model. In the image-ray converted model (Figure 4.4c), there are two near-vertical lines at distances of about 5 km and 7 km, where the converted velocities

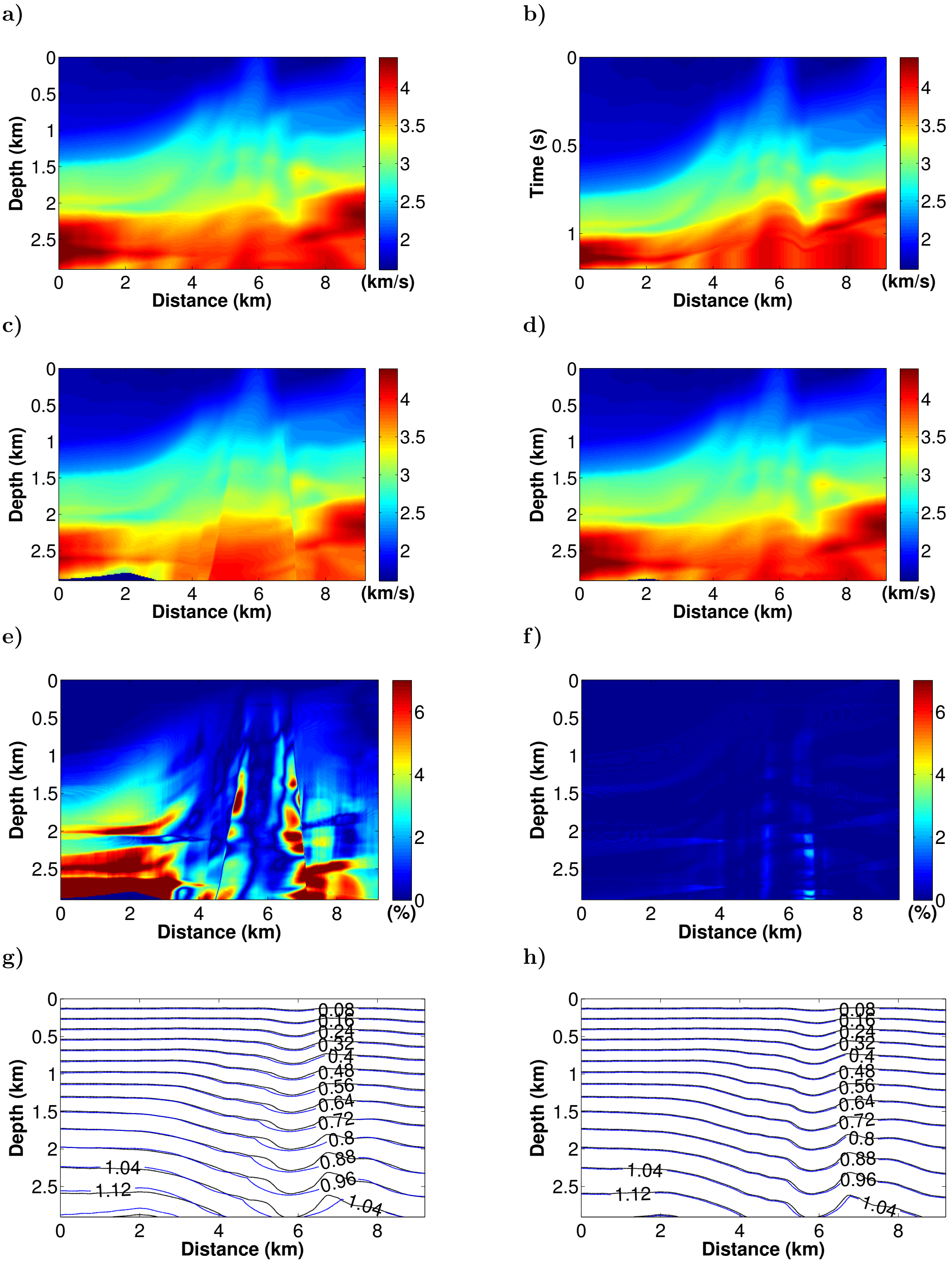

Figure 4.4: Test on a smoothed version of the Marmousi model of Figure 4.3a. One pass of a moving average with a 600 m×600 m (50 by 50 points) window. (a) True depth model. (b) Time interval velocity. Time-to-depth conversion by (c) image ray-tracing and (d) image-wavefront propagation. (e) Relative error of (c). (f) Relative error of (d). (g) Wavefronts (blue lines) in (c) and (h) wavefronts (blue lines) in (d), as compared to the wavefronts in the true model (black lines). Numbers indicate traveltimes in seconds.

change rather abrupt. These are caused by crossing image rays. This effect is not observable in the wavefront-propagation converted model (Figure 4.4d). The better quality of the latter model is also reflected in the better match of the wavefronts in Figure 4.4h than in the corresponding image-ray Figure 4.4g.

The second test confirms these findings. Here, we used a 1200 m×1200 m (100 by 100 points) window for the moving-average filter. The resulting reference model is depicted in Figure 4.5a. For this even smoother model, the converted models (Figures 4.5c and 4.5d) are even closer to the reference model, and the errors of both methods (Figures 4.5e and 4.5f) are smaller than in the previous case (up to 9% for image-ray conversion, 1.2% for wavefront-propagation conversion). The result of wavefront-propagation conversion (Figure 4.5d) is still superior to the one of image-ray conversion (Figure 4.5c), which is clearly visible in the error plots (Figures 4.5e and 4.5f) and also reflected in the better match of the wavefronts (Figures 4.5g and 4.5h). Though weaker, the abrupt velocity changes due to image-ray crossing are still visible in Figure 4.5c.

### 4.4.3 Migration results

We have seen above that time-to-depth converted velocity models depend on the technique employed for the conversion. Moreover, it is known that depth migration is more susceptible to velocity variations than time migration. Thus, an important means to evaluate the quality of the constructed depth velocity models is to use them for depth migration. In this work, we employed a two-dimensional Fourier finite-difference (FFD) migration with the complex Padé approximation as discussed in Amazonas et al. (2007). One of the reasons that led us to choose this method is that it was proven to be fast and robust. Another important point is that Amazonas et al. (2007) performed several depth migrations with different migration methods for the Marmousi data set and velocity model we use here. The use of their migration method allows us to compare our results to their migrated images, in this way increasing our information database.

For better comparison, all models presented in the last section were used to depth migrate the Marmousi data set with the same setup of Amazonas et al. (2007). We used a branch-cut rotation angle of $\alpha = 45°$, a depth extrapolation step size of 6 m, and the source wavefield was computed using a Ricker wavelet with a 25-Hz peak frequency. Figures 4.6, 4.7, and 4.8 show the migrated images obtained with the models presented in Figures 4.3, 4.4, and 4.5, respectively.

Figure 4.6 compares the migrated images of the Marmousi dataset using the true Marmousi model (part (a)) and using the wavefront-propagation converted

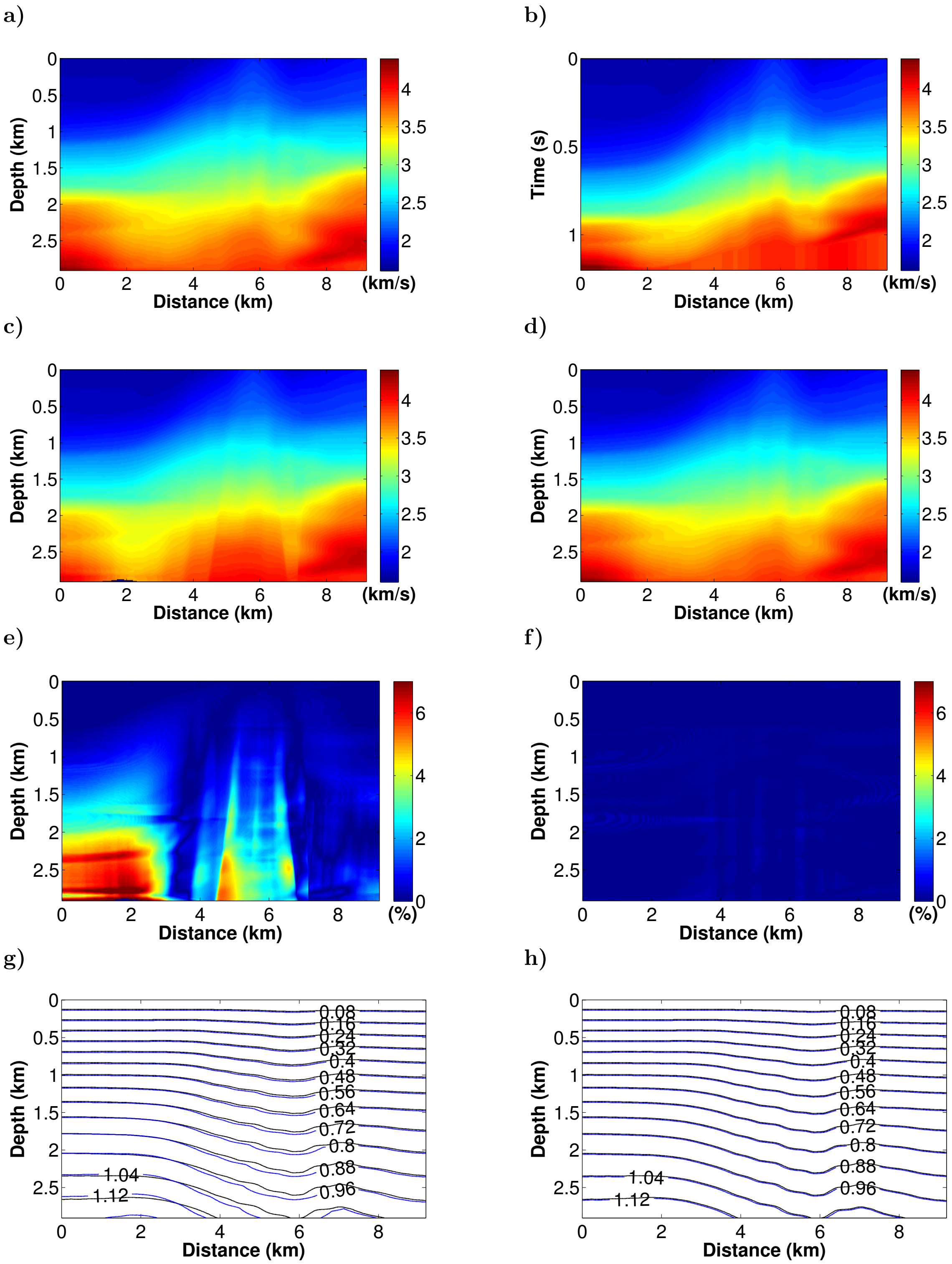

Figure 4.5: Test on a smoothed version of the Marmousi model of Figure 4.3a. One pass of a moving average with a 1200 m×1200 m (100 by 100 points) window. (a) Reference depth model. (b) Time interval velocity. Time-to-depth conversion by (c) image ray-tracing and (d) image-wavefront propagation. (e) Relative error of (c). (f) Relative error of (d). (g) Wavefronts (blue lines) in (c) and (h) wavefronts (blue lines) in (d), as compared to the wavefronts in the reference model (black lines). Numbers indicate traveltimes in seconds.

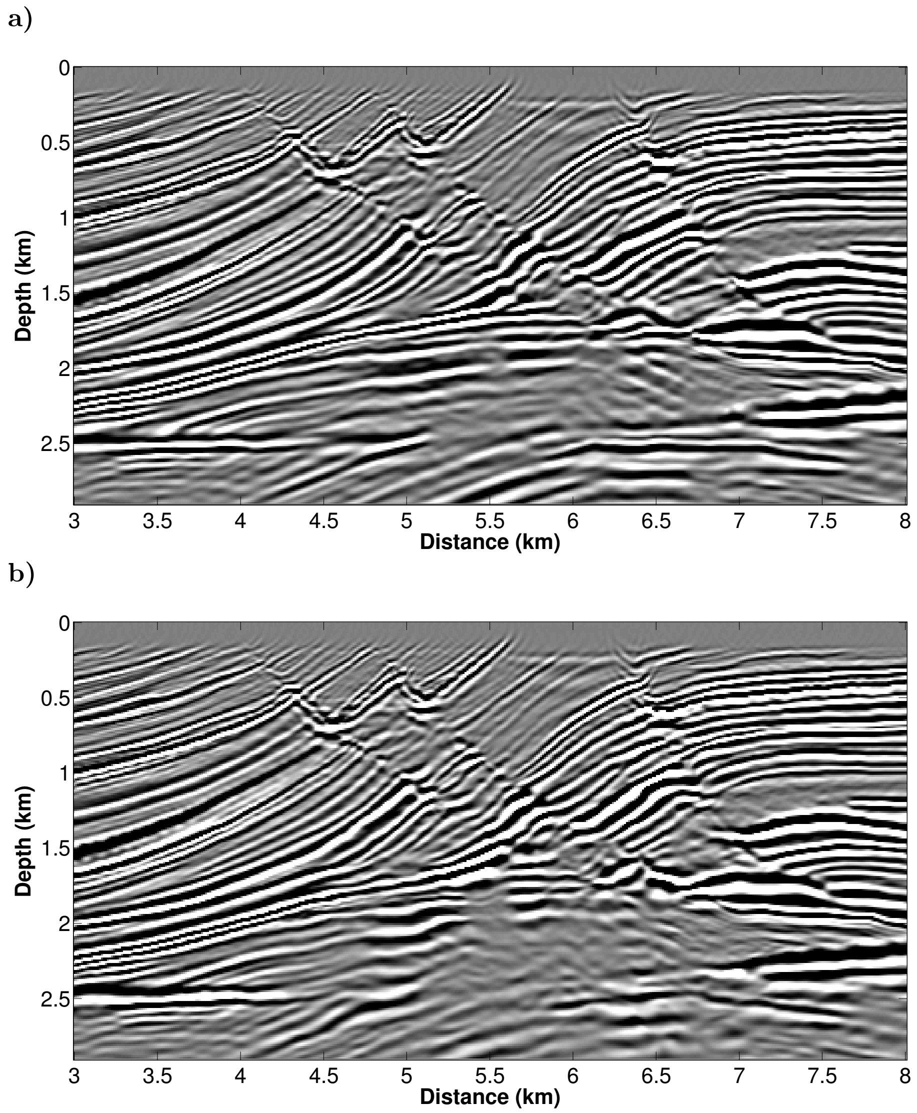

Figure 4.6: Prestack depth migrated sections of Marmousi data set using the velocity models of Figure 4.3a and (c), respectively.

unsmoothed model (part (b)). While we recognize a little bit of deterioration of the image in Figure 4.6b, particular in the lowermost part, the overall result is quite acceptable, indicating that the time-to-depth conversion has worked as expected.

Figure 4.7a shows the reference image for the second test, obtained using the first smoothed model of Figure 4.4a. We note that this image is already of a poorer quality than both images of Figure 4.6. The corresponding images obtained using the converted models (Figures 4.7b and 4.7c) are quite similar to Figure 4.7a. As expected from the velocity models, the image obtained with the wavefront-propagation model (Figure 4.7c) is a little closer to the one from the true smoothed model (Figure 4.7a), with the deviations in the image-ray image (Figure 4.7b) being located at and below the regions where the model errors are the largest (see Figure 4.4e).

The migrated images in Figure 4.8 are even more similar to each other. Closer inspection reveals that again, the strongest deviations from the reference image in Figure 4.8a, obtained with the true smoothed model, occur in the image-ray image (Figure 4.8b) at those parts where the model errors are the largest (see Figure 4.5e), while the image-wavefront propagation image (Figure 4.8c) is now virtually indistinguishable from Figure 4.8a.

### 4.4.4 Field data example

For a better comparison to the results of Cameron et al. (2008), we evaluate our time-to-depth strategy in a prestack time-migrated image from their North Sea data and corresponding time-migration velocity obtained by velocity continuation (Figure 4.9, adapted from Fomel, 2003a). This model has a significant lateral variation, mainly caused by a salt body.

We compare three different results. Figure 4.10 presents the depth velocity model obtained from conventional Dix inversion and the corresponding poststack depth migrated image. Figure 4.11 depicts the estimated velocity model, the corresponding poststack depth migrated image, and the prestack time migrated image of Figure 4.9b converted to depth using the image-ray tracing of Cameron et al. (2008). Finally, in Figure 4.12 we show the corresponding results using image-wavefront propagation.

While the time-to-depth converted velocity models are quite similar, the velocity model converted by the image-ray tracing differs from the others due to the geometric spreading of image rays (Figure 4.11a). This also affects the migrated images, mainly in the deeper parts close to the salt structure (Figure 4.11c).

Closer inspection reveals that both image ray-tracing and image-wavefront propagation improved the quality of the prestack time-migration image converted to depth, in particular near the salt flanks.

## 4.5 Conclusion

We have presented a new strategy to perform wavefront-construction in image-ray-based time-to-depth conversion of velocity models. We make use of geometric considerations on a rectangular grid to move the base points to vertical lines instead of following individual image rays. In this way, we can reduce the computation time without any loss in accuracy. Our method calculates the velocity and traveltime fields directly. By approximating the depth velocity with the Dix interval velocity, it allows to omit the computation of dynamic-ray-tracing quantities that are used in the image-ray-tracing method. In this way, the procedure requires only the knowledge of the image-wavefront at the previous time step.

We have tested our new procedure on a simple Gaussian velocity anomaly and in a more complex settings using smoothed and unsmoothed versions of the Marmousi model. We have found that our time-to-depth conversion provides satisfactory depth models. Since it does not rely on paraxial ray tracing, it even works in the presence of sharp velocity contrasts. In the smoothed models, it was able to provide remarkably accurate results down to greater depths than conventional methods that trace individual image rays.

Results of depth migration of the synthetic Marmousi data using the depth-converted models indicate that these models preserve the quality of the time-domain models used as their input. The application in a field data reinforces the applicability of this method in regions with a strong lateral variation including salt structures. In first tests (Santos et al., 2016d), the method has been successfully applied as a linker step to connect time-velocity models computed by automatic time-migration velocity analysis techniques (see, e.g., Schleicher and Costa, 2009), with more sophisticated tomographic or migration-velocity-analysis methods in depth.

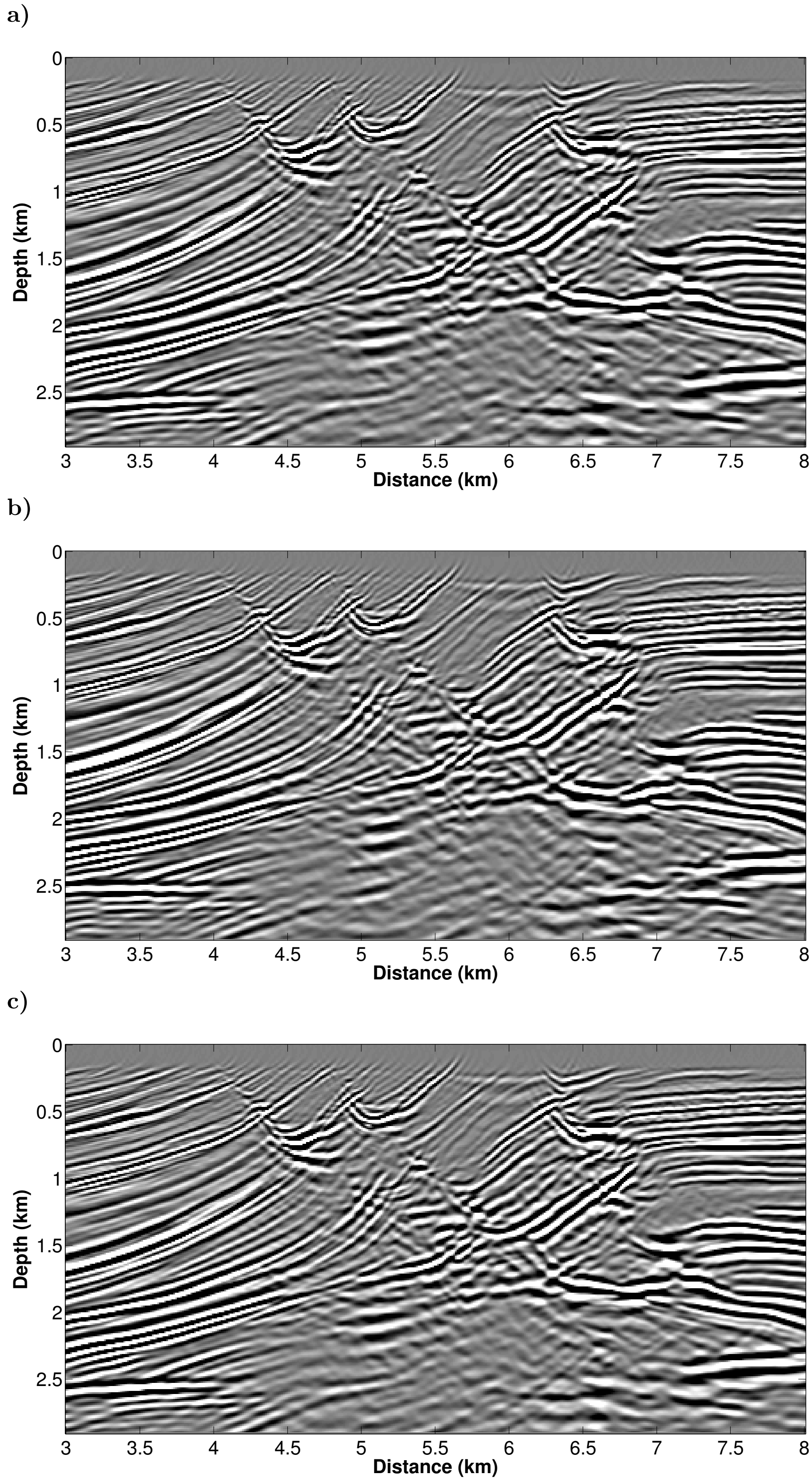

Figure 4.7: Prestack depth migrated sections of Marmousi data set using the velocity models of Figure 4.4a, (c), and (d), respectively.

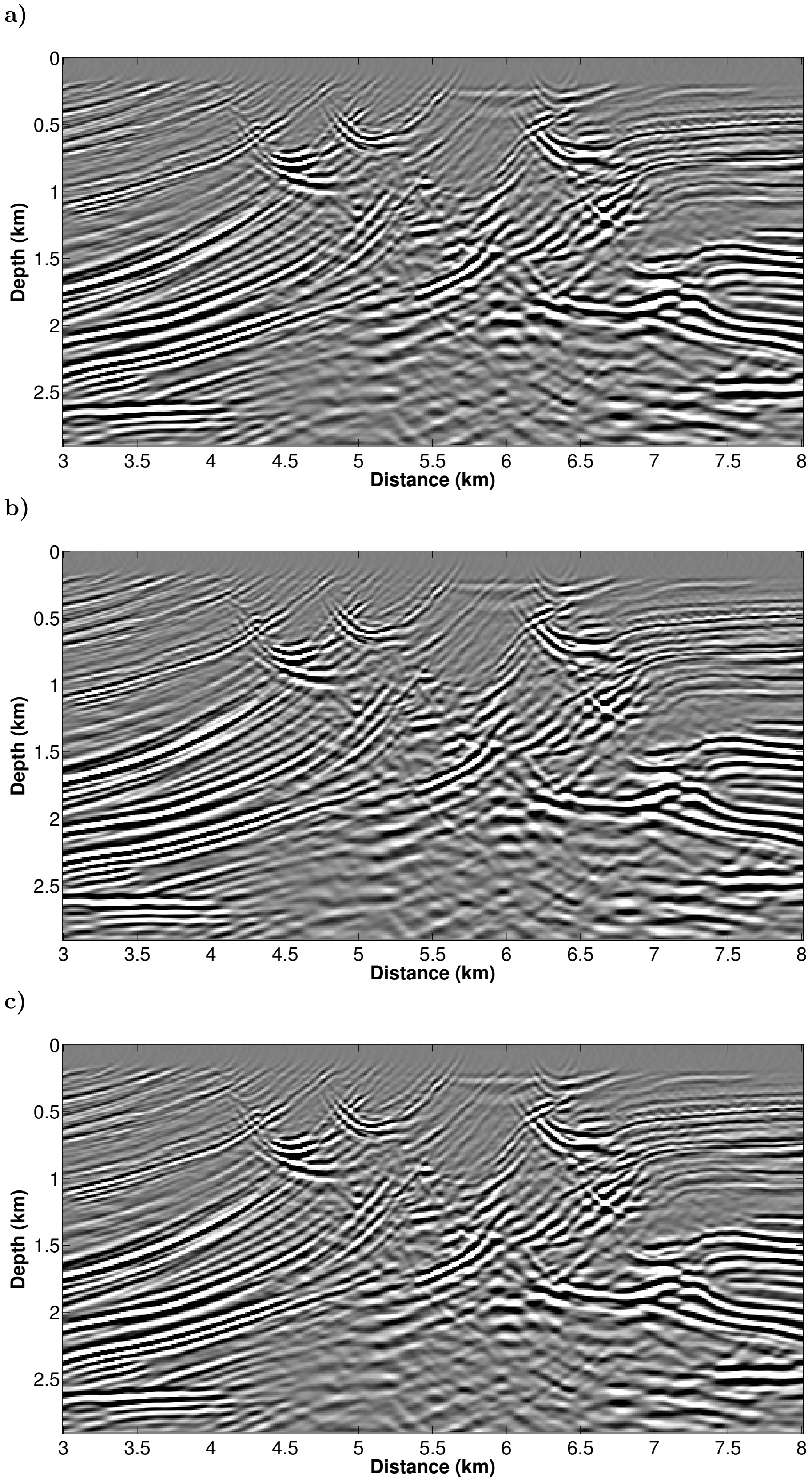

Figure 4.8: Prestack depth migrated sections of Marmousi data set using the velocity models of Figure 4.5a, (c), and (d), respectively.

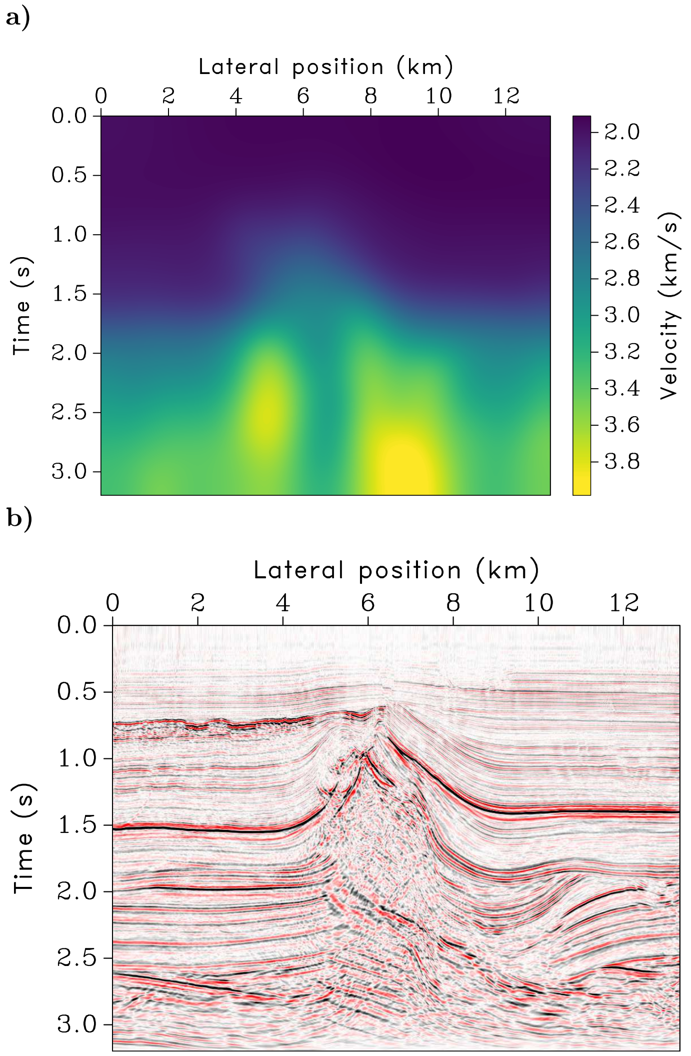

Figure 4.9: North Sea. (a) Time-migration velocity computed by velocity continuation (Fomel, 2003a). (b) Corresponding prestack time migration.

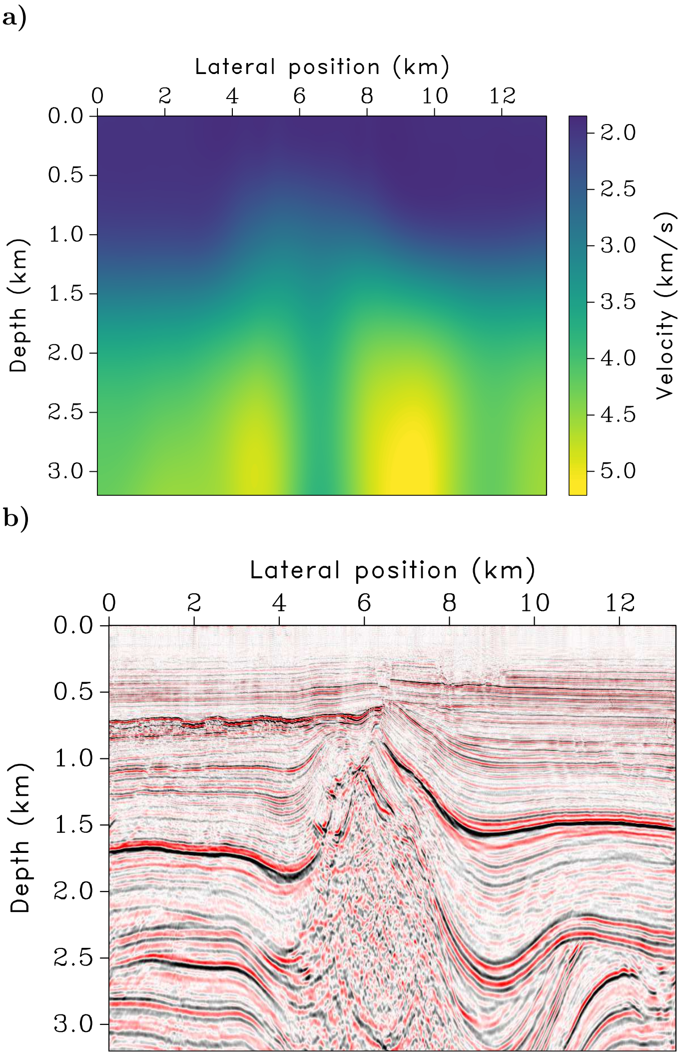

Figure 4.10: North Sea. (a) Dix velocity converted to depth. (b) Corresponding poststack depth migration.

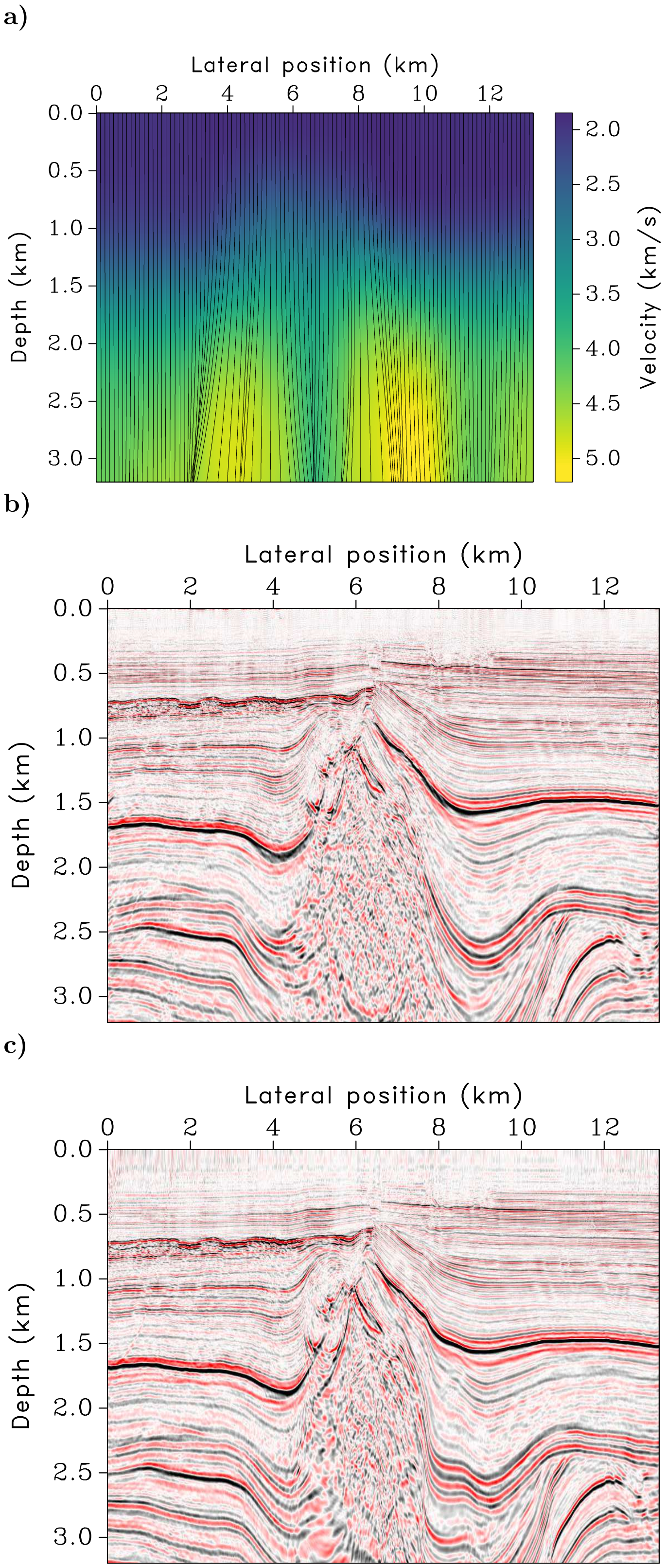

Figure 4.11: North Sea. (a) Estimated velocity model and the corresponding image rays. (b) Corresponding poststack depth migration. (c) Prestack time migration converted to depth (from Cameron et al., 2008).

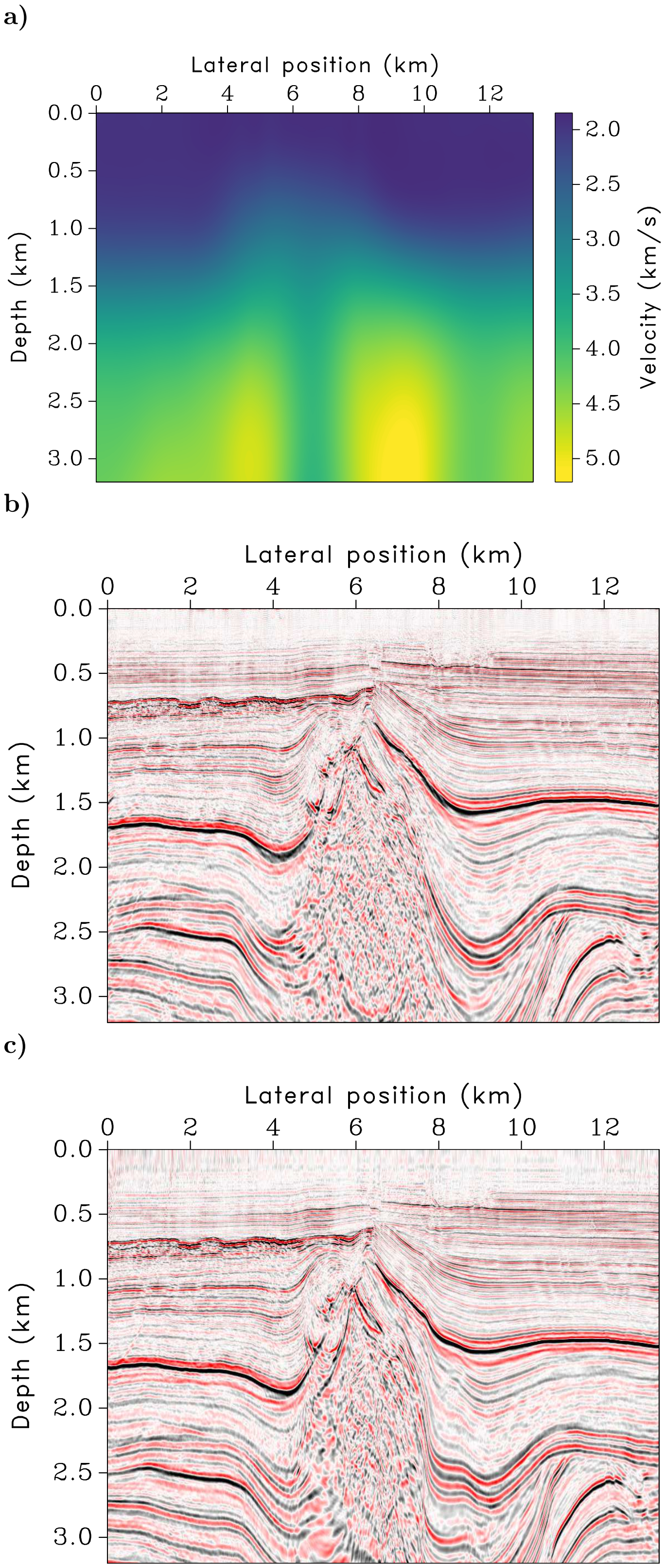

Figure 4.12: North Sea. (a) Estimated velocity model by image-wavefront propagation. (b) Corresponding poststack depth migration. (c) Prestack time migration converted to depth using our algorithm.

# Chapter 5

# Acoustic full waveform inversion

> *We call two problems inverses of one another if the formulation of each involves all or part of the solution of the other. Often, for historical reasons, one of the two problems has been studied extensively for some time, while the other is newer and not so well understood. In such cases, the former problem is called the* ***direct problem****, while the latter is called the* ***inverse problem****.*
>
> — Keller (1976), *Inverse problems.*

## 5.1 Summary

Full-waveform tomography[1] (FWT) is notorious for its strong dependence on the initial model. In this chapter, we present a workflow for the construction of initial velocity-models for FWT methods consisting of automatic time-migration velocity analysis by means of double multi-stack migration (Chapter 2), followed by time-to-depth conversion by image-ray wavefront propagation (Chapter 4). Evaluation of the converted velocity model as an initial velocity model in an acoustic FWT process indicates the potential of using a combination of these methods to achieve a fully automatic tool for initial-model building in an FWT workflow. Our tests on a modified version of the Marmousi-2 model have shown that correct background velocity information can be successfully extracted from automatic time-domain

---

[1] The word tomography is derived from the Greek *tomē* ("cut") or *tomos* ("part" or "section") and *graphein* ("to write"). Although the text does not semantically differentiate the words inversion and tomography, using them almost synonyms, we believe that the use of the word tomography is the most correct in the context of the present work.

migration velocity analysis even in media where time-migration cannot provide satisfactory seismic images.

## 5.2 Introduction

In 1984, Tarantola presented the basic idea of acoustic full waveform inversion (FWI) as a local optimization method that aims to minimize the least-squares misfit between observed and modeled seismograms. In other words, the aim of FWI is to find a subsurface model which explains the recorded seismic data (Symes, 2008). Toward the end of the 80's, Mora (1987a,b) and Tarantola (1986) extended the theory to the elastic case. Shortly after, Pratt and Worthington (1990) and Pratt (1990) introduced the frequency-domain version of FWI. While its high computational cost retarded its adoption for almost two decades, the advance of computing technology allowed to develop multiscale inversion, which became an area of very busy and active research, and it provided a hierarchical framework for robust inversion (Yang et al., 2015).

FWI proved to be an efficient tool for the determination of high-resolution details in multi-parameter models of complex subsurface structures, and it has been applied in different geophysical problem scales, ranging from ultrasonic data (Pratt, 1999) to seismological imaging (Fichtner et al., 2009).

However, being a highly nonlinear problem, FWI techniques face drawbacks other than their elevated computational cost. They are notorious for depending strongly on the choice of a good starting model for convergence at a geologically meaningful result (please, see Section 1.4 for further information). Particularly, the long-wavelength components are crucial in this respect. Analyzing this dependence, Mora (1989) recognized that FWI has a migration component and a tomographic component. To ensure convergence of the tomographic component, a possible strategy is to start the inversion processing from the low frequencies, but this does not avoid the need of accurate initial velocity models (Biondi and Almomin, 2014). A 1D graphical representation of the separation of scales concept is shown in Figure 5.1. The figure shows the trends on how industry is tightening the gap between the estimation of long and short wavelengths.

For this reason, quite some effort has been made to come up with initial models for FWI. Traveltime tomography, Laplace-domain inversion, and migration-based velocity analysis (MVA) are some examples of seismic techniques that have been investigated for this purpose (Prieux et al., 2012).

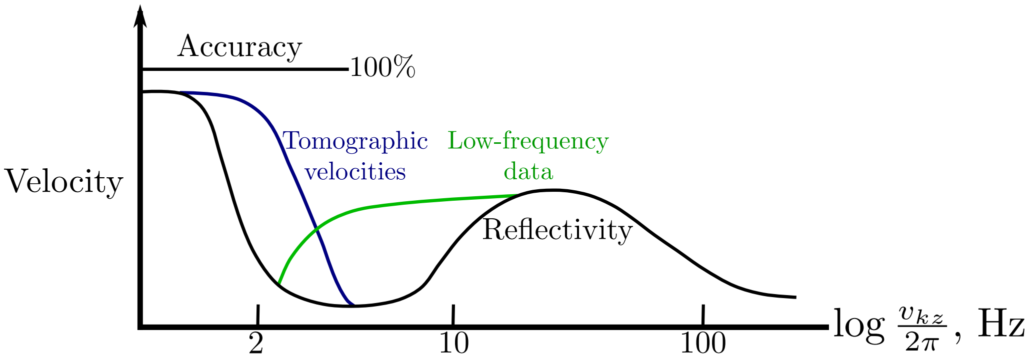

Figure 5.1: Simplified 1D graphical representation of the separation of scales in seismic imaging (black line) and the approach used by current industry to narrow the gap between the estimation of long wavelengths and short wavelengths (blue and green lines). (Adapted from "Imaging the Earth's Interior" of Claerbout, 1985; extracted and adapted from Biondi and Almomin, 2014).

In this Chapter, we investigate another possible strategy with potential to help the construction of initial velocity models for the FWT. We apply the double multi-stack technique of Schleicher and Costa (2009), adapted and discussed in Chapter 2, to perform a time-domain MVA. This is a fully automatic tool that is useful to obtain a time migrated image and its corresponding migration velocity model in a computationally effective way. We then convert the background part of the time-migration velocity model to the depth domain by means of the time-to-depth conversion strategy based on image-wavefront propagation of (Chapter 4). We evaluate the converted velocity model as an initial velocity model in an acoustic FWT process (Kurzmann et al., 2013). For comparison, in all the experiments, we carry out the same FWT using a smoothed version of the true velocity model.

Before presenting the numerical experiments, we will first review some of the fundamental aspects concerning the inversion theory and applications in seismic. In addition to the works mentioned before, the reader is referred to the treatises by Bohlen (1998), Kurzmann (2012), and Przebindowska (2013), for more in-depth accounts of the FWI theory and applications in high-performance computers which inspired most of the content of the upcoming sections.

## 5.3 Theory overview

In 1902, the French mathematician Hadamard realized that there was a certain relation between mathematical models and the reality they depict. According to Hadamard (1902), a problem is called *well-posed* if:

1. there exists a solution to the problem (existence);

2. there is at most one solution to the problem (uniqueness);
3. the solution depends continuously on the data (stability).

A problem which any of these properties are not satisfied is called an *ill-posed* problem. The concept of an ill-posed problem was introduced to distinguish between the *forward* or *direct* problem and the *inverse* problem (Keller, 1976).

The forward modeling is a well-posed problem. During the step of forwarding modeling, the use of a priori knowledge of some physical laws and mathematical models allow predicting the data. Furthermore, the forward modeling plays a crucial role in inversion process, which can be pictured as being a process of successive modeling steps. Besides the inversion process is related closely to forward modeling, this does not prevent inversion problems from being ill-posed ones. For example, there is more than one model that can fit the observed data (non-uniqueness).

Bringing to the context of seismic methods, where $\mathbf{d}_{mod}$ is the seismic data recorded at receivers on a medium represented by a set of model parameters $\mathbf{m}$, and $f$ is the nonlinear forward operator, we can write

$$\mathbf{d}_{mod} = f\left(\mathbf{m}\right) \ . \tag{5.1}$$

Inversion problem is the process of estimating the model parameters from the observed data $\mathbf{d}_{obs}$ while ensuring a good fit between $\mathbf{d}_{obs}$ and the data predicted by the forward modeling $\mathbf{d}_{mod}$ for a given model of the subsurface $\mathbf{m}$.

The seismic inverse problem is complicated because seismic waves are nonlinearly related to the unknown parameters of the medium. Furthermore, the existence of data and theoretical uncertainties make it virtually impossible to have the predicted data to be identical to the observed values. Thus, the forward problem is an approximation, and the predicted model is a simplified representation of the real system.

### 5.3.1 Inversion of non-linear problems

Several methods can be used to solve non-linear inverse problems. Usually, most of them can be divided into two main categories which are the *global methods* and the *local methods*. Global methods aim to search the model space to find the best solution. They can solve strongly non-linear problems however the numbers of parameters they can take into account is limited. The local methods are based on using local information about the gradient of the objective function to improve the initial model iteratively. Unlike the global methods, they can only be applied to solve weakly non-linear problems, but allow the use of a large number of parameters. Consequently, its solution has a strong dependency on the choice of starting models which is the case of the FWI. We will cover some of the local methods on the subsequent section.

### 5.3.2 Local optimization methods

The seismic inversion aims to find a set of model parameters $\mathbf{m}$, that provides the best fit between the observed data $\mathbf{d}_{obs}$ and the data predicted by the forward problem for a given model of the subsurface $\mathbf{d}_{mod}(\mathbf{m})$. So, to guarantee a good predicted model it is important to evaluate the data misfit, which can be defined as

$$\delta\mathbf{d} = \mathbf{d}_{mod} - \mathbf{d}_{obs} = f\left(\mathbf{m}\right) - \mathbf{d}_{obs}\,, \tag{5.2}$$

where $\delta\mathbf{d}$ is the data misfit vector of dimension $N$, and $\mathbf{m}$ is the model vector of dimension $M$. With the data misfit in hands, it is necessary to choose good criteria to fit the observed and predicted data. One of the most common criteria is to minimize the objective function described by the vector norm of the misfit between the predicted and observed data

$$E\left(\mathbf{m}\right) = \frac{1}{2}\delta\mathbf{d}^{T}\delta\mathbf{d} = \frac{1}{2}\sum_{i=1}^{N}\delta d_i^2\,, \tag{5.3}$$

where $E(\mathbf{m})$ is the objective function, and the superscript $^{T}$ denotes the matrix transpose.

Since the non-linearity, in the case of the seismic inversion, between the data and the model is weak, it is possible to linearize the inverse problem.

The most popular approach is the Born approximation, which consists in searching the best fitting model $\mathbf{m}$ in the vicinity of the starting model $\mathbf{m}_0$ such that

$$\mathbf{m} = \mathbf{m}_0 + \delta\mathbf{m}\,, \tag{5.4}$$

where $\delta\mathbf{m}$ is a perturbed model. It means that we consider our medium $\mathbf{m}$ as a perturbation of a reference medium $\mathbf{m}_0$.

So, it is possible to use the first-order Taylor series expansion for the objective function around the starting model to linearize the inverse problem

$$E\left(\mathbf{m}_0 + \delta\mathbf{m}\right) = E(\mathbf{m}) = E(\mathbf{m}_0) + \frac{\partial E(\mathbf{m}_0)}{\partial\mathbf{m}}\delta\mathbf{m} + \mathcal{O}(\mathbf{m}^2)\,, \tag{5.5}$$

the residuals of higher orders, $\mathcal{O}(\mathbf{m}^2)$, are neglected. Thus, to minimize the objective function $E(\mathbf{m})$ its derivative needs to be equal to zero

$$\frac{\partial E(\mathbf{m})}{\partial \mathbf{m}} = \frac{\partial E(\mathbf{m}_0)}{\partial \mathbf{m}} + \frac{\partial^2 E(\mathbf{m}_0)}{\partial \mathbf{m}^2}\delta\mathbf{m} = 0\,, \tag{5.6}$$

which leads to

$$\delta\mathbf{m} = -\left[\frac{\partial^2 E(\mathbf{m}_0)}{\partial \mathbf{m}^2}\right]^{-1}\frac{\partial E(\mathbf{m}_0)}{\partial \mathbf{m}}\,, \tag{5.7}$$

as the perturbation model.

From equation 5.3 it is possible to obtain the derivative of the objective function concerning the model parameters which is given by

$$\frac{\partial E(\mathbf{m}_0)}{\partial \mathbf{m}} = \left(\frac{\partial \mathbf{d}_{mod}(\mathbf{m}_0)}{\partial \mathbf{m}}\right)^T (\mathbf{d}_{mod}(\mathbf{m}_0) - \mathbf{d}_{obs}) = \mathbf{J}_0^T\delta\mathbf{d}\,, \tag{5.8}$$

where $\mathbf{J}^T$ is the transpose of the Jacobian matrix $\mathbf{J}$ also called the Fréchet derivate matrix, and the elements of the matrix can be written as

$$J_{ij} = \frac{\partial d_{mod}}{\partial m_j} \qquad (i = 1, 2, \ldots, N), (j = 1, 2, \ldots, M)\,. \tag{5.9}$$

From equation 5.8 we can calculate the second derivative of the objective function as

$$\frac{\partial^2 E(\mathbf{m}_0)}{\partial \mathbf{m}^2} = \mathbf{H}_0 = \mathbf{J}_0^T\mathbf{J}_0 + \left(\frac{\partial \mathbf{J}_0}{\partial \mathbf{m}}\right)^T \delta\mathbf{d}\,, \tag{5.10}$$

where $\mathbf{H}$ is the Hessian matrix of dimension $M \times M$. With equations 5.8 and 5.10 we can then rewrite equation 5.7 as

$$\delta\mathbf{m} = -\mathbf{H}_0^{-1}\mathbf{J}_0^T\delta\mathbf{d}\,. \tag{5.11}$$

If equation 5.3 is not quadratic, the **Newton method:** will not converge in one iteration. However, it is possible to use an iterative process, and the model update at iteration $n$ is given by

$$\mathbf{m}_{n+1} = \mathbf{m}_n - \mathbf{H}_n^{-1}\left(\frac{\partial E}{\partial \mathbf{m}}\right)_n\,. \tag{5.12}$$

However, the Newton Method requires a high computing cost and is not used very often. Commonly, the **Gauss-Newton method:** is used. This method applies an approximate Hessian matrix $\mathbf{H}_a$ for the updating model parameters

$$\mathbf{m}_{n+1} = \mathbf{m}_n - (\mathbf{H}_a^{-1})_n \left(\frac{\partial E}{\partial \mathbf{m}}\right)_n , \tag{5.13}$$

where the approximate Hessian matrix is derived from equation 5.10 neglecting the second term of the equation, which leads to

$$\mathbf{H}_a = \mathbf{J}^T \mathbf{J} \, . \tag{5.14}$$

The **Gradient method:** is another method that can be used to minimize the objective function and can be expressed as

$$\frac{\partial E}{\partial \mathbf{m}} = \mathbf{J}^T \delta \mathbf{d} \, . \tag{5.15}$$

This method consists of using the negative gradient of the objective function which will point toward a minimum of the function. Thus, the model is updated as

$$\mathbf{m}_{n+1} = \mathbf{m}_n - \mu_n \left(\frac{\partial E}{\partial \mathbf{m}}\right)_n , \tag{5.16}$$

where $\mu$ is the step length, which replaces the inverse of the Hessian in equation 5.12. Although this method requires less computational effort than the Newton method, it has a slow convergence rate and has a dependency on a reliable estimation for the step length (Virieux and Operto, 2009).

## 5.4 Time domain full waveform inversion

In this work, we use an acoustic time-domain full-waveform inversion code presented in Kurzmann (2012). This code was based on a general approach which was used in previous works (Tarantola, 1984; Mora, 1987b) and the algorithm will be presented in more details in Section 5.5.

The FWI aims to find a model for the subsurface while trying to minimize the residuals between the predicted and observed data. The minimization is achieved through the use of an iterative process using the gradient method. As we had seen before, the gradient method does not require the calculating of the inverse Hessian matrix, although it is still necessary to calculate the Fréchet derivative matrix **J**. To calculate this partial derivative explicit, it is necessary a perturbation for each model parameter separately, and to model the wavefield. So, for a single shot this would require as much as forward modeling as the number of unknown parameters.

Thus, to avoid the explicit calculation of the Fréchet matrix, the full waveform inversion calculates the gradient of the objective function $\nabla E^{\mathbf{m}}$ using the adjoint approach (Tarantola, 1984; Mora, 1987b; Plessix, 2006). This method uses the cross-correlation of the forward propagated wavefield and the backpropagated residual wavefield to calculate the gradient direction. The number of forward simulations required by this method is drastically inferior to the gradient methods, requiring only two times the number of shots of forward simulations. With that in mind, it is easy to see that this is an essential feature for the implementation of the full waveform inversion method.

### 5.4.1 The adjoint approach

As seen in previous sections, to solve the inverse problem, it is necessary to linearize the initial non-linear forward problem in the vicinity of the background model $\mathbf{m}_0$. So 5.1 can be rewritten as

$$\mathbf{d}_{mod} = f(\mathbf{m}) = f(\mathbf{m}_0 + \delta\mathbf{m}) \, , \tag{5.17}$$

where $\delta\mathbf{m}$ is the perturbed model. As shown in equation 5.5, we can then approximate $f$ using the Taylor series expansion of first order which yields to the expression

$$f(\mathbf{m}_0 + \delta\mathbf{m}) = f(\mathbf{m}) = f(\mathbf{m}_0) + \frac{\partial f(\mathbf{m}_0)}{\partial \mathbf{m}}\delta\mathbf{m} \, , \tag{5.18}$$

here the $\mathcal{O}(\mathbf{m}^2)$ of equation 5.5 was omitted since it is neglected in the approximation. From the equation above, we can then define a small perturbation in the data space $\delta\mathbf{d}$ derived from the small one of the model parameters $\delta\mathbf{m}$ as

$$\delta\mathbf{d} = f(\mathbf{m}_0 + \delta\mathbf{m}) - f(\mathbf{m}_0) \, . \tag{5.19}$$

Substituting equation 5.18 into equation 5.19 gives

$$\delta\mathbf{d} = f(\mathbf{m}_0) + \frac{\partial f(\mathbf{m}_0)}{\partial \mathbf{m}}\delta\mathbf{m} - f(\mathbf{m}_0) = \frac{\partial f(\mathbf{m}_0)}{\partial \mathbf{m}}\delta\mathbf{m} = \mathbf{J}_0\delta\mathbf{m} \tag{5.20}$$

From equation 5.20 it is possible to see that the data residuals $\delta\mathbf{d}$ has a linear dependency with the model perturbation $\delta\mathbf{m}$.

We can then rewrite equation 5.20 in the continuous form (Mora, 1987b) as

$$\delta\mathbf{d}(D) = \int_M dM \frac{\partial \mathbf{d}(D)}{\partial \mathbf{m}} \delta\mathbf{m}(M) \, , \tag{5.21}$$

where $M$ and $D$ indicate the model and the data space. So, if the Fréchet derivative matrix is known it is possible to calculate small perturbations in the wavefield resulting from a small perturbation in the model parameters. Analogously, equation 5.15 can also be written in the continuous form

$$\nabla E_m(M) = \int_D dD \left[\frac{\partial \mathbf{d}(D)}{\partial \mathbf{m}}\right]^* \delta\mathbf{d}(D)\,, \tag{5.22}$$

where, the superscript $(^*)$ denotes the adjoint of the operator $\frac{\partial \mathbf{d}(D)}{\partial \mathbf{m}}$.

### 5.4.2 The adjoint problem in the acoustic approximation

Now that we defined a relation to calculate the gradient of the objective function from the data residuals, we can now apply the adjoint approach to the acoustic approximation.

Therefore, the acoustic wave equation for a 2D inhomogeneous medium and a variable density is given by

$$\frac{1}{K(x,z)}\frac{\partial^2 p(x,z,t)}{\partial t^2} - \nabla\cdot\left(\frac{1}{\rho(x,z)}\nabla p(x,z,t)\right) = s(x,z,t)\,, \tag{5.23}$$

where $K = \rho V_P^2$ is the bulk modulus, $\rho$ is the density, $V_P$ is the P-wave velocity, and $s$ is the source term. The pressure data $p$ for a given model $\mathbf{m}$ is defined as $d_i = f(\mathbf{m}) = p(\mathbf{x}_r, t; \mathbf{x}_s)$ which is the pressure observed at the receiver locations $\mathbf{x}_r$ due to the source $\mathbf{x}_s$

$$s(\mathbf{x}, t; \mathbf{x}_s) = \delta(\mathbf{x} - \mathbf{x}_s)S(t)\,, \tag{5.24}$$

where $\delta(\mathbf{x})$ is the well-known Dirac delta function, and $S(t)$ is the source time function.

We can then apply this formulation for an acoustic wave in the equation 5.21 which gives

$$\delta d_i(\mathbf{x}_r, \mathbf{x}_s, t) = \int_V dV(\mathbf{x})\frac{\partial d_i(\mathbf{x}_r, \mathbf{x}_s, t)}{\partial \mathbf{m}(\mathbf{x})}\delta\mathbf{m}(\mathbf{x})\,, \tag{5.25}$$

which defines the perturbations of the pressure $\delta d_i$ corresponding to perturbations in the model parameters $\delta\mathbf{m}$. In the same way, we can express its adjoint problem equation given in equation 5.22 in the continuous form as

$$\nabla E_m(\mathbf{x}) = \sum_s \int dt \sum_r \frac{\partial d_i(\mathbf{x}_r, \mathbf{x}_s, t)}{\partial \mathbf{m}(\mathbf{x})}\delta d_i(\mathbf{x}_r, \mathbf{x}_s, t)\,, \tag{5.26}$$

which describes the gradient of the objective function in terms of the Fréchet derivative and the data residuals $\delta d_i$. The integrals of booth equations above are solved by using the Green's function theory.

The wavefield $p(\mathbf{x}, t; \mathbf{x}_s)$ is defined as

$$p(\mathbf{x}, t; \mathbf{x}_s) = \int_V dVG(\mathbf{x}, t; \mathbf{x}_s, 0) * s(\mathbf{x}, t; \mathbf{x}_s)\,, \tag{5.27}$$

where $G(\mathbf{x}, t; \mathbf{x}_s, 0)$ is the Green's function associated with equation 5.23, and the $(*)$ denotes the time convolution. It is possible to calculate the backpropagated wavefield $p^{'}(\mathbf{x}, t; \mathbf{x}_s)$ by propagating the data residuals backward in time, which leads to

$$p^{'}(\mathbf{x}, t; \mathbf{x}_s) = \sum_r G(\mathbf{x}, -t; \mathbf{x}_r, 0) * \delta d_i(\mathbf{x}_r, \mathbf{x}_s, t)\,, \tag{5.28}$$

where the residuals are backpropagated from all receiver locations that correspond to a given source $\mathbf{x}_s$.

From equation 5.23 it is possible to see that the forward and adjoint problem are parameterized to the bulk modulus, density, and source term. The entire derivation of the acoustic approximation can be seen in Tarantola (1984). So, the final model corrections for the bulk modulus $K$ and density $\rho$ can be calculated from the following equations

$$\delta K(\mathbf{x}) = \frac{1}{K^2(\mathbf{x})} = \sum_s \int_t dt \frac{\partial p(\mathbf{x}, t; \mathbf{x}_s)}{\partial t} \frac{\partial p^{'}(\mathbf{x}, t; \mathbf{x}_s)}{\partial t}\,,$$

$$\delta \rho(\mathbf{x}) = \frac{1}{\rho^2(\mathbf{x})} \sum_s \int_t dt \nabla p(\mathbf{x}, t; \mathbf{x}_s) \cdot \nabla p^{'}(\mathbf{x}, t; \mathbf{x}_s)\,, \tag{5.29}$$

where $p(\mathbf{x}, t; \mathbf{x}_s)$ and $p^{'}(\mathbf{x}, t; \mathbf{x}_s)$ are the pressure wavefield an the backpropagated residual wavefield describe above.

## 5.5 Full waveform inversion algorithm

The inversion code used in this work is originated from the work of Kurzmann (2012). Here we will present a brief overview of the algorithm for the full waveform inversion for a 2D acoustic mean in the time-domain.

### 5.5.1 Forward modeling

The acoustic wave equation can be expressed in the form of first-order partial differential equations in the pressure-velocity formulation

$$\frac{\partial p}{\partial t} = K\nabla \mathbf{w}\,, \tag{5.30}$$

$$\frac{\partial \mathbf{w}}{\partial t} = \frac{1}{\rho}\nabla \rho\,,$$

where $\mathbf{w}$ the particle velocity, $p$ is the pressure field, $K$ is the bulk modulus, and $\rho$ is the density. These equations are also known as the continuity equation (conservation of mass) and the conservation of momentum. So, we have

$$\frac{\partial p(x,z,t)}{\partial t} = K(x,z)\left(\frac{\partial w_x(x,z,t)}{\partial x} + \frac{\partial w_z(x,z,t)}{\partial z}\right)\,,$$

$$\begin{aligned} \frac{\partial w_x(x,z,t)}{\partial t} &= \frac{1}{\rho(x,z)}\frac{\partial p(x,z,t)}{\partial x}\,, \\ \frac{\partial w_z(x,z,t)}{\partial t} &= \frac{1}{\rho(x,z)}\frac{\partial p(x,z,t)}{\partial z}\,. \end{aligned} \tag{5.31}$$

Thus, to solve the 2D acoustic wave equation given by equation 5.31, it was used a second-order finite-difference approximation, a common technique in the numerical modeling for seismic wave propagation. To, apply the finite difference method it is necessary to discretize the space and time domain, which can be done as

$$\begin{aligned} x &= i\Delta h & \qquad i &= (1,2,\ldots,N_x)\,, \\ z &= j\Delta h & \qquad j &= (1,2,\ldots,N_z)\,, \\ t &= k\Delta h & \qquad k &= (1,2,\ldots,N_t)\,, \end{aligned} \tag{5.32}$$

where $\Delta h$ is the grid spacing, $N_x$, $N_z$ are the number of grid points in $x$ and $z$ directions, and $N_t$ is the total number of time steps.

To apply the discretization to the wave equation, it is necessary to substitute the partial derivatives by the finite-difference operators, which leads to

$$\frac{\partial w_x(x,z,t)}{\partial t} \approx \frac{w^{n+1/2}_{x|j,i+1/2} - w^{n-1/2}_{x|j,i+1/2}}{\Delta t} = \frac{1}{\rho_{j,i+1/2}}\frac{p^n_{j,i+1} - p^n_{j,i}}{\Delta h}\,,$$

$$\frac{\partial w_z(x,z,t)}{\partial t} \approx \frac{w^{n+1/2}_{z|j+1/2,i} - w^{n-1/2}_{z|j+1/2,i}}{\Delta t} = \frac{1}{\rho_{j+1/2,i}}\frac{p^n_{j+1,i} - p^n_{j,i}}{\Delta h}\,,$$

$$\frac{\partial p(x,z,t)}{\partial t} \approx \frac{p_{j,i}^{n+1} - p_{j,i}^{n}}{\Delta t} = K_{j,i} \frac{w_{x|j,i+1/2}^{n+1/2} - w_{x|j,i-1/2}^{n+1/2} + w_{z|j+1/2,i}^{n+1/2} - w_{z|j-1/2,i}^{n+1/2}}{\Delta h}\,. \tag{5.33}$$

### Initial and boundary conditions

To find the solution of a differential equation, it is necessary to specify the initial and boundary conditions. Assuming a medium at rest before the application of the excitation can be written as

$$p(x,z,t=0) = \partial_t p(x,z,t=0) = 0\,. \tag{5.34}$$

As for the boundary conditions, two different types were used, the *free surface boundary* and the *absorbing boundary.*

The free surface boundary can be modeled using the vacuum formalism (Zahradník et al., 1993; Bohlen and Saenger, 2006), which consist of considering the medium above the free surface as a vacuum. Another way to implement the free surface is the mirroring technique (Levander, 1988). However, this method has some differences in the implementation for various forward modeling codes, which are due to the location of the free surface on the standard staggered grid and leads to some discrepancies in the modeling.

The absorbing boundary is used when it is needed to attenuate the unwanted reflections from the computation edges of the model. Its approach is based on the application of the complex coordinate stretching (Berenger, 1994; Chew and Weedon, 1994) and includes the perfectly matched layers (PML). Thus, the pressure wavefield with the PML implementation requires additional equations to compute auxiliary PML variables (Kurzmann, 2012).

### Accuracy and stability

When accounting for numerical modeling one must concern about artifacts and instabilities. Since we used a truncated Taylor series to approximate the spatial derivatives, it is necessary to verify if the condition to avoid grid dispersion is satisfied. So, the following expression must be satisfied

$$\Delta h \leq \frac{\lambda_{min}}{n} = \frac{V_{P_{min}}}{n f_{max}}\,, \tag{5.35}$$

where $f_{max}$ is the maximum frequency of the wavefield, and $V_{P_{min}}$ is the minimum P-wave velocity, $n$ the number of grid points per minimum wavelength $\lambda_{min}$.

Furthermore, to guarantee the stability of the finite-difference modeling, it is necessary to ensure that the sampling criteria is satisfied. Therefore, the following expression must be satisfied

$$\Delta t \leq \frac{\Delta h}{\sqrt{2} V_{P_{max}}} \,, \tag{5.36}$$

where $v_{P_{max}}$ is the maximum P-wave velocity of the model. It is possible to see that to ensure the stability of the method the time step $\Delta t$ must be less than the propagation time between two neighboring grid points.

## 5.5.2 Inversion

### Conjugate gradient method

It is possible to improve the convergence rate of the gradient method by using the conjugate gradient (Mora, 1987b). In this method, the conjugate direction is given by a linear combination of the previous and the current descent direction, thus

$$\delta \mathbf{c}_n = \delta \mathbf{m}_n + \beta_n \delta \mathbf{c}_{n-1} \,, \tag{5.37}$$

where $\mathbf{c}_n$ is the conjugate gradient, $\delta \mathbf{m}_n$ is the steepest descent gradient, and $\beta$ is the scalar that ensures that $\delta \mathbf{c}_n$ and $\delta \mathbf{c}_{n-1}$ are conjugate. The $\beta$ factor is computed through Polak-Ribiere method (Nocedal and Wright, 2006)

$$\beta_n^{PR} = \frac{\delta \mathbf{m}_n^T (\delta \mathbf{m}_n - \delta m_{n-1})}{\delta m_{n-1}^T} \delta \mathbf{m}_{n-1} \,, \tag{5.38}$$

moreover the $\beta$ parameter is defined as

$$\beta_n = \max \{\beta_n^{PR}, 0\} \,. \tag{5.39}$$

### Step length estimation

To guarantee the convergence of the method, it is necessary to use a good step length. The estimation of an optimal step length $\mu_n$ can be made by following the steps below.

First, we have to define the test step lengths. So, we can assume three test step lengths at iteration $n$ as

$$\begin{aligned} \mu_{1,n} &= s\mu_{init,n} \,, \\ \mu_{2,n} &= \mu_{init,n} \,, \\ \mu_{3,n} &= \frac{\mu_{init,n}}{s} \,, \end{aligned} \tag{5.40}$$

where $s$ is the scaling factor. So, in this approach, it is required to define a test step length at the first iteration, and for the subsequent iterations, $n > 1$, the best optimal step length from the previous iteration becomes the initial for the next one.

After, we must update the current model using the $\mathbf{c}_n$ and the test step length we obtained such that we obtain three different model updates

$$\mathbf{m}_{\mu_1,n} = \mathbf{m}_n - \mu_{1,n}\delta\mathbf{c}_n \,, \tag{5.41}$$

$$\mathbf{m}_{\mu_2,n} = \mathbf{m}_n - \mu_{2,n}\delta\mathbf{c}_n \,, \tag{5.42}$$

$$\mathbf{m}_{\mu_3,n} = \mathbf{m}_n - \mu_{3,n}\delta\mathbf{c}_n \,. \tag{5.43}$$

Then, the test forward simulations are performed to obtain the predicted data for different model updates: $\mathbf{d}_{mod(\mu_1,n)}$, $\mathbf{d}_{mod(\mu_2,n)}$, $\mathbf{d}_{mod(\mu_3,n)}$, and then we calculate the corresponding objective function (misfit): $E(\mathbf{m}_{\mu_1,n})$, $E(\mathbf{m}_{\mu_2,n})$, $E(\mathbf{m}_{\mu_3,n})$.

After this, we must calculate the true misfit function by fitting a parabola through the three points $(\mu_{i,n}, E(\mathbf{m}_{\mu_i,n}))$, where $i \in \{1, 2, 3\}$, which leads us to the system

$$E(\mathbf{m}_{\mu_1,n}) = a\mu_{1,n}^2 + b\mu_{1,n} + c \,, \tag{5.44}$$

$$E(\mathbf{m}_{\mu_2,n}) = a\mu_{2,n}^2 + b\mu_{2,n} + c \,, \tag{5.45}$$

$$E(\mathbf{m}_{\mu_3,n}) = a\mu_{3,n}^2 + b\mu_{3,n} + c \,, \tag{5.46}$$

where $a$, $b$, $c$ are the unknowns, and the minimum of the parabola defines the optimal step length for the iteration $n$ as

$$\mu_n = \frac{-b}{2a} \,. \tag{5.47}$$

In this approach, we are assuming that the data objective function has a parabolic shape.

**Algorithm 5.1** FWI algorithm

```
procedure FWI($\mathbf{d}_{obs}$,$\mathbf{m}_0$,$S(0)$)        ▷ Start by calculating the FWD
    for $n = ni$ until $nf$ do
        Calculate $p(\mathbf{x}, t, \mathbf{x}_s)$
        Calculate $\mathbf{d}_{mod,n}$
        $\delta\mathbf{d}_n = \mathbf{d}_{mod,n} - \mathbf{d}_{obs}$
        $E(\mathbf{m}_n) = \frac{1}{2}\delta\mathbf{d}_n^T\delta\mathbf{d}_n$
        Calculate $p'(\mathbf{x}, t; \mathbf{x}_s)$ from $\delta\mathbf{d}_{n-1}$
        $\delta\mathbf{c}_n = \delta\mathbf{m}_n + \beta_n\delta\mathbf{c}_{n-1}$ for each $\delta\mathbf{m}_{n,s}$
    end for
    Calculate $\delta\mathbf{m} = \sum_{s=1}^{N_s}\delta\mathbf{m}_{n,s}$
    Apply $P$ to the gradient $\mathbf{p}_n = P\delta\mathbf{m}_n$
    if $n > 1$ then calculate $\mathbf{c}_n$ direction
    end if
    Estimate $\mu_n$
    $\mathbf{m}_{n+1} = \mathbf{m}_n - \mu_n\delta\mathbf{c}_n$
end procedure
```

### Model update

The model update used in the code was based on the work of Pica et al. (1990). However, an additional factor was used to scale the gradient to the maximum of the model parameter. Then, we have

$$\mu_n\delta\mathbf{c}_n = \mu_n\frac{\max(\mathbf{m}_n)}{\max(\mathbf{c}_n)}\mathbf{c}_n\,, \tag{5.48}$$

from this expression, it is possible to see that the gradient of each model parameter is normalized to its maximum value and the optimal step length is related to the maximum of the actual model. A detailed description can be found in Kurzmann et al. (2009) and Kurzmann (2012).

## 5.6 FWI algorithm

The full waveform inversion algorithm requires some external input to start. These inputs are the observed pressure data $\mathbf{d}_{obs}$, the starting model $\mathbf{m}_0$ and an initial source time function. Given these inputs, the code can start the process. For each iteration $n$, the acoustic FWI will start by solving the forward problem given in equation 5.23 for the current model $\mathbf{m}_n$ to generate the pressure wavefield $p(\mathbf{x}, t, \mathbf{x}_s)$ and the predicted data for the $n$th iteration $\mathbf{d}_{mod,n}$. Then, the data residuals given by $\delta\mathbf{d}_n = \mathbf{d}_{mod,n} - \mathbf{d}_{obs}$ are calculated as well as the objective function (misfit) $E(\mathbf{m}_n) = \frac{1}{2}\delta\mathbf{d}_n^T\delta\mathbf{d}_n$. The next step is to calculate the residual wavefield $p^{'}(\mathbf{x}, t; \mathbf{x}_s)$

by backpropagating the data residuals obtained in the previous step from the receiver positions. After this, the code calculates the gradient for each material parameter $\delta \mathbf{m}_{n,s}$. The steps above are done for each of the source located at $\mathbf{x}_s$. For all sources, it will calculate the sum of the gradient over all shots $\delta \mathbf{m} = \sum_{s=1}^{N_s} \delta \mathbf{m}_{n,s}$. Then, the preconditioning operator $P$ is applied to the gradient $\mathbf{p}_n = P\delta \mathbf{m}_n$. If $n > 1$ the conjugate gradient direction $\mathbf{c}_n$ must be calculated. Lastly, the code will estimate the step length $\mu_n$ by a parabolic fit and use it to update the model parameters $\mathbf{m}_{n+1} = \mathbf{m}_n - \mu_n \delta \mathbf{c}_n$. The Algorithm 5.1 summarizes the procedure.

## 5.7 FWI requirements

The FWI is based on a local optimization method; thus, we are looking for a solution that is only locally optimal and has no guarantee that we found the global minimum of the objective function. This implies in need of a good starting model for the method to succeed since a good starting model should be enough to guarantee that the algorithm will converge to the global minimum. That being said, a good starting model can be acquired by verifying if the data generated by the starting model correspond to the observed data within half a cycle of the minimum considered frequency (Sun and McMechan, 1992). If the traveltime does not respect this, a cycle-skipping will occur, which will result in the inversion fitting the calculated data to the wrong cycle of the observed data as shown in Figure 5.2 making it converge to a local minimum.

Given that, it would be useful to express a relation of the convergence regarding the travel time error $\delta t$ and the propagation distances. Thus, for a given seismic event the following expression must be satisfied

$$\frac{\delta t}{T} < \frac{\lambda}{2cT} \quad \text{or} \quad \frac{\delta t}{T} < \frac{1}{2N_\lambda}, \tag{5.49}$$

where $T$ is the total arrival time of the event, $N_\lambda$ is the propagation distance in wavelengths, and $c$ is the background velocity. This strict condition can be relaxed if the number of wavelengths $N_\lambda$ between the source and receiver is reduced.

Knowing that we can see that there are three different ways to reduce the travel time error $\delta t$ to improve the convergence: Improving the accuracy of the starting model, reducing the data offsets and using lower starting frequencies. However, due to the absence of very low frequencies in real data, this step has limited use. As shown by Sirgue (2003), the use of long offset data is useful, because the information they provide on the low wavenumber. This means that it is possible to obtain a better estimation of the velocity, but on the other hand, it increases the risk of cycle-skipping.

Therefore, the minimum frequency present in the data will determine the requirement for the starting model of the FWI. If low frequencies are absent, the starting model needs to have higher accuracy and must include the long-wavelength structures. The initial model for the FWI can be obtained in some different ways. Here we will describe some of these methods.

The first-arrival traveltime tomography (FATT) is a standard method to estimate the starting model (see, e.g., Pratt, 1999; Dessa, 2004; Ravaut et al., 2004; Brenders and Pratt, 2007; Malinowski and Operto, 2008; Bleibinhaus et al., 2009). The image supplied by this method is robust but has a low-resolution (Pratt, 1999). The spatial resolution of FATT is limited to the width of the first Fresnel zone, which is approximately given by $\sqrt{\lambda L}$, where $\lambda$ is the dominant wavelength, and $L$ is the propagation distance.

Another method used to obtain the initial model is the reflection traveltime tomography (RTT). This method implies in using the reflection traveltimes to build the velocity model. The resolution it provides is higher than the one from the FATT method; however, the fit between the direct arrivals of the predicted and observed data may be insufficient to allow the use of the FWI (Prieux et al., 2012).

Also, the stereotomography can be used to in the generation of the starting model. Here the initial velocity model is obtained from the inversion of traveltimes and slops of locally-coherent events in the prestack data. This method has the advantage of being a semi-automatic picking procedure, which is more comfortable than picking continuous events.

Lastly, we have the Laplace domain inversion, which considers the waveform in the Laplace domain as a zero frequency component for a damped wavefield in the time domain (Shin and Cha, 2008, 2009). The main advantage of this method is that it is capable of recovering a smooth, long-wavelength starting model from data that lacks low-frequency components. However, it has the disadvantage of the penetration depth being limited by the maximum offset of the data and on the choice of the Laplace domain constants.

## 5.8 Multi-scale inversion strategy

### 5.8.1 Selection of frequency bands

The contribution to the gradient image of a single source-receiver pair has only a single wavenumber component, given by $k_0(\hat{\mathbf{s}} + \hat{\mathbf{r}})$. For a 1D earth, the incident

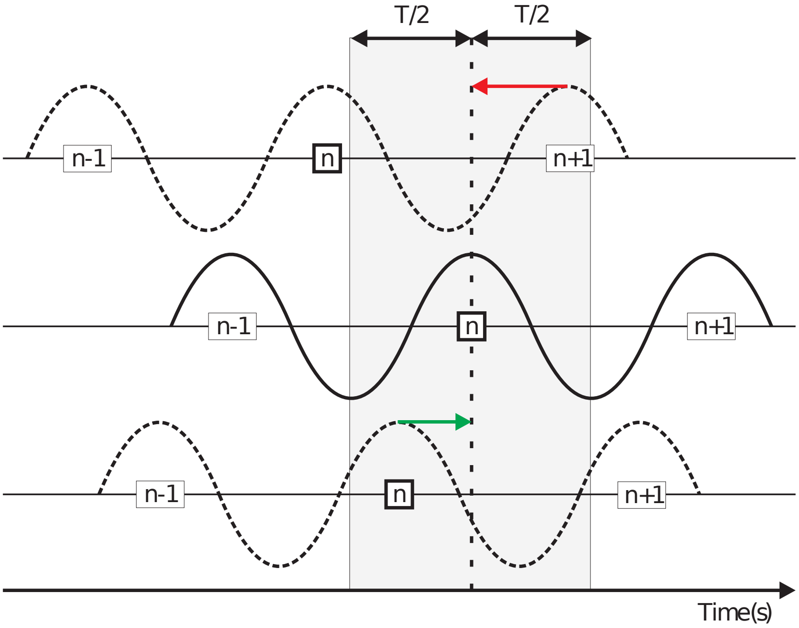

Figure 5.2: Schematic of cycle-skipping artifacts in FWI. Original image extracted from Przebindowska (2013) after Virieux and Operto (2009).

and scattering angles are symmetric, and can be expressed as

$$\begin{aligned} k_0\hat{\mathbf{s}} &= (k_0 \sin\theta, k_0 \cos\theta)\ , \\ k_0\hat{\mathbf{r}} &= (-k_0 \sin\theta, k_0 \cos\theta)\ , \end{aligned} \tag{5.50}$$

where the angles $\theta$ and $-\theta$ are the propagation directions of the source and receiver wave vectors, concerning the vertical axis. Then, we have

$$\begin{aligned} \cos\theta &= \frac{z}{\sqrt{h^2+z^2}}\ , \\ \sin\theta &= \frac{h}{\sqrt{h^2+z^2}}\ , \end{aligned} \tag{5.51}$$

where $h$ is the half-offset and $z$ is the depth of the scattering layer. Substituting 5.50 into equation 5.51, we obtain

$$\begin{aligned} k_x &= 0\,, \\ k_z &= 2k_0\alpha\,, \end{aligned} \tag{5.52}$$

which are the components of the vector $k_0(\hat{\mathbf{s}}+\hat{\mathbf{r}})$. With

$$\alpha_{min} = \cos\theta = \frac{1}{\sqrt{1+R_{max}^2}}\ , \tag{5.53}$$

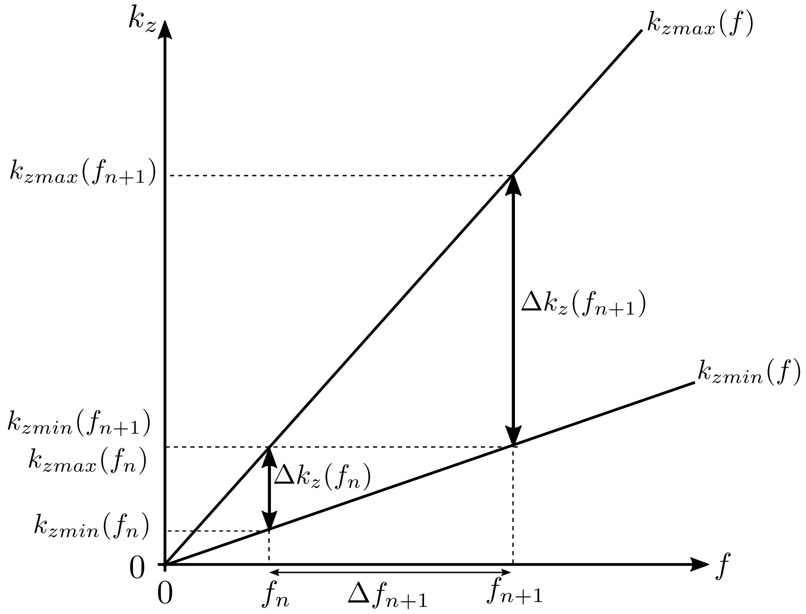

Figure 5.3: Frequency discretization strategy (after Sirgue and Pratt, 2004).

where $R = h/z$ is the half offset-to-depth ratio. We can then use the equations 5.52 and 5.53 to obtain the wavenumber coverage for a given offset. Considering a surface seismic acquisition with an offset range of $[0, x_{max}]$, we can estimate that the vertical wavenumber coverage $k_z$ for a given frequency is limited to the range $[k_{z\,\mathrm{min}}, k_{z\,\mathrm{max}}]$, where

$$\begin{aligned} k_{zmin} &= 2k_0\alpha_{min} \, , \\ k_{zmax} &= 2k_0 \, , \end{aligned} \tag{5.54}$$

with

$$\alpha_{min} = \frac{1}{\sqrt{1 + R_{max}^2}} \, , \tag{5.55}$$

where $R_{max} = h_{max}/z$ is the half offset-to-depth ratio at the maximum half-offset $h_{max}$, and $z$ is the depth of the target layer. Thus, it is possible to rewrite the equation 5.54 regarding the frequency $f$ as

$$\begin{aligned} k_{zmin} &= 4\pi f \alpha_{min}/c_0 \, , \\ k_{zmax} &= 4\pi f/c_0 \, , \end{aligned} \tag{5.56}$$

where $f$ is given in hertz and $c_0$ is the velocity in the background medium. With the expression above it is possible to define the wavenumber coverage of a multi-offset acquisition as

$$\Delta k_z \equiv |k_{zmax} - k_{zmin}| = 4\pi \left(1 - \alpha_{min}\right) f/c_0 \, , \tag{5.57}$$

while the bandwidth

$$\frac{k_{zmax}}{k_{zmin}} = \frac{1}{\alpha_{min}} = \sqrt{1 + R_{max}^2} \, . \tag{5.58}$$

So, we can see that the wavenumber coverage has a linear dependency on frequency, while the bandwidth is a function of the offset-to-depth ratio.

The strategy to choose frequencies is defined in a way that each frequency has a limited, finite-band contribution to the image spectrum. In order to recover the target accurately over a broad range of wavenumbers, the continuity of the coverage of the object in the wavenumber domain must be preserved as the imaging frequencies are selected. We choose

$$k_{zmin}(f_{n+1}) = k_{zmax}(f_n) \, , \tag{5.59}$$

where $f_{n+1}$ is the next frequency to be chosen following the frequency $f_n$. In other words, the maximum wavenumber of the smaller frequency must be equal the minimum wavenumber of the larger frequency (Figure 5.3). With the expressions 5.59 and 5.56 in hands, we obtain the following relation

$$f_{n+1} = \frac{f_n}{\alpha_{min}} \, , \tag{5.60}$$

which lead us to a discretization law where the frequency increment $\Delta f_{n+1}$ is given by

$$\Delta f_{n+1} = f_{n+1} - f_n = \left( \frac{1 - \alpha_{min}}{\alpha_{min}} \right) f_n = (1 - \alpha_{min}) \, f_{n+1} \, . \tag{5.61}$$

The equation above shows that the optimum-frequency increment is not constant and has a linear dependency on frequency. This is an interesting result as the commonly used frequency-domain sampling theorem sets the frequency increment to be constant and equal to

$$\Delta f_{st} = \frac{2}{T_{max}} \, , \tag{5.62}$$

where $T_{max}$ is the maximum recorded time.

## 5.9 Methodology

The attentive reader may observe that the flowchart (Figure 1.1) depicted in the Chapter 1 — the focus of this thesis — points out the main stages which constitutes the processing workflow itself, but it does not address (compel) which technique should be used in each of them. For example, the first workflow step “Time migration-velocity-analysis” could consider the MVA by image-wave propagation of

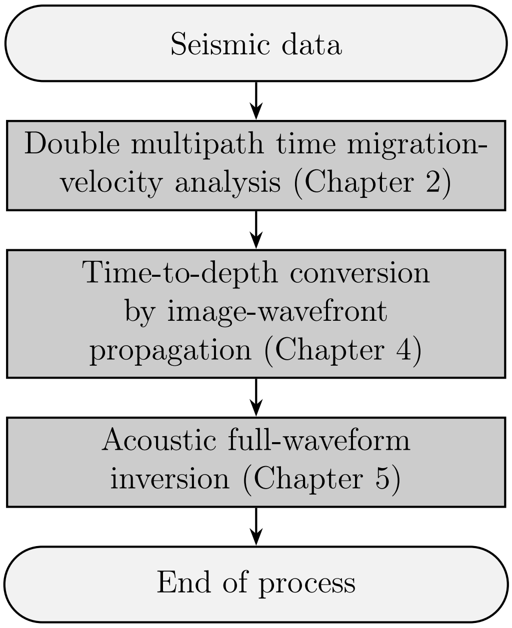

Figure 5.4: Velocity model building flowchart. In addition to the flowchart depicted in Figure 1.1, here we mention the methods used in numerical experiments.

CIGs, or MVA by double multi-stack migration (Chapter 2), or MVA using the remigration trajectories (Chapter 3), or even for any of the techniques we have revisited in Chapters 2 and 3. The same could apply to the second step of the workflow "Time-to-depth conversion" and the strategies discussed in Chapter 4. In this section, we provide a more in-depth description of the workflow for the construction of initial velocity-models for FWT methods. Our workflow (Figure 5.4) for initial-velocity model building and FWT is built upon the following techniques.

### 5.9.1 Step 1: MVA by double multi-stack migration

The workflow starts with the double multipath time migration-velocity analysis of Schleicher and Costa (2009) detailed in Chapter 2. This MVA technique is based on the multipath-summation imaging process of Landa et al. (2006). The fundamental idea of the latter is to stack the migration results for "all possible" velocities, or at least as many models as practically reasonable. Since only "good" models yield flat events in common-image gathers, these will prevail in the overall stacked image, which thus will show the geologic structure without the need for a migration-velocity model. A weighted double stack allows to determine the associated velocity values. Below, we will refer to this technique as multi-stack migration.

### 5.9.2 Step 2: Time-to-depth conversion

With this procedure (Section 5.9.1), we can automatically construct a time-migration velocity model. However, FWI requires an initial model in depth (Section 5.7). Therefore, we need to convert the multi-stack model to depth. For this objective, we chose the time-to-depth conversion of Valente (2013). First performance tests of that conversion procedure were reported by Valente et al. (2014).

The time-to-depth conversion of Valente (2013) is based on the algorithm of the level-set method. It pursues the construction of wavefronts instead of individual image rays. This strategy has the advantage of directly obtaining the velocity field $v(\mathbf{x})$ and the traveltime $\tau(\mathbf{x})$, avoiding to calculate the auxiliary functions $p(\mathbf{x})$ and $q(\mathbf{x})$ like in concurrent schemes (Cameron et al., 2007, 2008; Iversen and Tygel, 2008). By means of a modified fast-marching conversion algorithm, it directly determines the matrix $\gamma(\mathbf{x})$ of image-ray emergence points from the already known values of $v(\mathbf{x})$ and $\tau(\mathbf{x})$. For further details, please see Chapter 4.

### 5.9.3 Step 3: Acoustic full waveform tomography

#### Parallelize or perish

To test whether the so-obtained depth model has sufficient quality for FWI, we used a modified version of the 2D acoustic time-domain FWT code initially implemented by Kurzmann (2012) and Kurzmann et al. (2013). Here, we briefly summarize the underlying concepts already detailed in Sections 5.3 to 5.5. For those readers interested in the program used, we have included a brief description of the software named PROTEUS in Appendix B.2.

**Forward modeling.** The FWT implementation of Kurzmann et al. (2013) solves the homogeneous acoustic wave equation in the time domain by means of a time-domain finite-difference time-stepping method (Alford et al., 1974) with perfectly matched layer (PML) boundary condition (Berenger, 1994) and massive parallelization comprising domain decomposition (Bohlen, 2002) and shot parallelization (Kurzmann et al., 2009). Since most of the computational efforts of time-domain FWT account for seismic modeling — caused by the FD modeling (Section 5.5) —, the distribution of shots on different computers provides a reduction of network traffic and consequently a speedup of the inversion algorithm. Figure 5.5 represents the domain decomposition on a cluster computer which consists of two quad-core computers (nodes). It provides a fast computation of the wavefields but requires a high rate of data exchanges which slows down the entire computation when the network capacity is exceeded. On the other hand, the combination of domain decomposition and shot parallelization (Figure 5.6) provide computational improvements. The drawback is the huge memory consumption which would need the use of HPCs. In Appendix B.1, we present a list of all the computers used for the experiments.

**Inversion.** The objective of the code is the reconstruction of an acoustic velocity model. For simplicity, the density is considered constant and not a subject of the inversion. The solution of the inverse problem is based on the time-domain FWT of Tarantola (1984) and Mora (1987a). It comprises the adjoint method and the conjugate gradient method using a least-squares misfit function. For further details, please refer to Sections 5.4 and 5.5, and Kurzmann et al. (2013).

## 5.10 Numerical experiment I - proof of concepts

To test our initial-model construction, we apply it to one modified version of the original 2D Marmousi-2 model, namely EXPERIMENT I. For comparison and for the sake of completeness, in Appendix F we present the original $v_p$, $v_s$, and $\rho$ of the Marmousi-2 model created by Martin et al. (2002) based on Versteeg (1994).

### 5.10.1 Model description and acquisition geometry

We modified a section of the Marmousi-2 model (Figure 5.7) based on Versteeg (1994) and Martin et al. (2002). The velocities are clipped to the range of 1500 m/s to 4000 m/s to reduce computational efforts. The acquisition geometry simulates a marine streamer geometry with length of 5980 m, consisting of 187 shots and a maximum number of 300 receivers per source. Receiver spacing as 20 m and the nearest offset was 45 m. The source time function is a Ricker wavelet with peak frequency $f_{peak} = 9\,\text{Hz}$ represented by the blue line in Figure 5.8. The model size is 3 km × 10 km which, using a grid spacing of 5 m, resulting in a grid size of 600 × 2000 grid points. We set a PML of 150 m width to avoid artificial boundary reflections in finite-difference modeling. The recording time of the seismic data was 5.6 s with a time discretization of $7 \times 10^{-4}$ s. We chose these parameters to make the conditions for the FWT nearly ideal (please, see the comments of initial and boundary conditions and accuracy and stability in Section 5.5). Table 5.1 summarizes the general setup for the modeling, acquisition, and inversion for the Experiment I.

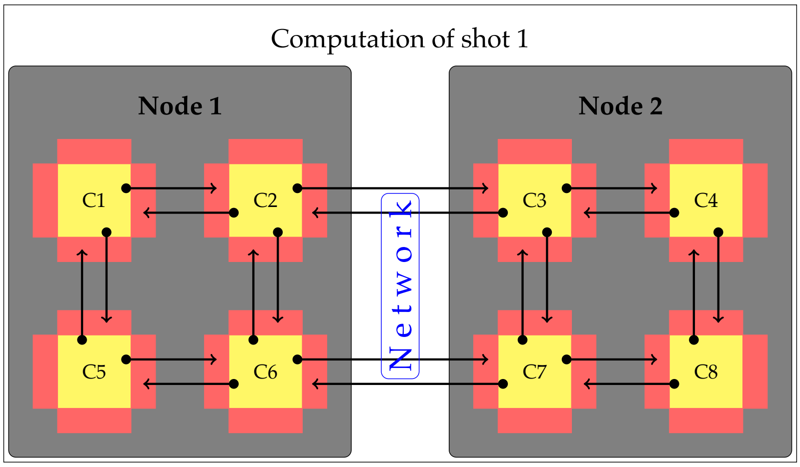

Figure 5.5: Computation of one shot using the domain decomposition, assuming we are using a cluster computer which consists of 2 nodes with 4 cores per node. The model is divided into 8 subdomains (yellow). The corresponding padding layers are colored in red. The exchange of the wavefield requires core communication and node communication(arrows) which is done by MPI (after Kurzmann, 2012).

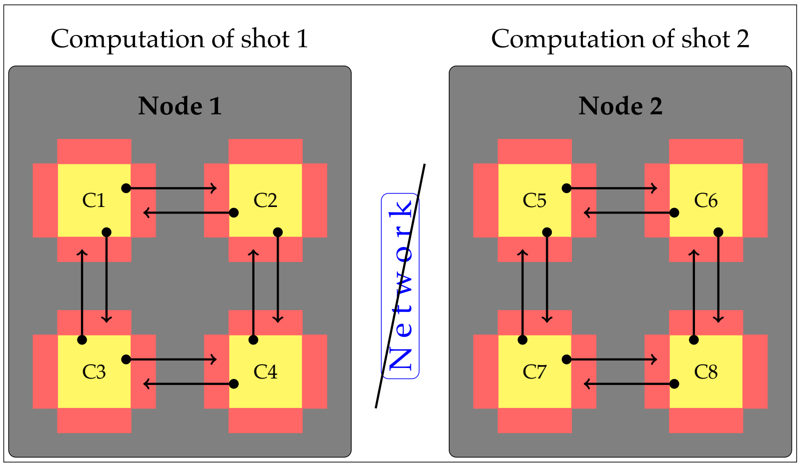

Figure 5.6: Computational of two shots using the shot parallelization on a cluster computer. Assuming the same computer architecture of Figure 5.5, we can compute each shot in one node, and use the domain decomposition internally for each node dividing the shot in 4 subdomains. The exchange of the wavefield at the model boundaries is then reduced to intra-node communication done with MPI (after Kurzmann, 2012).

### 5.10.2 Initial velocity models

To decrease the computational time for the migration velocity analysis, and to work under more realistic conditions, we resampled the seismic data to 4 ms and windowed the offsets processing only half of them. From these data we extracted a time-migration velocity model using the double multi-stack MVA with velocities between 1400 m/s and 4200 m/s at every 100 m/s. Based on the results presented in Chapter 2 and on the discussion in Appendix E, a B-spline interpolation with strong regularization Appendix C was used to construct a smoothed velocity model. The resulting model is depicted in Figure 5.10. It is important to note that the time-migration velocity model is less then perfect for a subsequent time migration (see Figure 5.11). This is to be expected because the central region of the Marmousi model has to strong lateral variations for a time migration to work.

We then converted the velocity model to depth using image-ray wavefronts as described above. To avoid the presence of possible artifacts created during the conversion step, we smoothed the depth-domain velocity model by one pass of a moving average with a 500 m × 500 m (100 by 100 points) window. The so-obtained model is depicted in Figure 5.12d.

For our evaluation, we compare the results of FWT with different initial velocity models. Figure 5.12a depicts a smooth initial velocity model, generated by application of a 2D Gaussian filter (size 1250 m × 1250 m, $\sigma$=51) to the sub-seafloor area of the true velocity model (Figure 5.7). This is the same P-wave velocity model used by Kurzmann et al. (2013) in their sensitivity analysis of attenuation. Our other FWT tests used a constant velocity of 3 km/s (Figure 5.12b) or a constant gradient below the see floor which ranges from 1.6 km/s on the upper part to 4 km/s on the bottom (Figure 5.12c).

### 5.10.3 Practical aspects and inversion workflow

As Kurzmann et al. (2013), we have considered 32 shots to perform the inversion (Figure 5.9b). Also, we set up a specific workflow, summarized in Table 5.2. The first column of the table shows how many steps the FWI workflow has. In other words, the first column is the number of rows that the table has. The second column of the table presents the number of iterations a row of the input file should be applied to. In case of using a stop criterion, this number is the minimum number of iterations per input line. The third column gives the threshold value — relative change of the misfit over three iterations (Sections 5.5 and 5.6) — used to switch to the next line automatically. Two conditions have to be fulfilled: (1) the number of iterations in the second column has to be completed and (2) the stop criterion in column three. Column four shows the total time (or the time-window if minimum and maximum values are specified) which will be taken into account. Similarly, column five shows offset-windowing. Finally, column six show the frequencies numbers to be considered to apply the time-domain filtering. This workflow is one of many possible approaches when we plan a multi-scale inversion strategy (Section 5.8). Different strategies will be explored in the future (Section 5.11).

All modeling and inversion tests showed here were performed with a 2D acoustic FWI tool developed by Kurzmann et al. (2013) (Section 5.9.3). The parallelization process is based on domain decomposition where the model is decomposed in subgrids (e.g., Bohlen, 2002) (Figure 5.5). Moreover, the acoustic code has a shot parallelization implemented (Figure 5.6). The distribution of shots on different computers provides a reduction of network traffic and consequently a speedup of inversion algorithm (Kurzmann et al., 2009).

### 5.10.4 FWT results

We then executed the FWT code on the original undecimated (i.e., almost ideal) data using the starting models of Figure 5.12. For better evaluation, we saved intermediate FWT processing results after 100 and 200 iterations of the inversion process. Figures 5.13 and 5.14 depict the recovered velocity models and their differences to the true one after 100 iterations, and Figures 5.15 and 5.16 show the corresponding results after 200 iterations. The final inverted models, after the FWT code reached convergence at the end of the workflow (Table 5.2), are shown in Figure 5.17 and their differences to the true one in Figure 5.18.

We see that the results using the depth-converted multi-stack model are comparable in quality to the ones obtained with the smoothed model or the true vertical gradient and clearly superior to the ones obtained with the constant starting model. Except for the boundary region, where the data are insufficient, the model inverted when starting at the converted time model is, at some places, even superior to the one obtained from the true vertical gradient and reaches the same quality as the one obtained from the smoothed model (compare difference images in Figure 5.18).

Table 5.1: Experiment I. General setup for the modeling, acquisition, and inversion for the modified version of the Marmousi-2 model.

| | **Attributes** | **Experiment I** |
|---|---|---|
| Model | Figure | 5.7 |
| | Size (lateral x depth) | 10 km x 3 km |
| | Average Vp | 2479.3 m/s |
| | Minimum Vp | 1500 m/s |
| | Maximum Vp | 4000 m/s |
| | Water layer thickness | 460 m |
| | Density (constant) | 2260 kg/m$^3$ |
| Acquisition geometry | Location | on top of half-space, sea surface |
| | Configuration | marine reflection geometry |
| | Number of shots | 187 |
| | Shot spacing | 20 m |
| | Shot depth | 5 m |
| | Max. no. of hydrophones | 300 (in a streamer) |
| | Hydrophone spacing | 20 m |
| | Hydrophone depth | 5 m |
| | Minimum offset | 45 m |
| | Maximum offset | 5980 m |
| Modeling parameters | Grid size | 2000 x 600 |
| | Grid spacing | 5 m |
| | Time sampling | 7e-4 s |
| | Number of time samples | 8000 |
| | Recording time | 5.6 s |
| | Source wavelet | Ricker |
| | Peak frequency | 9 Hz |
| | Time delay | 0.45 s |
| | PML boundary | 150 m (free surface) |
| General inversion parameters | Initial models | Figure 5.12 |
| | Preconditioning | wave-field based<br>user-defined: water layer is known |
| | Model update | hard constraint: Vp limit [1500, 4000] m/s<br>max. deviation from the initial model: 50% |

Table 5.2: Time-domain FWI workflow.

| # | **Iterations** | **Threshold** | **Time (s)** | **Offset (m)** | **Frequency (Hz)** |
|---|---|---|---|---|---|
| 1 | 15 | 0.005 | 5.6 | 45 - 5980 | 0.5 - 4 |
| 2 | 15 | 0.005 | 5.6 | 45 - 5980 | 1 - 6 |
| 3 | 15 | 0.005 | 5.6 | 45 - 5980 | 3 - 9 |
| 4 | 15 | 0.005 | 5.6 | 45 - 5980 | 5 - 15 |
| 5 | 200 | 0.005 | 5.6 | 45 - 5980 | full content |

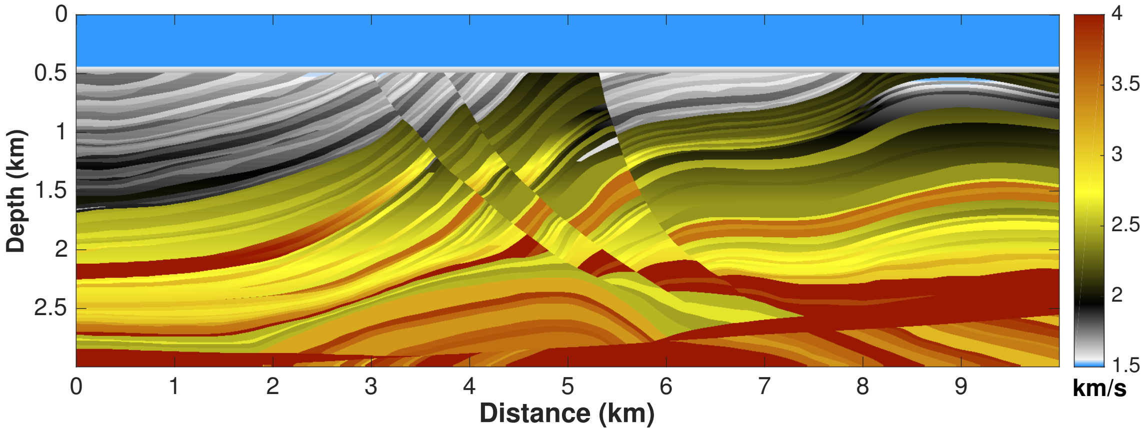

Figure 5.7: True velocity of the modified Marmousi-2 model.

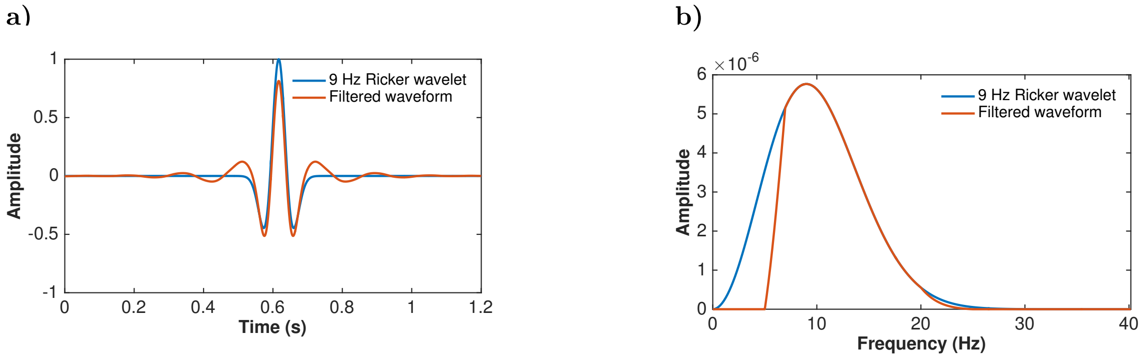

Figure 5.8: Ricker source wavelet and its spectrum. Original Ricker wavelet waveform with the central frequency of 9 Hz (blue line) and the wavelet after applying the band-pass filter with a cut-off frequency of 5 Hz (orange line). (a) Time domain representation, (b) amplitude spectrum.

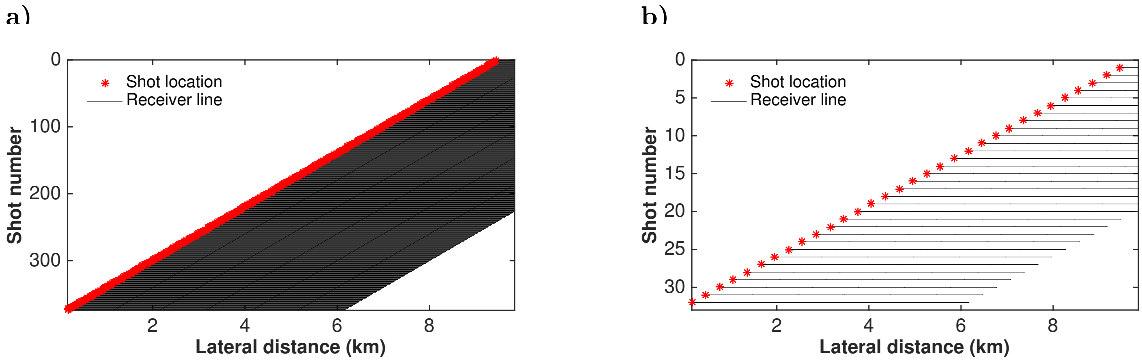

Figure 5.9: Marine streamer acquisition geometry with a maximum number of 300 hydrophones per receiver line: (a) 25 m shot spacing (373 shots), (b) 300 m shot spacing (32 shots). Red stars denote shot location and points represent hydrophones.

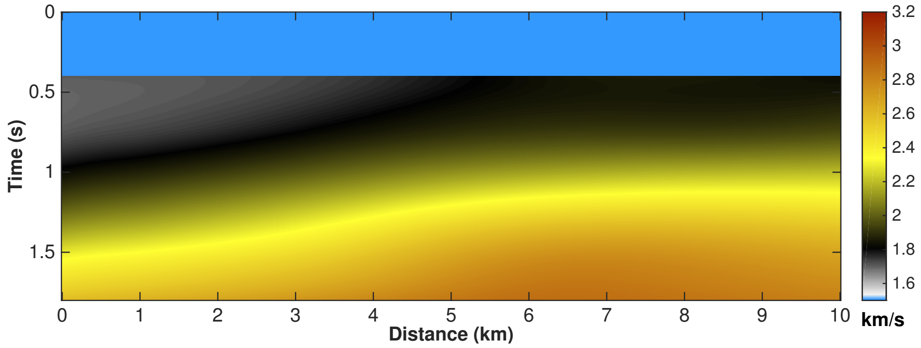

Figure 5.10: Time-migration velocity model obtained by the multi-stack MVA with strong regularization.

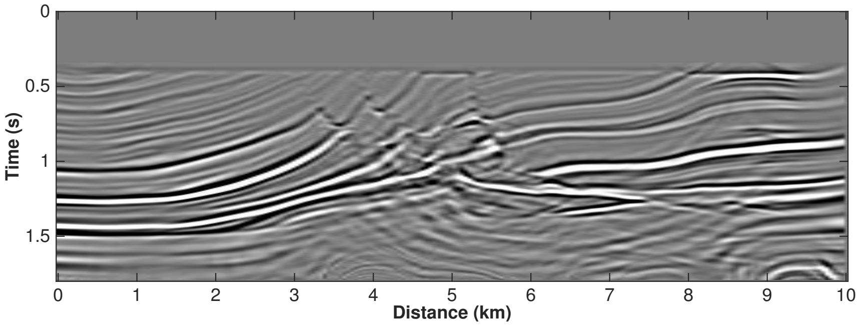

Figure 5.11: Time migrated image with the model obtained by the multi-stack MVA with strong regularization.

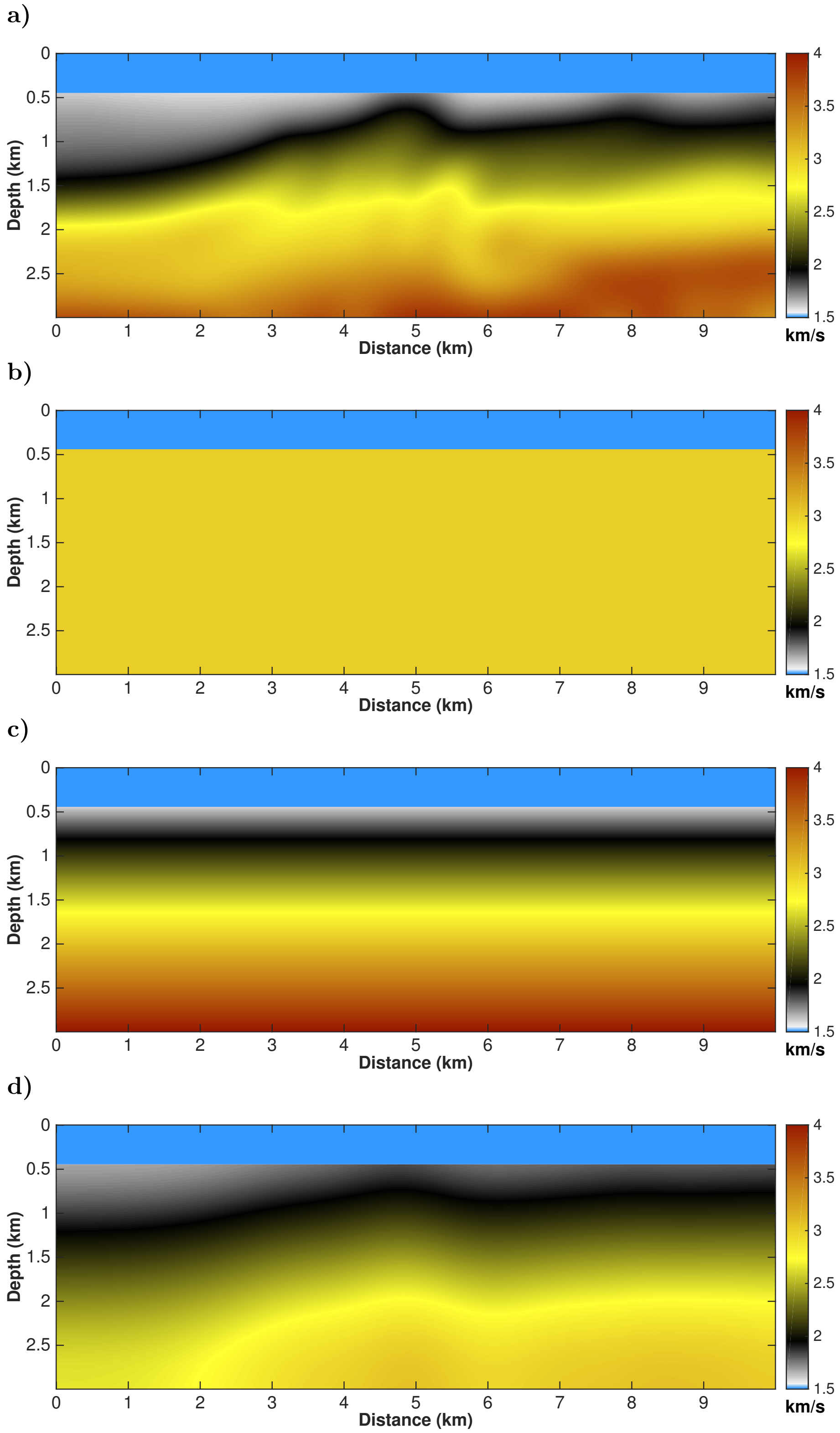

Figure 5.12: Initial models: (a) smoothed version obtained after low-pass filtering of the true model (Figure 5.7); (b) homogeneous velocity model ($v = 3\,\mathrm{km/s}$); (c) constant vertical gradient; (d) velocity model obtained by the double multi-stack MVA converted from time-to-depth using the image-wavefront propagation.

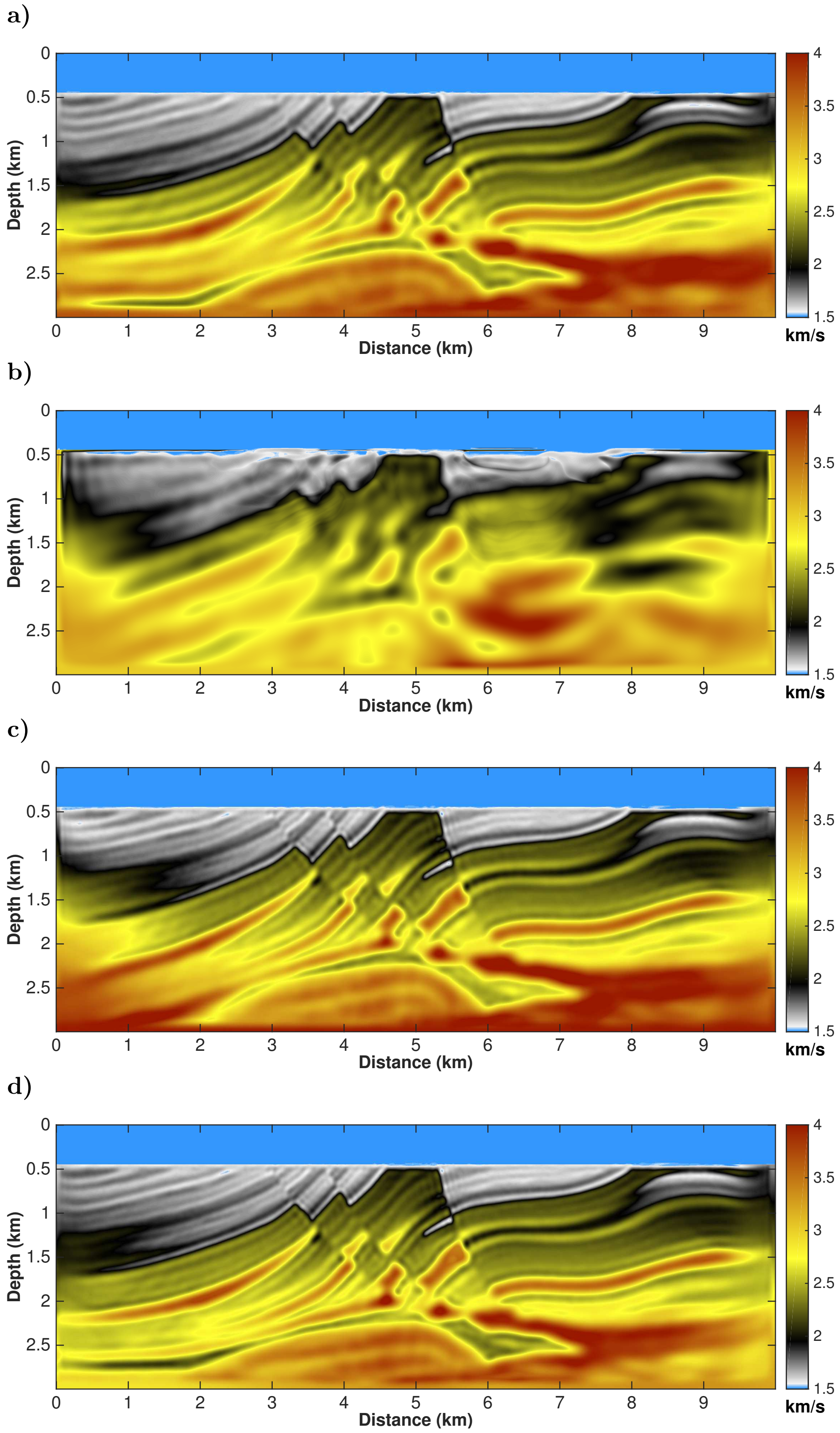

Figure 5.13: (a) to (d) show the recovered velocity models after 100 iterations for the acoustic FWI starting with the velocity model in Figure 5.12.

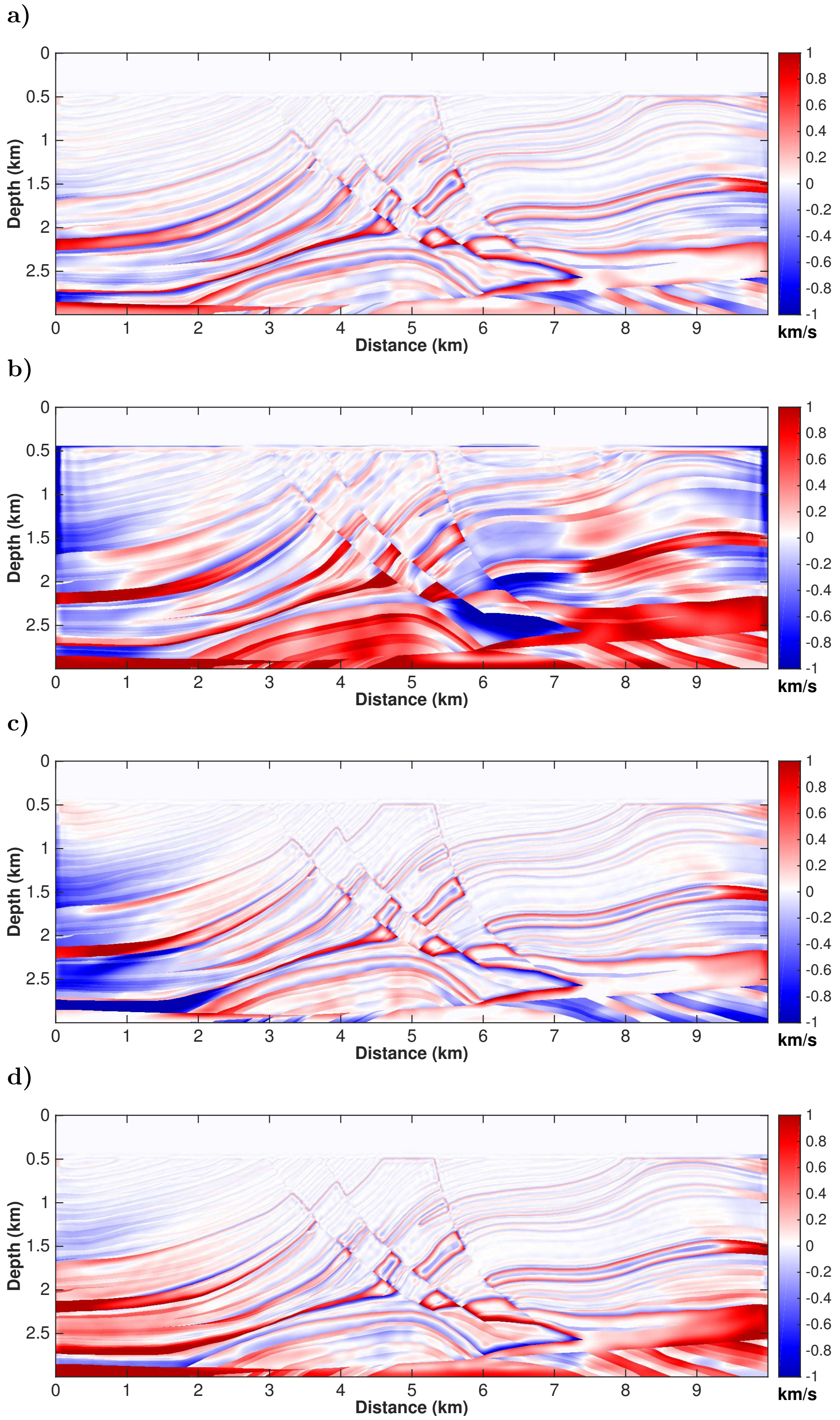

Figure 5.14: (a) to (d) show the difference of the results in Figure 5.13 with respect to the true model in Figure 5.7.

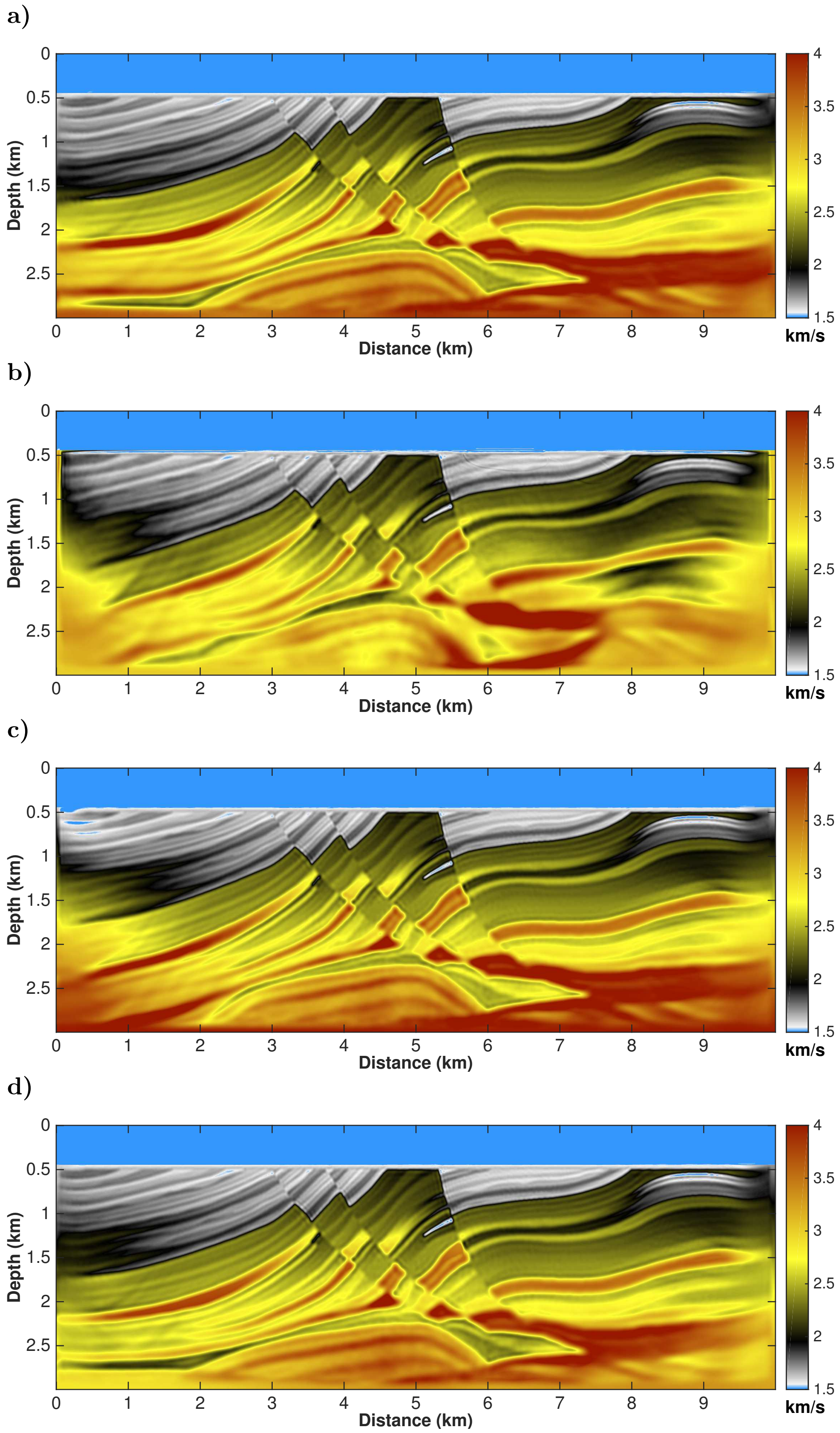

Figure 5.15: (a) to (d) show the recovered velocity models after 200 iterations for the acoustic FWI starting with the velocity model in Figure 5.12.

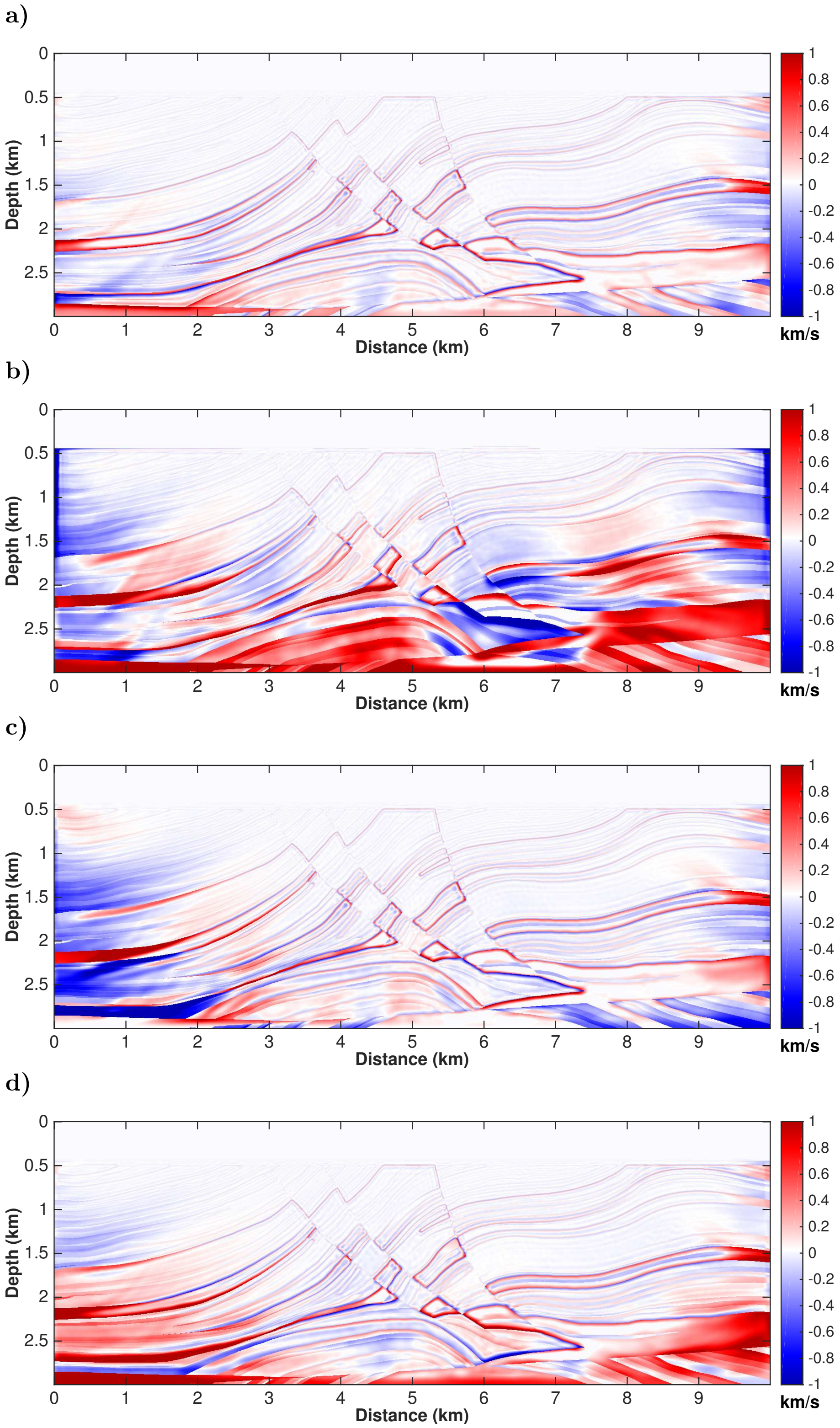

Figure 5.16: (a) to (d) show the difference of the results in Figure 5.15 with respect to the true model in Figure 5.7.

**a) 363 iterations (40353 seconds)**

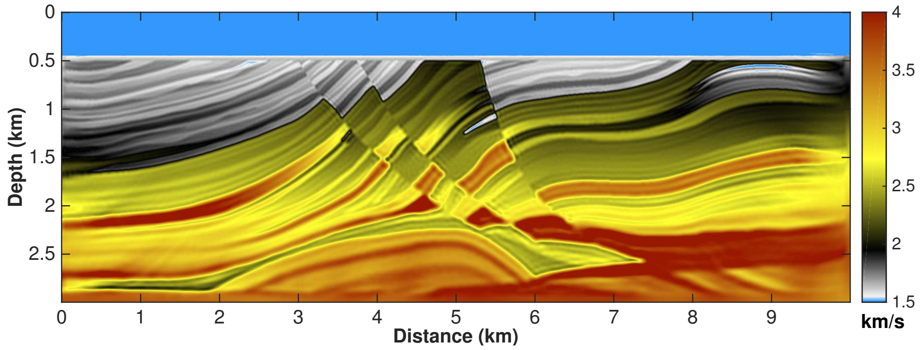

**b) 377 iterations (41726 seconds)**

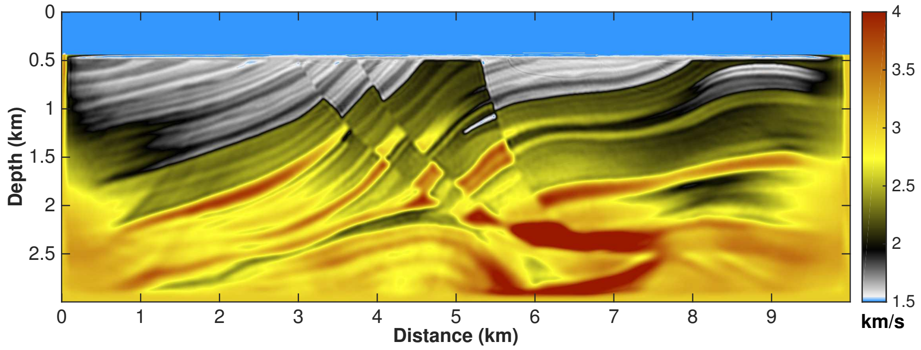

**c) 330 iterations (38485 seconds)**

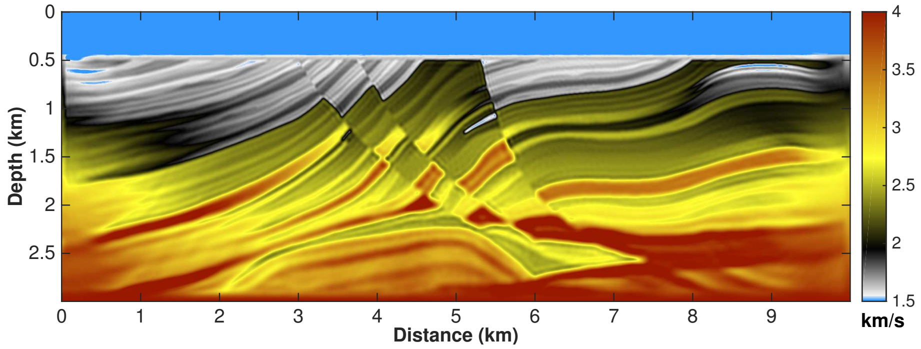

**d) 329 iterations (36081 seconds)**

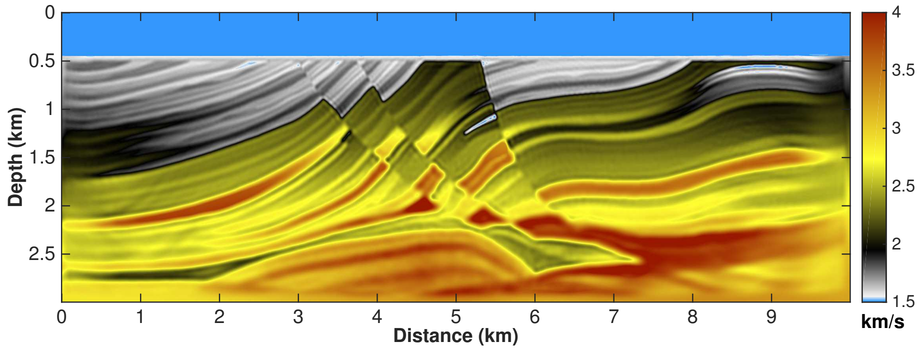

Figure 5.17: (a) to (d) show the recovered velocity models when they complete the inversion workflow for the acoustic FWI starting with the velocity model in Figure 5.12. The individual amount of required iterations differs from each other.

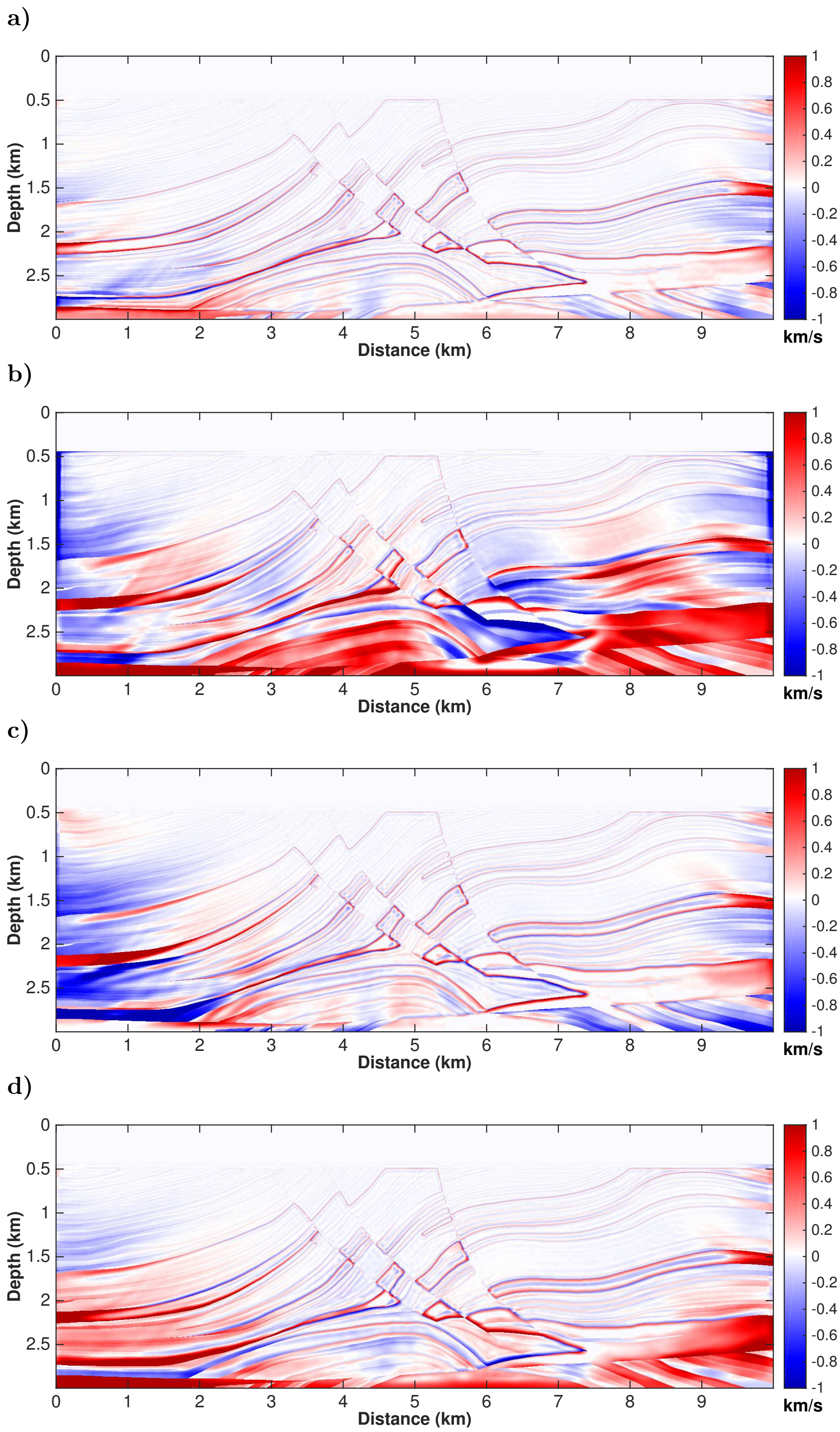

Figure 5.18: (a) to (d) show the difference of the results in Figure 5.17 with respect to the true model in Figure 5.7.

## 5.11 Numerical experiment II

### 5.11.1 Model description and acquisition geometry

Encouraged by the numerical results on Experiment I (Section 5.10), we set out for a more realistic test, namely EXPERIMENT II. Here, the data was modeled and preprocessed similarly to the previous experiment, using the modified version of the Marmousi-2 model (Figure 5.7). To clarify the differences between the two tests, Table 5.3 summarizes the general setup for the modeling, acquisition, and inversion for Experiment II. In the modeling, the main differences between the two experiments are in the number of shots and the frequency content of the source wavelet. The acquisition geometry simulates a marine streamer geometry with the length of 5980 m, consisting of 373 shots and a maximum number of 300 receivers per source (Figure 5.9a). Receiver spacing as 20 m and the nearest offset was 45 m. The source time function is a Ricker wavelet waveform with the peak frequency of $f_{peak} = 9\,\mathrm{Hz}$. It is known that seismic data are generally missing information below 5 Hz. To simulate the actual situation, we applied a band-pass filter with a cut-off frequency of 5 Hz (the corner frequencies of the band-pass filtering were 5 Hz, 7 Hz, 20 Hz, and 25 Hz; and on both ends, no taper was applied). The orange line in Figure 5.8 represents the filtered waveform and its spectrum. The purpose of using this wavelet is to eliminate unrealistic low frequencies in the data. From Figure 5.8, we can see that the filtering step produced “fake peaks” in the waveform (compare the orange line with the blue one), which contributes to the nonlinearity of the inversion.

### 5.11.2 Initial velocity models

We then contaminate those data with white random noise at a level of 30% of the maximum amplitude. To decrease the computational time for the migration velocity analysis, and to work under more realistic conditions, we resampled the seismic data to 4 ms and limited the maximum of time in 3.6 s. From these data, we extracted a time-migration velocity model using the double multi-stack MVA with velocities between 1400 m/s and 2500 m/s at every 25 m/s. B-spline interpolation with strong regularization Appendix C was used to construct a smoothed velocity model. We then converted the velocity model to depth using image-ray wavefronts, smoothed it by 100 passes of a moving average with a 50 m × 50 m (10 by 10 points) window, and fixed the water layer (1500 m/s). Figure 5.19d shows the resulting velocity model that is quite similar to a constant vertical gradient.

For our evaluation, we compare the results of FWT with different initial velocity models previously described in Section 5.10.2 and shown once again in Figures 5.19a to 5.19c to facilitate the comparison of the images.

### 5.11.3 Inversion tests

It is known that low-frequency information is vital for making the FWT more stable and for recovering the macrostructure of velocity models, as well as, the quality of the initial velocity model used in the inversion is imperative to decrease computation time. It is also known that FWT can benefit depending on the strategy chosen to carry it out (Section 5.8). The previous experiment (Section 5.10) has shown us that, at least under almost ideal conditions, our approach can provide an initial velocity model which is sufficient to perform the inversion. Here, the primary objective is to evaluate if our method can reconstruct the low frequency for seismic data without energy below 5 Hz.

We have proceeded in a similar way to that of Experiment I, therefore, the reader is referred to Section 5.10.3 for similar comments concerning the practical aspects of the FWT application. We have considered 32 shots to perform the FWT (Figure 5.9b). Because inversion is an expensive procedure, we started with a one-step workflow which limits the maximum number of iterations in the FWT to 100 (Tests 1 and 2 and Table 5.4). To evaluate our velocity model building workflow more deeply, we perform different inversion tests that are decomposed into multiple stages to reduce the non-linearity of the inverse problem and to mitigate the cycle-skipping phenomenon. Tables 5.4 to 5.8 summarizes all these tests.

We can subdivide our tests according to the source signature applied and the maximum offset of the data to be considered in the inversion. In Tests 1 and 3, the source signature is a Ricker wavelet with a central frequency of 9 Hz (blue line in Figure 5.8), and no frequency filtering is applied. Tests 2 and 4 to 7, however, consider a band-passed Ricker wavelet waveform with the central frequency of 9 Hz with a cut-off frequency of 5 Hz (orange line in Figure 5.8). Tests 1 to 4 and 7 use the full-offset of the data while in Tests 5 and 6 an offset windowing limited the maximum offset to 3 km, approximately the half of the full-offset.

We then executed the FWT code on the data using the starting models of Figure 5.19. Figure 5.20 to 5.33 depict the final inverted models and their corresponding differences to the true one (Figure 5.7) obtained from Test 1 to Test 7 respectively and detailed in the following.

**Test 1** considers the original Ricker wavelet waveform with the central frequency of 9 Hz (blue line in Figure 5.8), the maximum number of iterations is 100, the threshold value is 0.005, and no filtering or windowing is applied. Figures 5.20 and 5.21 depict the recovered velocity models and their differences to the true one (Figure 5.7) after the FWT code reached convergence at the end of the workflow (Table 5.4).

**Test 2** considers a band-passed Ricker wavelet waveform with the central frequency of 9 Hz with a cut-off frequency of 5 Hz (orange line in Figure 5.8), the maximum number of iterations is 100, the threshold value is 0.005, and no filtering or windowing is applied Figures 5.22 and 5.23 depict the recovered velocity models and their differences to the true one (Figure 5.7) after the FWT code reached convergence at the end of the workflow (Table 5.4).

**Test 3** considers the original Ricker wavelet waveform with the central frequency of 9 Hz (blue line in Figure 5.8), and no filtering or windowing is applied. Figures 5.24 and 5.25 depict the recovered velocity models and their differences to the true one (Figure 5.7) after the FWT code reached convergence at the end of the workflow (Table 5.5). It is the same workflow used in Experiment I.

**Test 4** considers a band-passed Ricker wavelet waveform with the central frequency of 9 Hz with a cut-off frequency of 5 Hz (orange line in Figure 5.8). Figures 5.26 and 5.27 depict the recovered velocity models and their differences to the true one (Figure 5.7) after the FWT code reached convergence at the end of the workflow (Table 5.5). It is the same workflow used in Experiment I.

**Test 5** considers a band-passed Ricker wavelet waveform with the central frequency of 9 Hz with a cut-off frequency of 5 Hz (orange line in Figure 5.8), with a maximum offset of 3 km (approximately the half of the full-offset). Figures 5.28 and 5.29 depict the recovered velocity models and their differences to the true one (Figure 5.7) after the FWT code reached convergence at the end of the workflow (Table 5.6).

**Test 6** considers a band-passed Ricker wavelet waveform with the central frequency of 9 Hz with a cut-off frequency of 5 Hz (orange line in Figure 5.8), with a maximum offset of 3 km (approximately the half of the full-offset). Figures 5.30 and 5.31 depict the recovered velocity models and their differences to the true one (Figure 5.7) after the FWT code reached convergence at the end of the workflow (Table 5.7).

**Test 7** considers a band-passed Ricker wavelet waveform with the central frequency of 9 Hz with a cut-off frequency of 5 Hz (orange line in Figure 5.8), Figures 5.32 and 5.33 depict the recovered velocity models and their differences to the true one (Figure 5.7) after the FWT code reached convergence at the end of the workflow (Table 5.8).

While in Experiment I all the initial velocity models were able to recover the desired $v_p$ model, in Experiment II only the smoothed model (Figure 5.19a) produced satisfactory results for all tests. As expected, the constant starting model (Figure 5.19b) is unable to invert $v_p$. Test 3 is an exception because it allows the low-frequency information in data, source signature, and in the frequency-filtering band, therefore is an ideal scenario (similar to FWT of Experiment I).

Numerous possibilities of workflow schemes can be considered. In Tests 6 and 7, we apply the multi-scale approaches shown in Tables 5.7 and 5.8 in order to reduce the non-linearity of the inverse problem, and through comparison, illustrate the effect of the starting frequency band. The maximum frequency for each frequency band was calculated using equation 5.60 (please, see Section 5.8). The depth to the target ($z = 3000\,\mathrm{m}$) is the maximum depth of the model and the maximum half-offset $h_{max} = 3012.5\,\mathrm{m}$, which results in $\alpha_{min} \approx 0.70$. The frequency bands are applied sequentially with the following maximum frequencies $f_{peak} = (5.0, 7.1, 10.0)$Hz in Test 6, and $f_{peak} = (3.0, 4.3, 6.0, 8.5)$Hz in Test 7. By application of low-pass filters, the inversion is performed moving from low to high frequencies. Moreover, the peak frequencies of low-pass-filtered data are not equidistantly spaced, as suggested by Sirgue and Pratt (2004).

Although still inferior, we see that the results using the depth-converted multi-stack model (Figure 5.19d) are comparable in quality to the ones obtained with the true vertical gradient (Figure 5.19c). Both models seem to benefit on the multi-scale inversion strategy, mitigating the ambiguity of the inverse problem especially by taking advantage of the frequency-filtering method within the scope of the workflow implementation.

Table 5.3: EXPERIMENT II. General setup for the modeling, acquisition, and inversion for the modified version of the Marmousi-2 model.

| | **Attributes** | **Experiment II** |
|---|---|---|
| Model | Figure | 5.7 |
| | Size (lateral x depth) | 10 km x 3 km |
| | Average Vp | 2479.3 m/s |
| | Minimum Vp | 1500 m/s |
| | Maximum Vp | 4000 m/s |
| | Water layer thickness | 460 m |
| | Density (constant) | 2260 kg/m$^3$ |
| Acquisition geometry | Location | on top of half-space, sea surface |
| | Configuration | marine reflection geometry |
| | Number of shots | 373 |
| | Shot spacing | 25 m |
| | Shot depth | 5 m |
| | Max. no. of hydrophones | 300 (in a streamer) |
| | Hydrophone spacing | 20 m |
| | Hydrophone depth | 5 m |
| | Minimum offset | 45 m |
| | Maximum offset | 5980 m |
| Modeling parameters | Grid size | 2000 x 600 |
| | Grid spacing | 5 m |
| | Time sampling | 7e-4 s |
| | Number of time samples | 8000 |
| | Recording time | 5.6 s |
| | Source wavelet | Ricker |
| | Peak frequency | 9 Hz |
| | Time delay | 0.45 s |
| | PML boundary | 150 m (free surface) |
| General inversion parameters | Initial models | Figure 5.12 |
| | Preconditioning | wave-field based<br>user-defined: water layer is known |
| | Model update | hard constraint: Vp limit [1500, 4000] m/s<br>max. deviation from the initial model: 50% |

Table 5.4: Time-domain FWI workflow of Tests 1 and 2.

| # | **Iterations** | **Threshold** | **Time (s)** | **Offset (m)** | **Frequency (Hz)** |
|---|---|---|---|---|---|
| 1 | 100 | 0.0050 | 5.6 | 45 - 5980 | full content |

Table 5.5: Time-domain FWI workflow of Tests 3 and 4.

| # | **Iterations** | **Threshold** | **Time (s)** | **Offset (m)** | **Frequency (Hz)** |
|---|---|---|---|---|---|
| 1 | 15 | 0.005 | 5.6 | 45 - 5980 | 0.5 - 4 |
| 2 | 15 | 0.005 | 5.6 | 45 - 5980 | 1 - 6 |
| 3 | 15 | 0.005 | 5.6 | 45 - 5980 | 3 - 9 |
| 4 | 15 | 0.005 | 5.6 | 45 - 5980 | 5 - 15 |
| 5 | 200 | 0.005 | 5.6 | 45 - 5980 | full content |

Table 5.6: Time-domain FWI workflow of Test 5.

| # | **Iterations** | **Threshold** | **Time (s)** | **Offset (m)** | **Frequency (Hz)** |
|---|---|---|---|---|---|
| 1 | 15 | 0.005 | 5.6 | 45 - 3000 | 0.5 - 4 |
| 2 | 15 | 0.005 | 5.6 | 45 - 3000 | 1 - 6 |
| 3 | 15 | 0.005 | 5.6 | 45 - 3000 | 3 - 9 |
| 4 | 15 | 0.005 | 5.6 | 45 - 3000 | 5 - 15 |
| 5 | 200 | 0.005 | 5.6 | 45 - 3000 | full content |

Table 5.7: Time-domain FWI workflow of Test 6.

| # | **Iterations** | **Threshold** | **Time (s)** | **Offset (m)** | **Frequency (Hz)** |
|---|---|---|---|---|---|
| 1 | 15 | 0.005 | 5.6 | 45 - 3000 | 5 - 11 |
| 2 | 15 | 0.005 | 5.6 | 45 - 3000 | 7.1 - 15 |
| 3 | 15 | 0.005 | 5.6 | 45 - 3000 | 10 - 20 |
| 4 | 200 | 0.005 | 5.6 | 45 - 3000 | full content |

Table 5.8: Time-domain FWI workflow of Test 7.

| # | **Iterations** | **Threshold** | **Time (s)** | **Offset (m)** | **Frequency (Hz)** |
|---|---|---|---|---|---|
| 1 | 15 | 0.005 | 5.6 | 45 - 5980 | 3 - 7 |
| 2 | 15 | 0.005 | 5.6 | 45 - 5980 | 4.3 - 9.5 |
| 3 | 15 | 0.005 | 5.6 | 45 - 5980 | 6 - 13 |
| 4 | 15 | 0.005 | 5.6 | 45 - 5980 | 8.5 - 18 |
| 5 | 200 | 0.005 | 5.6 | 45 - 5980 | full content |

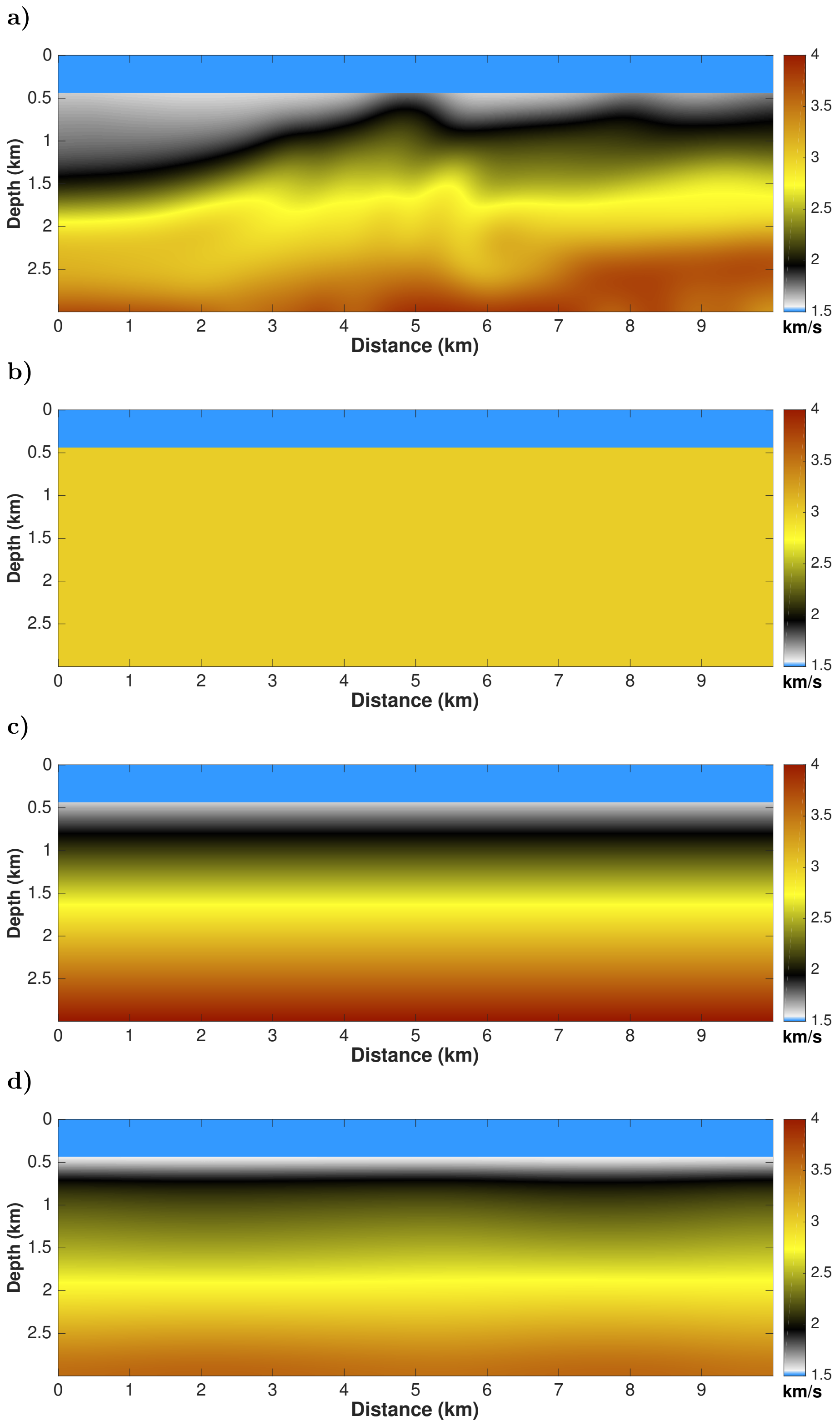

Figure 5.19: Initial models: (a) smoothed version obtained after low-pass filtering of the true model (Figure 5.7); (b) homogeneous velocity model ($v = 3\,\text{km/s}$); (c) constant vertical gradient; (d) velocity model obtained by the double multi-stack MVA converted from time-to-depth using the image-wavefront propagation.

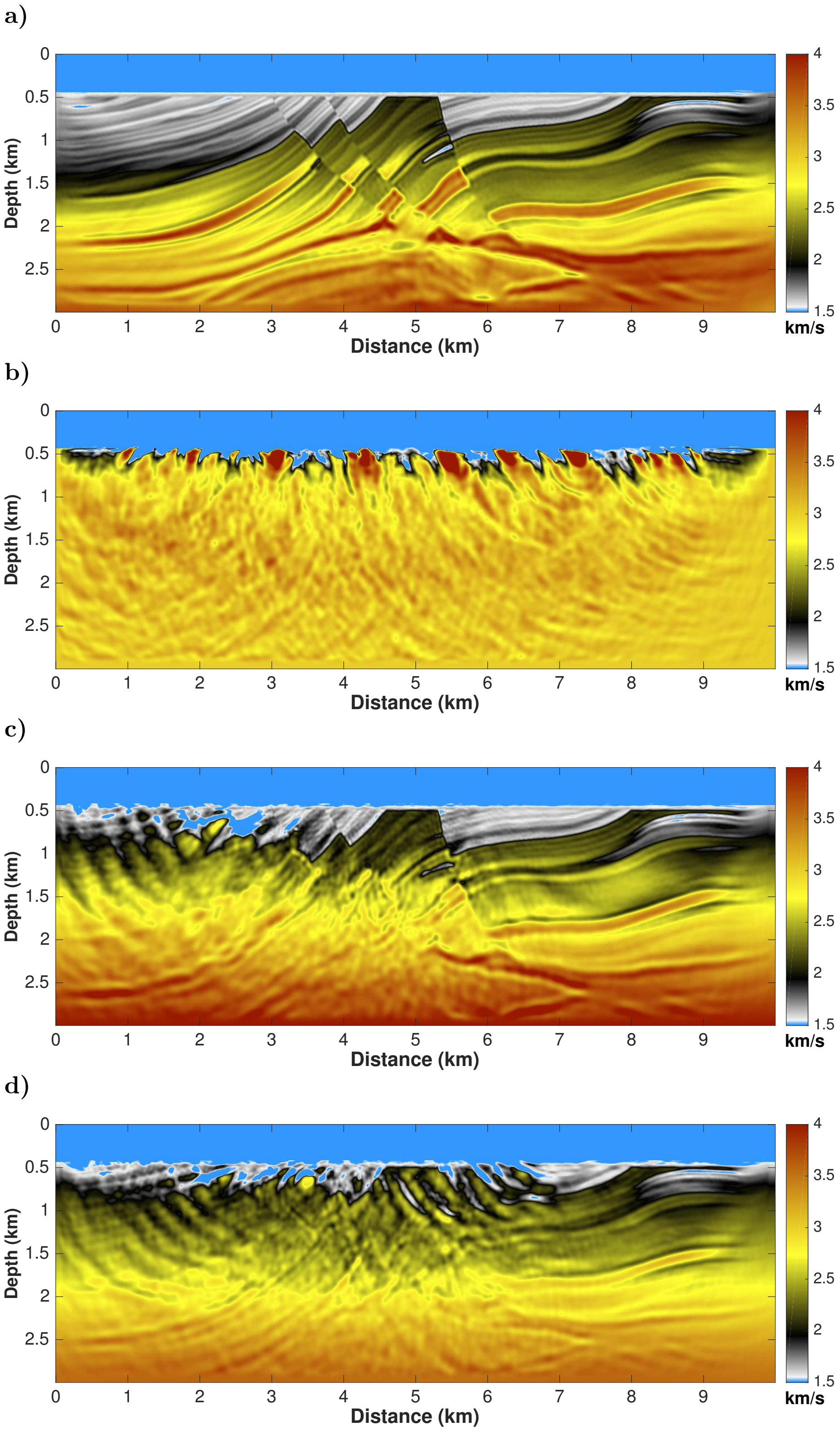

Figure 5.20: Test 1. Recovered velocity models from the initial models in Figure 5.19.

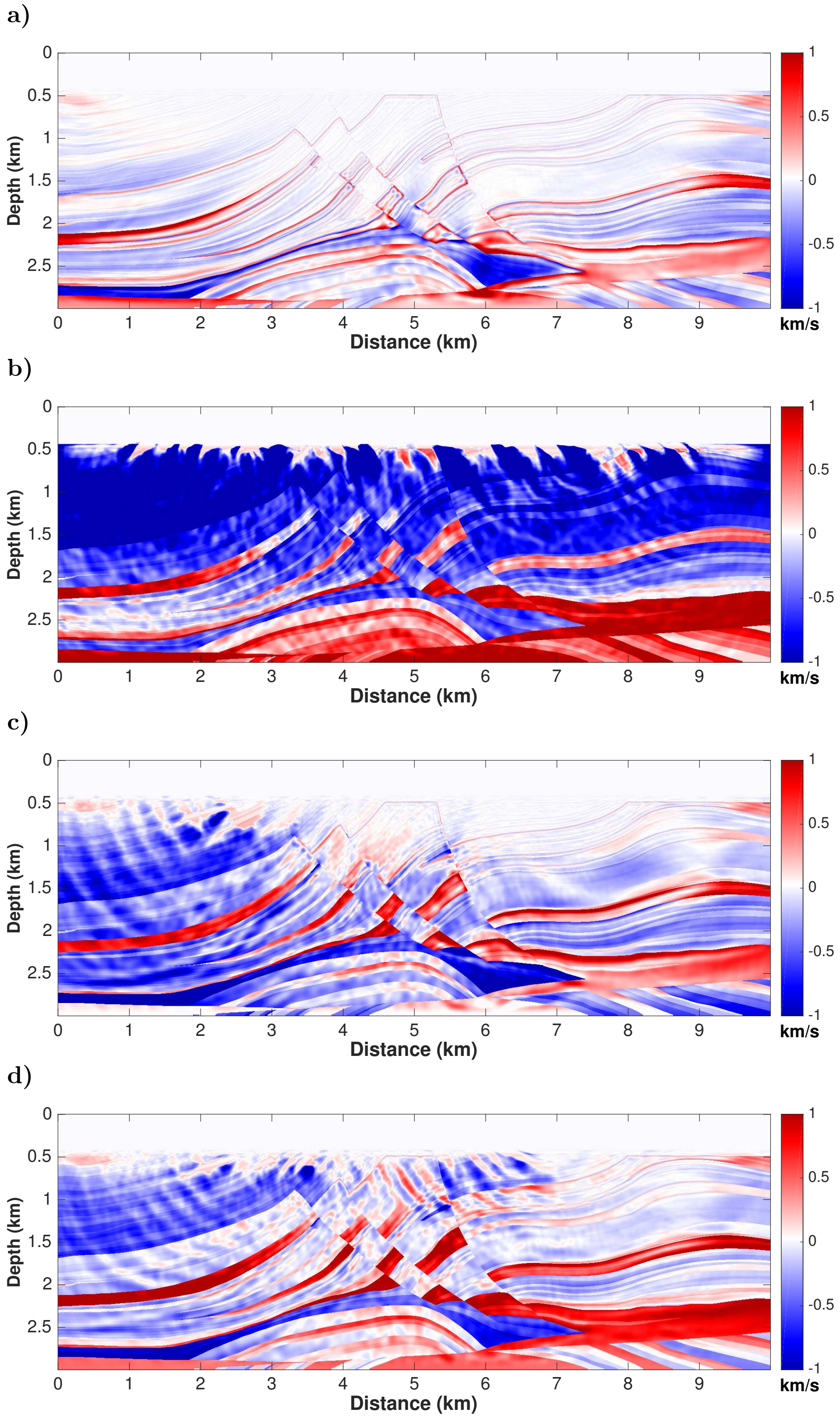

Figure 5.21: Test 1. Differences of the results in Figure 5.20 to the true model in Figure 5.19.

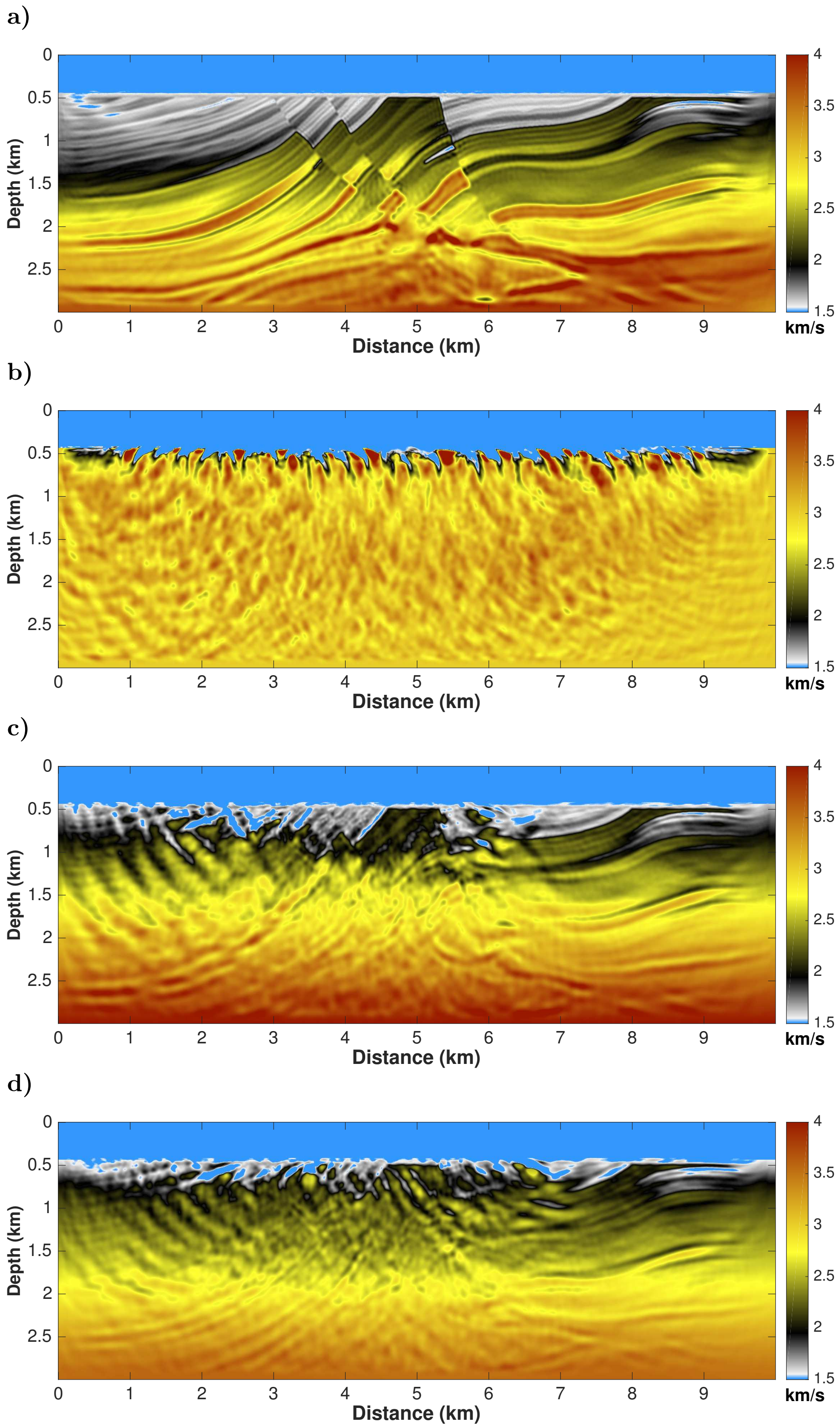

Figure 5.22: Test 2. Recovered velocity models from the initial models in Figure 5.19.

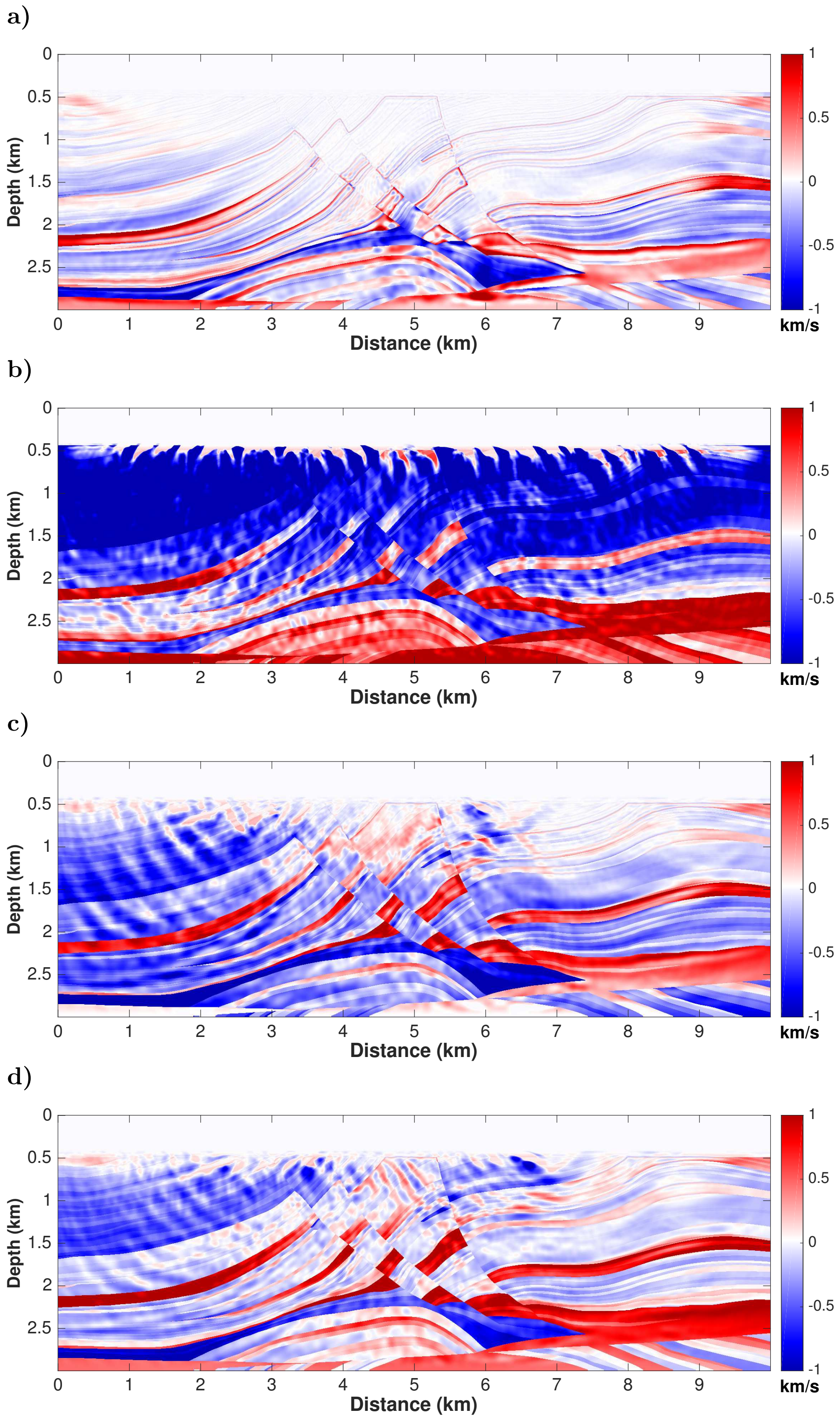

Figure 5.23: Test 2. Differences of the results in Figure 5.22 to the true model in Figure 5.19.

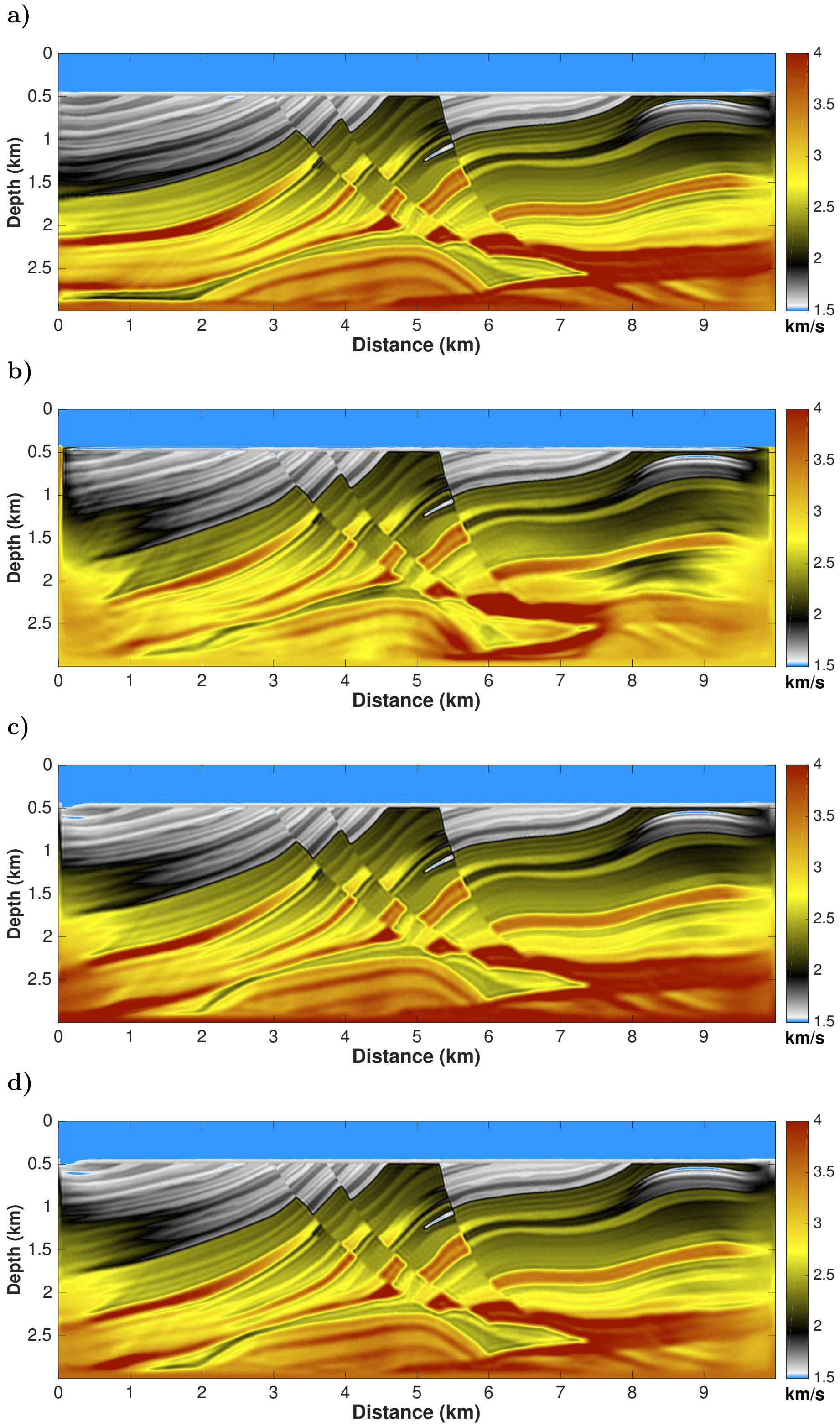

Figure 5.24: Test 3. Recovered velocity models from the initial models in Figure 5.19.

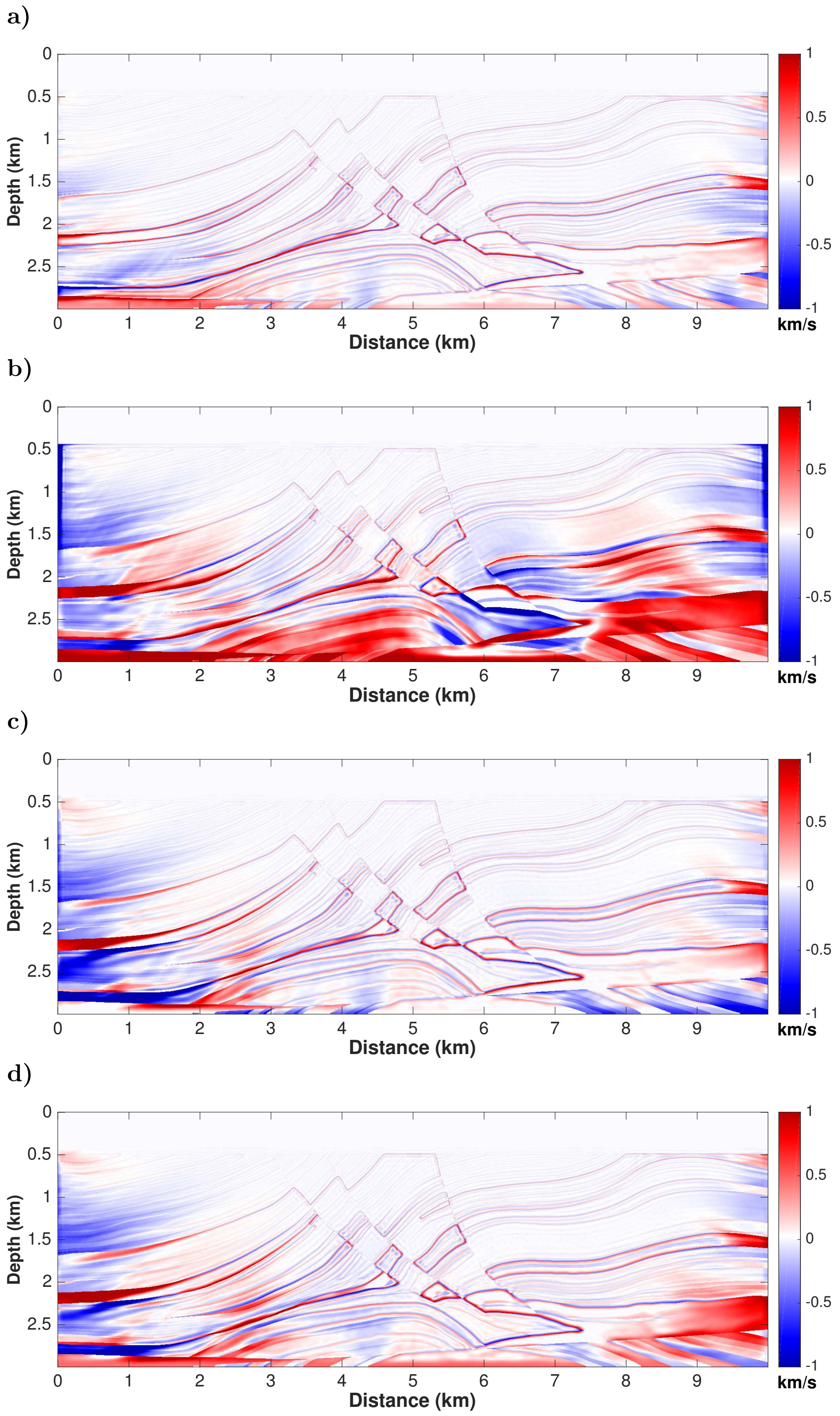

Figure 5.25: Test 3. Differences of the results in Figure 5.24 to the true model in Figure 5.19.

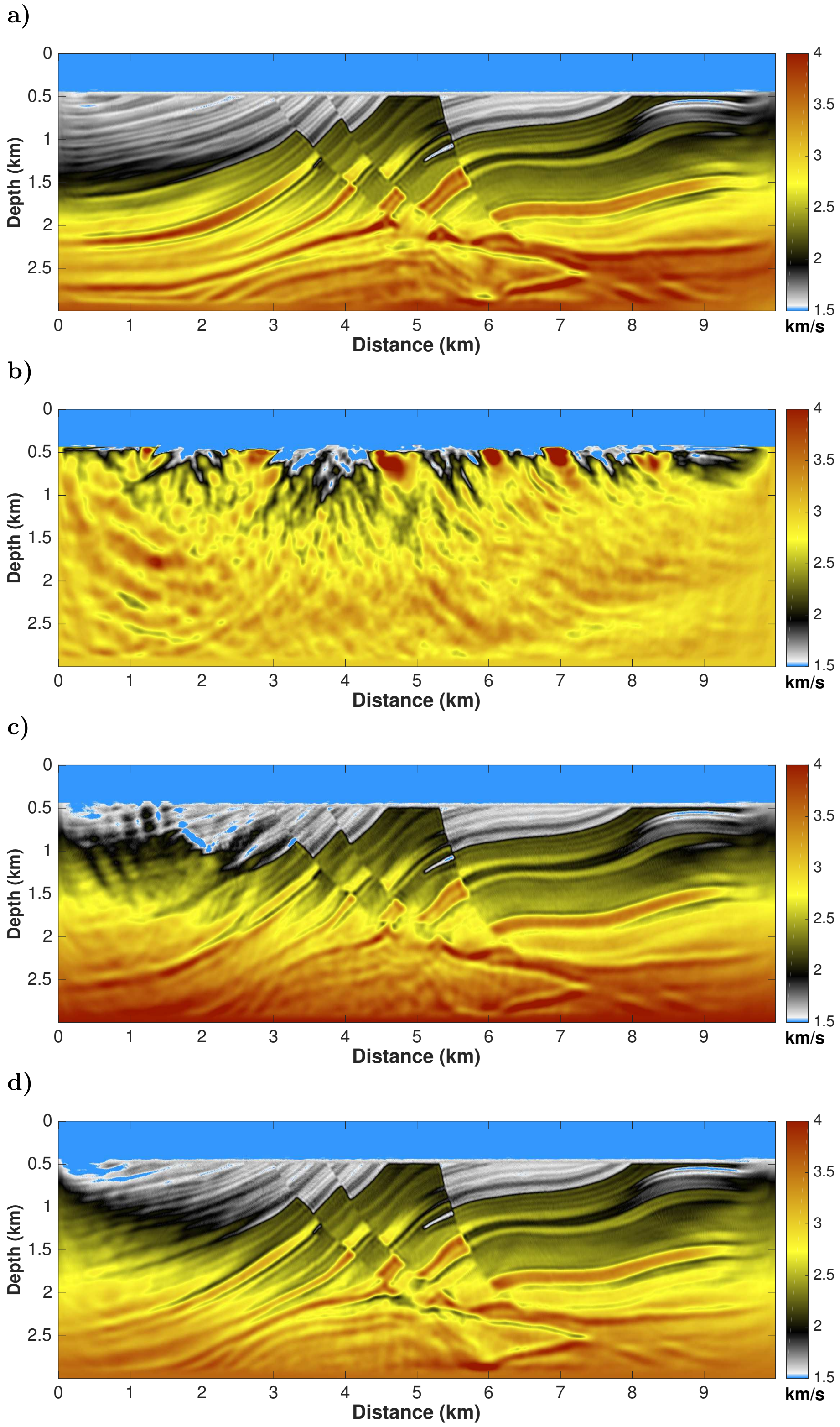

Figure 5.26: Test 4. Recovered velocity models from the initial models in Figure 5.19.

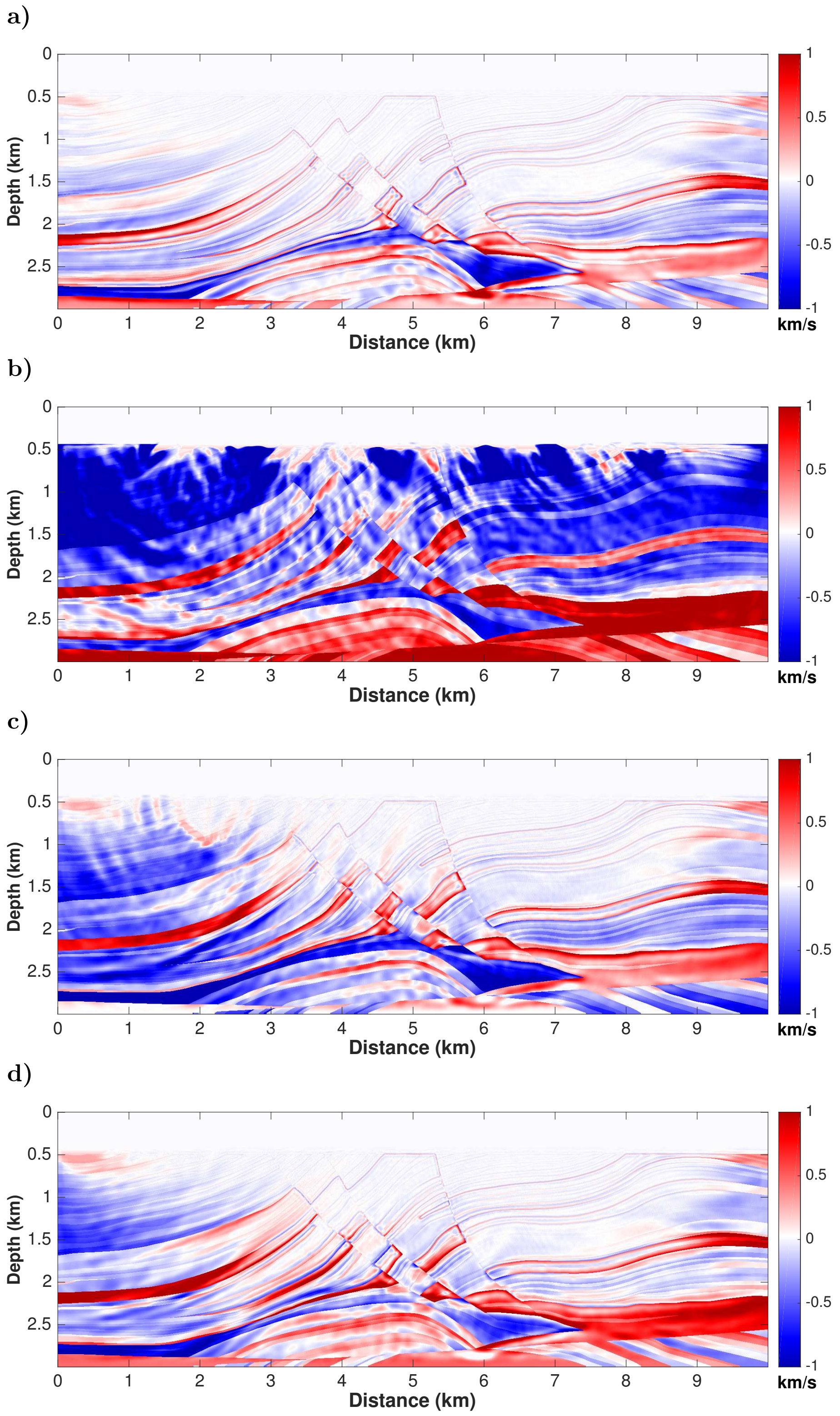

Figure 5.27: Test 4. Differences of the results in Figure 5.26 to the true model in Figure 5.19.

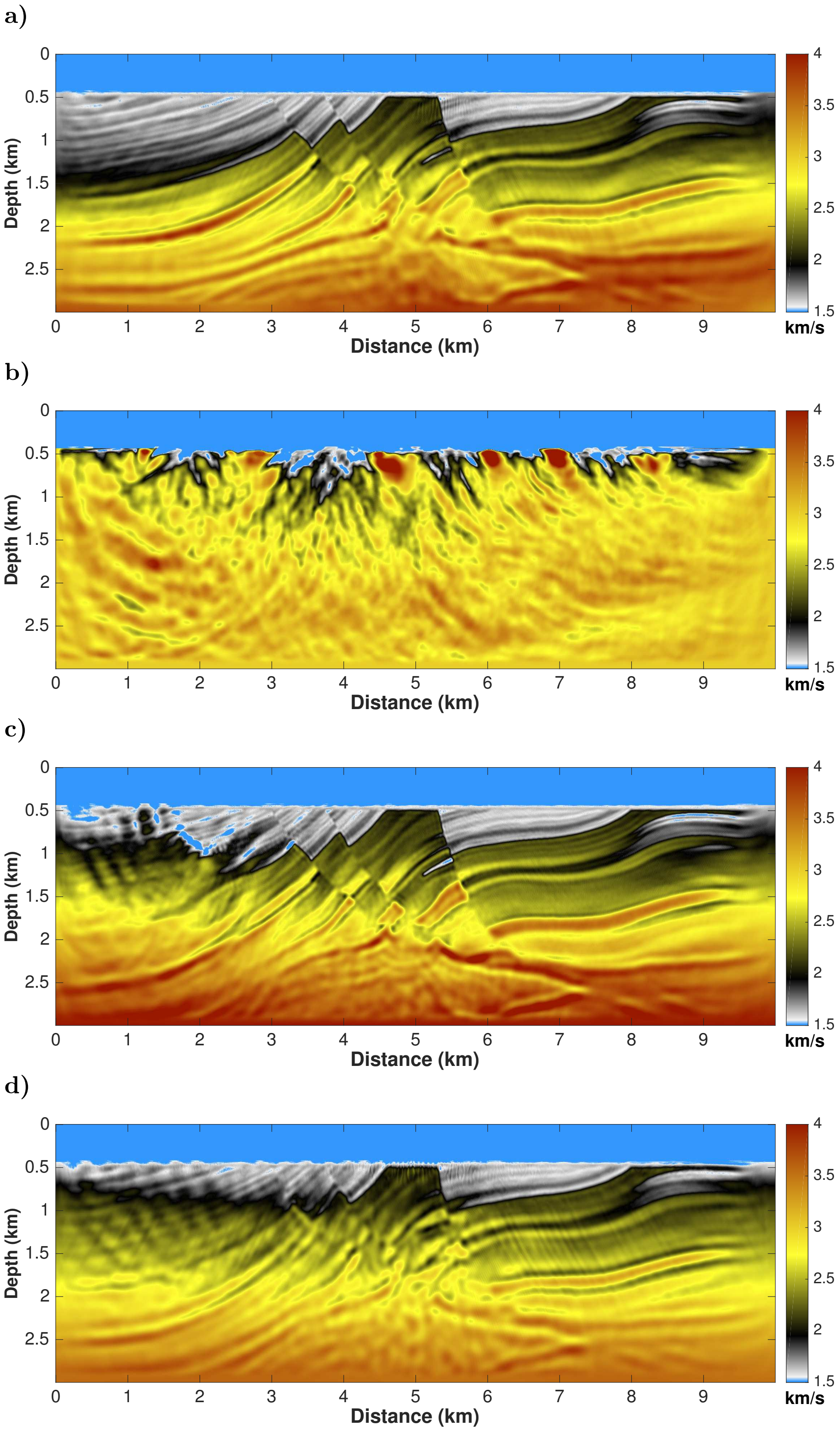

Figure 5.28: Test 5. Recovered velocity models from the initial models in Figure 5.19.

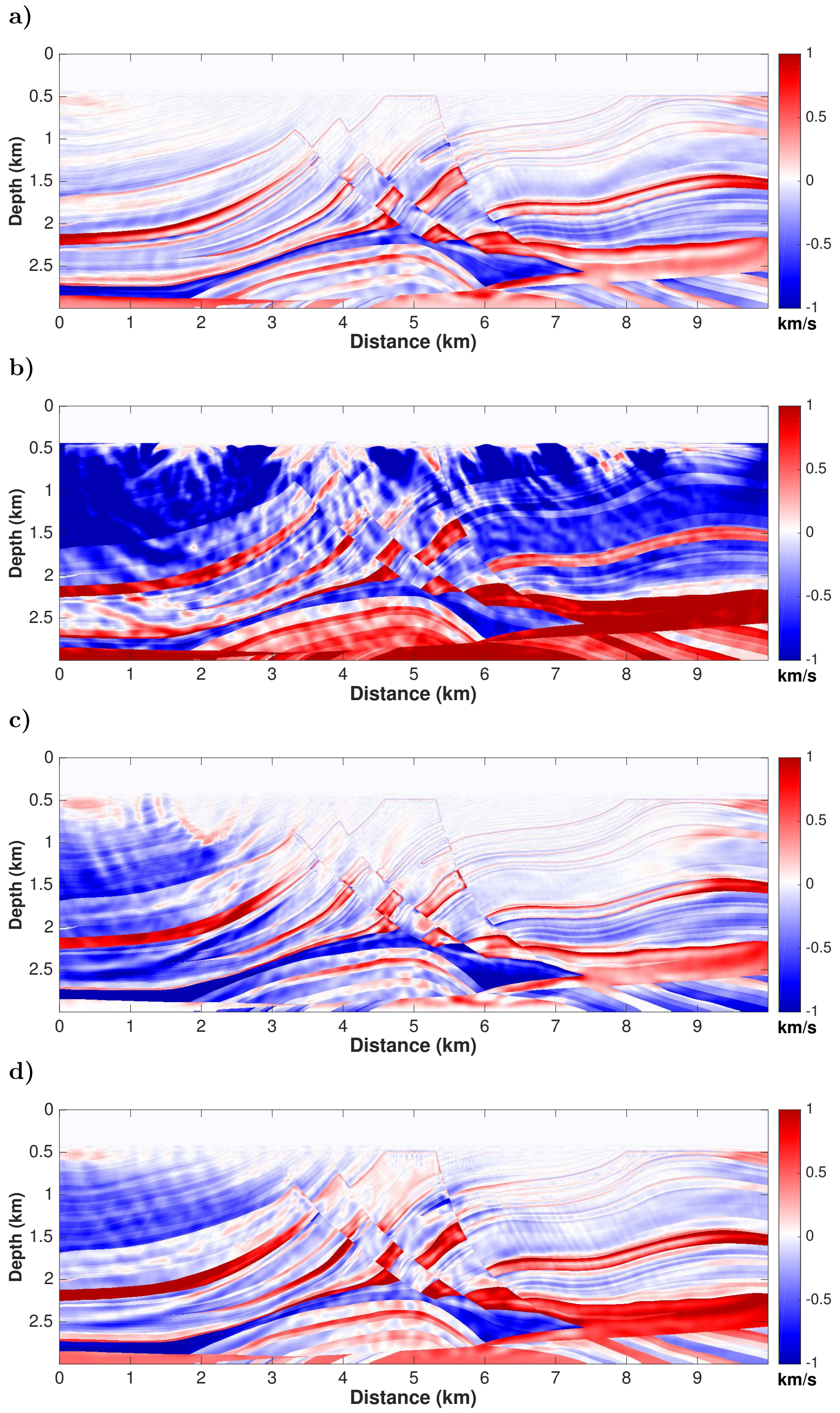

Figure 5.29: Test 5. Differences of the results in Figure 5.28 to the true model in Figure 5.19.

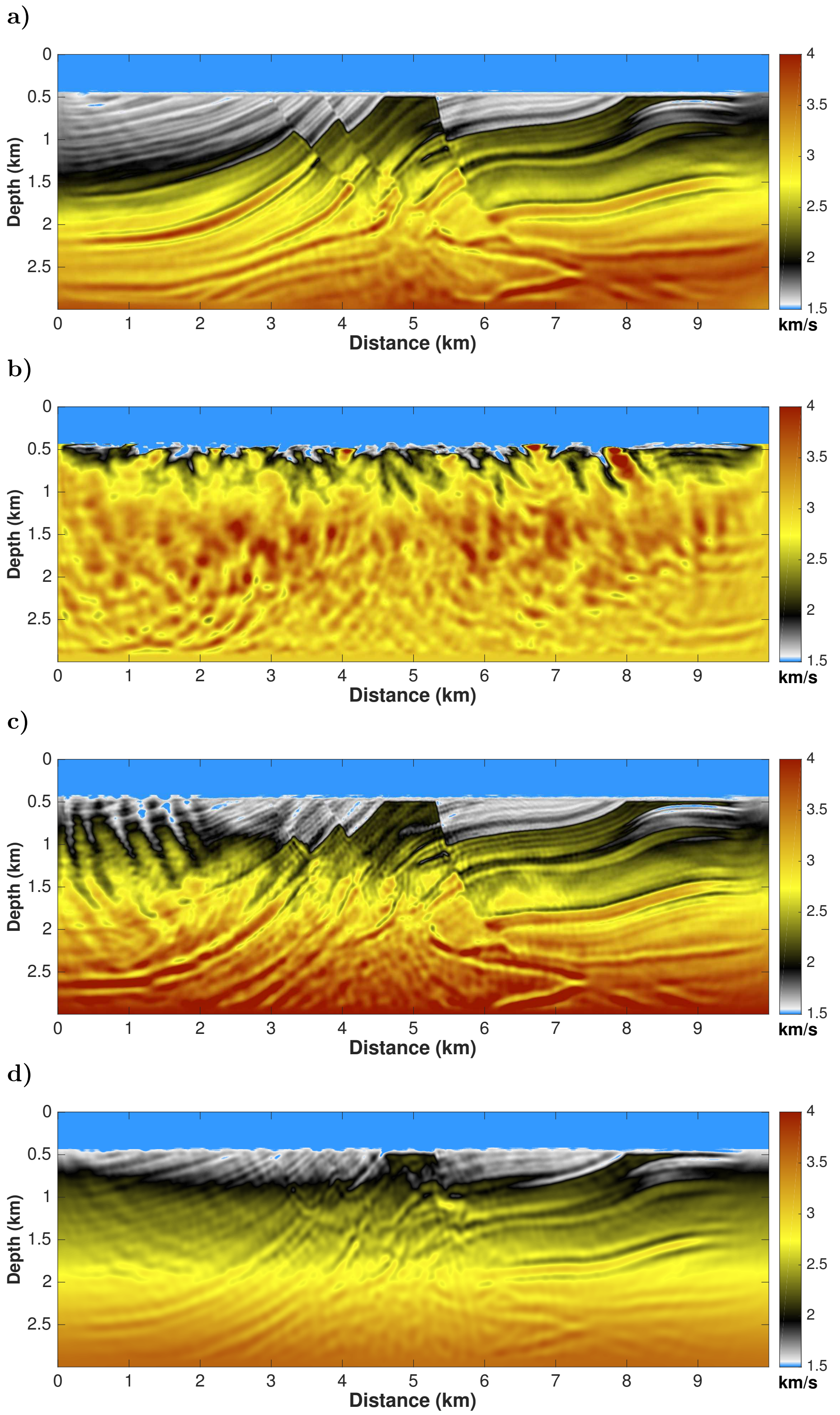

Figure 5.30: Test 6. Recovered velocity models from the initial models in Figure 5.19.

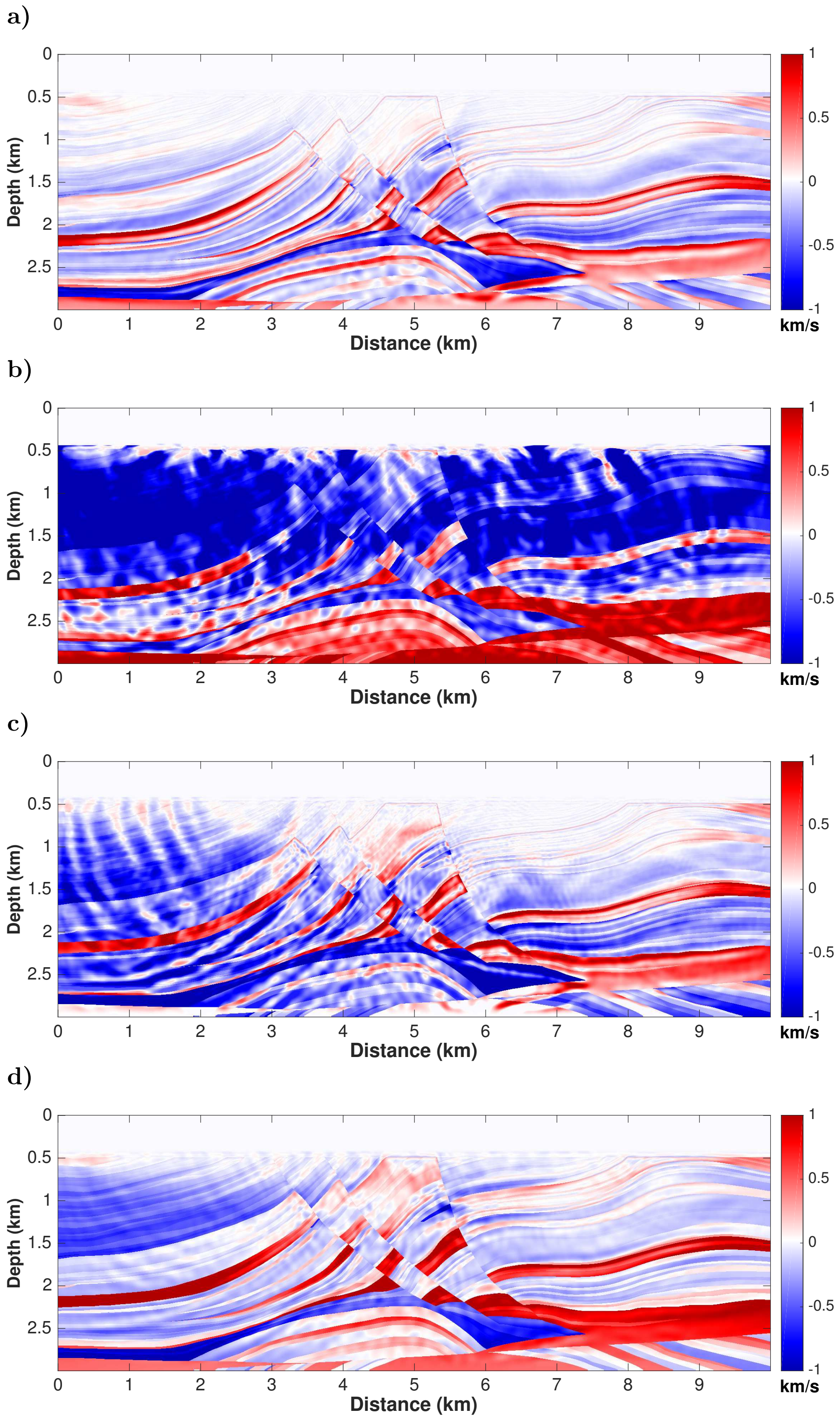

Figure 5.31: Test 6. Differences of the results in Figure 5.30 to the true model in Figure 5.19.

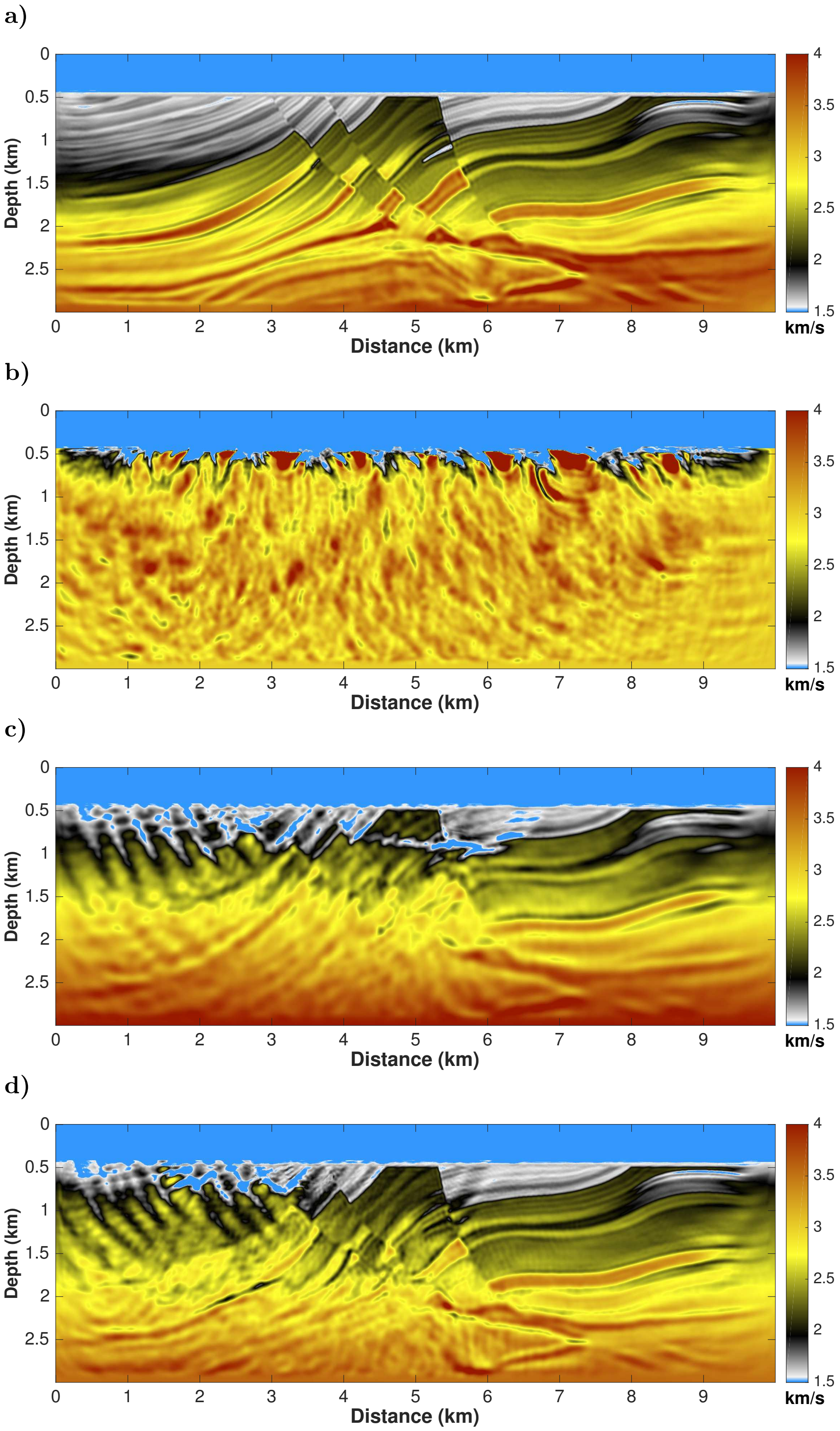

Figure 5.32: Test 7. Recovered velocity models from the initial models in Figure 5.19.

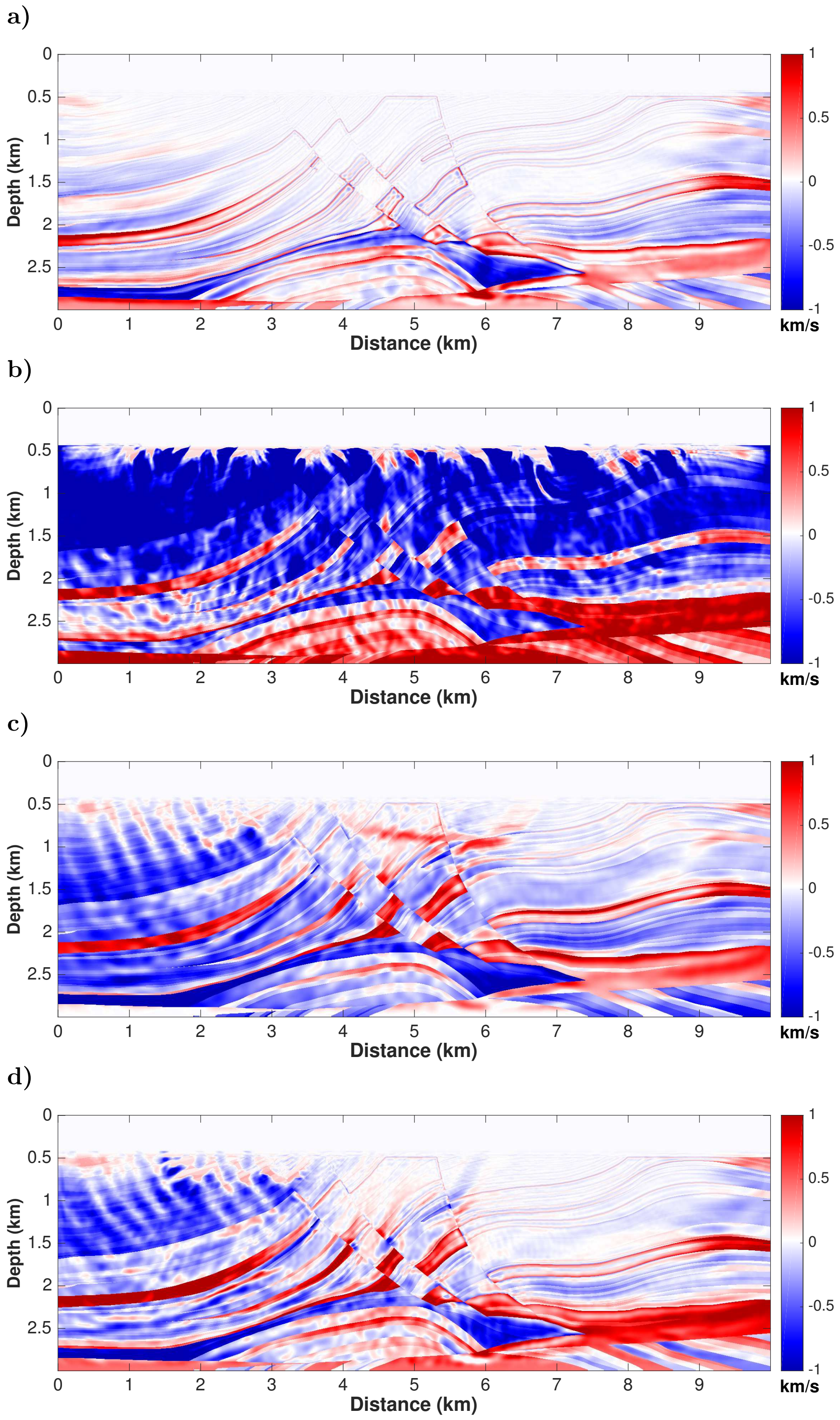

Figure 5.33: Test 7. Differences of the results in Figure 5.32 to the true model in Figure 5.19.

## 5.12 Conclusion

In this work, we have presented a workflow for the construction of initial velocity-models for FWT methods. In an attempt to aid the search for more efficient model-building tools, we investigate the applicability of a recent automatic time MVA method. This method stacks twice over migrated images for many models with different weights in order to extract stationary migration velocities from the ratio of the images. Thus, it is able to generate a velocity model and a time-migrated image without a priori information.

For the use of such a velocity model in FWT methods, the result needs to be converted from time to depth. For this purpose, we chose a strategy based only on image-ray wavefront propagation. The results confirmed the method's efficiency in very complex geology structures, i.e., models with strong velocity variations.

Our first numerical results indicate the potential of using a combination of these methods to achieve a fully automatic tool for initial-model building in an FWT workflow. In our tests, the method was able to produce a sufficiently accurate initial model for an FWT under nearly ideal conditions converges to a model of comparable quality as when starting at a smoothed version of the true model. This indicates that correct background velocity information can be successfully extracted from automatic time-domain migration velocity analysis even in media where time-migration cannot provide satisfactory seismic images.

Future investigations will have to show whether some model detail can be already introduced in the time domain or added in an additional depth-domain MVA step in order to reduce the number of necessary FWT iterations and if the inversion can still be successful from such initial models if the data are less than ideal.

# Chapter 6

# Final remarks

> *Learn from yesterday, live for today, hope for tomorrow. The important thing is not to stop questioning.*
>
> — Albert Einstein

We have presented methods for initial velocity-model building for seismic migration in the time- and depth-domains. They proved to be useful tools for automatic or semi-automatic processing of seismic data in various geology scenarios. Through the way we discussed and presented each method, we suggested intuitively to start the processing by means of those methods that are faster and require less human intervention, adding other tools and information as needed.

The time-domain methods, presented in Chapters 2 and 3, confirmed their ability to recover the most part of the sedimentary areas even in the presence of strong velocity variation.

The resulting MVA processing of the Marmousoft data by image-wave common-image-gather continuation, multi-stack migration, and remigration trajectory MVA revealed that even though rather different models are obtained, the associated time-migrated images exhibit fairly much the same quality, indicating that for the purpose of time-migration, all models are equivalent. On the other hand, the combination of some of these methods may be useful to decrease, for example, the influence of the noise in the data which will increase the coherence of the results. Further studies will combine all these methods, or at least, part of them or their results trying to achieve better velocity models.

For a better evaluation, the results need to be converted from the time to the depth domain, because methods in the depth-domain are more sensitive to velocity variations. Most conversion techniques are based on ray theory, which unfortunately suffers from quality decay in the presence of strong velocity variations. Chapter 4 demonstrates the application of a new strategy based only on image-wavefront propagation. The results confirmed the efficiency of the method in very complex geology structures, i.e., models with strong velocity variations.

It is important to emphasize that velocity building of salt structures and subsalt sediments is a hard work even for imaging methods in the depth domain as well as for full waveform inversion (FWI). In Chapter 5, we presented the preliminary results for a (semi) automatic and high computationally efficient workflow, useful to build initial velocity models applicable to FWI.

Certainly, there are a huge number of models, strategies and workflows to be tested with the tools presented here, aiming at better estimating velocity models and images of the subsurface. Future research will serve to combine some of the methods discussed here, in attempt to achieve some hybrid method and/or a workflow more computationally efficient or capable to provided more precise information. Other possible applications to be investigated include the assessment of model ambiguity and uncertainty.

# References

Adler, F., 2002, Kirchhoff image propagation: Geophysics, **6**7, 126–134, doi: 10.1190/1.1451409.

Agranovich, Z. S., and V. A. Marchenko, 1963, Inverse problem of scattering theory, 1 ed.: Gordon & Breach.

Al-Yahya, K., 1989, Velocity analysis by iterative profile migration: Geophysics, **5**4, 718–729, doi: 10.1190/1.1442699.

Alford, R. M., K. R. Kelly, and D. M. Boore, 1974, Accuracy of finite-difference modeling of the acoustic wave equation: Geophysics, **3**9, 834–842, doi: 10.1190/1.1440470.

Alkhalifah, T. A., 2014, Full waveform inversion in an anisotropic world - where are the parameters hiding?: EAGE Publications BV.

Allen, P., and J. Allen, 2013, Basin analysis: Principles and application to petroleum play assessment: Wiley.

Amazonas, D., J. C. Costa, J. Schleicher, and R. Pestana, 2007, Wide-angle FD and FFD migration using complex Padé approximations: Geophysics, **7**2, S215–S220, doi: 10.1190/1.2785813.

Bancroft, J., H. Geiger, and G. Margrave, 1998, The equivalent offset method of prestack time migration: Geophysics, **6**3, 2042–2053, doi: 10.1190/1.1444497.

Barton, D. C., 1932, Eötvös torsion balance: Physics, **3**, 29–38, doi: 10.1063/1.1745078.

Bednar, J. B., 2005, A brief history of seismic migration: Geophysics, **7**0, 3MJ–20MJ, doi: 10.1190/1.1926579.

Behura, J., K. Wapenaar, and R. Snieder, 2014, Autofocus imaging: Image reconstruction based on inverse scattering theory: Geophysics, **7**9, A19–A26, doi: 10.1190/geo2013-0398.1.

Bell, R. E., R. Anderson, and L. Pratson, 1997, Gravity gradiometry resurfaces: The Leading Edge, **1**6, 55–59, doi: 10.1190/1.1437431.

Berenger, J. P., 1994, A perfectly matched layer for the absorption of electromagnetic waves: Journal of Computational Physics, **1**14, 185–200, doi:

10.1006/jcph.1994.1159.

Berkhout, A. J., 1997, Pushing the limits of seismic imaging, part II: Integration of prestack migration, velocity estimation, and AVO analysis: Geophysics, **62**, 954–969, doi: 10.1190/1.1444202.

———, 2012, Combining full wavefield migration and full waveform inversion, a glance into the future of seismic imaging: Geophysics, **77**, S43–S50, doi: 10.1190/geo2011-0148.1.

Billette, F., S. L. Bégat, P. Podvin, and G. Lambaré, 2003, Practical aspects and applications of 2D stereotomography: Geophysics, **68**, 1008–1021, doi: 10.1190/1.1581072.

Billette, F., and G. Lambaré, 1998, Velocity macro-model estimation from seismic reflection data by stereotomography: Geophysical Journal International, **135**, 671–690, doi: 10.1046/j.1365-246x.1998.00632.x.

Biondi, B., and A. Almomin, 2014, Simultaneous inversion of full data bandwidth by tomographic full-waveform inversion: Geophysics, **79**, WA129–WA140, doi: 10.1190/geo2013-0340.1.

Biondi, B. L., 2006, 3D Seismic Imaging: Society of Exploration Geophysicists, doi: 10.1190/1.9781560801689.

Bishop, T. N., K. P. Bube, R. T. Cutler, R. T. Langan, P. L. Love, J. R. Resnick, R. T. Shuey, D. A. Spindler, and H. W. Wyld, 1985, Tomographic determination of velocity and depth in laterally varying media: Geophysics, **50**, 903–923, doi: 10.1190/1.1441970.

Blakely, R. J., 1995, Potential theory in gravity and magnetic applications: Cambridge University Press, doi: 10.1017/cbo9780511549816.

Bleibinhaus, F., R. W. Lester, and J. A. Hole, 2009, Applying waveform inversion to wide-angle seismic surveys: Tectonophysics, **472**, 238–248, doi: 10.1016/j.tecto.2008.08.023.

Bleistein, N., 1987, On the imaging of reflectors in the earth: Geophysics, **52**, 931–942, doi: 10.1190/1.1442363.

Bohlen, T., 1998, Viskoelastische FD-Modellierung seismischer Wellen zur Interpretation gemessener Seismogramme: PhD thesis, Christian-Albrechts-Universität zu Kiel.

———, 2002, Parallel 3-D viscoelastic finite difference seismic modelling: Computers & Geosciences, **28**, 887–899, doi: 10.1016/s0098-3004(02)00006-7.

Bohlen, T., and E. H. Saenger, 2006, Accuracy of heterogeneous staggered-grid finite-difference modeling of Rayleigh waves: Geophysics, **71**, T109–T115, doi: 10.1190/1.2213051.

Brenders, A. J., and R. G. Pratt, 2007, Full waveform tomography for lithospheric imaging: results from a blind test in a realistic crustal model: Geophysical Journal International, **1**68, 133–151, doi: 10.1111/j.1365-246x.2006.03156.x.

Broggini, F., and R. Snieder, 2012, Connection of scattering principles: a visual and mathematical tour: European Journal of Physics, **3**3, 593–613, doi: 10.1088/0143-0807/33/3/593.

Bunks, C., F. M. Saleck, S. Zaleski, and G. Chavent, 1995, Multiscale seismic waveform inversion: Geophysics, **6**0, 1457–1473, doi: 10.1190/1.1443880.

Cameron, M. K., Fomel, and J. A. Sethian, 2008, Time-to-depth conversion and seismic velocity estimation using time-migration velocity: Geophysics, **7**3, VE205–VE210, doi: 10.1190/1.2967501.

Cameron, M. K., S. B. Fomel, and J. A. Sethian, 2007, Seismic velocity estimation from time migration: Inversion Problems, **2**3, 1329–1369, doi: 10.1088/0266-5611/23/4/001.

Carroll, L., 1865, Alice's adventures in Wonderland: Macmillan Publishers Ltd.

Castagna, J. P., and M. M. Backus, eds., 1993, Offset-dependent reflectivity—theory and practice of AVO analysis: Society of Exploration Geophysicists, doi: 10.1190/1.9781560802624.

Černy, V., 2001, Seismic ray theory: Cambridge University Press.

Chapman, S., and J. Bartels, 1940, Geomagnetism: Oxford.

Chauris, H., and A. M. Noble, 2001, Two-dimensional velocity macro model estimation from seismic reflection data by local differential semblance optimization: applications to synthetic and real data sets: Geophysical Journal International, **1**44, 14–26, doi: 10.1046/j.1365-246x.2001.00279.x.

Chen, J., and G. M. Hoversten, 2012, Joint inversion of marine seismic AVA and CSEM data using statistical rock-physics models and Markov random fields: Geophysics, **7**7, R65–R80, doi: 10.1190/geo2011-0219.1.

Chew, W. C., and W. H. Weedon, 1994, A 3D perfectly matched medium from modified maxwell's equations with stretched coordinates: Microwave and Optical Technology Letters, **7**, 599–604, doi: 10.1002/mop.4650071304.

Claerbout, J. F., 1970, Coarse grid calculations of waves in inhomogeneous media with application to delineation of complicated seismic structure: Geophysics, **3**5, 407–418, doi: 10.1190/1.1440103.

———, 1971, Toward a unified theory of reflector mapping: Geophysics, **3**6, 467–481, doi: 10.1190/1.1440185.

———, 1985, Imaging the Earth's interior: Blackwell Scientific Publications, Inc.

Clapp, R. G., B. L. Biondi, and J. F. Claerbout, 2004, Incorporating geologic information into reflection tomography: Geophysics, **69**, 533–546, doi: 10.1190/1.1707073.

Cohen, J. K., and J. J. W. Stockwell, 2014, CWP/SU: Seismic Un*x Release No. 43R6: An open source software package for seismic research and processing: Center for Wave Phenomena, Colorado School of Mines.

Coimbra, T., H. B. Santos, J. Schleicher, and A. Novais, 2014, Prestack Migration Velocity Analysis Using Time-remigration Trajectories: Presented at the 76th EAGE Conference and Exhibition 2014, EAGE Publications, doi: 10.3997/2214-4609.20141498.

Coimbra, T. A., J. J. S. de Figueiredo, A. Novais, and J. Schleicher, 2011, Migration velocity analysis with diffraction events using residual moveout: Annual WIT report, **15**, 57–70.

Coimbra, T. A., J. J. S. de Figueiredo, A. Novais, J. Schleicher, and S. Arashiro, 2013a, Migration velocity analysis using residual diffraction moveout in the prestack depth domain: Annual WIT report, **17**, 44–53.

Coimbra, T. A., J. J. S. de Figueiredo, J. Schleicher, A. Novais, and J. Costa, 2013b, Migration velocity analysis using residual diffraction moveout in the poststack depth domain: Geophysics, **78**, S125–S135, doi: 10.1190/geo2012-0340.1.

Coimbra, T. A., J. J. S. de Figueiredo, J. Schleicher, A. Novais, and J. C. Costa, 2012, Migration velocity analysis with diffraction events using residual moveout: Application to SIGSBEE 2B data: Annual WIT report, **16**, 45–58.

Coimbra, T. A., H. B. Santos, J. Schleicher, and A. Novais, 2013c, Migration Velocity Analysis using Time-Remigration Trajectory in Prestack Data: Presented at the 13th International Congress of the Brazilian Geophysical Society & EXPOGEF, SBGf, doi: 10.1190/sbgf2013-319.

———, 2013d, Prestack migration velocity analysis using time-remigration trajectories: Annual WIT Report No. 17.

Colombo, D., G. McNeice, N. Raterman, M. Zinger, D. Rovetta, and E. S. Curiel, 2014, Exploration beyond seismic: The role of electromagnetics and gravity gradiometry in deep water subsalt plays of the red sea: Interpretation, **2**, SH33–SH53, doi: 10.1190/int-2013-0149.1.

Commer, M., and G. A. Newman, 2008, New advances in three-dimensional controlled-source electromagnetic inversion: Geophysical Journal International, **172**, 513–535, doi: 10.1111/j.1365-246x.2007.03663.x.

Cordsen, A., M. Galbraith, and J. Peirce, 2000, Planning land 3-D seismic surveys: Society of Exploration Geophysicists, doi: 10.1190/1.9781560801801.

Costa, J. C., F. J. da Silva, E. N. Gomes, J. Schleicher, L. A. Melo, and D. Amazonas, 2008, Regularization in slope tomography: Geophysics, **7**3, VE39–VE47, doi: 10.1190/1.2967499.

Costa, J. C., and J. Schleicher, 2011, Double path-integral migration velocity analysis: a real data example: Journal of Geophysics and Engineering, **8**, 154–161, doi: 10.1088/1742-2132/8/2/003.

da Costa Filho, C. A., M. Ravasi, A. Curtis, and G. A. Meles, 2014, Elastodynamic Green's function retrieval through single-sided Marchenko inverse scattering: Physical Review E, **9**0, doi: 10.1103/physreve.90.063201.

Dagum, L., and R. Menon, 1998, OpenMP: an industry standard API for shared-memory programming: IEEE Computational Science and Engineering, **5**, 46–55, doi: 10.1109/99.660313.

Dash, R., G. Spence, R. Hyndman, S. Grion, Y. Wang, and S. Ronen, 2009, Wide-area imaging from OBS multiples: Geophysics, **7**4, Q41–Q47, doi: 10.1190/1.3223623.

de Oliveira Lyrio, J. C. S., L. Tenorio, and Y. Li, 2004, Efficient automatic denoising of gravity gradiometry data: Geophysics, **6**9, 772–782, doi: 10.1190/1.1759463.

DeGolyer, E., 1935, Notes on the early history of applied geophysics in the petroleum industry: Trans. Soc. Pet. Geophys., **6**, 652–654. (Reprinted in *Early Geophysica Papers of the Society of Exploration Geophysicists*, pp. 245-54. Tulsa: Society of Exploration Geophysicists, 1947.).

Deregowski, S., 1990, Common-offset migrations and velocity analysis: First Break, **8**, doi: 10.3997/1365-2397.1990011.

Dessa, J.-X., 2004, Multiscale seismic imaging of the eastern Nankai trough by full waveform inversion: Geophysical Research Letters, **3**1, doi: 10.1029/2004gl020453.

Dix, C. H., 1955, Seismic velocities from surfaces measurements: Geophysics, **2**0, 68–86, doi: 10.1190/1.1438126.

Domenico, N., 1996, The Mintrop mechanical seismograph: The Leading Edge, **1**5, 1049–1052, doi: 10.1190/1.1437415.

Etgen, J., S. H. Gray, and Y. Zhang, 2009, An overview of depth imaging in exploration geophysics: Geophysics, **7**4, WCA5–WCA17, doi: 10.1190/1.3223188.

Feynman, R. P., and A. R. Hibbs, 1965, Quantum mechanics and path integrals, 1st ed. International series in pure and applied physics: McGraw Hill Book Company.

Fichtner, A., 2011, Full seismic waveform modelling and inversion: Springer Berlin Heidelberg, doi: 10.1007/978-3-642-15807-0.

Fichtner, A., B. L. N. Kennett, H. Igel, and H.-P. Bunge, 2009, Full seismic waveform tomography for upper-mantle structure in the australasian region using adjoint methods: Geophysical Journal International, **1**79, 1703–1725, doi: 10.1111/j.1365-246x.2009.04368.x.

Fleury, C., and I. Vasconcelos, 2013, Adjoint-state reverse time migration of 4C data: Finite-frequency map migration for marine seismic imaging: Geophysics, **7**8, WA159–WA172, doi: 10.1190/geo2012-0306.1.

Fomel, S., 1994, Method of velocity continuation in the problem of seismic time migration: Russian Geology and Geophysics, **3**5, no. 5, 100–111.

———, 2003a, Time migration velocity analysis by velocity continuation: Geophysics, **6**8, 1662–1672, doi: 10.1190/1.1620640.

———, 2003b, Velocity continuation and the anatomy of residual prestack time migration: Geophysics, **6**8, 1650–1661, doi: 10.1190/1.1620639.

Fomel, S., E. Landa, and M. T. Taner, 2007, Poststack velocity analysis by separation and imaging of seismic diffractions: Geophysics, **7**2, U89–U94, doi: 10.1190/1.2781533.

Fomel, S., P. Sava, I. Vlad, Y. Liu, and V. Bashkardin, 2013, Madagascar: open-source software project for multidimensional data analysis and reproducible computational experiments: Journal of Open Research Software, **1**, e8, doi: 10.5334/jors.ag.

Forel, D., and G. H. F. Gardner, 1988, A three-dimensional perspective on two-dimensional dip moveout: Geophysics, **5**3, 604–610, doi: 10.1190/1.1442495.

Gabriel, E., G. E. Fagg, G. Bosilca, T. Angskun, J. J. Dongarra, J. M. Squyres, V. Sahay, P. Kambadur, B. Barrett, A. Lumsdaine, R. H. Castain, D. J. Daniel, R. L. Graham, and T. S. Woodall, 2004, Open MPI: Goals, concept, and design of a next generation MPI implementation: Proceedings, 11th European PVM/MPI Users' Group Meeting, 97–104.

Gazdag, J., 1978, Wave equation migration with the phase-shift method: Geophysics, **4**3, 1342–1351, doi: 10.1190/1.1440899.

Gazdag, J., and P. Sguazzero, 1984, Migration of seismic data by phase shift plus interpolation: Geophysics, **4**9, 124–131, doi: 10.1190/1.1441643.

Gillies, G. T., and R. C. Ritter, 1993, Torsion balances, torsion pendulums, and related devices: Review of Scientific Instruments, **6**4, 283–309, doi: 10.1063/1.1144248.

Gray, S. H., J. Etgen, J. Dellinger, and D. Whitmore, 2001, Seismic migration problems and solutions: Geophysics, **6**6, 1622–1640, doi: 10.1190/1.1487107.

Hadamard, J., 1902, Sur les problèmes aux dérivées partielles et leur signification physique: Princeton University Bulletin, **13**, 49–52.

Hagedoorn, J. G., 1954, A process of seismic reflection interpretation: Geophysical Prospecting, **2**, 85–127, doi: 10.1111/j.1365-2478.1954.tb01281.x.

Hale, D., 1984, Dip-moveout by Fourier transform: Geophysics, **49**, 741–757, doi: 10.1190/1.1441702.

Harradon, H. D., 1943, Some early contributions to the history of geomagnetism: I: Journal of Geophysical Research, **48**, 3–17, doi: 10.1029/te048i001p00003.

Hemon, C., 1978, Equations d'onde et modeles: Geophysical Prospecting, **26**, 790–821, doi: 10.1111/j.1365-2478.1978.tb01634.x.

Hertweck, T., J. Schleicher, and J. Mann, 2007, Data stacking beyond CMP: The Leading Edge, **26**, 818–827, doi: 10.1190/1.2756859.

Hokusai, K., 1830, Under the Wave off Kanagawa (*Kanagawa oki nami ura*), also known as The Great Wave. Thirty-six views of Mount Fuji (*Fugaku sanjūrokkei*): The Metropolitan Museum of Art, New York. (polychrome woodblock print, ink and color on paper, 25.7 cm × 37.8 cm (10.1 in × 14.9 in)).

Hoversten, G. M., F. Cassassuce, E. Gasperikova, G. A. Newman, J. Chen, Y. Rubin, Z. Hou, and D. Vasco, 2006, Direct reservoir parameter estimation using joint inversion of marine seismic AVA and CSEM data: Geophysics, **71**, C1–C13, doi: 10.1190/1.2194510.

Hubral, P., 1977, Time migration - some ray theoretical aspects: Geophysical Prospecting, **25**, 738–745, doi: 10.1111/j.1365-2478.1977.tb01200.x.

Hubral, P., J. Schleicher, and M. Tygel, 1996a, A unified approach to 3-D seismic reflection imaging, Part I: Basic concepts: Geophysics, **61**, 742–758, doi: 10.1190/1.1444001.

Hubral, P., M. Tygel, and J. Schleicher, 1996b, Seismic image waves: Geophysical Journal International, **125**, 431–442, doi: 10.1111/j.1365-246x.1996.tb00009.x.

Inkscape, 2015, Version 0.91 (r13725): The Inkscape Project.

Iversen, E., 2006, Velocity rays for heterogeneous anisotropic media: Theory and implementation: Geophysics, **71**, T117–T127, doi: 10.1190/1.2227525.

Iversen, E., and M. Tygel, 2008, Image-ray tracing for joint 3D seismic velocity estimation and time-to-depth conversion: Geophysics, **73**, S99–S114, doi: 10.1190/1.2907736.

Jäger, R., J. Mann, G. Höcht, and P. Hubral, 2001, Common-reflection-surface stack: Image and attributes: Geophysics, **66**, 97–109, doi: 10.1190/1.1444927.

Jannane, M., W. Beydoun, E. Crase, D. Cao, Z. Koren, E. Landa, M. Mendes, A. Pica, M. Noble, G. Roeth, S. Singh, R. Snieder, A. Tarantola, D. Trezeguet, and

M. Xie, 1989, Wavelengths of earth structures that can be resolved from seismic reflection data: Geophysics, **54**, 906–910, doi: 10.1190/1.1442719.

Jones, I., 2010, An introduction to: Velocity model building: EAGE Publications BV, doi: 10.3997/9789073781849.

Keller, J. B., 1976, Inverse problems: The American Mathematical Monthly, **83**, 107, doi: 10.2307/2976988.

Kelly, K. R., R. W. Ward, S. Treitel, and R. M. Alford, 1976, Synthetic seismograms: a finite-difference approach: Geophysics, **41**, 2–27, doi: 10.1190/1.1440605.

Keppner, G., 1991, Ludger mintrop: The Leading Edge, **10**, 21–28, doi: 10.1190/1.1436838.

Keydar, S., 2004, Homeomorphic imaging using path integrals: 66th EAGE Conference & Exhibition, EAGE Publications, 1–4.

Keydar, S., and V. Shtivelman, 2005, Imaging zero-offset sections using multipath summation: First Break, **23**, 21–24, doi: 10.3997/1365-2397.2005016.

Knight, S., 2005, Building software with SCons: Computing in Science and Engineering, **7**, 79–88, doi: 10.1109/mcse.2005.11.

Kolb, P., F. Collino, and P. Lailly, 1986, Pre-stack inversion of a 1-D medium: Proceedings of the IEEE, **74**, 498–508, doi: 10.1109/proc.1986.13490.

Kono, M., 2015, Geomagnetism: An introduction and overview, *in* Treatise on Geophysics: Elsevier, 1–31, doi: 10.1016/b978-0-444-53802-4.00095-6.

Kurzmann, A., 2012, Applications of 2D and 3D full waveform tomography in acoustic and viscoacoustic complex media: PhD thesis, Karlsruhe Institute of Technology.

Kurzmann, A., D. Koehn, A. Przebindowska, N. Nguyen, and T. Bohlen, 2009, 2D acoustic full waveform tomography – performance and optimization: Presented at the 71st EAGE Conference and Exhibition incorporating SPE EUROPEC 2009, EAGE Publications BV, doi: 10.3997/2214-4609.201400012.

Kurzmann, A., A. Przebindowska, D. Kohn, and T. Bohlen, 2013, Acoustic full waveform tomography in the presence of attenuation: a sensitivity analysis: Geophysical Journal International, **195**, 985–1000, doi: 10.1093/gji/ggt305.

Lailly, P., 1983, The seismic inverse problem as a sequence of before stack migrations, *in* Inverse Scattering Theory and Application: Society for Indistrial and Applied Mathematics (SIAM), 206–220.

Lamport, L., 1986, LaTeX: A document preparation system: Addison-Wesley Longman Publishing Co., Inc.

Landa, E., 2004, Imaging without a velocity model using path-summation approach: SEG Technical Program Expanded Abstracts 2004, Society of Exploration

Geophysicists, 1818–1821, doi: 10.1190/1.1845174.

Landa, E., S. Fomel, and T. Moser, 2006, Path-integral seismic imaging: Geophysical Prospecting, **5**4, 491–503, doi: 10.1111/j.1365-2478.2006.00552.x.

Landa, E., M. Reshef, and V. Khaidukov, 2005, Imaging without a velocity model by path- summation approach: this time in depth: 67th EAGE Conference & Exhibition, EAGE Publications, 1–4. (P011).

Larner, K., and C. Beasley, 1987, Cascaded migrations: Improving the accuracy of finite-difference migration: Geophysics, **5**2, 618–643, doi: 10.1190/1.1442331.

Lax, P. D., 1954, Weak solutions of hyperbolic equations and their numerical computation: Communications in Pure and Applied Mathemetics, **7**, 159–193, doi: 10.1002/cpa.3160070112.

Levander, A. R., 1988, Fourth-order finite-difference *P-SV* seismograms: Geophysics, **5**3, 1425–1436, doi: 10.1190/1.1442422.

Liptow, F., and P. Hubral, 1995, Migrating around in circles: The Leading Edge, **1**4, 1125–1127, doi: 10.1190/1.1437083.

Liu, Z., 1997, An analytical approach to migration velocity analysis: Geophysics, **6**2, 1238–1249, doi: 10.1190/1.1444225.

Liu, Z., and N. Bleistein, 1995, Migration velocity analysis: Theory and an iterative algorithm: Geophysics, **6**0, 142–153, doi: 10.1190/1.1443741.

Lomax, A., 1999, Path-summation waveforms: Geophysical Journal International, **1**38, 702–716, doi: 10.1046/j.1365-246x.1999.00889.x.

Malcolm, A. E., B. Ursin, and M. V. de Hoop, 2009, Seismic imaging and illumination with internal multiples: Geophysical Journal International, **1**76, 847–864, doi: 10.1111/j.1365-246x.2008.03992.x.

Malinowski, M., and S. Operto, 2008, Quantitative imaging of the Permo-Mesozoic complex and its basement by frequency domain waveform tomography of wide-aperture seismic data from the Polish Basin: Geophysical Prospecting, **5**6, 805–825, doi: 10.1111/j.1365-2478.2007.00680.x.

Marchenko, V. A., 1955, Reconstruction of the potential energy from the phases of the scattered waves: JORNAL: Doklady Akademii Nauk SSSR, **1**04, 695—698. (In Russian).

Martin, G. S., K. J. Marfurt, and S. Larsen, 2002, Marmousi-2: An updated model for the investigation of AVO in structurally complex areas: Presented at the SEG Technical Program Expanded Abstracts 2002, Society of Exploration Geophysicists, doi: 10.1190/1.1817083.

MATLAB, 2015, Version 8.6.0.267246 (R2015b): The MathWorks Inc.

Mayne, W. H., 1962, Common reflection point horizontal data stacking techniques: Geophysics, **27**, 927–938, doi: 10.1190/1.1439118.

Menke, W., 1989, Geophysical data analysis: Discrete inverse theory: Academic Press, Inc.

Mickus, K. L., and J. H. Hinojosa, 2001, The complete gravity gradient tensor derived from the vertical component of gravity: a Fourier transform technique: Journal of Applied Geophysics, **46**, 159–174, doi: 10.1016/s0926-9851(01)00031-3.

Mikhailov, V., G. Pajot, M. Diament, and A. Price, 2007, Tensor deconvolution: A method to locate equivalent sources from full tensor gravity data: Geophysics, **72**, I61–I69, doi: 10.1190/1.2749317.

Milani, E. J., J. A. S. L. Brandão, P. V. Zalán, and L. A. P. Gamboa, 2000, Petróleo na margem continental brasileira: geologia, exploração, resultados e perspectivas: Revista Brasileira de Geofísica, **18**, 352–396, doi: 10.1590/s0102-261x2000000300012.

Mitchell, A. C., 1946, Chapters in the history of terrestrial magnetism: Journal of Geophysical Research, **51**, 323, doi: 10.1029/te051i003p00323.

Mohriak, W., P. Szatmari, and S. Anjos, 2008, Sal: geologia e tectônica – exemplo nas bacias brasileiras: Beca.

Mora, P., 1987a, Elastic inversion of field data: SEP report, **51**, 211–218.

———, 1987b, Nonlinear two-dimensional elastic inversion of multioffset seismic data: Geophysics, **52**, 1211–1228, doi: 10.1190/1.1442384.

———, 1989, Inversion = migration + tomography: Geophysics, **54**, 1575–1586, doi: 10.1190/1.1442625.

Moser, T. J., S. K. Keydar, V. Shtivelman, and M. Mikenberg, 2008, 3D prestack time migration by multipath summation: Presented at the 70th EAGE Conference and Exhibition incorporating SPE EUROPEC 2008, EAGE Publications BV, doi: 10.3997/2214-4609.20147855.

MPIF, 1994, MPI: A Message-Passing Interface Standard: Technical report, Knoxville, TN, USA.

Nabighian, M. N., M. E. Ander, V. J. S. Grauch, R. O. Hansen, T. R. LaFehr, Y. Li, W. C. Pearson, J. W. Peirce, J. D. Phillips, and M. E. Ruder, 2005, Historical development of the gravity method in exploration: Geophysics, **70**, 63ND–89ND, doi: 10.1190/1.2133785.

Needham, J., 1962, Science and Civilisation in China. Physics and Physical Technology, Part 1 Physics, **4**: Cambridge University Press.

Nemeth, T., C. Wu, and G. T. Schuster, 1999, Least-squares migration of incomplete reflection data: Geophysics, **64**, 208–221, doi: 10.1190/1.1444517.

Nocedal, J., and S. J. Wright, 2006, Numerical optimization, 2nd ed.: Springer, doi: 10.1007/978-0-387-40065-5.

Novais, A., J. Costa, and J. Schleicher, 2008, GPR velocity determination by image-wave remigration: Journal of Applied Geophysics, **6**5, 65–72, doi: 10.1016/j.jappgeo.2008.05.001.

Oldenburg, D. W., 1974, The inversion and interpretation of gravity anomalies: Geophysics, **3**9, 526–536, doi: 10.1190/1.1440444.

Pajot, G., O. de Viron, M. Diament, M.-F. Lequentrec-Lalancette, and V. Mikhailov, 2008, Noise reduction through joint processing of gravity and gravity gradient data: Geophysics, **7**3, I23–I34, doi: 10.1190/1.2905222.

Parker, R. L., 1973, The rapid calculation of potential anomalies: Geophysical Journal International, **3**1, 447–455, doi: 10.1111/j.1365-246x.1973.tb06513.x.

Patashnik, O., 1988, BibTeXing. Documentation for general BibTeX users.

Pedreira, A., M. de Aragão, A. Magalhães, and A. Viana, 2008, Ambientes de sedimentação siliciclástica do Brasil: Beca.

Pica, A., J. P. Diet, and A. Tarantola, 1990, Nonlinear inversion of seismic reflection data in a laterally invariant medium: Geophysics, **5**5, 284–292, doi: 10.1190/1.1442836.

Planke, S., E. Alvestad, and O. Eldholm, 1999, Seismic characteristics of basaltic extrusive and intrusive rocks: The Leading Edge, **1**8, 342–348, doi: 10.1190/1.1438289.

Plessix, R.-E., 2006, A review of the adjoint-state method for computing the gradient of a functional with geophysical applications: Geophysical Journal International, **1**67, 495–503, doi: 10.1111/j.1365-246x.2006.02978.x.

Popov, M. M., 2002, Ray theory and Gaussian beam method for Geophysicists: EDUFBA, Federal University of Bahia, Brazil.

Popov, M. M., I. Pšenčík, and V. Červený, 1978, Computation of ray amplitudes in inhomogeneous media with curved interfaces: Studia Geophysica et Geodaetica, **2**2, 248–258, doi: 10.1007/bf01627902.

Pratt, R. G., 1990, Inverse theory applied to multi-source cross-hole tomography. Part 2: elastic wave-equation method: Geophysical Prospecting, **3**8, 311–329, doi: 10.1111/j.1365-2478.1990.tb01847.x.

———, 1999, Seismic waveform inversion in the frequency domain, Part 1: Theory and verification in a physical scale model: Geophysics, **6**4, 888–901, doi: 10.1190/1.1444597.

Pratt, R. G., Z.-M. Song, P. Williamson, and M. Warner, 1996, Two-dimensional velocity models from wide-angle seismic data by wavefield inversion: Geophysical

Journal International, **1**24, 323–340, doi: 10.1111/j.1365-246x.1996.tb07023.x.

Pratt, R. G., and M. H. Worthington, 1990, Inverse theory applied to multi-source cross-hole tomography. Part 1: acoustic wave-equation method: Geophysical Prospecting, **3**8, 287–310, doi: 10.1111/j.1365-2478.1990.tb01846.x.

Prieux, V., G. Lambaré, S. Operto, and J. Virieux, 2012, Building starting models for full waveform inversion from wide-aperture data by stereotomography: Geophysical Prospecting, **6**1, 109–137, doi: 10.1111/j.1365-2478.2012.01099.x.

Przebindowska, A., 2013, Acoustic full waveform inversion of marine reflection seismic data: PhD thesis, Karlsruher Instituts für Technologie.

Ramírez, A. C., and A. B. Weglein, 2009, Green's theorem as a comprehensive framework for data reconstruction, regularization, wavefield separation, seismic interferometry, and wavelet estimation: A tutorial: Geophysics, **7**4, W35–W62, doi: 10.1190/1.3237118.

Ravaut, C., S. Operto, L. Improta, J. Virieux, A. Herrero, and P. Dell'Aversana, 2004, Multiscale imaging of complex structures from multifold wide-aperture seismic data by frequency-domain full-waveform tomography: application to a thrust belt: Geophysical Journal International, **1**59, 1032–1056, doi: 10.1111/j.1365-246x.2004.02442.x.

Ribeiro, H., 2001, Estratigrafia de seqüências: fundamentos e aplicações: Editora da Universidade do Vale do Rio dos Sinos.

Rieber, F., 1936a, A new reflection system with controlled directional sensitivity: Geophysics, **1**, 97–106, doi: 10.1190/1.1437082.

———, 1936b, Visual presentation of elastic wave patterns under various structural conditions: Geophysics, **1**, 196–218, doi: 10.1190/1.1437093.

Robertson, H., 1986, Everette Lee DeGolyer: The Leading Edge, **5**, 14–21, doi: 10.1190/1.1439195.

———, 2000, A historic correspondence regarding the introduction of the torsion balance to the United States: The Leading Edge, **1**9, 652–654, doi: 10.1190/1.1438688.

Rocca, F., and L. Salvador, 1982, Residual migration: Presented at the SEG Technical Program Expanded Abstracts 1982, Society of Exploration Geophysicists, doi: 10.1190/1.1807575.

Rose, J. H., 1989, Elastic wave inverse scattering in nondestructive evaluation: Pure and Applied Geophysics PAGEOPH, **1**31, 715–739, doi: 10.1007/bf00876270.

———, 2001, "Single-sided" focusing of the time-dependent Schrödinger equation: Physical Review A, **6**5, doi: 10.1103/physreva.65.012707.

———, 2002, “Single-sided” autofocusing of sound in layered materials: Inverse Problems, **18**, 1923–1934, doi: 10.1088/0266-5611/18/6/329.

Rossum, G., 1995, Python reference manual: Technical report, Amsterdam, The Netherlands, The Netherlands.

Rothman, D. H., S. A. Levin, and F. Rocca, 1985, Residual migration: Applications and limitations: Geophysics, **50**, 110–126, doi: 10.1190/1.1441822.

Sacchi, M. D., 1998, A bootstrap procedure for high-resolution velocity analysis: Geophysics, **63**, 1716–1725, doi: 10.1190/1.1444467.

Sandwell, D. T., 1987, Biharmonic spline interpolation of GEOS-3 and SEASAT altimeter data: Geophysical Research Letters, **14**, 139–142, doi: 10.1029/gl014i002p00139.

Santos, E. B., H. B. Santos, I. Vitorello, and M. B. de Pádua, 2013a, 2-D magnetotelluric inversion of the central part of Paraná Basin: Presented at the AGU Fall Meeting, American Geophysical Union.

Santos, E. B., H. B. Santos, I. Vitorello, and M. B. Pádua, 2013b, Joint Interpretation of Magnetotelluric and Gravimetric Data from the South American Paraná Basin: Presented at the Meeting of the Americas, AGU, American Geophysical Union.

———, 2013c, Joint Interpretation of Magnetotelluric and Gravimetric Data in the Paraná Basin: Presented at the 13th International Congress of the Brazilian Geophysical Society & EXPOGEF, SBGf, doi: 10.1190/sbgf2013-354.

Santos, H., D. Macedo, E. Santos, J. Schleicher, and A. Novais, 2014a, Specific target determination by planting anomalous densities applied to seismic migration-velocity improvements: Presented at the EGU General Assembly 2014, Copernicus GmbH (Copernicus Publications).

Santos, H., E. Yokoyama, E. Santos, E. P. Leite, and J. C. Ferreira, 2013d, 3D Forward Gravity Modeling of Vargeão Impact Structure: Preliminary Results: Presented at the EGU General Assembly 2013, Copernicus GmbH (Copernicus Publications).

Santos, H. B., T. A. Coimbra, J. Schleicher, and A. Novais, 2014b, Remigration-trajectory velocity analysis: Improved derivation and proof of concept: Annual WIT Report No. 18.

———, 2015a, Migration velocity analysis using time-remigration trajectory: regions with strong velocity variations: SEG Technical Program Expanded Abstracts 2015, Society of Exploration Geophysicists, 5295–5299, doi: 10.1190/segam2015-5932576.1.

———, 2015b, Prestack time-migration velocity analysis using remigration trajectories: Geophysics, **80**, S151–S163, doi: 10.1190/geo2014-0205.1.

———, 2015c, Remigration-trajectory time-migration velocity analysis in regions with strong velocity variations: Presented at the 77th EAGE Conference and Exhibition 2015, EAGE Publications, doi: 10.3997/2214-4609.201413048.

———, 2015d, Remigration-trajectory time-migration velocity analysis in regions with strong velocity variations: Presented at the 14th International Congress of the Brazilian Geophysical Society & EXPOGEF, SBGf, doi: 10.1190/sbgf2015-209.

Santos, H. B., D. L. Macedo, E. B. Santos, J. Schleicher, and A. Novais, 2013e, Construction of an initial velocity model for migration velocity analysis from gravimetric inversion: Presented at the AGU Fall Meeting, American Geophysical Union.

———, 2014c, Use of 3D gravity inversion to aid seismic migration-velocity building: Annual WIT Report No. 18.

———, 2015e, Use of 3D gravity inversion to aid seismic migration-velocity building: Presented at the 14th International Congress of the Brazilian Geophysical Society & EXPOGEF, SBGf, doi: 10.1190/sbgf2015-274.

———, 2015f, Use of 3D gravity inversion to aid seismic migration-velocity building: SEG Technical Program Expanded Abstracts 2015, Society of Exploration Geophysicists, 1520–1525, doi: 10.1190/segam2015-5929222.1.

Santos, H. B., J. Schleicher, and A. Novais, 2013f, Initial-model Construction for MVA Techniques: 75th EAGE Conference & Exhibition incorporating SPE EUROPEC 2013, EAGE Publications BV, 10–13, doi: 10.3997/2214-4609.20130939.

———, 2013g, Initial-model construction for MVA techniques: Annual WIT Report No. 17.

Santos, H. B., J. Schleicher, A. Novais, A. Kurzmann, and T. Bohlen, 2015g, Robust time-domain migration velocity analysis methods for initial-model building in a full waveform tomography workflow: Annual WIT Report No. 19.

———, 2016a, Robust time-domain migration velocity analysis for initial-model building in a full-waveform tomography workflow: SEG Technical Program Expanded Abstracts 2016, Society of Exploration Geophysicists, 5307–5312, doi: 10.1190/segam2016-13967472.1.

———, 2016b, Robust time-domain migration velocity analysis methods for initial-model building in a full waveform tomography workflow: Presented at the 78th EAGE Conference and Exhibition 2016, EAGE Publications, doi: 10.3997/2214-4609.201600638.

———, 2016c, Robust time-domain migration velocity analysis methods for initial-model building in a full waveform tomography workflow: Presented at the VII Simpósio Brasileiro de Geofísica (SimBGf), Sociedade Brasileira de Geofísica (SBGf).

Santos, H. B., J. Schleicher, M. A. Schleicher, A. Kurzmann, and T. Bohlen, 2016d, Robust time-domain migration velocity analysis for initial-model building in a full-waveform tomography workflow: SEG Technical Program Expanded Abstracts, Society of Exploration Geophysicists, 5307–5312, doi: 10.1190/segam2016-13967472.1.

Santos, H. B., L. S. S. Valente, J. C. Costa, and J. Schleicher, 2015h, Time-to-depth conversion and velocity estimation by wavefront-propagation: Presented at the SEG International Exposition and 85th Annual Meeting, Society of Exploration Geophysicists, doi: 10.1190/segam2015-5922300.1.

Santos, H. B., E. Yokoyama, E. B. Santos, E. P. Leite, and J. C. Ferreira, 2013h, Gravity Gradient Tensor of Vargeao Impact Structure, South Brazil: 75th EAGE Conference & Exhibition incorporating SPE EUROPEC 2013, EAGE Publications, 10–13, doi: 10.3997/2214-4609.20130592.

Sattlegger, J. W., 1975, Migration velocity determination: Part I. Philosophy: Geophysics, **40**, 1–5, doi: 10.1190/1.1440512.

Sava, P., B. Biondi, and J. Etgen, 2005, Wave-equation migration velocity analysis by focusing diffractions and reflections: Geophysics, **70**, U19–U27, doi: 10.1190/1.1925749.

Schleicher, J., A. Novais, and J. C. Costa, 2008, Vertical image waves in elliptically inhomogeneous media: Studia Geophysica et Geodaetica, **52**, 101–122.

Schleicher, J., and R. Aleixo, 2007, Time and depth remigration in elliptically anisotropic media using image-wave propagation: Geophysics, **72**, S1–S9, doi: 10.1190/1.2374857.

Schleicher, J., and R. Biloti, 2007, Dip correction for coherence-based time migration velocity analysis: Geophysics, **72**, S41–S48, doi: 10.1190/1.2400844.

———, 2008, A frequency criterion for optimal node selection in smoothing with cubic splines: Geophysical Prospecting, **56**, 229–237, doi: 10.1111/j.1365-2478.2007.00663.x.

Schleicher, J., and J. C. Costa, 2009, Migration velocity analysis by double path-integral migration: Geophysics, **74**, WCA225–WCA231, doi: 10.1190/1.3162482.

Schleicher, J., J. C. Costa, and A. Novais, 2008, Time-migration velocity analysis by image-wave propagation of common-image gathers: Geophysics, **73**, VE161–VE171, doi: 10.1190/1.2968952.

Schleicher, J., J. C. Costa, L. T. Santos, A. Novais, and M. Tygel, 2009, On the estimation of local slopes: Geophysics, **74**, P25–P33, doi: 10.1190/1.3119563.

Schleicher, J., P. Hubral, G. Höcht, and F. Liptow, 1997, Seismic constant-velocity remigration: Geophysics, **62**, 589–597, doi: 10.1190/1.1444168.

Schleicher, J., M. Tygel, and P. Hubral, 2007, Seismic true-amplitude imaging: Society of Exploration Geophysicists, doi: 10.1190/1.9781560801672.

Schlottmann, R. B., 1999, A path integral formulation of acoustic wave propagation: Geophysical Journal International, **137**, 353–363, doi: 10.1046/j.1365-246x.1999.00793.x.

Schneider, W. A., 1978, Integral formulation for migration in two and three dimensions: Geophysics, **43**, 49–76, doi: 10.1190/1.1440828.

Schuster, G. T., 2009, Seismic interferometry: Cambridge University Press.

Schuster, G. T., J. Yu, J. Sheng, and J. Rickett, 2004, Interferometric/daylight seismic imaging: Geophysical Journal International, **157**, 838–852, doi: 10.1111/j.1365-246x.2004.02251.x.

Sethian, J. A., 1999a, Fast marching methods: SIAM Review, **41**, 199–235, doi: 10.1137/s0036144598347059.

———, 1999b, Level set methods and fast marching methods: Cambridge University Press.

Shapiro, S. A., and P. Hubral, 1999, Elastic waves in random media: Fundamentals of seismic stratigraphic filtering. Lecture Notes in Earth Sciences: Springer Berlin Heidelberg, doi: 10.1007/bfb0117709.

Shaw, H., and E. Lancaster-Jones, 1922, The Eötvös torsion balance: Proceedings of the Physical Society of London, **35**, 151–166, doi: 10.1088/1478-7814/35/1/319.

Shaw, P. R., and J. A. Orcutt, 1985, Waveform inversion of seismic refraction data and applications to young Pacific crust: Geophysical Journal International, **82**, 375–414, doi: 10.1111/j.1365-246x.1985.tb05143.x.

Sheriff, R., and L. Geldart, 1995, Exploration seismology: Cambridge University Press.

Shin, C., and Y. H. Cha, 2008, Waveform inversion in the laplace domain: Geophysical Journal International, **173**, 922–931, doi: 10.1111/j.1365-246x.2008.03768.x.

———, 2009, Waveform inversion in the Laplace-Fourier domain: Geophysical Journal International, **177**, 1067–1079, doi: 10.1111/j.1365-246x.2009.04102.x.

Shtivelman, V., and S. Keydar, 2005, Imaging shallow subsurface inhomogeneities by 3D multipath diffraction summation: First Break, **23**, doi: 10.3997/1365-2397.2005001.

———, 2008, Weighted multipath summation as a tool for imaging localized near-surface inhomogeneities: Presented at the Near Surface 2008 - 14th EAGE European Meeting of Environmental and Engineering Geophysics, EAGE Publications BV, doi: 10.3997/2214-4609.20146237.

Silva, E. F. F., R. Portugal, and A. Vicentini, 2009, Model rays for depth-to-time conversion: 11th International Congress of the Brazilian Geophysical Society & EXPOGEF 2009, Salvador, Bahia, Brazil, 24-28 August 2009, Society of Exploration Geophysicists and Brazilian Geophysical Society, 990–993, doi: 10.1190/sbgf2009-213.

Sirgue, L., 2003, Inversion de la forme d'onde dans le domaine fréquentiel de données sismiques grands offsets: PhD thesis, Université Paris and Queen's University.

Sirgue, L., and R. G. Pratt, 2004, Efficient waveform inversion and imaging: A strategy for selecting temporal frequencies: Geophysics, **69**, 231–248, doi: 10.1190/1.1649391.

Staal, X. R., and D. J. Verschuur, 2012a, Velocity estimation using internal multiples: Presented at the SEG Technical Program Expanded Abstracts 2012, Society of Exploration Geophysicists, doi: 10.1190/segam2012-1580.1.

———, 2012b, Velocity model estimation by full waveform tomography of seismic reflection data: Presented at the 74th EAGE Conference and Exhibition incorporating EUROPEC 2012, EAGE Publications BV, doi: 10.3997/2214-4609.20148590.

Stockwell Jr., J. W., 1999, The CWP/SU: Seismic Un*x package: Computers & Geosciences, **25**, 415–419, doi: 10.1016/s0098-3004(98)00145-9.

Stolt, R. H., 1978, Migration by Fourier transform: Geophysics, **43**, 23–48, doi: 10.1190/1.1440826.

Stolt, R. H., and A. B. Weglein, 2011, Seismic imaging and inversion: Application of linear inverse theory: Cambridge University Press, doi: 10.1017/cbo9781139056250.

Stork, C., 1992, Reflection tomography in the postmigrated domain: Geophysics, **57**, 680–692, doi: 10.1190/1.1443282.

Sun, R., and G. A. McMechan, 1992, 2-D full-wavefield inversion for wide-aperture, elastic, seismic data: Geophysical Journal International, **111**, 1–10, doi: 10.1111/j.1365-246x.1992.tb00550.x.

Symes, W. W., 2008, Migration velocity analysis and waveform inversion: Geophysical Prospecting, **56**, 765–790, doi: 10.1111/j.1365-2478.2008.00698.x.

Szabó, Z., 2015, The history of the 125 year old Eötvös torsion balance: Acta Geodaetica et Geophysica, **51**, 273–293, doi: 10.1007/s40328-015-0126-4.

Tarantola, A., 1984, Inversion of seismic reflection data in the acoustic approximation: Geophysics, **49**, 1259–1266, doi: 10.1190/1.1441754.

———, 1986, A strategy for nonlinear elastic inversion of seismic reflection data: Geophysics, **51**, 1893–1903, doi: 10.1190/1.1442046.

———, 1987, Inverse problem theory: Methods for data fitting and model parameter estimation.

Telford, W., W. M. Telford, L. Geldart, and R. Sheriff, 1990, Applied geophysics. Monograph series: Cambridge University Press.

Tygel, M., J. Schleicher, and P. Hubral, 1996, A unified approach to 3-D seismic reflection imaging, Part II: Theory: Geophysics, **61**, 759–775, doi: 10.1190/1.1444002.

Tygel, M., J. Schleicher, P. Hubral, and C. Hanitzsch, 1993, Multiple weights in diffraction stack migration: Geophysics, **58**, 1820–1830, doi: 10.1190/1.1443397.

Valente, L. S. S., 2013, Evaluation of algorithms for the conversion of velocity models from time to depth: Master's thesis, Federal University of Pará. (In Portuguese).

Valente, L. S. S., J. C. Costa, and J. Schleicher, 2009, Evaluation of time to depth conversion algorithms for depth velocity model building: Annual WIT Report, **13**, 131–142.

Valente, L. S. S., H. B. Santos, J. C. Costa, and J. Schleicher, 2014, A strategy for time-to-depth conversion and velocity estimation: Annual WIT Report No. 18.

———, 2015a, 2D robust time-to-depth conversion by wavefront-propagation: Presented at the 14th International Congress of the Brazilian Geophysical Society & EXPOGEF, SBGf, doi: 10.1190/sbgf2015-239.

———, 2015b, A wavefront-propagation strategy for time-to-depth conversion: Presented at the 77th EAGE Conference and Exhibition 2015, EAGE Publications, doi: 10.3997/2214-4609.201413051.

———, 2017, Time-to-depth conversion and velocity estimation by image-wavefront propagation: Geophysics, **82**, U75–U85, doi: 10.1190/geo2016-0570.1.

Vasconcelos, I., 2013, Source-receiver, reverse-time imaging of dual-source, vector-acoustic seismic data: Geophysics, **78**, WA123–WA145, doi: 10.1190/geo2012-0300.1.

Vasconcelos, I., P. Sava, and H. Douma, 2010, Nonlinear extended images via image-domain interferometry: Geophysics, **75**, SA105–SA115, doi: 10.1190/1.3494083.

Vasconcelos, I., and R. Snieder, 2008a, Interferometry by deconvolution: Part 1 — theory for acoustic waves and numerical examples: Geophysics, **73**, S115–S128, doi: 10.1190/1.2904554.

———, 2008b, Interferometry by deconvolution: Part 2 — theory for elastic waves and application to drill-bit seismic imaging: Geophysics, **73**, S129–S141, doi: 10.1190/1.2904985.

Vasconcelos, I., R. Snieder, and H. Douma, 2009, Representation theorems and green's function retrieval for scattering in acoustic media: Physical Review E, **80**, doi: 10.1103/physreve.80.036605.

Vasconcelos, I., R. Snieder, and B. Hornby, 2008, Imaging internal multiples from subsalt VSP data — examples of target-oriented interferometry: Geophysics, **73**, S157–S168, doi: 10.1190/1.2944168.

Verschuur, D. J., 2006, Seismic multiple removal techniques: past, present and future. Education tour series: EAGE Publications BV.

Verschuur, D. J. E., and A. J. G. Berkhout, 2011, Seismic migration of blended shot records with surface-related multiple scattering: Geophysics, **76**, A7–A13, doi: 10.1190/1.3521658.

Versteeg, R., 1994, The Marmousi experience: Velocity model determination on a synthetic complex data set: The Leading Edge, **13**, 927–936, doi: 10.1190/1.1437051.

Versteeg, R. J., 1993, Sensitivity of prestack depth migration to the velocity model: Geophysics, **58**, 873–882, doi: 10.1190/1.1443471.

Vinje, V., E. Iversen, and H. Gjøystdal, 1993, Traveltime and amplitude estimation using wavefront construction: Geophysics, **58**, 1157–1166, doi: 10.1190/1.1443499.

Virieux, J., and S. Operto, 2009, An overview of full-waveform inversion in exploration geophysics: Geophysics, **74**, WCC1–WCC26, doi: 10.1190/1.3238367.

Wapenaar, K., F. Broggini, E. Slob, and R. Snieder, 2013, Three-dimensional single-sided marchenko inverse scattering, data-driven focusing, green's function retrieval, and their mutual relations: Physical Review Letters, **110**, doi: 10.1103/physrevlett.110.084301.

Wapenaar, K., J. Thorbecke, J. van der Neut, F. Broggini, E. Slob, and R. Snieder, 2014, Marchenko imaging: Geophysics, **79**, WA39–WA57, doi: 10.1190/geo2013-0302.1.

Weglein, A. B., F. A. Gasparotto, P. M. Carvalho, and R. H. Stolt, 1997, An inverse-scattering series method for attenuating multiples in seismic reflection data: Geophysics, **62**, 1975–1989, doi: 10.1190/1.1444298.

While, J., A. Jackson, D. Smit, and E. Biegert, 2006, Spectral analysis of gravity gradiometry profiles: Geophysics, **71**, J11–J22, doi: 10.1190/1.2169848.

Yang, P., J. Gao, and B. Wang, 2015, A graphics processing unit implementation of time-domain full-waveform inversion: Geophysics, **80**, F31–F39, doi: 10.1190/geo2014-0283.1.

Yilmaz, Ö., and J. F. Claerbout, 1980, Prestack partial migration: Geophysics, **45**, 1753–1779, doi: 10.1190/1.1441064.

Zahradník, J., P. Moczo, and F. Hron, 1993, Testing four elastic finite-difference schemes for behavior at discontinuities: Bulletin of the Seismological Society of America, **83**, 107–129.

Zhu, J., L. Lines, and S. Gray, 1998, Smiles and frowns in migration/velocity analysis: Geophysics, **63**, 1200–1209, doi: 10.1190/1.1444420.

# Appendix A

# Summary of publications

In this appendix, I provide a short appreciation of all publications that originated from the work developed during this Ph.D. thesis, some of which are included in this thesis.

In essence, my doctoral studies concentrated on three segments, being the MVA methods in time; the techniques for converting velocity models (or its corresponding migrated image) in the time domain to depth; and FWI methods.

I started my research by comparing new MVA techniques with conventional ones. In Chapter 2, I discussed two recent time MVA methods, being common-image-gather image-wave propagation and double multi-stack migration, and compared their potential for the construction of initial models for more sophisticated MVA techniques. I analyzed the practical aspects of their applications, such as computational cost, quality of the obtained model, human interaction required, to evaluate the methods quantitatively and qualitatively. The experiments showed that both methods could be used in a fully automated procedure to produce a velocity model and a time-migrated image without a-priori information at a comparable cost. In 2013, my initial results were published in one expanded abstract in the proceedings of an international conference (Santos et al., 2013f). I also produced a technical report (Santos et al., 2013g).

The work on migration-velocity analysis using remigration trajectories presented in Chapter 3 was published in five expanded abstracts in the proceedings of international conferences (Coimbra et al., 2013c, 2014; Santos et al., 2015c,d,a), two reports (Coimbra et al., 2013d; Santos et al., 2014b), and in one journal article (Santos et al., 2015b).

In the intermediate stage of my doctoral thesis, I investigated the quality of the velocity models converted from the time domain to the depth. Despite being an attractive method, time-to-depth conversion is an ill-posed problem, aggregating the limitations of all involved steps (e.g., the constraints involved in time migration, ray-tracing, and Dix-based velocity conversion). This motivated me to seek a more stable technique, an alternative algorithm for the time-to-depth conversion, which does not require the tracing of individual image rays. Instead, it simulates the propagation of an image wavefront in the subsurface as discussed in Chapter 4. The content of this chapter was published in three expanded abstracts in the proceedings of international conferences (Valente et al., 2015b,a; Santos et al., 2015h), one report (Valente et al., 2014), and was accepted in a journal article (Valente et al., 2017).

The third and last segment that makes up my thesis was discussed in Chapter 5, in which my studies focused on the FWT applications, attempting to achieve a fully automatic tool for initial-model building in an FWT workflow. I presented a workflow for the construction of initial velocity-models for FWT methods consisting of automatic time-migration velocity analysis employing double multi-stack migration, followed by time-to-depth conversion by image-ray wavefront propagation. The content of this chapter as published in one scientific report (Santos et al., 2015g), and will be presented as expanded abstracts in the proceedings of upcomming international conferences (Santos et al., 2016b,a,c), and a manuscript is under preparation.

In addition to the results presented in this thesis, Santos et al. (2013e, 2014a,c, 2015e,f) develop a 3D depth-velocity model building based on 3D gravity inversion. The method consists in determine the density distribution of specific bodies (targets), and replace them by coherent velocity values. This initial velocity model can be used together with migration velocity analysis tools, which in turn, can provide sufficient information to updated the initial geometric parameters for a recent gravity inversion. The main advantage of this technique is that it provide an iterative and robust algorithm that does not require the solution of an equation system. This joint processing and interpretation shows to be a fast alternative to improve the knowledge of complex structures like salt structures and sub-salt sediments.

Santos et al. (2013b,c,a) present the resulting Paraná Basin lithospheric model, obtained from processing and inversion of broadband and long-period magnetotelluric soundings along an E-W profile across the central part of the basin. The results are complemented by a qualitative joint interpretation of gravimetric data, in order to obtain a more precise geoelectric model of the deep structure of the region.

Santos et al. (2013d,h): present the gravity gradient tensor (GGT) of the residual Bouguer anomaly over the Dome Vargeão area. Since the GGT is more sensitivity to density variation, it can be a useful tool to understand the crater's geology. The results show that the center of the crater has a predominant negative density-contrast, characteristic of a region with sediments. However, the heterogeneities in this region are best observed in GGT. Furthermore, the crater is not symmetric mainly on east-west direction, suggesting that the eastern part of Vargeão's edge is more extensive and deep.

I have also contributed to other open-source projects, all of which can be accessed through my Github profile (https:/github.com/hbueno).

The full list of my publications can be found on Currículo Lattes (Brazilian online resume; http://lattes.cnpq.br/4062685231290581).

# Appendix B

# Used hard- and software

> *Computers are useless. They can only give you answers.*
>
> — Pablo Picasso

Throughout the course of the doctorate I used, adapted and developed several software packages. Moreover, I utilized different hardware resources for diverse tasks and needs. In this appendix, I provide detailed information for the most relevant requirements for the development of this Ph.D. thesis.

## B.1 Hardware

Within the scope of this work, I employed several computers, workstations, or high-performance computers (HPCs) to develop, test or obtain the preliminary results or those shown in this thesis.

For the development and testing of computational codes, preparation and adjustment of experiments, elaboration of this thesis and other ordinary tasks, the following computers were used:

- Notebook MacBook Pro®: Processor 2.9 GHz Intel® Core i7™; Memory 8 GB 1600 MHz DDR; System OS X® 10.9.5.
- Desktop Dell™ OptiPlex™ 780: Processor Intel® Core™2 Quad (4 Cores) Q9650, 12 MB L2 Cache, 3.00 GHz, 1333 MHz FSB; Memory 8 GB RAM; System Linux Ubuntu 12.04 LTS.

The work on migration-velocity analysis using the common-image-gather image-wave propagation and double multi-stack migration in Chapter 2, and the depth migrations shown in Chapter 4, were performed in the workstations at LGC (for more information, see `http://www.lgc.ime.unicamp.br/?page_id=1517`):

- Workstation Dell™ Precision™ R5500: Processor 2 × 6-cores (12 threads) Intel®, Xeon® X5675, 12 MB SmartCache, 3.06 GHz, 6.40 GT/s Intel® QPI; Memory 192 GB RAM 1333 MHz DDR; System Linux Ubuntu 12.04 LTS.
- Workstation Dell™ PowerEdge™ R420: Processor 2 × 8-cores (16 threads) Intel®, Xeon® E5-2450, 20 MB SmartCache, 2.10 GHz, 8.00 GT/s Intel® QPI; Memory 192 GB RAM 1333 MHz DDR; System Linux Ubuntu 12.04 LTS.

The following list includes all the HPCs required to perform the full waveform inversions results shown in Chapter 5. Their configurations are omitted for the sake of simplicity, but relevant addresses for on-line information are provided:

- Jülich Research on Petaflop Architectures (JUROPA) at Jülich Supercomputing Centre (JSC). More information:
  `http://www.fz-juelich.de/portal/EN/Research/ITBrain/Supercomputer/JUROPA.html`
- Universal HPC cluster of Baden-Württemberg's universities (bwUniCluster) at Steinbuch Centre for Computing (SCC) at Karlsruhe Institute of Technology (KIT). More information:
  `http://www.bwhpc-c5.de/wiki/index.php/Category:BwUniCluster`
- InstitutsCluster II (IC2) at SCC at KIT. More information:
  `http://www.scc.kit.edu/dienste/ic2.php`
- ForHLR at SCC at KIT, funded by Ministry of Science, Research and the Arts Baden-Württemberg and the German Research Foundation (DFG, "Deutsche Forschungsgemeinschaft"). More information:
  `https://wiki.scc.kit.edu/hpc/index.php/Category:ForHLR`

## B.2 Software

We used computers with the following operating systems: **OS X® 10.9.5**, **Linux Ubuntu 12.4 LST**, **Linux OpenSUSE 13.1**, and **SUSE Linux Enterprise Server (SLES) 11 Service Pack 4 (SP4)** as the basic operating system on HPCs. We list below the most relevant programs (in alphabetical order):

**CIGCONT** Fortran 90 code for velocity analysis by velocity continuation of common-image gathers, based on the theory proposed by Schleicher et al. (2008). The program package consists of programs in Fortran 90 and Shell scripts. The execution of the procedure also depends on some programs of SU, which must be accessible via the search path. In Chapter 2, we presented the theory and tested the use of an automatic picking avoiding the human interaction. To get it, one must contact the authors.

**CWP/SU: Seismic Un*x** Also known as SU, it is an open-source software package for seismic research and processing, developed and distributed by Center for Wave Phenomena (CWP), Colorado School of Mines (CSM), United States, under a FreeBSD-style license. More information can be found Stockwell Jr. (1999) and `http://www.cwp.mines.edu/cwpcodes/`.

**FDVEPS** 2D viscoelastic FD modeling implementation (now SOFI2D) by Bohlen (1998, 2002). Their domain decomposition is the basis for the parallel code of PROTEUS. To get it, one must contact the author (`thomas.bohlen@kit.edu`).

**FVELAN** Parallel Fortran 90 code for multi-stack migration velocity analysis based on the theory proposed by Schleicher and Costa (2009). To get it, one must contact the authors.

**GCC** Produced by the GNU Project and distributed by the Free Software Foundation (FSF, `https://www.fsf.org/`) under the GNU General Public License Version 3 (GNU GPLv3), the GNU Compiler Collection (GCC) is a compiler system which supports various programming languages. Among the different tools (and versions) used to develop this thesis, we highlight the compilers, debuggers, and some libraries for C/C++ and FORTRAN. More information: `https://gcc.gnu.org/`.

**Inkscape** Free and open-source software for vector graphics creation and edition, developed by The Inkscape Project (Team) licensed under GPL. The vector graphics shown in this thesis were drawn in Inkscape 0.91 (Inkscape, 2015). For more information `https://inkscape.org`.

**Intel Composer XE Suite** Developed and distributed by Intel® Corporation under commercial license, the Intel® Parallel Studio is a software development product that consists of tools to compile and debug C/C++ and FORTRAN (parallel) programs. The choice of compilers can influence processing time

(Kurzmann et al., 2009; Kurzmann, 2012). We compiled FVELAN with Intel® Fortran Compiler (ifort version 15.0.3). Moreover, to speed up the FWI calculation presented in Chapter 5, we used the Intel® C/C++ Compiler (icc) version 15.0.3 (gcc version 4.8.5 compatibility) and the Intel® MPI Library 5.0. More information: `https://www.intel.com`.

**LaTeX** Shortening of Lamport TeX, originally developed by Lamport (1986). LaTeX is a document preparation system, working as macro package for the typesetting system **TeX** (Patashnik, 1988). It is free software, distributed under the LaTeX Project Public License (LPPL). This thesis was written using the version **LaTeX 2$_\varepsilon$** together with several extensions. The bibliography was generated with **BibTeX**. Detailed information can be found at The LaTeX Project website: `https://www.latex-project.org/`.

**Lustre** Lustre® file system is a parallel distributed file system employed for HPCs simulation environments. This open-source software is available under the GNU GPL Version 2 only (GPLv2). More details can be seen in `http://lustre.org/`.

**Madagascar** Open-source research-software project designed for analysis of large-scale multidimensional data (Fomel et al., 2013). It is distributed in the online GitHub repository (`https://github.com/ahay/src`) under the terms of the GPLv2. More information can be found in the Madagascar website: `http://www.ahay.org/`.

**MATLAB** MATLAB® (MATrix LABoratory) is a high-level numerical computing system developed by MathWorks®, Inc., Natick, Massachusetts, United States. Different versions and releases were used during the development of this thesis, being, the newest one, the Release 2015b (MATLAB, 2015). More information can be found at `https://www.mathworks.com/`.

**MPICH** High-performance portable implementation of the Message Passing Interface (MPI) standard (MPIF, 1994) distributed under a BSD-like license. More information: `http://www.mpich.org/`.

**MVATRAJ** A set of MATLAB scripts to perform the prestack time-migration velocity analysis using remigration trajectories, based on the theory proposed by Santos et al. (2015b), which is the origin to the content seen in Chapter 3. To get it, one must contact the authors.

**OpenMP** The Open Multi-Processing (OpenMP) is an Application Programming Interface (API) that allows one to parallelize code over multi-platform shared-memory system (Dagum and Menon, 1998). More information: `http://www.openmp.org/`.

**Open MPI** The Open MPI Project is an open source MPI implementation (Gabriel et al., 2004) developed by the Open MPI Team under the New BSD License (`https://opensource.org/licenses/BSD-3-Clause`). More information: `https://www.open-mpi.org/`.

**PROTEUS** Parallel 2D acoustic time-domain FWT program based on FD modeling. Originally developed by Kurzmann (2012), is based, among other things, on the theories presented by Tarantola (1984) and Mora (1987b). Other aspects of seismic waves modeling are based on the massive parallelization comprising domain decomposition (Bohlen, 1998) and shot parallelization (Kurzmann et al., 2009). It is written in C and can be freely redistributed or modified under the terms of the GNU GPLv2 (`https://www.gnu.org/licenses/gpl-2.0.html`). The FWT results of Chapter 5 were obtained using an updated and adapted version of PROTEUS.

**Python** Created by Rossum (1995), Python is a free, high-level programming language currently maintained by the Python Software Foundation (PSF), Delaware, United States, under the terms of the Python Software Foundation License (PSFL). `https://docs.python.org/3/license.html`. Official website: `https://www.python.org`.

**Scons** Open-source software construction tool (Knight, 2005) maintained by The SCons Foundation and distributed under the MIT license. It is a Python-based make-like utility used here to assemble data analysis workflows from Madagascar programs, through the use of Scons configuration files, also known as SConstruct scripts. The primary source of information is the website: `http://www.scons.org/`.

**Slurm Workload Manager** Formerly known as Simple Linux Utility for Resource Management (SLURM), it is an open-source cluster resource management and job scheduling system for Linux and Unix-like kernels. This software is distributed under the GNU GPL in the online repository (`https://github.com/SchedMD/slurm`). For more information: `https://slurm.schedmd.com/`.

**SOFI2D** 2D viscoelastic time-domain FD seismic modeling. Written in C, it is a massive parallel modeling code for P- and SV-waves. It is free software under the terms of the GNU GPLv2 (`https://www.gnu.org/licenses/gpl-2.0.html`). SOFI2D is published and distributed on a GitLab (`https://about.gitlab.com/`) server located at the KIT. The following link leads to the latest release: `https://git.scc.kit.edu/GPIAG-Software/SOFI2D/tree/Release`.

# Appendix C

# B-splines regularization

*When in doubt, smooth.*

— Sir Harold Jeffreys

The purpose of this appendix it to present detailed information of the regularization used in the B-spline smoothing discussed in Chapter 2. We derived the expressions of a smoothness constraint for slope tomography proposed by Costa et al. (2008). The approach minimizes the velocity gradient in the dip direction of a possibly present reflector at an image point.

## C.1 Slope tomographic inversion

Following the notation of Costa et al. (2008), let us start defining the data space by

$$\boldsymbol{d} = \left[ \left( \boldsymbol{x}_s, \boldsymbol{x}_r, s_s, s_r, \boldsymbol{T}_{sr} \right)_n \right] (n = 1, ..., N) \ , \tag{C.1}$$

where $\boldsymbol{x}_s$ and $\boldsymbol{x}_r$ are the source and receiver positions, $s_s$ and $s_r$ are the slowness-vector projections into the source and receiver lines, $\boldsymbol{T}_{sr}$ are the traveltimes, and $N$ is the number of selected events.

The model vector in two dimensions is

$$\boldsymbol{m} = \left\{ \boldsymbol{p}, \left( \boldsymbol{X}, \theta_s, \theta_r, \tau_s, \tau_s \right)_n \right\} (n = 1, ..., N) \ , \tag{C.2}$$

where $\boldsymbol{p}$ is the parameters describing the velocity model, $\boldsymbol{X}$ is the scattering-point coordinates, $\theta_s$ and $\theta_r$, are the emergence angles, and $\tau_s$ and $\tau_r$, are the ray traveltimes.

We define the difference $\delta \boldsymbol{d} = \boldsymbol{d}^o - \boldsymbol{d}^c$, where $\boldsymbol{d}^o$ is the observed data, and $\boldsymbol{d}^c$ is the synthetic data computed (equation C.1) by ray tracing in the reference model. Thus, we need to define an initial reference model $\boldsymbol{m}_0$ to solve the inverse problem using linear iterations. However, in the $k$th iteration, we have

$$\delta \boldsymbol{d}_k = D\boldsymbol{F}(\boldsymbol{m}_k)\delta \boldsymbol{m}_k \ , \tag{C.3}$$

where $\delta \boldsymbol{d}_k$ is the deviation in the $k$th iteration, and the operator $D\boldsymbol{F}(\boldsymbol{m}_k)$ is the Fréchet derivative (Menke, 1989). The solution of the linear system (equation C.3) determines a new reference model,

$$\boldsymbol{m}_{k+1} = \boldsymbol{m}_k + \delta \boldsymbol{m}_k \ . \tag{C.4}$$

This procedure is repeated iteratively until a minimum of the norm of the deviation $\|\delta \boldsymbol{d}_k\|$ is reached or until a maximum number of steps. As in the work of Costa et al. (2008), in this thesis (Chapter 2), we use the Euclidian norm, also known as $L_2$ norm (Menke, 1989).

Costa et al. (2008) construct a model for the square of the medium velocity, which is represented using the tensor product of third-order B-splines as

$$p\left(x_1, x_3\right) = \sum_{k=1}^{N_1} \sum_{l=1}^{N_3} p^{kl} B_k(x_1) B_l(x_3) \ , \tag{C.5}$$

where $p^{kl}$ are the interpolation coefficients to be estimated by slope tomography, $B_k(x_j)$ are the base functions of the interpolator along $x_j$, and $N_j$ are the number of B-splines nodes in that direction.

## C.2 Regularization

The data are incomplete, so it is necessary to include conditions that reinforce those properties of the result that are desired. In other words, seismic tomographic inversions are ill-posed and require additional constraints in the form of regularization to impose smoothness on the solution.

The regularization parameter controls how much smoothness is applied to the inversion result. Applied in a least-squares sense at each node of the B-splines mesh, these constraints require the evaluation of first and second partial derivatives of the velocity model with respect to the spatial coordinates

$$\frac{\partial^n}{\partial x_1^n} p(x_1, x_3) = \sum_{k=1}^{N_1} \sum_{l=1}^{N_2} p^{kl} \frac{\partial^n B_k(x_1)}{\partial x_1^n} B_l(x_3) \ , \tag{C.6}$$

and correspondingly for the derivatives with respect to coordinate $x_3$.

Costa et al. (2008) discussed alternatives to enforce a geologically meaningful smoothing that does not rely on a priori information. For example, the distribution of the scattering points in depth when we assume that all the events to be used in the tomography are reflections. At each iteration of slope tomography, we take the angle $\alpha$ between the normal to the potential reflector and the vertical direction

$$\alpha = \frac{\theta_s + \theta_r}{2} \ . \tag{C.7}$$

Note that from equation C.7, the regularization is a little more data consistent. Moreover, it is not difficult to observe that the extracted dip field is smooth (a direct consequence of the ray-tracing in a smooth velocity background).

Now, let us add the regularization constraint

$$\boldsymbol{n}(\alpha; \boldsymbol{X}) \times \nabla p(\boldsymbol{X}) = \boldsymbol{0} \ , \tag{C.8}$$

which computes the velocity gradient at the scattering point $\boldsymbol{X}$ to smooth the velocity model along the potential reflectors.

In the dip regularization proposed by Costa et al. (2008), the dip information is obtained from ray tracing in the reference model during the inversion. Thus, it differs from other previous assumptions in the literature (see, e.g., Clapp et al., 2004, who applied reflection tomography to better flatten post-tomography common-image gathers).

Denoting the smoothing operator of equation C.8 by $\boldsymbol{D}_R$, and combining these regularizations, leads to the objective function

$$\begin{aligned}\Phi(\boldsymbol{m}) = {} & ||\boldsymbol{d} - \boldsymbol{F}(\boldsymbol{m})||_2^2 + \lambda_D^2 ||\boldsymbol{m} - \boldsymbol{m}_r||_2^2 + \lambda_{Lap}^2 ||(\boldsymbol{D}_1^2 \\ & + \boldsymbol{D}_3^2)(\boldsymbol{m} - \boldsymbol{m}_r)||_2^2 + \lambda_{C1}^2 ||\boldsymbol{D}_1^2(\boldsymbol{m} - \boldsymbol{m}_r)||_2^2 \\ & + \lambda_{C3}^2 ||\boldsymbol{D}_3^2(\boldsymbol{m} - \boldsymbol{m}_r)||_2^2 + \lambda_{G1}^2 ||\boldsymbol{D}_1(\boldsymbol{m} - \boldsymbol{m}_r)||_2^2 \\ & + \lambda_{G3}^2 ||\boldsymbol{D}_3(\boldsymbol{m} - \boldsymbol{m}_r)||_2^2 + \lambda_R^2 ||\boldsymbol{D}_R(\boldsymbol{m} - \boldsymbol{m}_r)||_2^2 \, ,\end{aligned} \tag{C.9}$$

where $\boldsymbol{m}_r$ is a background model, and where the factors $\lambda$ are Lagrangian multipliers that weight the contributions of regularization in the objective function.

Here, $\lambda_D$ determines the damping applied to all model parameter updates. The factors $\lambda_{Lap}$, $\lambda_{C1}$, $\lambda_{C3}$, $\lambda_{G1}$, and $\lambda_{G3}$ determine the smoothing weight applied to the isotropic curvature (Laplacian), as well as curvature (second derivative) and gradient (first derivative) in the $x_1$ and $x_3$ directions, respectively. These six constraints are applied only to the velocity parameters. The value of $\lambda_R$ controls the degree of smoothing of the velocity along potential reflectors.

At each iteration, we need to solve the linear system

$$\begin{bmatrix} D\boldsymbol{F}(\boldsymbol{m}_k) \\ \lambda_D \boldsymbol{I} \\ \lambda_{Lap}(\boldsymbol{D}_1^2 + \boldsymbol{D}_3^2) \\ \lambda_{C1}\boldsymbol{D}_1^2 \\ \lambda_{C3}\boldsymbol{D}_3^2 \\ \lambda_{G1}\boldsymbol{D}_1 \\ \lambda_{G3}\boldsymbol{D}_3 \\ \lambda_R \boldsymbol{D}_R \end{bmatrix} \delta\boldsymbol{m}_k = \begin{bmatrix} \delta\boldsymbol{d}_k \\ -\lambda_D(\boldsymbol{m}_k - \boldsymbol{m}_r) \\ -\lambda_{Lap}(\boldsymbol{D}_1^2 + \boldsymbol{D}_3^2)(\boldsymbol{m}_k - \boldsymbol{m}_r) \\ -\lambda_{C1}\boldsymbol{D}_1^2(\boldsymbol{m}_k - \boldsymbol{m}_r) \\ -\lambda_{C3}\boldsymbol{D}_3^2(\boldsymbol{m}_k - \boldsymbol{m}_r) \\ -\lambda_{G1}\boldsymbol{D}_1(\boldsymbol{m}_k - \boldsymbol{m}_r) \\ -\lambda_{G3}\boldsymbol{D}_3(\boldsymbol{m}_k - \boldsymbol{m}_r) \\ -\lambda_R\boldsymbol{D}_R(\boldsymbol{m}_k - \boldsymbol{m}_r) \end{bmatrix} \tag{C.10}$$

where $\boldsymbol{m}_r$ is a background model that can be chosen in different ways. For example, through the updating procedure known as creeping (Shaw and Orcutt, 1985). We can choose $\boldsymbol{m}_r = \boldsymbol{m}_k$, the current model from the previous iteration, which allows to tie the model to the initial model $\boldsymbol{m}_r = \boldsymbol{m}_0$, or some a priori model $\boldsymbol{m}_r = \boldsymbol{m}_p$.

## C.3 Lagrange Multipliers

We test different constraints for the velocity model in the objective function (equation C.9). The Lagrange multipliers for the B-splines regularization used on this thesis are given in the table below.

Here we have $\lambda_d$ as the weight applied to adjust the whole data, $\lambda_\tau$ and $\lambda_x$ the gradient and $\lambda_{\tau\tau}$ and $\lambda_{xx}$ the curvature in time and in the horizontal direction respectively.

Table C.1: Regularization setup formed by seven different sets of Lagrangian multipliers where $\lambda_d$ is the weight used to adjust the data, $\lambda_\tau$ for the time derivative, $\lambda_x$ for the horizontal derivative, and $\lambda_{\tau\tau}$ and $\lambda_{xx}$ for the second derivatives.

| **Regularization** | **Lagrangian multipliers** | | | | |
|---|---|---|---|---|---|
| | $\lambda_d$ | $\lambda_\tau$ | $\lambda_x$ | $\lambda_{\tau\tau}$ | $\lambda_{xx}$ |
| very hard | 1 | $10^{-3}$ | $2 \cdot 10^{-3}$ | $10^{-4}$ | $10^{-4}$ |
| hard | 1 | $10^{-4}$ | $2 \cdot 10^{-4}$ | $10^{-5}$ | $10^{-5}$ |
| strong | 1 | $10^{-5}$ | $2 \cdot 10^{-5}$ | $2.5 \cdot 10^{-6}$ | $2.5 \cdot 10^{-6}$ |
| intermediate | 1 | $10^{-6}$ | $2 \cdot 10^{-6}$ | $2.5 \cdot 10^{-7}$ | $2.5 \cdot 10^{-7}$ |
| weak | 1 | $10^{-7}$ | $10^{-7}$ | $2.5 \cdot 10^{-8}$ | $2.5 \cdot 10^{-8}$ |
| soft | 1 | $10^{-8}$ | $10^{-8}$ | $2.5 \cdot 10^{-9}$ | $2.5 \cdot 10^{-9}$ |
| very soft | 1 | $10^{-9}$ | $10^{-9}$ | $2.5 \cdot 10^{-10}$ | $2.5 \cdot 10^{-10}$ |

# Appendix D

# Residual migration

In the main text (Chapter 2), we discuss the concepts of residual migration primary stated by Rocca and Salvador (1982). In this appendix, we summarize the mathematical deduction to residual migration as presented by Rothman et al. (1985). We describe the process of migration as mapping the apparent dip $dt/dx$ to the correct dip $d\tau/dx$ using the following expressions:

$$\sin\theta = \frac{v}{2}\frac{dt}{dx}\ , \tag{D.1}$$

and

$$\tan\theta = \frac{v}{2}\frac{d\tau}{dx}\ , \tag{D.2}$$

resolving the system for $\theta$,

$$\frac{d\tau}{dx} = \frac{dt}{dx}\left[1 - \left(\frac{v}{2}\frac{dt}{dx}\right)^2\right]^{-1/2}\ . \tag{D.3}$$

This equation gives a relation between the time dip on the migrated section in regarding time dip on the unmigrated data. If the migrated dip described by equation D.3 is used as input to another migration using velocity $v'$, the new migrated slope can be expressed as

$$\frac{d\tau'}{dx} = \frac{d\tau}{dx}\left[1 - \left(\frac{v'}{2}\frac{dt}{dx}\right)^2\right]^{-1/2} = \frac{dt}{dx}\left[1 - \frac{v^2+v'^2}{4}\left(\frac{dt}{dx}\right)^2\right]^{-1/2}\ , \tag{D.4}$$

which is equation D.3 with $v$ replaced by $\sqrt{v^2 + v'^2}$.

Supposing that the initial migration velocity $v_m$ is wrong and that the true velocity is $v$, it is necessary to correct the migrated data. This can be done by making a migration with a new residual velocity $v_\varepsilon$ given by

$$v_\varepsilon = v \left[ 1 - \left( \frac{v_m}{v} \right)^2 \right]^{1/2} , \quad \text{when } v_m < v \ , \tag{D.5}$$

or modeling, i.e., unmigrating with

$$v_\varepsilon = v \left[ \left( \frac{v_m}{v} \right)^2 - 1 \right]^{1/2} , \quad \text{when } v_m > v \ . \tag{D.6}$$

# Appendix E

# Initial depth velocity model building

In Chapter 2 we discuss the application of two recent time MVA techniques, being common-image-gather image-wave propagation and double multi-stack migration. We have seen that both methods can provide a broad range of differently smoothed velocity models that produce equivalent image quality in time migration.

In attempt to evaluate which one of the used parameterization can lead to a best-suited starting model, we converted from time-to-depth domain all the time migration velocity models and their corresponding images produced by these two techniques using different regularizations (Table C.1). Some of our results can be see in Figures E.2 to E.5. For comparison, we depth migrated the Marmousoft data (Billette et al., 2003) using its true depth velocity model depicted in Figure E.1. In general, our results present a good match in the sedimentary parts of the model but yield some visible differences in the geologically complex central part.

Figures E.2 and E.3 show the time-to-depth conversion of the velocity models and images obtained after five iteration of the image-wave propagation method using, respectively, the auto-picks at the maxima of horizontal semblance (Figure 2.20, EXPERIMENT 1) and the auto-picks at the maxima of smoothed horizontal semblance (Figure 2.22, EXPERIMENT 2). Both velocity models present boundary effects of the B-splines interpolation and the produced images looks quite similar.

Figures E.4 and E.5 depict the time-to-depth conversion of the results obtained by the multi-stack MVA using a very hard regularization (Figure 2.30, EXPERIMENT 5) and a intermediate regularization (Figure 2.31, EXPERIMENT 5) respectively. We note the intermediate regularization produced results more similar those ones depicted in Figures E.2 and E.3. On the other hand, the smoothed velocity model (Figure E.4) has no clear evidence of boundary effects caused by the B-splines interpolation. Moreover, their corresponding time-to-depth converted

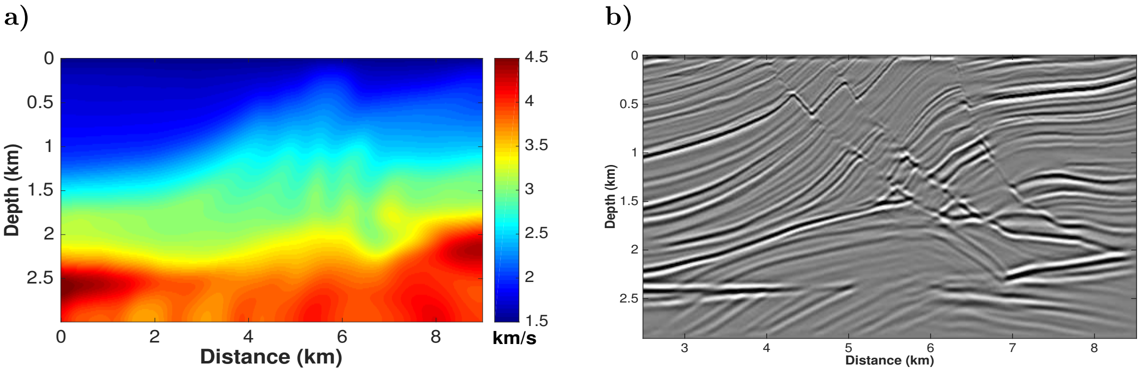

Figure E.1: (a) Marmousoft depth velocity model (Billette et al., 2003) and (b) depth migration.

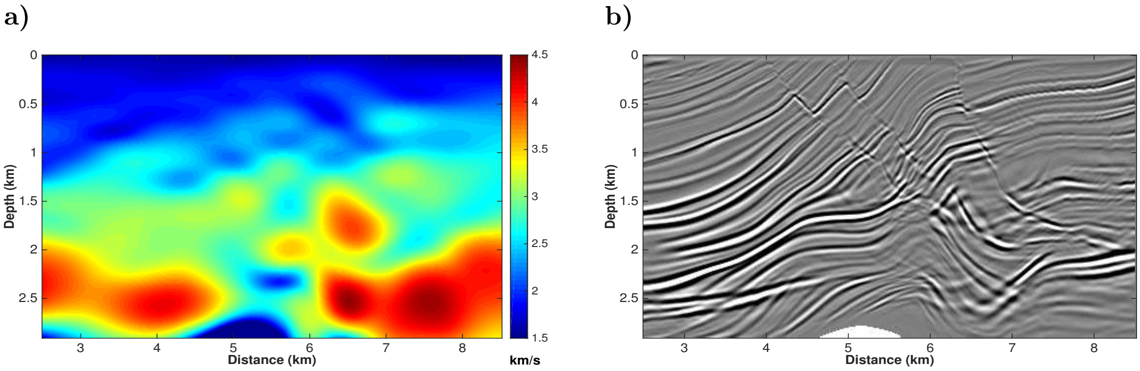

Figure E.2: Time-to-depth conversion of the velocity model (a) and image (b) obtained after five iteration of the image-wave propagation method discussed in Chapter 2, Figure 2.20 (Experiment 1).

image in Figure E.4 shows to be more similar with the depth migration using the true depth velocity model (Figure E.1).

These preliminary results suggest that specially in the depth domain, smoothed velocity models are able to produce better migrated images. Further research will evaluate if a smoothing step after the domain-conversion leads to better results. Furthermore, a prestack depth-migration velocity analysis should contribute with more informations. Anyway, the results presented here indicate that the direct connection of the time-MVA techniques with time-to-depth conversion strategies can be used as an efficient first step in seismic velocity model building.

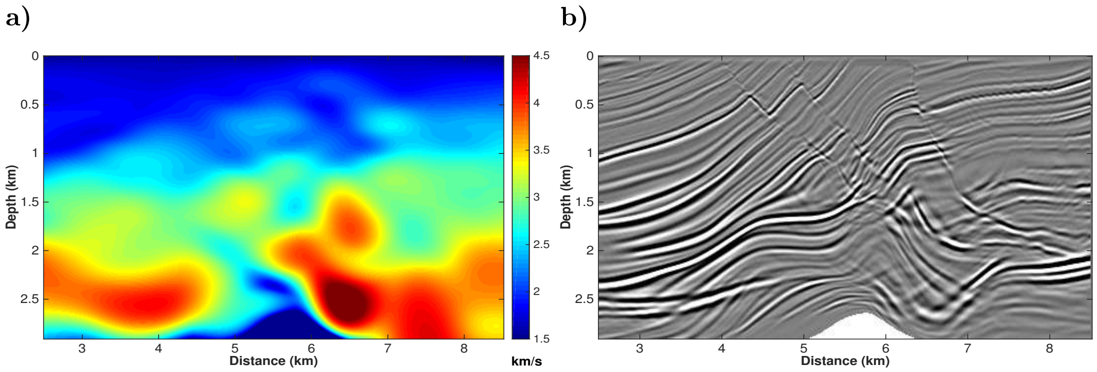

Figure E.3: Time-to-depth conversion of the velocity model (a) and image (b) obtained after five iteration of the image-wave propagation method discussed in Chapter 2, Figure 2.22 (Experiment 2).

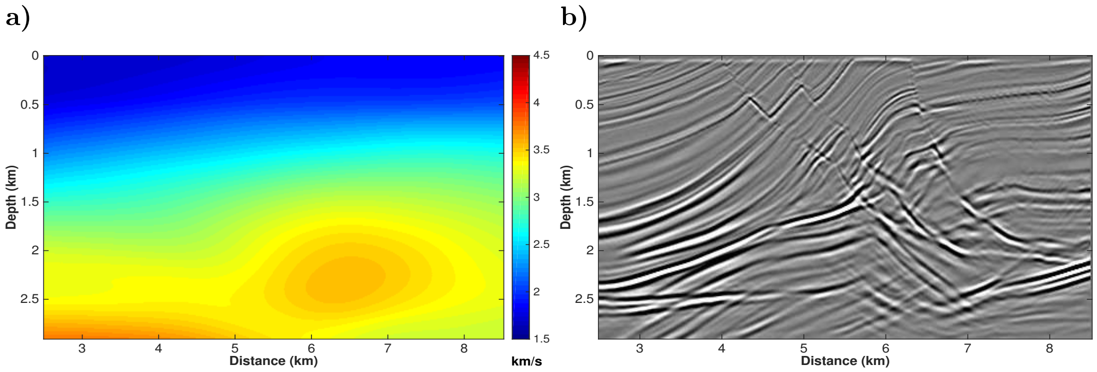

Figure E.4: Time-to-depth conversion of the velocity model (a) and image (b) obtained by a multi-stack MVA with very hard regularization, discussed in Chapter 2, Figure 2.30 (Experiment 5).

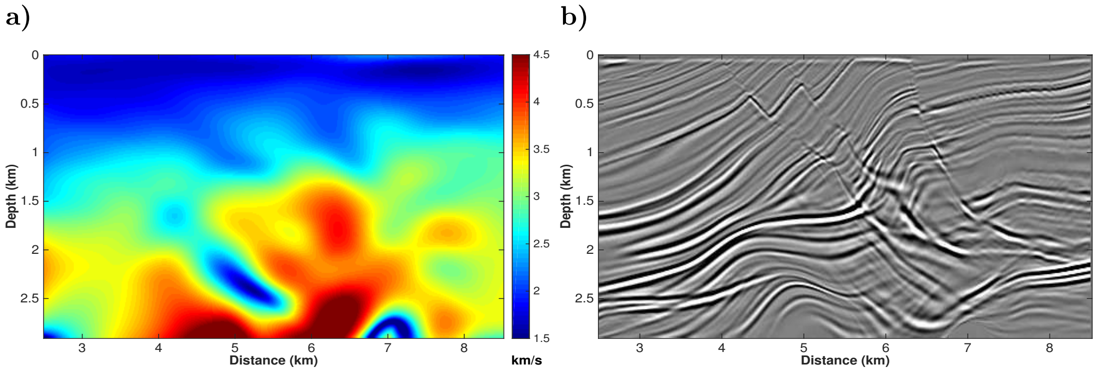

Figure E.5: Time-to-depth conversion of the velocity model (a) and image (b) obtained by a multi-stack MVA with intermediate regularization, discussed in Chapter 2, Figure 2.31 (Experiment 5).

# Appendix F

# The original Marmousi-2 model

In the main text, we show numerical experiments using modified versions of the 2D Marmousi model. For comparison and for the sake of completeness, we present the original $v_p$, $v_s$, and $\rho$ Marmousi-2 model created by Martin et al. (2002) based on Versteeg (1994). Whilst we have not used the S-wave velocity model in our analysis, the density model and the P-wave velocity model were the starting points for the forward modeling and inversion tests we have shown in Chapter 5. The model size is 3.5 km × 17 km which, using a grid spacing of 1.25 m, resulting in a grid size of 13 601 × 2801 grid points. In the $v_p$ model, values range from 1028 m/s to 4700 m/s.

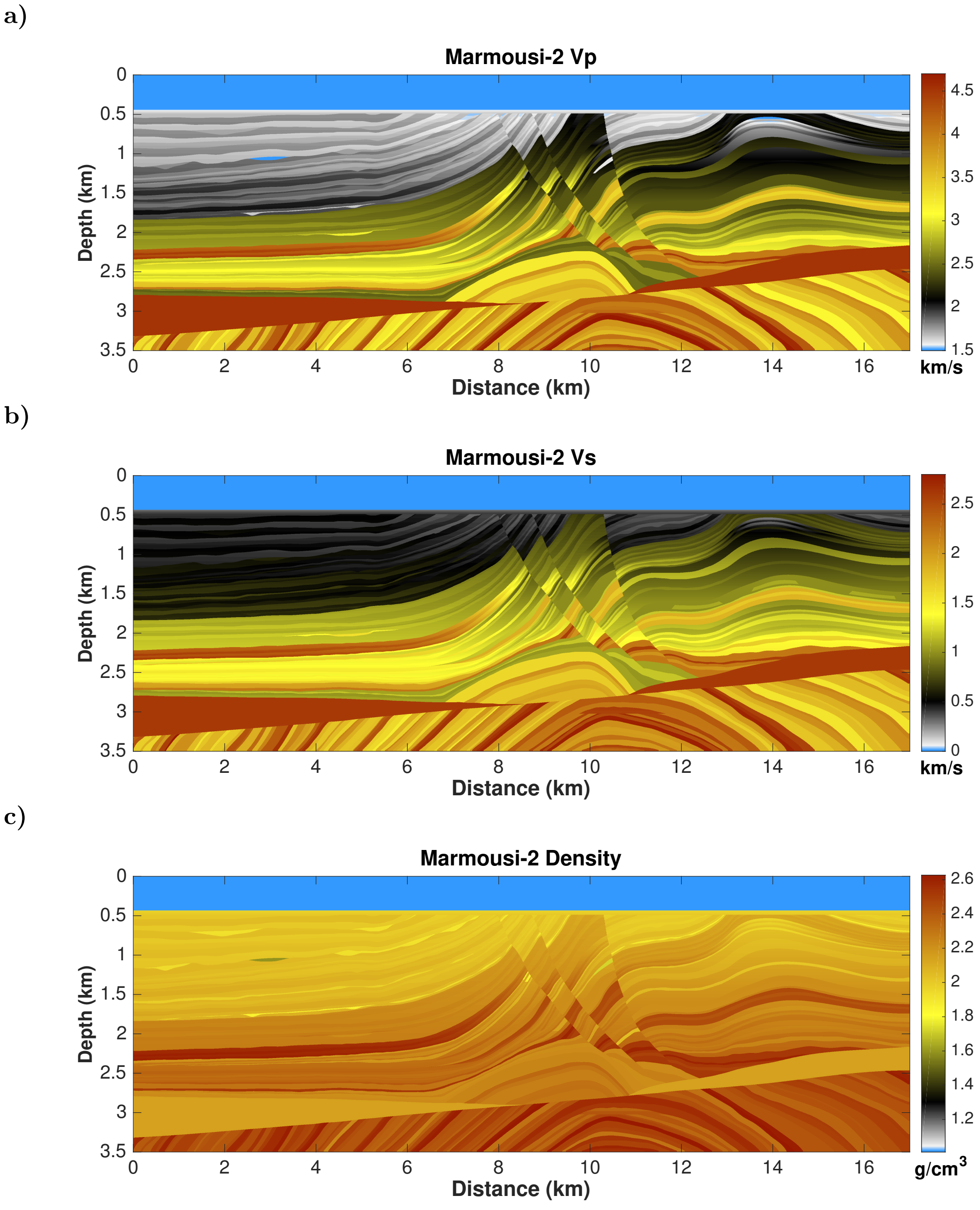

Figure F.1: The original Marmousi-2 model: (a) P-wave velocity ($v_p$), (b) S-wave velocity ($v_s$), and (c) density ($\rho$).